2020

Development of Advanced Anode Materials for Next Generation Lithium Batteries

Jaewoo Lee
University of Wollongong

UNIVERSITY
OF WOLLONGONG
AUSTRALIA

Development of Advanced Anode Materials for Next Generation Lithium Batteries

Jaewoo Lee

This thesis is presented as part of the requirements for the

Award of the Degree of Doctor of Philosophy

Institute for Superconducting & Electronic Materials
Australian Institute of Innovative Materials
University of Wollongong

August 2020

Certification

I, Jaewoo Lee, declare that this thesis is submitted in partial fulfilment of the requirements for the award of Doctor of Philosophy, in the Institute for Superconducting & Electronic Materials (ISEM), the Australian Institute of Innovative Materials (AIIM), University of Wollongong, NSW, Australia. This thesis is wholly my own work unless otherwise referenced or acknowledged. All the experimental data in this thesis is original. This thesis has never been submitted for qualifications at any other academic institutions.

Jaewoo Lee

August 2020

Acknowledgements

I would like to express my deepest gratitude to my principal supervisor, Prof. Jung Ho Kim for his professional supervision and even his valuable counsel. I also would like to express my utmost respect and appreciation to my co-supervisors and advisors, Prof. Hua Kun Liu, Prof. Shi Xue Dou, Prof. Min-Sik Park, Kyung Hee University and Prof. Hansu Kim, Hanyang University for their strong supports and professional instruction and suggestions.

My deep gratitude goes to my co-workers, Prof. Janghyuk Moon, Prof. Jong-Won Lee, Prof. Yoon-Uk Heo, Dr. Sang-Min Lee, Prof. Yusuke Yamauchi, Dr. Victor Malgras, Prof. Junghun Kim, Dr. Lok Kumar Shrestha, Prof. Katsuhiko Ariga, Junyoung Kim, and Seung Hyun Choi.

I would like to thank my group members and good friends, Dr. Kadhim Al-Attafi, Fanar Hussein Jawdat, Dr. Kyubin Shim, Dr. Suhun Kim, Dr. Shunsuke Tanaka, Dr. Sang A Han, Hamzeh Qutaish and Yuhwan Hyeon.

Finally, I would like to express my deep appreciation and love to my parents, sisters and brother, and especially to my beloved wife, Sohyun and my lovely son, Juwon. “Thank you for being by my side all the time.”

Abstract

For the past few decades, lithium-based batteries have played a crucial role in facilitating more rapid growth of portable electric devices and electric vehicle markets, because of their fascinating higher energy density and operating voltage than those of previous secondary batteries. However, in recent years, the development of lithium-based batteries is beyond increasing demands for energy storage devices due to the difficulties in further progress with the current transition metal oxides-graphite system. To resolve this issue, the exploration of new advanced materials is required to achieve a major breakthrough as well as, to change to next generation lithium batteries.

From the point of view of anode materials, both silicon (Si) and lithium (Li)-metal are regarded as the two most promising alternatives to replace the graphite anode due to their substantially high theoretical capacities (3590 mAh g^{-1} for Si and 3860 mAh g^{-1} for Li-metal). Thus, many researchers have endeavoured to explore these two candidates for achieving "beyond graphite". However, applying Si and Li-metal into their practical applications as anodes has still many hurdles to clear to each of them. Firstly, Si-based anodes suffer from poor cycling performance and dimensional instability induced by large volume changes during cycling. To resolve such problems, for example, nanostructured Si-based materials with delicately controlled microstructure and interfaces should be intensively investigated. Secondly, repeated Li plating/stripping during Li-metal anode cell operation forms dendritic Li and irreversible Li (dead-Li), leading to internal short-circuit and capacity fading. To resolve such problems, for example, strategically designed host structure for stable Li-metal storage should be suitably introduced.

Based on above aspects, in this thesis, considerable factors that each Si and Li-metal anode materials should satisfy were studied and strategical material designs for each Si and Li-metal

anode materials were suggested. In detail, first of all, it is demonstrated that the strategic design and synthesis of a gyroid three-dimensional network in a Si@SiOx/C nanoarchitecture with synergetic interaction between the computational prediction and the synthetic optimization. This silicon-based anode formed by a cost-effective one-pot synthetic route, exhibits not only excellent electrochemical performance, but also enhanced thermal stability. In addition, the theoretical capacities of a series of Si/SiOx with different oxygen contents were estimated by using X-ray photoelectron spectroscopy, and then those results were compared with empirical results in order to find out the relations between oxygen contents of the Si/SiOx and their electrochemical performances. Thirdly, the physical properties of nanoporous zeolitic imidazolate frameworks (ZIFs)-derived carbons which can be controlled by different ratios of zinc/cobalt ion metallic precursors, were studied. This approach informed to achieve tailored ZIF-derived carbons with different pore volumes, pore sizes, surface areas and even degrees of graphitization. Because of their large pore volumes and adjustable physical properties, it is suggested that the electrochemical performances of these ZIF-derived carbons as Li-metal storage host, can be maximized by controlling the properties of those. Finally, by controlled synthesis of bimetallic ZIF-derived carbon, cobalt nanoparticle embedded highly mesoporous N-graphite is proposed as new innovative Li-metal host anode. This material shows high Li affinity as well as high lithiophilic surface chemistry and, as a result, the anode shows excellent electrochemical performances with high Li-metal reversible capacity and even stable long-term cyclability with no dead-Li formation.

It can be concluded that the outcomes in this thesis which successfully confirm the progress in the developments of Si and Li-metal anode materials, can give more insight on the development of advanced anode materials for next generation Li batteries.

Table of Contents

Chapter 1. Introduction

1.1. Research Background

Over the past 160 years, the rechargeable battery technologies have steadily evolved from the lead-acid battery in the 1850s to the lithium-ion battery (LIB) in the present day, providing more convenience in our daily lives[1-4]. In particular, the battery industry has made tremendous progress toward large capacity, good safety features, and long cycle life since the LIB was commercialized in 1991[5-7]. Moreover, since lithium (Li) has been used in the rechargeable batteries, the cell potential of these batteries has dramatically increased, as shown in Figure 1.1a. Thus, LIBs are playing an essential role in applications from advanced mobile information technology (IT) devices to electric vehicle (EV) technology. These provide satisfactory energy for small portable IT devices, but they are still insufficient for EVs to completely replace petrol-powered internal combustion engine vehicles due to their long charging time, short driving range, and safety issues[8-10]. These issues affect the survival of EVs, which entirely depends on the performance of batteries. In this context, constant advances in battery technology are taking place in the direction of increasing gravimetric and volumetric energy density, as shown in Figure 1.1b[11,12]. Still, the performance of current EVs has not yet reached the range of internal combustion engine vehicles under general conditions[13]. Battery modules for EVs are constructed by stacking many batteries, and each battery cell is composed of an anode, cathode, separator, and electrolyte. Among these components, the specific capacity and operating voltage of both anode and cathode mainly determine the battery cell's energy density. In other words, the anode and cathode materials used in the battery affect each battery's energy density and determine the performance of the entire battery module.

Silicon (Si) has been proposed as a promising anode material on account of its high theoretical specific capacity ($Li_{15}Si_4$, 3580 mA h g^{-1}) and relatively low redox potential *versus* Li/Li^+ (~0.4

V), as compared with the conventional graphite system, which shows intrinsically less theoretical capacity (372 mA h g^{-1})[14-17]. Severe volume expansion/contraction occurs, however, when the Si active materials are reacting with lithium (Li) in alloying/dealloying processes (> 300 %)[18]. The mechanical stress on the surface caused by the volume changes leads to the pulverization of the Si particles and the loss of electrical contact[19]. Consequently, it causes rapid capacity degradation during cycling. To overcome these drawbacks, recently, various approaches have been proposed, which are mainly divided into two research strategies. Firstly, to create morphological variations of Si active materials is mainstream research to reduce the mechanical stress. Secondly, various types of Si-based composites have been introduced in order to compensate for the deficiencies of Si, such as Si/carbon composites.

Meanwhile, Li-metal is a highly desirable anode material for Li storage devices because it has an ultrahigh theoretical capacity (3860 mAh g^{-1}) as well as the lowest standard reduction potential (-3.04 V versus standard hydrogen electrode)[20-22]. Moreover, a battery using lightweight Li, instead of the heavier graphite, would yield at least three-fold higher energy than the conventional LIB. Nevertheless, Li-metal has a fatal weakness in that it is still subject to unavoidable dendrite growth and the formation of dead Li during Li plating/stripping, which is directly related to safety issues and cell failure[23-29]. Safety is a prerequisite for all energy storage materials, but the risk to safety from Li-metal is still much higher than for any other anode materials, even Si[30,31]. Furthermore, recent studies have shown that dead lithium formed during cell operation is the main reason for the cell failure in Li-metal based rechargeable batteries.

In fact, primary batteries using Li-metal were commercialized in the 1970s, and there were many attempts to use it in rechargeable batteries as well. In the 1980s, Moli Energy marketed Li-metal rechargeable batteries with MoS_2 cathode, but their failure to control the Li-metal

dendrites caused severe safety issues, such as the ignition problem[32-33]. Subsequently, carbonaceous anode-based LIBs were successfully developed and used predominantly, which made the Li-metal batteries naturally fade out[11]. The growing demands for energy storage devices with high energy density have revived the necessity of Li-metal anode, however, and greater fundamental understanding based on more advanced analytic techniques is accumulating to find the solution for safely using Li-metal anode.

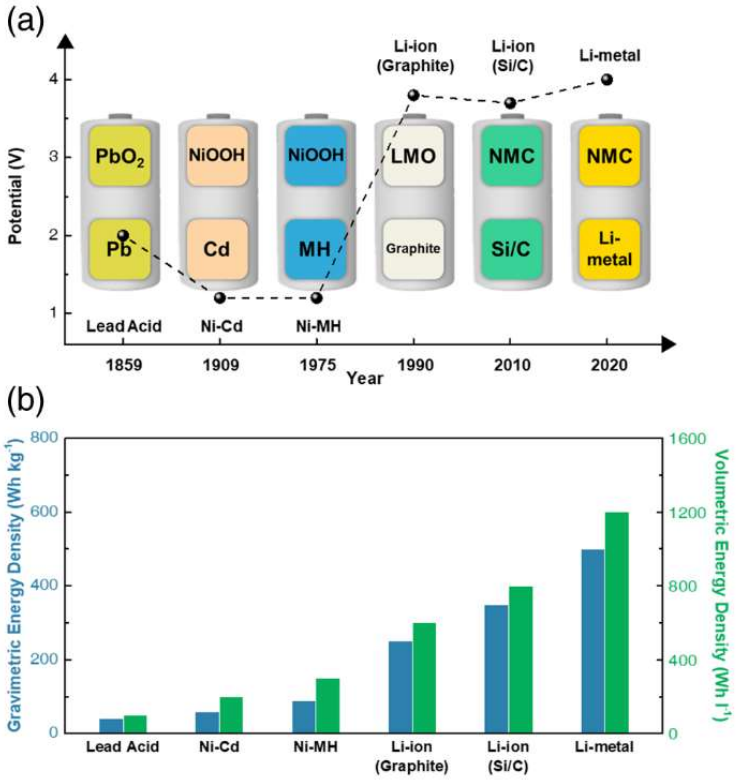

Figure 1.1. (a) Development history of representative rechargeable batteries and cell potential of each battery cell. LMO: $LiMn_2O_4$ NMC: $LiNiMnCoO_2$. (b) The gravimetric and volumetric energy density of rechargeable batteries.

1.2. Research Objectives

In this doctoral work, the main goal is, firstly, to understand the challenges that advanced anode materials face currently, as well as to explore how to overcome those for stepping forward to “beyond graphite”. Second, my research subjects are, hence, to develop high energy density Si-based/Li-metal storage anodes by nanoarchitectural design of the materials. In detail:

1. The development of Si-based anode material enabling outstanding energy density and mass production, by converting mesoporous silica source, in order to prevent volume expansion of Si.
2. The study of Li/Si reaction mechanisms by the interpretations of both electrochemical and structural analyses, in order to design preferable anode materials from the view point of electrochemical performance.
3. The study about how to control the physical properties of metal organic frameworks-derived porous carbons, by appropriate synthetic variations, in order to find out applicable materials to Li-metal storage medium.
4. The development of high energy Li-metal storage medium, by optimized metal organic framework-derived porous carbon as Li-metal host anode, in order to store Li-metal safely and efficiently.

1.3. Thesis Outline

The scope of this doctoral thesis is briefly summarized as follows (Figure 1.2):

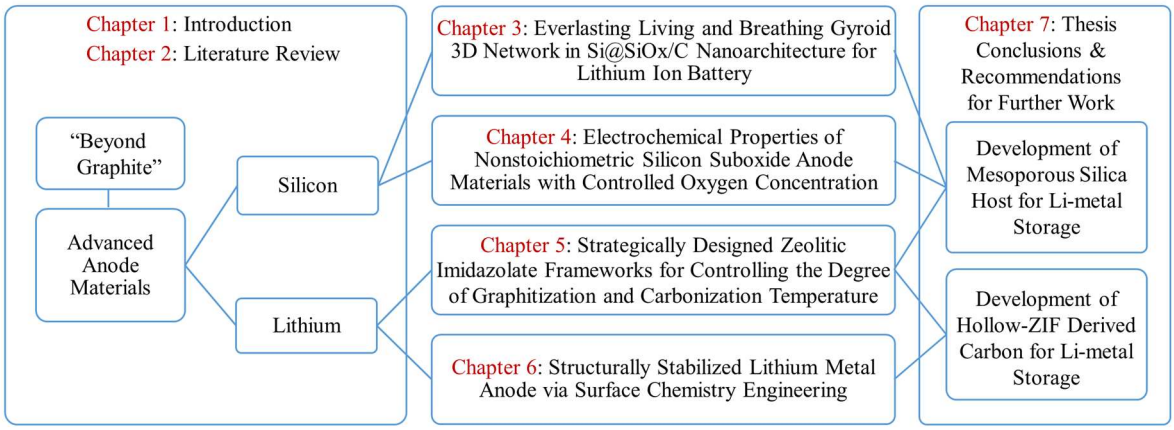

Figure 1.2. Thesis structure

Chapter 1 concisely introduces the general background and research objectives for the development of anode materials for next generation lithium batteries.

Chapter 2 provides a literature review on both Si anode, Li-metal anode and zeolitic imidazolate framework (ZIF)-derived carbons for lithium battery materials, consisting of general principles, basic concepts and various types of current approaches.

In **Chapter 3**, it is demonstrated that the strategic design and synthesis of a gyroid three-dimensional network in a Si@SiOx/C nanoarchitecture with synergetic interaction between the computational prediction and the synthetic optimization. This silicon-based anode formed by a cost-effective one-pot synthetic route, exhibits not only excellent electrochemical performance, but also enhanced thermal stability.

In **Chapter 4**, the theoretical capacities of a series of Si/SiOx with different oxygen contents were estimated by using X-ray photoelectron spectroscopy, and then those results were compared with empirical results in order to find out the relations between oxygen contents of the Si/SiOx and their electrochemical performances.

In **Chapter 5**, the physical properties of nanoporous zeolitic imidazolate frameworks (ZIFs)-derived carbons which can be controlled by different ratios of zinc/cobalt ion metallic precursors, were studied. This approach informed to achieve tailored ZIF-derived carbons with different pore volumes, pore sizes, surface areas and even degrees of graphitization. Because of their large pore volumes and adjustable physical properties, it is suggested that the electrochemical performances of these ZIF-derived carbons as Li-metal storage host, can be maximized by controlling the properties of those.

In **Chapter 6**, by controlled synthesis of bimetallic ZIF-derived carbon, cobalt nanoparticle embedded highly mesoporous N-graphite is proposed as new innovative Li-metal host anode. This material shows high Li affinity as well as high lithiophilic surface chemistry and, as a result, the anode shows excellent electrochemical performances with high Li-metal reversible capacity and even stable long-term cyclability with no dead-Li formation.

Chapter 7 covers the main conclusion of this thesis and proposes future prospects, which includes combinational research on both Si and Li-metal materials.

Main chapters (**Chapter 3-6**) were compiled from the articles which were already published or submitted on journals. Detailed information about the articles is as below (Table 1.1).

Table 1.1. Journal articles for the thesis compilation.

Chapter 3	**Jaewoo Lee**, Janghyuk Moon, Sang A Han, Junyoung Kim, Victor Malgras, Yoon-Uk Heo, Hansu Kim, Sang-Min Lee, Hua Kun Liu, Shi Xue Dou, Yusuke Yamauchi, Min-Sik Park, Jung Ho Kim "*Everlasting living and breathing gyroid 3D network in Si@ SiOx/C nanoarchitecture for lithium ion battery*" **ACS Nano** 13 (2019) 9607-9619

Chapter 4	**Jaewoo Lee**, Sang A Han, Sang-Min Lee, Min-Sik Park, Jung Ho Kim "*Electrochemical properties of nonstoichiometric silicon suboxide anode materials with controlled oxygen concentration*" **Composites Part B: Engineering** 171 (2019) 107024
Chapter 5 -1	Sang A Han, **Jaewoo Lee**, Kyubin Shim, Jianjian Lin, Mohammed Shahabuddin, Jong-Won Lee, Sang-Woo Kim, Min-Sik Park, Jung Ho Kim "*Strategically designed zeolitic imidazolate frameworks for controlling the degree of graphitization*" **Bulletin of the Chemical Society of Japan** 91 (2018) 1474-1480
Chapter 5 -2	**Jaewoo Lee**, Sang A Han, Hamzeh Qutaish, Hien Thi Thu Pham, Min-Sik Park, Jung Ho Kim "*The effect of carbonization temperature on zeolitic imidazolate framework derived carbon nanoarchitecture*" Submitted to **Materials Today Communications** in August 2020 (under review)
Chapter 5 -3	**Jaewoo Lee**, Sang A Han, Hamzeh Qutaish, Lok Kumar Shrestha, Katsuhiko Ariga, Jung Ho Kim "*Zeolitic Imidazolate Framework-Derived Nanoarchitectures for Lithium Metal Storage Medium*" **General Chemistry**" (2019) doi: 10.21127/yaoyigc20190011
Chapter 6	**Jaewoo Lee**, Seung Hyun Choi, Hamzeh Qutaish, Yuhwan Hyeon, Sang A Han, Yoon-Uk Heo, Dongmok Whang, Jong-Won Lee, Janghyuk Moon, Min-Sik Park, Jung Ho Kim "*Structurally Stabilized Lithium-Metal Anode via Surface Chemistry Engineering*" Submitted to **Energy Storage Materials** in October 2020 (under review)

1.4. References

[1] M. Armand, J.-M. Tarascon, *Nature* **2008**, 421. 652.

[2] J. W. Choi, D. Aurbach, *Nat. Rev. Mater.* **2016**, 1, 16013.

[3] B. Dunn, H. Kamath, J.-M. Tarascon, *Science* **2011**, 334, 928

[4] J. Kim, J. H. Kim, K. Ariga, *Joule* **2017**, 1, 739.

[5] J. B. Goodenough, K.-S. Park, *J. Am. Chem. Soc.* **2013**, 135, 1167.

[6] E. C. Evarts, *Nature* **2015** 526, S93.

[7] L. Grande, E. Paillard, J. Hassoun, J.-B. Park, Y.-J. Lee, Y.-K. Sun, S. Passerini, B. Scrosati, *Adv. Mater.* **2015**, 27, 784.

[8] P. G. Bruce, S. A. Freunberger, L. J. Hardwick, J.-M. Tarascon, *Nat. Mater.* **2012**, 11, 19.

[9] X. Shen, H. Liu, X.-B. Cheng, C. Yan, J.-Qi. Huang, *Energy Storage Mater.* **2018**, 12, 161.

[10] J. Lang, L. Qi, Y. Luo, H. Wu, *Energy Storage Mater.* **2017**, 7, 115.

[11] J.-M. Tarascon, M. Armand, *Nature* **2001**, 414, 359.

[12] M. M. Thackeray, C. Wolverton, E. D. Isaacs, *Energy Environ. Sci.* **2012**, 5, 7854.

[13] L. Ma, J. Cui, S. Yao, X. Liu, Y. Luo, X. Shen, J.-K. Kim, *Energy Storage Mater.* **2020**, 27, 522.

[14] C.-M. Park, J.-H. Kim, H. Kim, H.-J. Sohn, *Chem. Soc. Rev.* **2010**, 39, 3115.

[15] C. K. Chan, H. Peng, G. Liu, K. McIlwrath, X. F. Zhang, R. A. Huggins, Y. Cui, *Nat. Nanotechnol.* **2007**, 3, 31.

[16] S. Chae, M. Ko, K. Kim, K. Ahn, J. Cho, *Joule* **2017**, 1, 47.

[17] X. Zuo, J. Zhu, P. Müller-Buschbaum, Y.-J. Cheng, *Nano Energy* **2017**, 31, 113.

[18] U. Kasavajjula, C. Wang, A. J. Appleby, *J. Power Sources* **2007**, 163, 1003.

[19] W.-J. Zhang, *J. Power Sources* **2011**, 196, 13.

[20] W. Xu, J. Wang, F. Ding, X. Chen, E. Nasybulin, Y. Zhang, J.-G. Zhang, *Energy Environ. Sci.* **2014**, 7, 513.

[21] Y. Sun, N. Liu, Y. Cui, *Nat. Energy* **2016**, 1, 16071.

[22] X.-B. Cheng, Q. Zhang, *J. Mater. Chem. A* **2015**, 3, 7207.

[23] C. Brissot, M. Rosso, J.-N. Chazalviel, S. Lascaud, *J. Power Sources* **1999**, 81-82, 925.

[24] M. D. Tikekar, S. Choudhury, Z. Tu, L. A. Archer, *Nat. Energy* **2016**, 1, 16114.

[25] Y. Liu, Q. Liu, L. Xin, Y. Liu, F. Yang, E. A. Stach, J. Xie, *Nat. Energy* **2017**, 2, 17083.

[26] H. Yang, C. Guo, A. Naveed, J. Lei, J. Yang, Y. Nuli, J. Wang, *Energy Storage Mater.* **2018**, 14, 199.

[27] L. Wang, Z. Zhou, X. Yan, F. Hou, L. Wen, W. Luo, J. Liang, S. X. Dou, Energy Storage Mater. **2018**, 14, 22.

[28] K.-H. Chen, K. N. Wood, E. Kazyak, W. S. LePage, A. L. Davis, A. J. Sanchez, N. P. Dasgupta, *J. Mater. Chem. A* **2017**, 5, 11671.

[29] D. Lu, Y. Shao, T. Lozano, W. D. Bennett, G. L. Graff, B. Polzin, J. Zhang, M. H. Engelhard, N. T. Saenz, W. A. Henderson, P. Bhattacharya, J. Liu, J. Xiao, Adv. Energy Mater. **2015**, 5, 1400993.

[30] J. Lee, J. Moon, S. A Han, J. Kim, V. Malgras, Y.-U. Heo, H. Kim, S.-M. Lee, H. K. Liu, S. X. Dou, Y. Yamauchi, M.-S. Park, J. H. Kim, *ACS Nano* **2019**, 13, 9607.

[31] J. Lee, S. A Han, S.-M. Lee, M.-S. Park, J. H. Kim, *Compos. B Eng.* **2019**, 174, 107024.

[32] M. S. Whittingham, Chem. Rev. **2004**, 10, 4271.

[33] K. Brandt, *Solid State Ionics* **1994**, 69, 173.

Chapter 2. Literature Review

2.1. Research on Si Anode

2.1.1. Fundamental Problems of Si-Based Anodes

Silicon(Si) has been proposed as an alternative anode material on account of its high theoretical specific capacity ($Li_{15}Si_4$, 3580 mA h g^{-1}) and relatively low redox potential versus Li/Li^+(~0.4 V)[1-3]. However, severe volume expansion/contraction occurs when Si active materials are reacting with Li by alloying/dealloying process (>300 %)[4]. The mechanical stress on the surface caused by volume changes affects a rapid capacity degradation during cycling. Repeated volume expansion/contraction causes, after all, following three main fundamental problems (Figure 2.1):

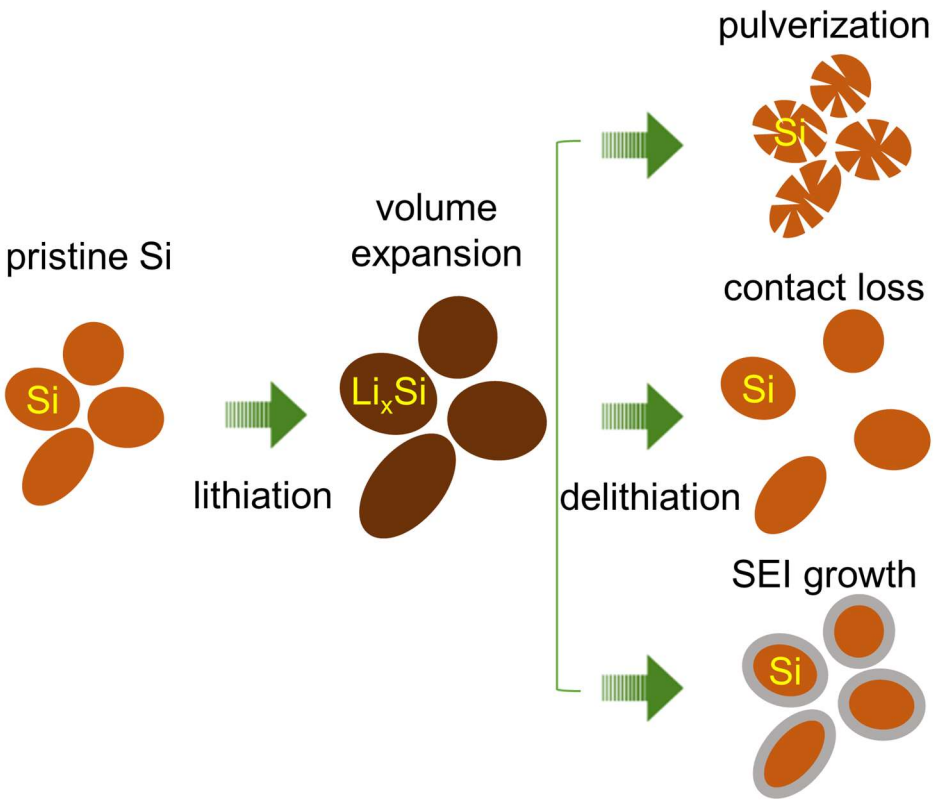

Figure 2.1. Schematic diagram of fundamental problems of Si-based anodes.

i) Lithiation and delithiation converts transforms crystalline Si to lithium silicide (Li_xSi), and transforms into amorphous Si. During this process, Si occurs severe mechanical stress on its surface. After all, it rerults in fracture and pulverization of the particle[5].

ii) Huge volume expansion leads the separation of each particle, then detached particle losses its electrical contact and react no more as active material[5,6].

iii) Repeated volume expansion/contractions leads to unceasing growth of solid electrolyte interphase (SEI), then it results in interference of Li diffusion, loss of electrolyte, and low coulombic efficiency[7].

To overcome these drawbacks, recently, various approaches which are divided into mainly three research strategies have been proposed: i) nanostructural design (2.1.2), ii) Si-based composites (2.1.3), and iii) binders & electrolytes (2.1.4).

2.1.2. Nanostructural Design

To give morphological variations on Si active materials is maintream researches to reduce the mechanical stress such as, nanoparticles(0D)[8-10], nanorods/nanotubes(1D)[11-13], nanosheets(2D)[14,15], and porous materials(3D)[16-19]. As a feasible strategy, these approaches are aimed at relieving volume expansion (Figure 2.2). These Si materials shows not only excellent cyclic performances but also high reversable specific capacities due to its enhanced anti-pulverization characteristics. However, it might be infeasible to apply to large-scale production because the meterials preperations require high-cost synthetic routes or even uses of harzadous chemicals.

As one of these approaches, Jia et al.[20] synthesized a mesoporous silicon material by magnesiothermic reduction of SBA-15 silica and further coated with carbon by chemical vapor

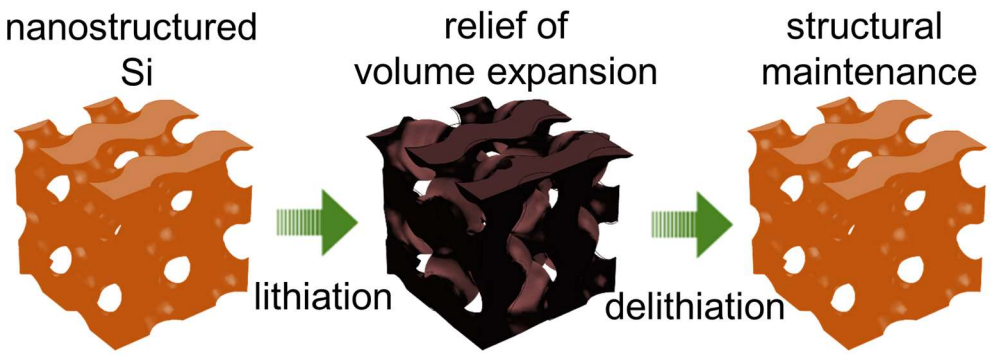

Figure 2.2. Schematic diagram of Si-based anode strategies through a nanostructural design.

deposition(CVD) method (Figure 2.3). This material presented a high reversible capacity of 1500 mA h g^{-1} even after 100 cycles. However, the content of active materials was only 60 % and its initial coulombic efficiency was 73.6 %. These results indicate that this material might not show a high energy density, whereas its specific capacity is sufficiently high. Moreover, an aceltylene carbon source used in the CVD method is toxic and unsafe, so that further utilization is needed for commercial-scale production.

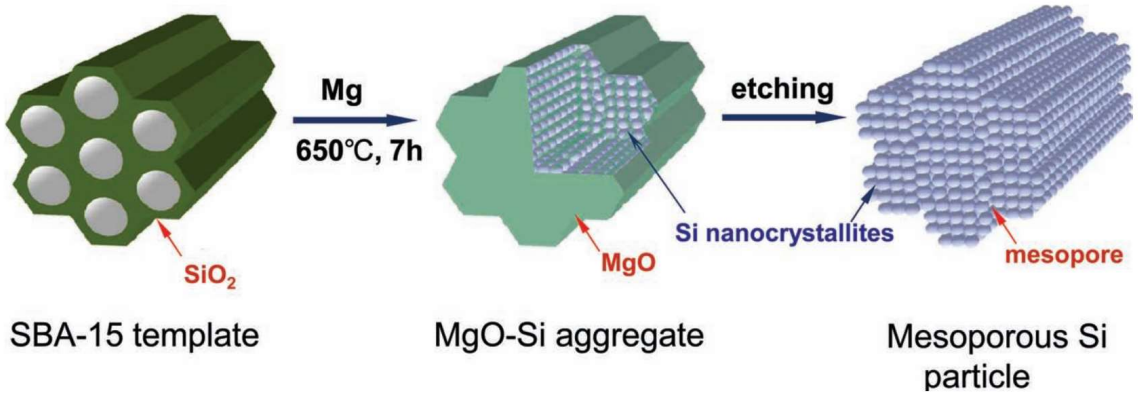

Figure 2.3. Schematic illustration of the preparation process of the 3D mesoporous silicon anode material[20].

2.1.3. Si-Based Composites

Various types of Si-based composites have been introduced in order to compensate the defect of Si such as, Si/carbon composites[21-24], Si/SiO_x composites[25,26], Si/metal composites[27,28]. These approaches are mainly aimed at preventing volume expansion by introduction of compatible composites with Si (Figure 2.4). Although these composites also show moderate cycle performances, each materials are not enough to overwhelm the performance of conventional graphite owing to different weaknesses such as low initial coulombic efficiency, high-cost synthesises or high-cost precursors.

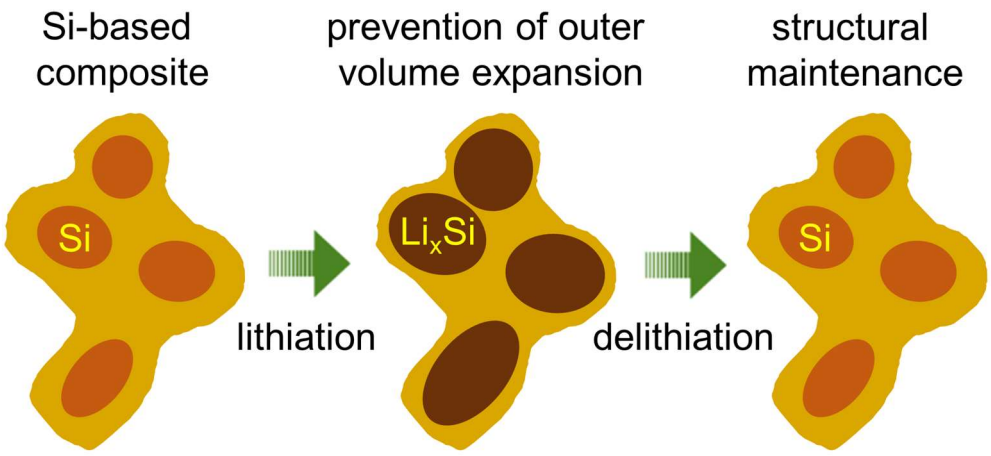

Figure 2.4. Schematic diagram of Si-based anode strategies through a Si-based composite.

Park et al[26]. introduced commercial Si nanoparticle embedded SiO_x nanocomposite prepared via sol-gel reaction of triethoxysilane (Figure 2.5). This material showed a high reversible capacity of 1914 mA h g^{-1} at a current density of 200 mA g^{-1} and good cycle performance up to 100 cycles. However, in case of non-carbon coated samples, around 20 % of capacity degradation was shown within first few cycles. This irreversibility may result from the side

reaction of large amount SiO_x and low electrical conductivity due to its intrinsic material(SiO_x, insulator) and structural(nanoparticle) properties.

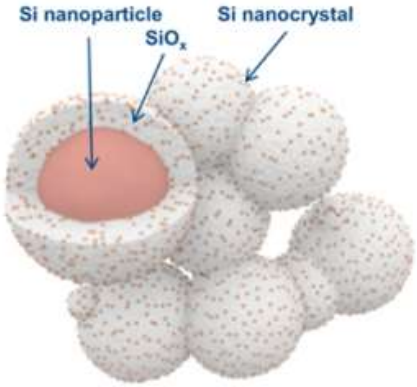

Figure 2.5. illustration of Si-nanoparticle embedded Si/SiO_x anode material[26].

2.1.4. Binders & Electrolytes

In order to increase the mechanical strength of Si anode material, Si-specific binders also being studied. such as, carboxymethyl cellulose, alginate, poly(acrylic acid)[29-31]. These binders not only relieve the volume expansion, but also maintain good conductivity. Choi et al.[ref] reported polyrotaxane-poly(acrylic acid) mixture binder shows extraordinary elasticity enabling cycle performance for even Si microparticle anode. In addition, as Wang et al. reported (Figure 2.6)[32], self-healing polymer binder enables Si anode electrode to maintain elastic adhesion and to heal by itself, even though Si particles undergo harsh fracture.

Electrolyte also can play critical role in Si anode performance[33-35]. Based on common electrolytes such as, ethylene carbonate (EC), dimethyl carbonate (DMC) and diethyl carbonate (DEC), additives can stabilize SEI formation between electrolyte and Si surface. For example, fluoroethylene carbonate (FEC) is one of the best additives to improve cycle performance of

Si anode. FEC induces ordered reorientation of EC molecules on Si surface and this up-right orientation might be helpful for Li diffusion (Figure 2.7)[36].

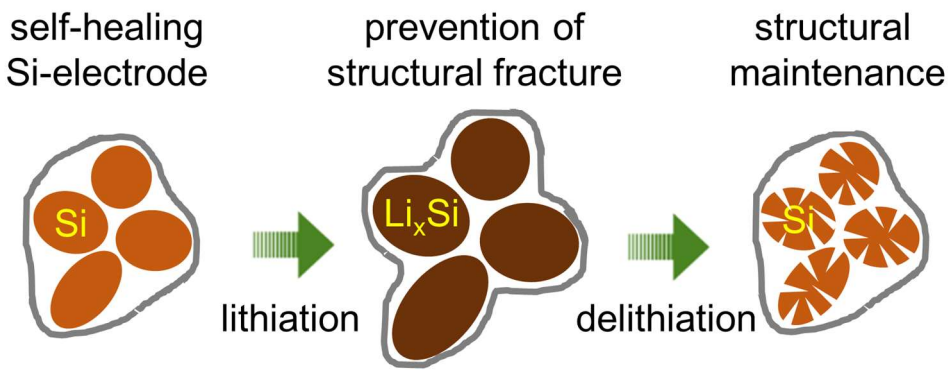

Figure 2.6. Schematic diagram of Si-based anode strategies through a binder[32].

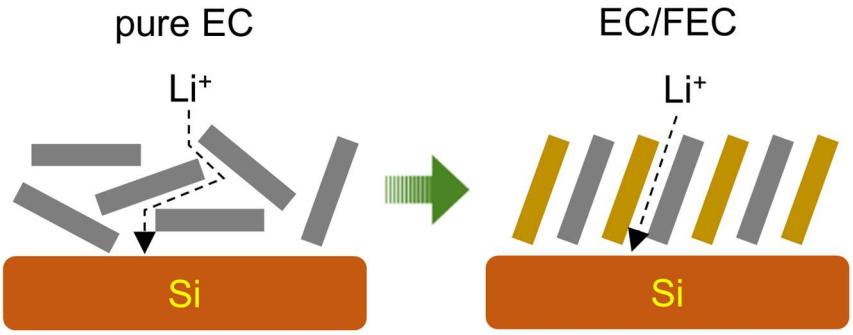

Figure 2.7. Schematic diagram of Si-based anode strategies through an electrolyte[36].

2.2. Research on Li-metal Anode

2.2.1. Failure Mechanism

Figure 2.8a shows the fundamental problems that occur during Li plating/stripping. Since Li-metal is highly reactive, it easily reacts with almost all conventional organic liquid electrolytes to form insoluble solid-electrolyte interphase (SEI) on the Li-metal surface. The SEI layer is ionically conductive but electrically insulating, and it prevents the loss of additional Li and electrolyte when the SEI stably blocks electron transfer. Even so, the SEI layer is too fragile to endure mechanical deformation resulting from the Li-metal volume changes that occur during cell cycling[37-39]. Once there are cracks in the SEI layer, fresh Li underneath is exposed to the electrolyte through the cracks, commonly called "hot spots", and the Li-ion flux and current are locally focused on the hot spots[38]. The growth of Li dendrites that starts at hot spots is accelerated during repeated Li plating/stripping. Meanwhile, Li dendrites continuously generate an abundance of inactive 'dead' Li during repeated Li plating/stripping, resulting in severe capacity fading and even cell failure[40,41].

The Li‖Li symmetric cell provides important information for the evaluation of Li-metal performance without the need to separate out the effects of cathode. Furthermore, the Li‖Li symmetric cell is very helpful for determining the failure mechanism of Li-metal[40]. Figure 2.8b shows the voltage profile of an Li‖Li symmetric cell cycled at 5 mA cm^{-2} for 200 cycles in carbonate electrolyte. There is a different shape of voltage profile between earlier cycles and later cycles. At earlier cycles, the apparent double peak in the voltage profile is limited by reaction kinetics, due to the evolving morphology (Figure 2.8c and 2.8e)[40,42]. On the other hand, the arc/plateau shape in the later cycles originates from the limited mass transport caused by the accumulation of dead Li (Figure 2.8d and 2.8f). As the resistive dead Li layer becomes thicker and thicker, the increasing internal resistance results in more pronounced arcs and

increasing overpotential. Even in an Li-metal full cell coupled with nickel cobalt aluminum oxide (NCA), a highly resistive layer on Li-metal that is formed during cell operations causes cell failure[41]. That is, Li dendritic growth and dead Li formation are fundamental problems that can stop operation of the Li-metal battery. The following effective strategies are representative alternative methods for using Li-metal with stable performance.

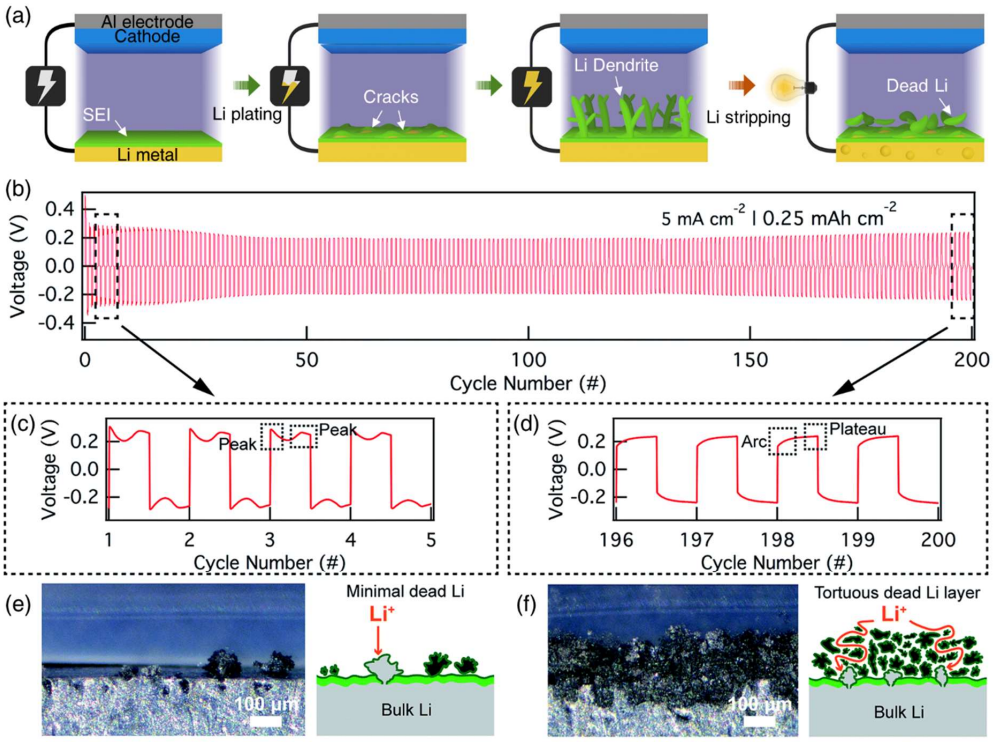

Figure 2.8. (a) Schematic illustration showing the Li plating/stripping process and the problems encountered. (b) Galvanostatic cycling voltage profiles for Li‖Li symmetric coin cell at a current density of 5 mA cm^{-2} with an areal capacity of 0.25 mAh cm^{-2} for 200 cycles. (c) Earlier cycles exhibiting peaking behavior and (d) later cycles exhibiting arc/plateau behavior. Cross-sectional *operando* microscopy images of the interphase and corresponding schematic illustration at (e) earlier cycles and (f) later cycles. The scanning electron microscopy (SEM) images in (e) and (f) show the anode appearance after Li plating[40].

2.2.2. Artificial SEI

Fundamentally, the limitations of Li-metal result from the interface chemistry between Li-metal and liquid electrolyte. In particular, chemically and mechanically stable SEI films are

necessary because the stability of the SEI significantly affects the formation of Li dendrites on the Li-metal. Optimal SEI layers are very complex, however, and only limited understanding has been achieved on what they consist of and how they affect the cell performance. Thus, instead of the natural SEI made during cell cycling, there are some strategies to form artificial SEI films with the desired properties on the Li surface before cell cycling (Figure 2.9)[43-53]. Representatively, LiF is considered an excellent material as an artificial SEI owing to its low solubility in electrolyte ($< 4 \times 10^{-4}$ mol/L in diethyl carbonate (DEC)) and high chemical stability[47]. Moreover, its mechanical strength is high enough (shear modulus of 55.1 GPa) to prevent the growth of Li dendrites and the side reactions occurring between Li-metal and electrolyte[48].

Li_3PO_4 was also suggested as an effective artificial SEI to suppress dendrite formation, owing to its excellent chemical stability and high Young's modulus[49,50]. Recently, a thin (~ 50 nm) Li_3PO_4 artificial SEI on Li-metal was used due to its superior properties, and the modified electrode withstood over 200 cycles without visible Li dendrite growth[49]. In addition to this, various types of artificial SEI, such as poly-(ethyl α-cyanoacrylate), obtained by polymerization of ethyl α-cyanoacrylate with $LiNO_3$ additive[51], Li_3N coating by *ex-situ* nitridation[52], and tetraethoxysilane-generated silicate film[53], have been proposed to solve the Li-dendrite problem. Nevertheless, artificial SEI formation has a fatal disadvantage in that it requires highly sensitive control of the reaction conditions and contamination.

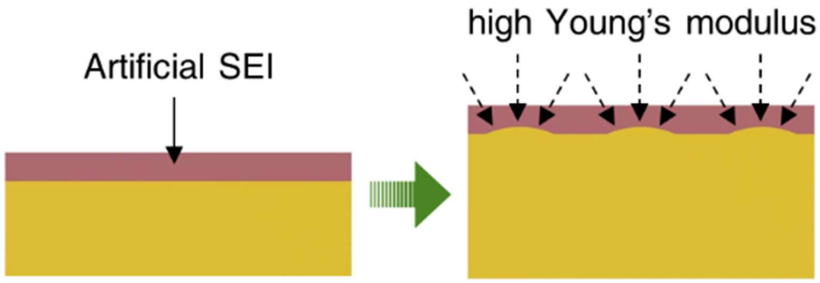

Figure 2.9. Schematic diagram of Li-metal research strategies through an artificial SEI.

2.2.3. Interfacial Layer

Unlike the artificial SEI, this strategy installs a chemically stable and mechanically strong scaffold on the Li-metal to induce the formation of an SEI film on top of the interfacial layer to prevent dendritic growth of Li. The SEI film is formed on the interfacial layer, and the Li-ions can freely pass through the interfacial layer to deposit Li-metal under the scaffold. Thus, the interfacial layer should have relatively low electrical conductivity to prevent the unwanted plating of the Li-metal on the top of the interfacial layer. It should also have relatively weak interaction with the current collector to accommodate the Li-metal volume changes during Li plating/stripping[54]. For instance, a monolayer of interconnected amorphous hollow carbon nanospheres can be used as a proper interfacial layer to induce the formation of column-like Li and facilitate the formation of a stable SEI layer, as shown in Figure 2.10[55]. This method showed significantly improved Coulombic efficiency and cyclability (~ 99% for more than 150 cycles) compared to the unmodified case (rapid Coulombic efficiency decay in fewer than 100 cycles). Two-dimensional (2D) hexagonal boron nitride (h-BN) and graphene directly grown on copper (Cu) substrate were also proposed as interfacial layers, based on their outstanding chemical stability and mechanical strength. These 2D layers promote smooth Li-metal deposition without dendritic and mossy Li formation[56]. This strategy has a weakness, however, in that dendritic growth can be accelerated if defects such as tearing occur in the interfacial layer.

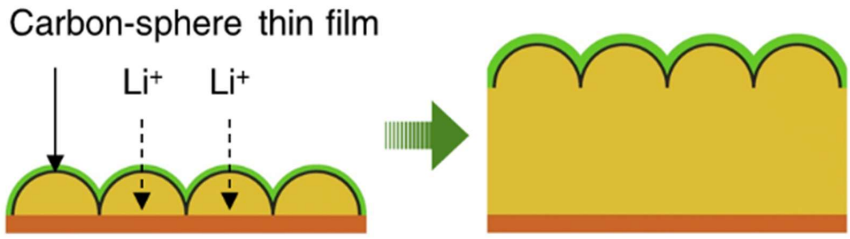

Figure 2.10. Schematic diagram of Li-metal research strategies through an interfacial layer.

2.2.4. Three-Dimensional Structured Electrode

The current collector is also considered a vital component of the anode and has a significant influence on Li plating. In the initial stage of Li deposition, the current collector affects not only the Li nucleation, but also the successive growth of Li-metal[57]. In most cases, conventional planar Cu foil is used as the current collector, which is likely to cause spatial inhomogeneity of the Li-ion distribution, as shown in Fig. 2.11. On the other hand, replacing the planar current collector with a three-dimensional (3D) electrode can prevent concentration of the current density and improve the contact area with the electrolyte[58-62]. This makes the Li-ion flux more uniform, causing even Li nucleation and further preventing the growth of Li dendrites.

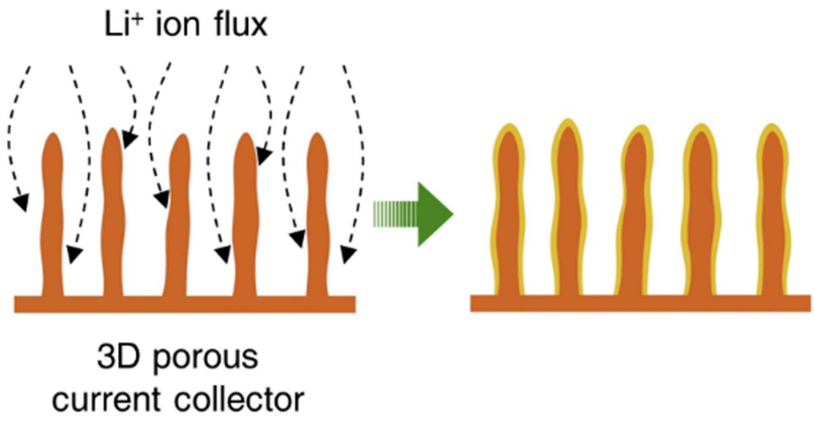

Figure 2.11. Schematic diagram of Li-metal research strategies through a 3D structured electrode.

Using a lithiophilic gradient electrode or an electrical gradient electrode is also an excellent approach in this context[63-65]. When tan electrode with a lithiophilic-lithiophobic gradient is applied as the anode, the bottom lithiophilic layer facilitates uniform SEI formation, while the top lithiphobic layer facilitates Li diffusion toward bottom[65]. Also, in the case of a current collector with an electrical gradient, the Li-ion flux is focused on the highly conductive bottom layer because of the sequestration of electrons on the electrically insulating top layer[66,67].

Although these approaches are valid, they are difficult to apply as a fundamental solution to resolve the non-ideal growth of Li-metal. These structures would be more effective when used in combination with a more theoretical approach.

2.2.5. Stable Host for Li Storage

This approach starts from the view point of using stable host materials with sufficient room for accommodating metallic Li to minimize the volume expansion during Li plating/stripping. Also, depending on the affinity of the host materials with Li, Li-metal can be safely stored without dendrite formation. For example, the nanogaps of a reduced graphene oxide (rGO) film fabricated through spark reaction provide room for Li storage. The lithiophilic edge sites of the rGO film induce the infusion of molten Li-metal into the nanogaps, as shown in Figure 2.12[68]. Occasionally, the strategies facilitating suitable host materials for Li-metal storage are categorized as follows: (i) One is storing Li-metal in the pores or gaps of the host structures; and (ii) the other is inducing the nucleation and growth of Li-metal in the desired direction on the surfaces of some scaffolds. In this literature review, however, we will group these two into one category because the ideas of the two strategies are inseparable, and both are critical elements for Li storage.

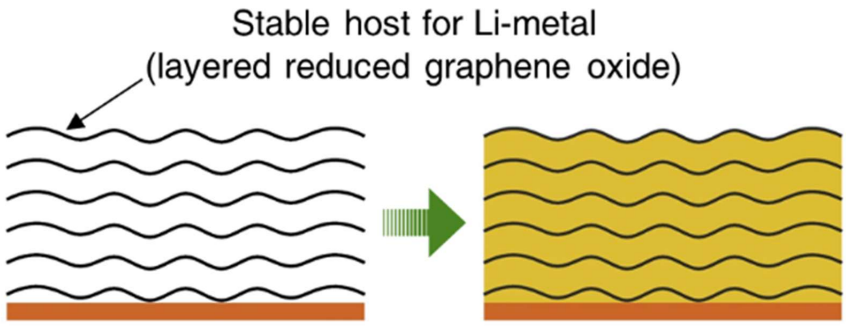

Figure 2.12. Schematic diagram of Li-metal research strategies through a stable host for Li storage[68].

Table 2.1 summarizes the representative types of host materials, such as porous carbon materials (layered rGO film[68], hollow carbon shell[69], asphalt-derived porous carbon[70]), functionalized carbon foam (amine-functionalized carbon fiber film[71], nitrogen (N)-doped graphitic carbon foam[72], Si-coated carbon fiber[73], graphene-carbon nanotube[74]), polymer scaffolds (poly melamine formaldehyde (PMF)[75], polyimide (PI) with a zinc oxide (ZnO) shell[76]), and metal-organic framework (MOF)-derived carbon structures[77-79]. These types of materials stably stored Li-metal and exhibited remarkable electrochemical performances during repeated Li plating/stripping. For example, N-doped graphitic carbon foam showed stable voltage hysteresis with a very small overpotential of 15 mV at a current density of 2 mA cm^{-2} with the areal capacity of 1 mAh cm^{-2} [72]. Porous carbon structures from MOFs also showed very small overpotential with the areal capacity of 1 mAh cm^{-2}, which indicated that they are superior host materials[77-79]. Also, the average Coulombic efficiency of porous carbon from asphalt was observed to be 99.0 % with only a small deviation over 500 cycles at a current density of 2.5 mA cm^{-2} with the areal capacity of 2 mAh cm^{-2} [70]. Furthermore, a full-cell battery test was conducted by coupling an amine-functionalized carbon fiber film with lithium nickel manganese cobalt oxide (NMC) cathode, leading to an energy density of 350-380 Wh kg^{-1} over 200 cycles[71].

Table 2.1. Representative host materials for Li-metal storage and the electrochemical performance of each material.

Active materials	Structural features	Electrochemical performance
Sparked reduced graphene oxide film [68]	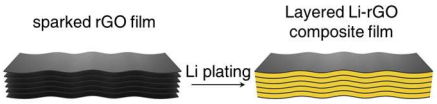	Overpotential of ~ 80 mV at a current density of 3 mA cm^{-2} with the areal capacity of 1 mAh cm^{-2}
Hollow carbon shell [69]	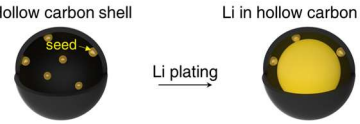	Overpotential of 20 mV at a current density of 0.5 mA cm^{-2} with the areal capacity of 1 mAh cm^{-2}
Porous carbon from asphalt [70]	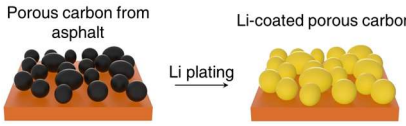	Average Coulombic efficiency of 99.0 % for 505 cycles at a current density of 2.5 mA cm^{-2} with the areal capacity of 2 mAh cm^{-2}
Amine-functionalized carbon fiber [71]	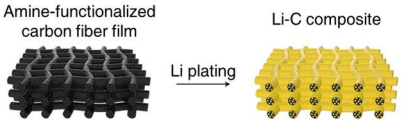	Energy density of 353 Wh kg^{-1} with NMC622[a] Energy density of 381 Wh kg^{-1} with NMC811[b] up to 200 cycles
Nitrogen-doped graphitic carbon foam (NGCF) [72]	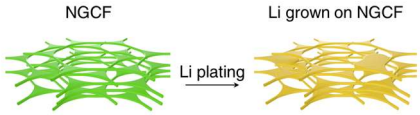	Overpotential of 15 mV at a current density of 2 mA cm^{-2} with the areal capacity of 1 mAh cm^{-2}
Si-coated carbon fiber [73]	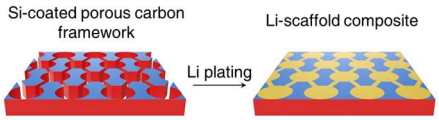	Overpotential of ~ 90 mV at a current density of 3 mA cm^{-2} with the areal capacity of 1 mAh cm^{-2}
Graphene-carbon nanotube (GCNT) [74]	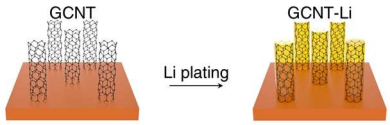	Overpotential of ~ 50 mV at a current density of 2 mA cm^{-2} with the areal capacity of 0.7 mAh cm^{-2}
Poly-melamine-formaldehyde (PMF) [75]	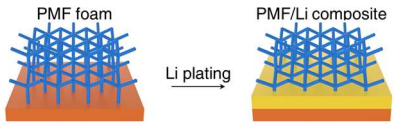	Coulombic efficiency of 94.7 % for 50 cycles at a current density of 10 mA cm^{-2} with the areal capacity of 1 mAh cm^{-2}
Polyimide (PI) with ZnO shell [76]	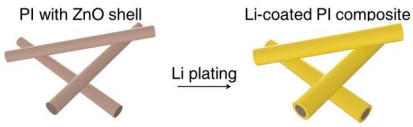	Overpotential of ~ 35 mV at a current density of 1 mA cm^{-2} with the areal capacity of 1 mAh cm^{-2}
ZnO/carbon framework [77]	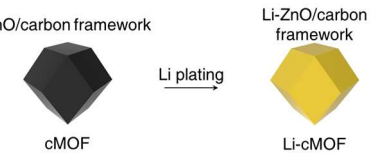	Overpotential of ~ 14 mV at a current density of 1 mA cm^{-2} with the areal capacity of 1 mAh cm^{-2}
Carbonized metal-organic framework (cMOF) [78]		Overpotential of 29 mV at a current density of 1 mA cm^{-2} with the areal capacity of 1 mAh cm^{-2}
Porous carbon framework (PCF) [79]	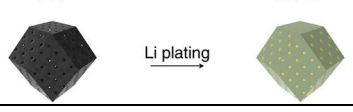	Overpotential of 24.4 mV at a current density of 0.5 mA cm^{-2} with the areal capacity of 1 mAh cm^{-2}

a) NMC622: $LiNi_{0.6}Mn_{0.2}Co_{0.2}O_2$, b) NMC811: $LiNi_{0.8}Mn_{0.1}Co_{0.1}O_2$

2.3. Suitable Host Framework for Li-Metal Storage

Among the various methods using Li-metal, this literature review focuses on a strategy to store Li-metal in host materials. This approach is an alternative method due to the unavoidable loss of gravimetric capacity from considering the weight of host structures, but it is expected to sufficiently satisfy the growing demand for high-energy-density energy storage devices. In practice, although many conceptual host materials were introduced in Table 2.1, it would be difficult to simply compare which materials are better, because not only are the electrochemical testing conditions for each result markedly different, but also because the electrochemical performances from coin cell tests are remarkably different from those of practical cells. In this Review, we would like to understand the suitable properties for host materials for Li-metal storage and suggest one candidate group with these properties. If rationally designed host frameworks are used to store Li-metal, they can be expected to solve dendrite formation problems and the huge volume changes of Li-metal anode.

2.3.1. Suitable Properties for Safe Storage

In suitable host materials for Li-metal storage, the host framework should fulfill the following requirements, as illustrated in Figure 2.13a[78,79]: (i) It has an adequate pore size that effectively facilitates the transport of Li ions in the electrolyte. (ii) It also has a lithiophilic surface to promote the nucleation of Li-metal through heteroatom doping and improve wettability towards the Li-metal; (iii) It has a large pore volume to accommodate an adequate amount of Li-metal; (iv) It has a large specific surface area to reduce the effective current densities of the electrodes; and (v) It has acceptable electrical conductivity so as not to interfere with the electrochemical redox reactions (Li plating/stripping). Finally, for commercialization, (vi) it should be cost-effective compared to commercial graphite and also involve an acceptable

process. A material having all these properties is considered an optimal host framework for Li-metal storage.

The optimal host materials have to stably accommodate Li-metal, and for this purpose, the pore structures and the lithiophilicity of the host materials are especially important [71,80-82]. According to classical nucleation theory, the heterogeneous nucleation of the energy barrier ($\Delta G^*_{\mathrm{het}}$) is determined by shape factor ($S(\theta)$) and the energy barrier for homogeneous nucleation ($\Delta G^*_{\mathrm{hom}}$) as expressed by Equation (1).

$$\Delta G^*_{\mathrm{het}} = S(\theta) \times \Delta G^*_{\mathrm{hom}} \quad (1)$$

where the shape factor ($S(\theta)$) is related to the contact angle (θ) by

$$S(\theta) = \frac{(2+cos\ \ )(1-cos\ \ )^2}{4} \quad (2)$$

The shape factor decreases monotonically with the contact angle from 1 at θ = 180º (non-wetting; homogeneous nucleation) to 0 at θ = 0º. Furthermore, even if $\Delta G^*_{\mathrm{het}}$ is greater than 0, the nucleation energy barrier goes to 0 if the sum of the contact angle of the nucleus on the substrate and the half-angle of the cavity is less than 90º, as shown in Figure 2.13b[83]. This suggests that the pore structures or cavities play a role in preferred nucleation sites[71]. Furthermore, the lithiophilic surface induces uniformly dispersed nucleation of Li-metal over the whole surface and even inside the pores, while it also helps to grow Li-metal along the surfaces of the host material[71]. In this context, Si[73] or ZnO[76] coating on the carbon surface has been proposed to effectively increase the wettability towards Li, because general carbon materials are lithiophobic and inappropriate as host materials to store Li-metal. Amine functionalization or N-doping of carbon materials is also an effective way to improve wettability for Li[71].

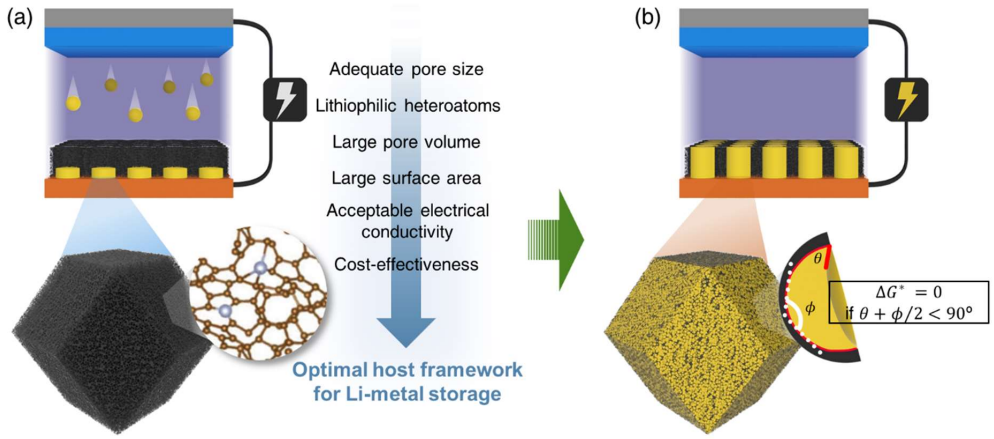

Figure 2.13. (a) Requirements for suitable host material to store Li-metal and (b) schematic diagram showing the Li-metal stored in lithiopilic pore of suitable host material.

2.3.2. Zeolitic Imidazolate Framework (ZIF)-Derived Carbonaceous Nanoarchitectures as Li-Metal Hosts

The nucleation of Li-metal on some metal substrates, such as Ag, Au, and Zn, does not require an overpotential because of the definite solubility of the substrate in Li-metal, which leads to the formation of a solid solution buffer layer before the actual formation of pure Li-metal[69]. Furthermore, 3D structures can provide a large surface area and large pore volume, which provides not only a uniform electric field distribution to avoid charge accumulation, but also the abundant space to accommodate Li-metal. Therefore, 3D porous structures with effective nucleation seeds, a large specific surface area, and a large pore volume are highly desirable in rechargeable Li-metal batteries. From these perspectives, a ZIF-derived carbon structure would be an excellent candidate, because it has all the essential requirements as a suitable host.

ZIFs are a subclass of MOFs, and they have unique pore structures and different pore sizes depending on the choice of metal ions and linkers, as shown in Figure 2.14[84-86]. Unlike typical MOFs, ZIFs exhibit excellent thermal and chemical stability due to their zeolite-like

topologies[85]. Moreover, ZIFs are not only easily carbonized without any addition of secondary carbon sources, but also are hard to collapse after carbonization due to the highly stable nature of ZIFs[87]. That is, the carbonaceous materials obtained by calcination of ZIFs still have a large specific surface area and large pore volume, as well as lithiophilic surfaces due to N-doping and their metal nanoparticles. In addition, the electrical properties of carbonaceous materials derived from ZIFs can be controlled by the calcination conditions such as temperature and atmosphere[88].

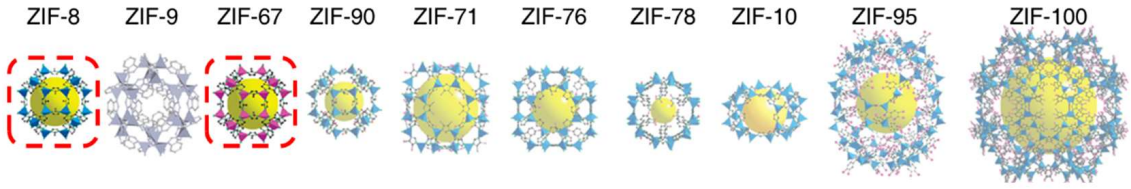

Figure 2.14. Illustrations of typical zeolitic imidazolate frameworks (ZIFs)[86].

2.3.3. ZIF-8, ZIF-67, and Hybrid ZIF-Derived Carbon Materials

Given the suitable properties for an optimum Li-metal host, the ZIF-derived carbon materials are one of the superior types of candidates. The pore structure, pore volume, and lithiophilicity are especially important factors for sufficient Li storage and stable extended cycling. In order to use ZIF-derived carbon materials as host structures properly, a thorough understanding of the ZIF and ZIF-derived carbon is necessary. ZIF-derived carbon hosts can offer improved storage capacity and stability based on these understanding.

ZIF-8 and ZIF-67 have representative sodalite (SOD) type topology, and zinc (Zn) and cobalt (Co) ions are firmly coordinated with 2-methylimidazolate (2-MIM) organic linkers, respectively. These ZIFs have the crystal shape of a rhombic dodecahedron with a large cavity

(11.6 Å), and they are attractive due to their large specific surface area (> 1700 m^2 g^{-1}), large pore volume (> 0.7 cm^3 g^{-1}), relatively simple synthesis, and high yield[89]. Also, these ZIFs can also be directly converted to hierarchically nanoporous carbon structures without secondary carbon precursors. The carbon structures derived from ZIF-8 have micropores with a relatively large pore volume and high N content (Figure 2.15a)[90]. On the other hand, the carbon structures from ZIF-67 are composed of good crystalline carbons, exhibiting good electrical conductivity and mesopores (Figure 2.15b). They have a relatively low pore volume, however, and low N content. In terms of Li-metal storage, carbon materials from ZIF-8 are expected to show high lithiophilicity due to their high N content, and the relatively large pore volume can be expected to accommodate more Li-metal storage. On the other hand, although carbon materials derived from ZIF-67 are expected to store less Li-metal due to their relatively low pore volume, they are sufficient with the use of a small amount of conducting agents due to their high electrical conductivity. In addition, compared to the micropores in carbon materials derived from ZIF-8, the mesopores would be more advantageous for fast Li storage due to the easier transfer of electrolyte. Investigation of these aspects is still ongoing and should be confirmed through further research.

That is, carbon materials derived from ZIFs containing one type of metal ion would have both advantages and disadvantages for Li-metal storage. To compensate for each drawback, it is possible to form hybrid type ZIFs such as bimetallic ZIFs and core-shell ZIFs, which can also be converted to carbonaceous materials. For example, bimetallic ZIFs can be easily synthesized by combining Zn^{2+} and Co^{2+}, since the fundamental structures of both ZIF-8 and ZIF-67 are the same (Figure 2.15c). Each bimetallic ZIF has different properties, according to the ratio of the two metal ions, and bimetallic ZIF-derived carbonaceous materials also have different physical/electrical properties, depending on the initial ratio of Zn^{2+} to Co^{2+} [91-93].

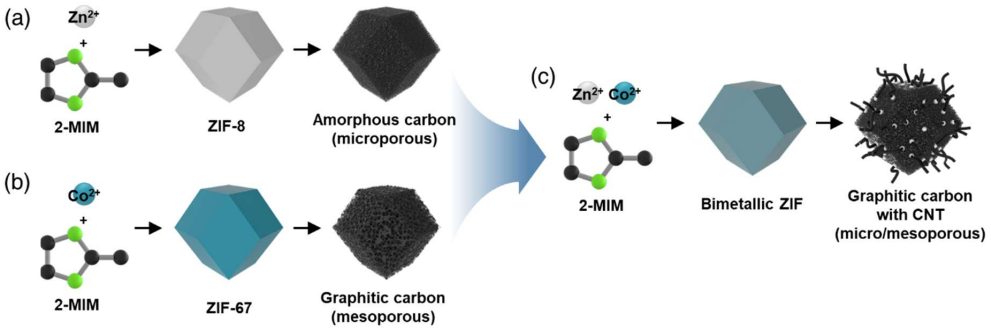

Figure 2.15. The synthesis and carbonization processes for (a) ZIF-8, (b) ZIF-67, and (c) a bimetallic ZIF.

2.3.4. Electrochemical Results on ZIF-Derived Carbonaceous Hosts

To date, there have been few studies using ZIF-derived carbon materials as Li-metal hosts. Among them, most studies used only nanoporous carbon materials derived from ZIF-8 as Li-metal hosts. Representatively, Zhang et al. were inspired by the fact that lithiophilic ZnO quantum-dot decorated hierarchical porous carbon serves as an excellent host[77,96]. They fabricated a ZnO/porous carbon matrix by a one-step process using the carbonization of ZIF-8, as shown in Figure 2.16a. Cell tests were performed using a ZnO/porous carbon matrix as a host for Li-metal storage. At a current density of 1 mA cm^{-2} with an areal capacity of 1 mAh cm^{-2}, bare Li-metal exhibited a large overpotential (> 100 mV), which increased sharply at around the 170^{th} cycle. In contrast, the ZnO/porous carbon framework showed a much lower overpotential (~ 14 mV) over 200 cycles (Figure 2.16b).

As shown in Figure 2.16c, Yang et al. reported Li-cMOFs, where cMOFs are carbonized metal-organic frameworks (ZIF-8-derived carbon), which were obtained through molten Li infusion as a stable Li-metal host material based on the lithiophilic property of Zn clusters[78]. A very low overpotential (~ 29 mV) was achieved in the case of Li-cMOFs compared with bare Li-metal

at a current density of 1 mA cm^{-2} with an areal capacity of 1 mAh cm^{-2}. In addition, after an extended 350 cycles, the overpotential of Li-cMOFs still remained low and stable (52 mV), as shown in Figure 2.16d. Furthermore, they confirmed that there were distinct differences in the deposition behavior of Li-metal with and without Zn clusters. After thorough removal of Zn species through acid etching, a clear interface was observed between the host material film and the deposited Li-metal.

Finally, Park et al. suggested the dual functionality of Li storage in porous carbon hosts using porous carbon frameworks (PCFs) derived from ZIF-8[79]. As shown in Figure 2.16e, PCFs store Li in the dual-phase, which is Li adsorbed on a carbon structure (lithiation) and metallic Li storage in a large pore volume (metallization). Uniquely, PCFs with tailored properties were prepared by optimized acid etching of the Zn clusters (PCF-E). For the cycling test, the cells were firstly charged to 2.0 mAh cm^{-2} and cycled at 0.2 mA cm^{-2} with an areal capacity of 0.2 mAh cm^{-2}. Compared with a Li||Super-P cell (voltage spikes at 88 cycles), the Li||PCF-E cell exhibited stable cycling performance over 350 cycles (Figure 2.16f). This implies that highly conductive carbon structures without pore structures are unsuitable as host materials for Li-metal storage.

All the results using nanoporous carbon obtained from ZIF-8 as host material have shown the dramatic suppression of huge volume expansion during Li plating/stripping. In addition, N and Zn (or ZnO) nanoparticles within the host structures improved the affinity with Li, which was attributed to the preferred nucleation and stable growth of Li-metal. Due to these advantages, ZIF-derived carbon hosts showed dramatically improved cell cycling compared to Li-metal or non-porous carbon materials.

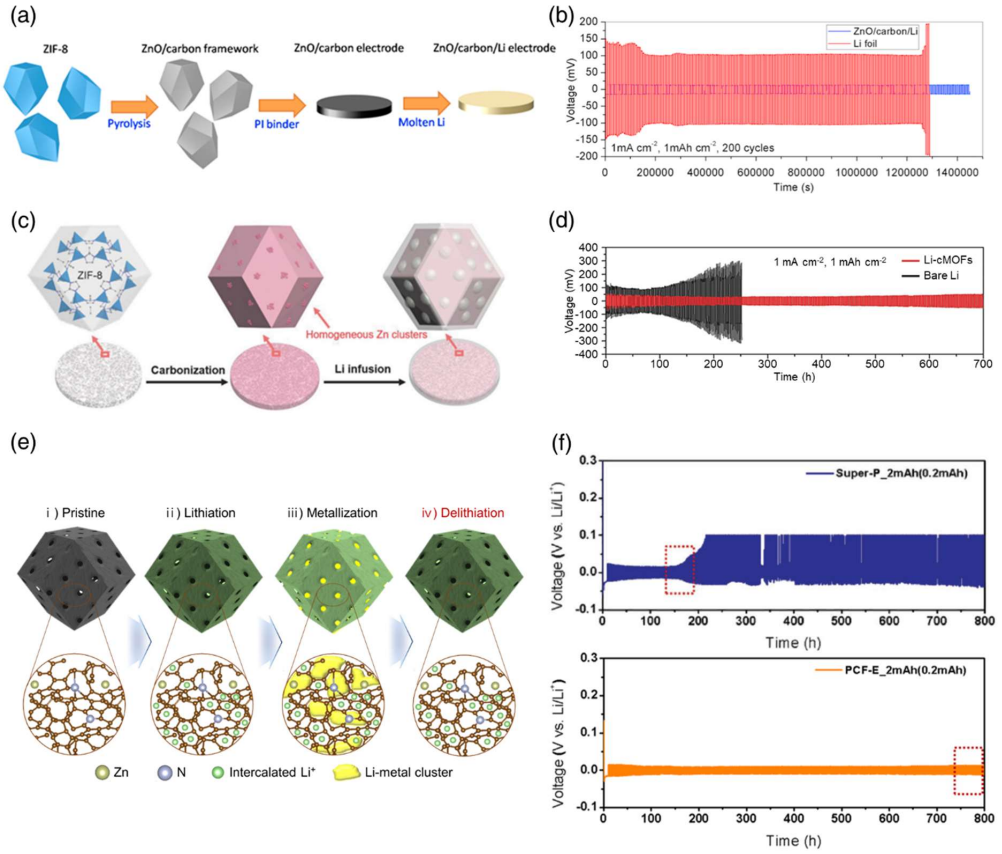

Figure 2.16. (a, c, e) Schematic illustrations showing representative host materials for Li-metal storage based on ZIF-derived carbon[77]. (a) ZnO/carbon framework[78], (c) cMOFs[79], and (e) PCF. (b, d, f) Electrochemical characterization corresponding to each host material.

2.3.5. Additional Strategies for Improvement

There have been many attempts to tailor the microstructure of porous carbon materials through various types of physical/chemical activation[97]. Notably, the chemical activation of different kinds of carbon materials using potassium hydroxide (KOH) has attracted considerable attention because of the relatively low activation temperature, high yield, and well-defined pore size distribution[97-102]. ZIF-derived carbon can have more micro/mesopores in the range from 1 to 4 nm, as shown in Figure 2.17a Zhang et al. reported ZIF-derived carbon with a significantly improved specific surface area (3680.6 $m^2 g^{-1}$) and pore volume (1.93 cm^3

g^{-1})[99]. The mesopores are expected to facilitate diffusion of the electrolyte, and the increased pore volume provides additional room for storing Li-metal.

Hollow ZIFs can be made through simple tannic acid etching of as-prepared ZIFs, and direct carbonization can be used to produce hollow ZIF-derived carbon structures while keeping their original shapes, as shown in Figure 2.17a[103-105]. This is an effective way to overcome the limitations of the shape and structure of ZIFs created by traditional approaches. Cui et al. confirmed that the growth of Li-metal occurs predominantly inside the hollow carbon spheres containing nanoparticle seeds with no nucleation barriers to Li-metal during Li plating[69]. The hollow ZIF-derived carbon materials formed through a simple acid etching strategy can also be expected to have a unique role as Li-metal storage hosts. As another strategy that can be suggested, the previous ZIF structures can be further developed by using polystyrene (PS) templates[106,107]. Well-stacked PS templates help the ZIF structure to transform into three-dimensional-ordered macro-microporous (3-DOM) ZIFs. These ZIF structures are easily converted to 3-DOM carbon structures through facile carbonization, as shown in Figure 2.17a. Zhang et al. synthesized $CoSe_2$ impregnated 3-DOM carbon materials (3-DOM $CoSe_2$@C) through a facile carbonization-selenization treatment using ZIF-67 as a precursor and applied it as a cathode material for aluminum (Al)-ion batteries[107]. 3-DOM $CoSe_2$@C exhibited excellent reversible rate capacity (86 mAh g^{-1} at 5.0 A g^{-1}) and remarkable cycling performance (125 mAh g^{-1} after 1000 cycles at 2.0 A g^{-1}). These outstanding results were possible because regularly interconnected macropores effectively promote the diffusion of large-sized chloroaluminate anions ($Al_xCl_y^-$) and also expose more active sites. Similar effects can be expected by applying this structure in constructing Li-metal anode since the improved internal macropores can accommodate more Li-metal, which is directly related to the increased storage capacity. In addition to these methods, many results have been reported for various approaches

to design the pore structure and increase the pore volume of ZIF-based carbon materials[108-113].

It is expected that tailored host materials with suitable properties can be developed.

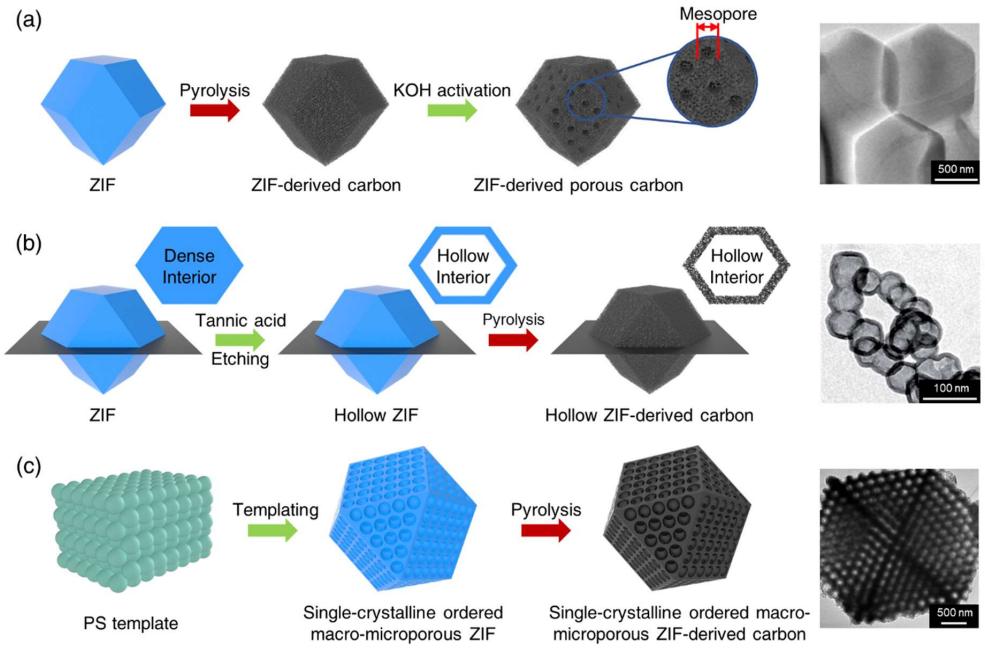

Figure 2.17. Schematic illustrations showing further strategies to improve the pore structure of ZIF-derived carbon and the corresponding transmission electron microscope (TEM) images. (a) KOH activation[99], (b) hollow carbon activated by tannic acid etching[103], and (c) ordered macro-microporous structure via polystyrene (PS) templating[107].

2.4. Findings from Literature Review

Human beings can now carry their own electrical energy supply, due to the development of rechargeable batteries, and their utilization has been vastly diversified with the development of Li-ion batteries. Moreover, the demand for high-energy-density applications, such as EVs, is increasing continuously. In this regard, it is extremely attractive to use Si and Li-metal with high theoretical capacity and a low reduction potential as the anode in energy storage devices.

For the past decade, Si anode material technology has been rapidly advanced and it maybe overwhelms the overall electrochemical performances of conventional graphite anode. However, to reach the stage of commercialization, there are still remaining issues to solve, such as, mass production possibilities by cost effective ways and compatibilities with other battery compositions (e.g. cathode, binder and electrolyte). Thus, future researches for Si anode material should be conducted with those aspects in company with, needless to say, the electrochemical performances.

As well, the fundamental issues for Li-metal anode, however, such as dendrite growth and huge volume changes, are hindering its commercialization. These problems have promoted research on almost all parts of an Li-metal battery, such as on the anode, the interfacial chemistry of the anode and electrolyte, the electrolyte, and the separator. Among them, progress on the Li-metal anode is absolutely necessary and has inspired various studies to solve the issues.

The storage of Li-metal in stable host materials has been introduced as an effective way to stably use Li-metal, and this literature review suggests the possibility of ZIF-derived carbon materials as suitable host structures for Li storage. Carbonaceous materials derived from ZIFs have all the suitable properties for Li-metal hosts, and their physical/electrical properties can be controlled depending on the type of ZIF or the carbonization conditions. In particular, these

carbon structures have a large pore volume, which serves as a physical space for storing Li-metal, and a lithiophilic surface for preferred nucleation and growth. Through various approaches to enlarge the pore volume, the capacity for Li storage can be further improved. In addition to the methods suggested in this literature review, there are numerous possible candidates to improve Li storage. This means that the storage capability of ZIF-derived carbon can be further enhanced in the future. Based on all of these desirable features, ZIF-derived carbon host materials are expected to play a critical role in next-generation energy storage devices.

2.5. References

[1] C.-M. Park, J.-H. Kim, H. Kim, H.-J. Sohn, *Chem. Soc. Rev.* **2010**, 39, 3115.

[2] M. Armand, J. M. Tarascon, *Nature* **2008**, 451, 652.

[3] C. K. Chan, H. Peng, G. Liu, K. McIlwrath, X. F. Zhang, R. A. Huggins, Y. Cui, *Nat. Nanotechnol.* **2007**, 3, 31.

[4] U. Kasavajjula, C. Wang, A. J. Appleby, *J. Power Sources* **2007**, 163, 1003.

[5] W.-J. Zhang, *J. Power Sources* **2011**, 196, 13.

[6] R. Mukherjee, R. Krishnan, T.-M. Lu, N. Koratkar, *Nano Energy* **2012**, 1, 518–533.

[7] J. Ryu, D. Hong, S. Choi, S. Park, *ACS Nano* **2016**, 10, 2843.

[8] N. Liu, H. Wu, M. T. McDowell, Y. Yao, C. Wang, Y. Cui, *Nano Lett.* **2012**, 12, 3315.

[9] L. Y. Yang, H. Z. Li, J. Liu, Z. Q. Sun, S. S. Tang, M. Lei, *Sci. Rep.* **2015**, 5, 10908.

[10] G. Liang, X. Qin, J. Zou, L. Luo, Y. Wang, M. Wu, H. Zhu, G. Chen, F. Kang, B. Li, *Carbon* **2018**, 127, 424.

[11] A. M. Chockla, K. C. Klavetter, C. B. Mullins, B. A. Korgel, *Chem. Mater.* **2012**, 24, 3738.

[12] A. Gohier, B. Laïk, J.-P. Pereira-Ramos, C. S. Cojocaru, P. Tran-Van, *J. Power Sources* **2012**, 203, 135.

[13] Z. Wen, G. Lu, S. Mao, H. Kim, S. Cui, K. Yu, X. Huang, P. T. Hurley, O. Mao, J. Chen, *Electrochem. Commun.* **2013**, 29, 67.

[14] X. Wang, L. Sun, X. Hu, R. A. Susantyoko, Q. Zhang, *J. Power Sources* **2015**, 280, 393.

[15] X. Yu, F. Xue, H. Huang, C. Liu, J. Yu, Y. Sun, X. Dong, G. Cao, Y. Jung, *Nanoscale* **2014**, 6, 6860.

[16] Y. Liu, B. Chen, F. Cao, H. L. W. Chan, X. Zhao, J. Yuan, *J. Mater. Chem.* **2011**, 21, 17083.

[17] Z. Jiang, C. Li, S. Hao, K. Zhu, P. Zhang, *Electrochim. Acta* **2014**, 115, 393.

[18] Q. Xiao, M. Gu, H. Yang, B. Li, C. Zhang, Y. Liu, F. Liu, F. Dai, L. Yang, Z. Liu, X. Xiao, G. Liu, P. Zhao, S. Zhang, C. Wang, Y. Lu, M. Cai, *Nat. Commun.* **2015**, 6, 8844.

[19] J.-I. Lee, K. T. Lee, J. Cho, J. Kim, N.-S. Choi, S. Park, *Angew. Chem. Int. Ed.* **2012**, 51, 2767.

[20] H. Jia, P. Gao, J. Yang, J. Wang, Y. Nuli, Z. Yang, *Adv. Energy Mater.* **2011**, 1, 1036.

[21] R. Zhang, Y. Du, D. Li, D. Shen, J. Yang, Z. Guo, H. K. Liu, A. A. Elzatahry, D. Zhao, *Adv. Mater.* **2014**, 26, 6749.

[22] A. Magasinski, P. Dixon, B. Hertzberg, A. Kvit, J. Ayala, G. Yushin, *Nat. Mater.* **2010**, 9, 353.

[23] M. Ko, S. Chae, S. Jeong, P. Oh, J. Cho, *ACS Nano* **2014**, 8, 8591.

[24] J.-K. Yoo, J. Kim, Y. S. Jung, K. Kang, *Adv. Mater.* **2012**, 24, 5452.

[25] H. Wu, G. Chan, J. W. Choi, I. Ryu, Y. Yao, M. T. McDowell, S. W. Lee, A. Jackson, Y. Yang, L. Hu, Y. Cui, *Nat. Nanotechnol.* **2012**, 7, 310.

[26] E. Park, H. Yoo, J. Lee, M.-S. Park, Y.-J. Kim, H. Kim, *ACS Nano* **2015**, 9, 7690.

[27] R. Ma, Y. Liu, Y. Yang, M. Gao, H. Pan, *Appl. Phys. Lett.* **2014**, 105, 213901.

[28] H. Jung, Y.-U. Kim, M.-S. Sung, Y. Hwa, G. Jeong, G.-B. Kim, H.-J. Sohn, *J. Mater. Chem.* **2011**, 21, 11213.

[29] H. Chen, M. Ling, L. Hencz, H. Y. Ling, G. Li, Z. Lin, G. Liu, S. Zhang, *Chem. Rev.* **2018**, 118, 8936.

[30] S. Kim, Y. K. Jeong, Y. Wang, H. Lee, J. W. Choi, *Adv. Mater.* **2018**, 30, 1707594.

[31] S. Guo, H. Li, Y. Li, Y. Han, K. Chen, G. Xu, Y. Zhu, X. Hu, *Adv. Energy Mater.* **2018**, 8, 1800434.

[32] C. Wang, H. Wu, Z. Chen, M. T. McDowell, Y. Cui, Z. Bao, *Nat. Chem.* **2013**, 5, 1042.

[33] Y. Horowitz, H.-L. Han, F. A. Soto, W. T. Ralston, P. B. Balbuena, G. A. Somorjai, *Nano Lett.* **2018**, 18, 1145.

[34] A. Schiele, B. Breitung, T. Hatsukade, B. B. Berkes, P. Hartmann, J. Janek, T. Brezesinski, *ACS Energy Lett.* **2017**, 2, 2228.

[35] Y. Okuno, K. Ushirogata, K. Sodeyama, Y. Tateyama, *Phys. Chem. Chem. Phys.* **2016**, 18, 8643.

[36] Y. Horowitz, H.-L. Han, F. A. Soto, W. T. Ralston, P. B. Balbuena, G. A. Somorjai, *Nano Lett.* **2018**, 18, 1145.

[37] C. M. López, J. T. Vaughey, D. W. Dees, *J. Electrochem. Soc.* **2000**,156, A726.

[38] Y. S. Cohen, Y. Cohen, D. Aurbach, *J. Phys. Chem. B* **2000**, 104, 12282.

[39] D. Aurbach, *J. Power Sources* **2000**, 89, 206.

[40] K.-H. Chen, K. N. Wood, E. Kazyak, W. S. LePage, A. L. Davis, A. J. Sanchez, N. P. Dasgupta, *J. Mater. Chem. A* **2017**, 5, 11671.

[41] D. Lu, Y. Shao, T. Lozano, W. D. Bennett, G. L. Graff, B. Polzin, J. Zhang, M. H. Engelhard, N. T. Saenz, W. A. Henderson, P. Bhattacharya, J. Liu, J. Xiao, *Adv. Energy Mater.* **2015**, 5, 1400993.

[42] K. N. Wood, E. Kazyak, A. F. Chadwick, K.-H. Chen, J.-G. Zhang, K. Thornton, N. P. Dasgupta, *ACS Cent. Sci.* **2016**, 2, 790

[33] X.-B. Cheng, Q. Zhang, *J. Mater. Chem. A* **2015**, 3, 7207.

[34] L. Wang, L. Zhang, Q. Wang, W. Li, B. Wu, W. Jia, Y. Wang, J. Li, H. Li, *Energy Storage Mater.* **2018**, 10, 16.

[35] L. Fan, H. L. Zhuang, L. Gao, Y. Lu, L. A. Archer, *J. Mater. Chem. A* **2017**, 5, 3483.

[36] X. Zhang, T. Liu, S. Zhang, X. Huang, B. Xu, Y. Lin, B. Xu, L. Li, C.-W. Nan, Y. Shen, *J. Am. Chem. Soc.* **2017**, 139, 13779.

[37] J. Zhao, L. Liao, F. Shi, T. Lei, G. Chen, A. Pei, J. Sun, K. Yan, G. Zhou, J. Xie, C. Liu, Y. Li, Z. Liang, Z. Bao, Y. Cui, *J. Am. Chem. Soc.* **2017**, 139, 11550.

[38] J. Lang, Y. Long, J. Qu, X. Luo, H. Wei, K. Huang, H. Zhang, L. Qi, Q. Zhang, Z. Li, H. Wu, *Energy Storage Mater.* **2019**, 16, 85.

[39] N.-W. Li, Y.-X. Yin, C.-P. Yang, Y.-G. Guo, *Adv. Mater.* **2016**, 28, 1853.

[40] L. Wang, Q. Wang, W. Jia, S. Chen, P. Gao, J. Li, *J. Power Sources* **2017**, 342, 175.

[41] Z. Hu, S. Zhang, S. Dong, W. Li, H. Li, G. Cui, L. Chen, *Chem. Mater.* **2017**, 29, 4682.

[42] Y. J. Zhang, W. Wang, H. Tang, W. Q. Bai, X. Ge, X. L. Wang, C. D. Gu, J. P. Tu, *J. Power Sources* **2015**, 277, 304.

[43] G. A. Umeda, E. Menke, M. Richard, K. L. Stamm, F. Wudl, B. Dunn, *J. Mater. Chem* **2011**, 21, 1593.

[44] D. Lin, Y. Liu, Y. Cui, *Nat. Nanotechnol.* **2017**, 12, 194.

[45] G. Zheng, S. W. Lee, Z. Liang, H.-W. Lee, K. Yan, H. Yao, H. Wang, W. Li, S. Chu, Y. Cui, *Nat. Nanotechnol.* **2014**, 9, 618.

[46] K. Yan, H.-W. Lee, T. Gao, G. Zheng, H. Yao, H. Wang, Z. Lu, Y. Zhou, Z. Liang, Z. Liu, S. Chu, Y. Cui, *Nano Lett.* **2014**, 14, 6016.

[47] A. Pei, G. Zheng, F. Shi, Y. Li, Y. Cui, *Nano Lett.* **2017**, 17, 1132.

[48] C.-P. Yang, Y.-X. Yin, S.-F. Zhang, N.-W. Li, Y.-G. Guo, *Nat. Commun.* **2015**, 6, 8058.

[49] Q. Yun, Y.-B. He, W. Lv, Y. Zhao, B. Li, F. Kang, Q.-H. Yang, *Adv. Mater.* **2016**, 28, 6932.

[50] A. Zhamu, G. Chen, G. Liu, D. Neff, Q. Fang, Z. Yu, W. Xiong, Y. Wang, X. Wang, B. Z. Jang, *Energy Environ. Sci.* **2012**, 5, 5701.

[51] X. Ji, D.-Y. Liu, D. G. Prendiville, Y. Zhang, X. Liu, G. D. Stucky, *Nano Today* **2012**, 7, 10.

[52] M.-H. Ryou, D. J. Lee, J.-N. Lee, Y. M. Lee, J.-K. Park, J. W. Choi, *Adv. Energy Mater.* **2012**, 2, 645.

[53] H. Zhang, X. Liao, Y. Guan, Y. Xiang, M. Li, W. Zhang, X. Zhu, H. Ming, L. Lu, J. Qiu, Y. Huang, G. Cao, Y. Yang, L. Mai, Y. Zhao, H. Zhang, *Nat. Commun.* **2018**, 9, 3729.

[54] H. Zheng, Q. Zhang, Q. Chen, W. Xu, Q. Xie, Y. Cai, Y. Ma, Z. Qiao, Q. Luo, J. Lin, L. Wang, B. Qu, B. Sa, D.-L. Peng, *J. Mater. Chem. A* **2020**, 8, 313.

[55] X. Yan, Q. Zhang, W. Xu, Q. Xie, P. Liu, Q. Chen, H. Zheng, L. Wang, Z.-Z. Zhu, D.-L. Peng, *J. Mater. Chem. A* **2020**, 8, 1678.

[56] J. Li, P. Zou, S. W. Chiang, W. Yao, Y. Wang, P. Liu, C. Liang, F. Kang, C. Yang, *Energy Storage Mater.* **2020**, 24, 700.

[57] S.-H. Hong, D.-H. Jung, J.-H. Kim, Y.-H. Lee, S.-J. Cho, S. H. Joo, H.-W. Lee, K.-S. Lee, S.-Y. Lee, *Adv. Funct. Mater.* **2020**, 30, 1908868.

[58] D. Lin, Y. Liu, Z. Liang, H.-W. Lee, J. Sun, H. Wang, K. Yan, J. Xie, Y. Cui, *Nat. Nanotechnol.* **2016**, 11, 626.

[59] K. Yan, Z. Lu, H.-W. Lee, F. Xiong, P.-C. Hsu, Y. Li, J. Zhao, S. Chu, Y. Cui, *Nat. Energy* **2016**, 1, 16010.

[60] T. Wang, R. V. Salvatierra, A. S. Jalilov, J. Tian, J. M. Tour, *ACS Nano* **2017**, 11, 10761.

[61] C. Niu, H. Pan, W. Xu, J. Xiao, J.-G. Zhang, L. Luo, C. Wang, D. Mei, J. Meng, X. Wang, Z. Liu, L. Mai, J. Liu, *Nat. Nanotechnol.* **2019**, 14, 594.

[62] L. Liu, Y.-X. Yin, J.-Y. Li, S.-H. Wang, Y.-G. Guo, L.-J. Wan, *Adv. Mater.* **2018**, 30, 1706216.

[63] Z. Liang, D. Lin, J. Zhao, Z. Lu, Y. Liu, C. Liu, Y. Lu, H. Wang, K. Yan, X. Tao, Y. Cui, *Proc. Natl. Acad. Sci.* USA **2016**, 113, 2862.

[64] A.-R. O. Raji, R. V. Salvatierra, N. D. Kim, X. Fan, Y. Li, G. A. L. Silva, J. Sha, J. M. Tour, *ACS Nano* **2017**, 11, 6362.

[65] L. Fan, H. L. Zhuang, W. Zhang, Y. Fu, Z. Liao, Y. Lu, *Adv. Energy Mater.* **2018**, 8, 1703360.

[66] Y. Liu, D. Lin, Z. Liang, J. Zhao, K. Yan, Y. Cui, *Nat. Commun.* **2016**, 7, 10992.

[67] L. Wang, X. Zhu, Y. Guan, J. Zhang, F. Ai, W. Zhang, Y. Xiang, S. Vijayan, G. Li, Y. Huang, G. Cao, Y. Yang, H. Zhang, *Energy Storage Mater.* **2018**, 11, 191.

[68] M. Zhu, B. Li, S. Li, Z. Du, Y. Gong, S. Yang, *Adv. Energy Mater.* **2018**, 8, 1703505.

[69] J. Kim, J. Lee, J. Yun, S. H. Choi, S. A Han, J. Moon, J. H. Kim, J.-W. Lee, M.-S. Park, *Adv. Funct. Mater.* **2020**, 30, 1910538.

[70] H. K. Christenson, *CrystEngComm* **2013**, 15, 2030.

[71] R. Zhang, X.-R. Chen, X. Chen, X.-B. Cheng, X.-Q. Zhang, C. Yan, Q. Zhang, *Angew. Chem. Int. Ed.* **2017**, 56, 7764.

[72] X. Chen, X.-R. Chen, T.-Z. Hou, B.-Q. Li, X.-B. Cheng, R. Zhang, Q. Zhang, *Sci. Adv.* **2019**, 5, eaau7728.

[73] C. A. Scholl, N. H. Fletcher, *Acta Metall.* **1970**, 18, 1083.

[74] R. Banerjee, A. Phan, B. Wang, C. Knobler, H. Furukawa, M. O'Keeffe, O. M. Yaghi, *Science* **2008**, 319, 939.

[75] K. S. Park, Z. Ni, A. P. Côté, J. Y. Choi, R. Huang, F. J. Uribe-Romo, H. K. Chae, M. O'Keeffe, O. M. Yaghi, *Proc. Natl. Acad. Sci.* USA **2006**, 103, 10186.

[76] A. Phan, C. J. Doonan, F. J. Uribe-Romo, C. B. Knobler, M. O'Keeffe, O. M. Yaghi, *Acc. Chem. Res.* **2010**, 43, 58.

[77] R. R. Salunkhe, Y. V. Kaneti, J. Kim, J. H. Kim, Y. Yamauchi, *Acc. Chem. Res.* **2016**, 49, 2796.

[78] R. R. Salunkhe, J. Tang, Y. Kamachi, T. Nakato, J. H. Kim, Y. Yamauchi, *ACS Nano* **2015**, 9, 6288.

[79] J. Tang, R. R. Salunkhe, H. Zhang, V. Malgras, T. Ahamad, S. M. Alshehri, N. Kobayashi, S. Tominaka, Y. Ide, J. H. Kim, Y. Yamauchi, *Sci. Rep.* **2016**, 6, 30295.

[80] C. Young, R. R. Salunkhe, J. Tang, C.-C. Hu, M. Shahabuddin, E. Yanmaz, M. S. A. Hossain, J. H. Kim, Y. Yamauchi, *Phys. Chem. Chem. Phys.* **2016**, 18, 29308.

[81] J. Kim, C. Young, J. Lee, Y.-U. Heo, M.-S. Park, M. S. A. Hossain, Y. Yamauchi, J. H. Kim, *J. Mater. Chem. A* **2017**, 5, 15065.

[82] J. Kim, C. Young, J. Lee, M.-S. Park, M. Shahabuddin, Y. Yamauchi, J. H. Kim, *Chem. Commun.* **2016**, 52, 13016.

[83] Y.-Z. Chen, C. Wang, Z.-Y. Wu, Y. Xiong, Q. Xu, S.-H. Yu, H.-L. Jiang, *Adv. Mater.* **2015**, 27, 5010.

[84] S. A Han, J. Lee, K. Shim, J. Lin, M. Shahabuddin, J.-W. Lee, S.-W. Kim, M.-S. Park, J. H. Kim, *Bull. Chem. Soc. Jpn.* **2018**, 91, 1474.

[85] J. Lee, S. A Han, H. Qutaish, L. K. Shrestha, K. Ariga, J. H. Kim, *Gen. Chem.* **2019**, 5, 190011.

[86] C. Jin, O. Sheng, J. Luo, H. Yuan, C. Fang, W. Zhang, H. Huang, Y. Gan, Y. Xia, C. Liang, J. Zhang, X. Tao, *Nano Energy* **2017**, 37, 177.

[87] J. Wang, S. Kaskel, *J. Mater. Chem.* **2012**, 22, 23710.

[88] J. Kim, J. Kim, J. H. Kim, H. S. Park, *Chem. Eng. J.* **2020**, 382, 122996.

[89] R. Wang, D. Jin, Y. Zhang, S. Wang, J. Lang, X. Yan, L. Zhang, *J. Mater. Chem. A* **2017**, 5, 292.

[90] S.-H. Yoon, S. Lim, Y. Song, Y. Ota, W. Qiao, A. Tanaka, I. Mochida, *Carbon* **2004**, 42, 1723.

[91] Y. Lv, F. Zhang, Y. Dou, Y. Zhai, J. Wang, H. Liu, Y. Xia, B. Tu, D. Zhao, *J. Mater. Chem.* **2012**, 22, 93.

[92] P. Han, M. Cheng, D. Luo, W. Cui, H. Liu, J. Du, M. Wang, Y. Zhao, L. Chen, C. Zhu, J. Xu, *Energy Storage Mater.* **2020**, 24, 486.

[93] W. Zhang, X. Jiang, Y. Zhao, A. Carné-Sánchez, V. Malgras, J. Kim, J. H. Kim, S. Wang, J. Liu, J.-S. Jiang, Y. Yamauchi, M. Hu, *Chem. Sci.* **2017**, 8, 3538.

[94] M. Wu, C. Li, J. Zhao, Y. Ling, R. Liu, *Dalton Trans.* **2018**, 47, 7812.

[95] Q. Li, M. Wu, J. Zhao, Q. Lü, L. Han, R. Liu, *J. Electron. Mater.* **2019**, 48, 3050.

[96] K. Shen, L. Zhang, X. Chen, L. Liu, D. Zhang, Y. Han, J. Chen, J. Long, R. Luque, Y. Li, B. Chen, *Science* **2018**, 359, 206.

[97] H. Hong, J. Liu, H. Huang, C. A. Etogo, X. Yang, B. Guan, L. Zhang, *J. Am. Chem. Soc.* **2019**, 141, 14764.

[98] H. J. Lee, W. Cho, M. Oh, *Chem. Commun.* **2012**, 48, 221.

[99] H. Chen, K. Shen, J. Chen, X. Chen, Y. Li, *J. Mater. Chem. A* **2017**, 5, 9937.

[100] A. Almasoudi, R. Mokaya, *J. Mater. Chem.* **2012**, 22, 146.

[101] L. He, L. Li, L. Zhang, S. Xing, T. Wang, G. Li, X. Wu, Z. Su, C. Wang, *CrystEngComm* **2014**, 16, 6534.

[102] Z. Zou, S. Li, D. He, X. He, K. Wang, L. Li, X. Yang, H. Li, *J. Mater. Chem. B* **2017**, 5, 2126.

[103] Y. Wu, M. Zhou, B. Zhang, B. Wu, J. Li, J. Qiao, X. Guan, F. Li, *Nanoscale* **2014**, 6, 1105.

Chapter 3. Everlasting Living and Breathing Gyroid 3D Network in Si@SiOx/C Nanoarchitecture for Lithium Ion Battery

3.1. Abstract

Silicon-based materials are the most promising candidates to surpass the capacity limitation of conventional graphite anode for lithium-ion batteries. Unfortunately, Si-based materials suffer from poor cycling performance and dimensional instability induced by the large volume changes during cycling. To resolve such problems, nanostructured silicon-based materials with delicately controlled microstructure and interfaces have been intensively investigated. Nevertheless, they still face problems related to their high synthetic cost and their limited electrochemical properties and thermal stability. To overcome these drawbacks, we demonstrate the strategic design and synthesis of a gyroid three-dimensional network in a Si@SiO_x/C nanoarchitecture (3D-Si@SiO_x/C) with synergetic interaction between the computational prediction and the synthetic optimization. This 3D-Si@SiO_x/C exhibits not only excellent electrochemical performance due to its structural stability and superior ion/electron transport, but also enhanced thermal stability due to the presence of carbon, which was formed by a cost-effective one-pot synthetic route. We believe that our rationally designed 3D-Si@SiO_x/C will lead to the development of anode materials for the next generation lithium-ion batteries.

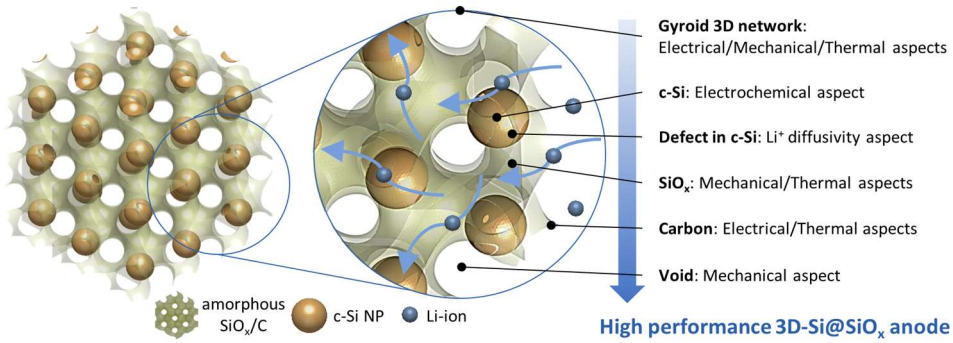

Figure 3.1. Graphical abstract

3.2. Introduction

Silicon (Si) has been proposed as a promising anode material on account of its high theoretical specific capacity ($Li_{15}Si_4$, 3580 mA h g^{-1}) and relatively low redox potential *versus* Li/Li^+ (~0.4 V), as compared with the conventional graphite system, which shows intrinsically less theoretical capacity (372 mA h g^{-1}).[1-5] Severe volume expansion/contraction occurs, however, when the Si active materials are reacting with lithium (Li) in alloying/dealloying processes (> 300 %).[6] The mechanical stress on the surface caused by the volume changes leads to the pulverization of the Si particles and the loss of electrical contact.[7] Consequently, it causes rapid capacity degradation during cycling. To overcome these drawbacks, recently, various approaches have been proposed, which are mainly divided into two research strategies. Firstly, to create morphological variations of Si active materials is mainstream research to reduce the mechanical stress such as with zero-dimensional (0D) nanoparticles,[8-10] one-dimensional (1D) nanorods/nanotubes,[11-13] two-dimensional (2D) nanosheets,[14,15] and three-dimensional (3D) porous materials,[16-19] as well as microparticles.[20,21] These Si materials show not only excellent cycling performances, but also highly reversible specific capacities due to their enhanced anti-pulverization characteristics. It might be infeasible, however, to apply them in large-scale production because the material preparation requires high-cost synthetic routes or even the use of hazardous chemicals. Secondly, various types of Si-based composites have been introduced in order to compensate for the deficiencies of Si, such as Si/carbon composites,[22-25] Si/SiO_x (Si suboxides, $0<x<2$) composites,[26,27] and Si/alloy composites.[28,29] Although these composites also show moderate cycling performances, none of these materials is adequate enough to overcome the performance of conventional graphite, owing to different weaknesses, such as low initial Coulombic efficiency, high-cost synthesis, or high-cost precursors.

By considering previous research, it is argued that simultaneous troubleshooting on various aspects is a prerequisite for applying the Si-based anode materials in the next generation of Li-ion batteries (LIBs). To be specific, the Si-based anode materials should first have high reversible capacity with an acceptable initial Coulombic efficiency in order to surpass the energy density of the conventional graphite system. Unless these characteristics are sufficiently high, it might be nothing but a meaningless performance based on relatively low density structured materials such as nanosized or porous materials.[30] Secondly, they should have, needless to say, good cyclability assisted by structural modifications such as control of the particle size and the introduction of a robust framework for preventing the fracturing of the materials when they react with Li.[5] Thirdly, ion/electron conductivity and thermal stability are also essential factors that the Si-based anode materials should have. Regardless of the intrinsically insufficient properties of Si, these can be compensated by designing the suitable structures such as a 3D network, as well as the incorporation of carbon, which enhances the conductivity and the thermal stability.[23,31] Finally, the synthesis of the material should be conducted by using safe, nontoxic, and cost-effective methods for mass-scale production. Accordingly, these factors should be considered from the material design step. To sum up, we aim to achieve the development of Si-based materials for practical use under the consideration of 1) the high energy density (*e.g.* Si content), 2) robust structure with a combination of stable components (*e.g.* 3D network SiO_x), 3) high conductivity and thermal properties (*e.g.* carbon incorporation), and 4) facile synthesis.

On the basis of our strategies for material design, we engaged in computational predictions of the volume changes of various structures, as well as exploring how to realize the ideal material from the predictions with the aid of continuous feedback. By continuum scale analysis, simulation, and prediction of volume changes for both the unit cell and Si particles interior models were constructed to aid in the structural design of anode materials. We thus determined

that our 3D network structured Si/SiO_x composite could prevent volume expansion as well as providing better ion/electron conductivity with Si-based anode. In this study, we consequently demonstrate a gyroid 3D network of Si embedded in SiO_x with a carbon shell (denoted as 3D-Si@SiO_x/C) which was synthesized *via* one-step magnesiothermic reduction[32] and carbonization[33] with double-gyroid highly ordered mesoporous silica (denoted as KIT-6), including polymer template as a precursor. The 3D-Si@SiO_x/C has a mesoporous structure with 10 nm-sized, defect-rich Si nanoparticles interconnected in a SiO_x/C network frame. With this nanoarchitecture, the 3D-Si@SiO_x has delivered the reversible capacity of 1635 mAh g^{-1}, and its initial Coulombic efficiency is over 80 % due to its structural stability. The 3D-Si@SiO_x has also demonstrated 83.3% stable capacity retention up to 100 cycles and 85.0 % rate capability at a current density of 4000 mA g^{-1} compared to 200 mA g^{-1}. In addition, highly thermostable properties were confirmed by a high temperature cycling test at 60 °C and differential scanning calorimetry (DSC) analysis of the electrode after lithiation. As a result, we argue that rationally designed 3D-Si@SiO_x/C is the best candidate for the practical use of cost-effective and safe Si-based anode material for the next generation of LIBs.

3.3 Experimental

3.3.1 Numerical Simulation Modeling

Finite element analysis of the mechanical models was carried out using COMSOL Multiphysics. For diffusion-induced stress analysis of Li_xSi as function of Li concentration, Young's modulus from 90 to 40 GPa and Poisson's ratio from 0.28 to 0.24 was adopted.[59] Although the Li_xSiO_2 also shows elastic softening due to Li insertion, we assumed that silica rarely reacts with lithium in this study.

The increment of elastic strain, $d\varepsilon_{ij}^{e}$, represents the Hooke's law:

$$d\varepsilon_{ij}^{e} = \frac{1}{E(c)}\left[\left(1 + v(c)\right)d\sigma_{ij} - v(c)d\sigma_{kk}\delta_{ij}\right] \quad (1)$$

where $E(c)$ and $v(c)$ are the Young's modulus and Poisson's ratio as function of Li concentration, respectively. σ_{kk} is the diagonal components of stress and δ_{ij} is the Kronecker delta.

The classical J2-flow plasticity theory is employed to determine the increment of the plasticity strain, $d\varepsilon_{ij}^{p}$, refered to as:

$$d\varepsilon_{ij}^{p} = \dot{\lambda}\sigma_{ij}' \quad (2)$$

where $\dot{\lambda}$ is a scalar coefficient calculated by solving the boundary value problem. The yield strength of pristine Si is set at 1.75 GPa. Due to the lack of reported values of for the yield strength of Li_xSiO_2, we found the yield point of 20 GPa for $Li_{0.125}SiO_2$.

Analogously, the increment of the compositional strain obeys following equation (3):

$$d\varepsilon_{ij}^{c} = \frac{\Omega dc}{3}\delta_{ij} \quad (3)$$

where Ω is the partial molar volume of the solute. As lithium is inserted into the silicon, the mechanical deformation arising from lithiation is divided into the reversible elasticity, irreversible plasticity, and compositional swelling contribution. The total incremental strain is the sum of each component as expressed in the equation (4):

$$d\varepsilon = d\varepsilon_{ij}^{e} + d\varepsilon_{ij}^{p} + d\varepsilon_{ij}^{c} \quad (4)$$

A diffusion model containing two-phase interfaces is needed to investigate the stress evolution in c-Si during the sequencial lithiation. Based on the classical diffusion equation (5) , the two-phase diffusion model is easily developed.

$$\frac{\partial c}{\partial t} = \nabla \cdot (D \nabla c) \quad (5)$$

where c is the normalized Li concentration (c = 0 for pure Si and c = 1 for $Li_{3.75}Si$) and D is the Li diffusivity. The sharp phase boundary is represented by a nonlinear diffusion coefficient as function of Li contents.[60]

$$D = D_0 \left[\frac{1}{1-c} - 2\alpha c \right] \quad (6)$$

where D_0 is the chemical diffusion coefficient and α is a constant to determine the thickness of phase boundary. The parameters are assigned as $\alpha = 1.95$ and $D_0 = 2.04 \times 10^{-1}$ $(\mathrm{cm}^2/\mathrm{s})$. We set $D_0 = 10^{-10}(\mathrm{cm}^2/\mathrm{s})$ in the twin defect.

3.3.2. Material Preparation

Preparation of the KIT-6 including polymer template: Pluronic P123 was dissolved in HCl solution and *n*-butanol was added and stirred at 35 °C for 1 hour to form a clear solution. After that, tetraethyl orthosilicate (12.9 g) was gently dropped into the above solution and kept at 35 °C for 24 hours under stirring. The mixture was then held at 120 °C for 24 hours for

hydrothermal treatment. After washing in ethanol/HCl solution and drying, KIT-6 including the polymer template (KIT-6 w/ polymer template) was finally obtained. Also, the KIT-6 w/o polymer template was obtained through further calcination of the KIT-6 w/ polymer template at 600 °C for 2 hours under air atmosphere.[35]

Preparation of the 3D-Si@SiO_x/C: the KIT-6 w/ polymer template (0.5 g) and magnesium powder (0.5 g, Sigma Aldrich, >99 %) were put separately inside an argon-filled and sealed stainless steel reactor (with inner volume of 3 cm^3), and then heated in a tube furnace at 750 °C for 2 hours under argon atmosphere with the ramping rate kept at 10 °C min^{-1}. The obtained black powder was first put into 1 M HCl (100 ml) for 12 hours under stirring, then washed with a mixed distilled water/ethanol solution by centrifugation for 5 times, and finally filtered and dried in a vacuum oven at 100 °C for 12 hours. By this process, magnesium oxide and magnesium silicide were removed, and the 3D-Si@SiO_x/C was obtained.

3.3.3. Structural Characterizations

Morphological observations and structural investigations of the prepared samples were conducted using a field emission scanning electron microscopy (FESEM, JEOL JSM-7000F) and transmission electron microscopy (TEM, JEOL JEM-2100F) equipped with electron energy loss spectroscopy (EELS). The X-ray diffraction patterns were collected using an X-ray diffractometer (Empyrean-XRD, PANalytical) with Cu Kα radiation (λ = 1.54056 Å). Raman spectra were obtained using a micro-Raman spectrometer (Bruker, Senterra) with a 532 nm laser. Thermogravimetric analysis (TGA) for determining the carbon content of of prepared samples was conducted using a TGA instrument (TG/DTA 6300, Perkin-Elmer) under air atmosphere. Specific surface areas and average pore diameters of the prepared samples were measured using a surface area and pore size analyzer (Tristar II 3020, Micromeritics) and

calculated using the Brunauer-Emmett-Teller (BET) and Barrett-Joyner-Halenda (BJH) methods. To determine the surface and in-depth chemistry of the 3D-Si@SiO_x/C, X-ray photoelectron spectroscopy (XPS) measurements were performed using a surface analysis instrument (Sigma probe, Thermo Scientific) equipped with an argon ion beam sputtering system. In XPS measurements, XPS signals were continuously collected for a total of 21 times for 120 seconds with 6 second intervals of sputtering. The thermal stability of the 3D-Si@SiO_x/C and 3D-Si@SiO_x anodes were investigated using differential scanning calorimetry (DSC) measurements (STARe system, Mettler Toledo) at the state of full lithiation with the electrolyte.

3.3.4. Electrochemical Measurements

Working electrodes were prepared by coating a slurry containing 80 wt % active materials, 10 wt % polyacrylic acid (PAA) binder, and 10 wt % Super-P carbon conductor onto Cu foil 10 μm in thickness. After drying the electrodes in a convection oven at 80 °C for 6 hours and further drying in a vacuum oven at 120 °C for 12 hours, the electrodes were pressed to obtain the pre-set electrode density of 0.4 g cc^{-1}. The loading level of each electrode was fixed at 3.0 mg cm^{-2} for electrochemical measurements and 1.0 mg cm^{-2} for microscopy observations. CR2032 coin-type cells were assembled in an argon-filled glove box. In the coin cells, lithium metal foil and polyethylene membrane were used as the counter electrode and separator, respectively. 1 M $LiPF_6$ dissolved in mixed ethylene carbonate (EC) and ethyl methyl carbonate (EMC) with a volume ratio of 1:2, including 2 wt % of the additive fluoroethylene carbonate (FEC), was used as the electrolyte. The electrochemical tests were performed using a WBCS3000 (WonATech) workstation, and the cells were galvanostatically charged/discharged at various current densities within the voltage range of 0.01 V to 2.0 V *vs.*

Li/Li^+. The electrochemical performance of the 3D-Si@SiO_x/C anode was also measured at high temperature (60 °C) to examine its thermal stability.

3.3.5. Density Functional Theory (DFT) Calculations

Ab-initio calculations for c-Si and twin boundary were performed using the DFT method with the generalized gradient approximation developed by Perdew, Burke and Ernzerhof (GGA-PBE). The projector augmented wave (PAW) method with a plane-wave basis set is employed using the Vienna *Ab-initio* Simulation Package (VASP).[61,62] To describe the electron configurations for Si and Li, the valence subshells were set as $3s^2 3p^2$ for Si and $1s^2 2s^1$ for Li. With an energy cut-off of 500 eV, atomic structures, system energies, and mechanical stresses were calculated. A k-point mesh in the reciprocal-space was set to 5 × 5 × 5 for bulk Si and 5 × 5 × 1 for Si twin boundary using the Monkhorst−Pack scheme. Both the atomic positions and the supercell shape of c-Si were fully relaxed until the residual forces on each reached below 0.04 eV $Å^{-1}$. The lattice parameters of Si twin boundary were fixed at the initial values and then released in [111] direction only to ensure structural stability. To valid the Li diffusion behavior in the c-Si environment, Li migration pathways and activation energy barriers were calculated by the nudged elastic band (NEB) method.

3.4. Results and Discussion

3.4.1. Prediction of Volume Changes and the Consequent Structural Design

For finite element analysis, the 3D-Si@SiO_x/C structure with the Schoen's gyroid structure was modeled by level surfaces according to trigonometric functions as follows[34]:

$$\sin(x)\cos(y) + \sin(y)\cos(z) + \sin(z)\cos(x) = t \tag{7}$$

where t is the constant of the level surface to control the volume fraction of gyroid networks which can be defined by the ratio of volume enclosed by the level surface to the other side. For the Si particle, the diameter of the sphere was defined by 10 nm, and the position of sphere was placed where the space was maximized in the gyroid structure. The threshold of the level surface was set to be $t = \pm 0.02$, which satisfies the condition that pore diameter of gyorid structure is 8 nm (Figure 3.2).

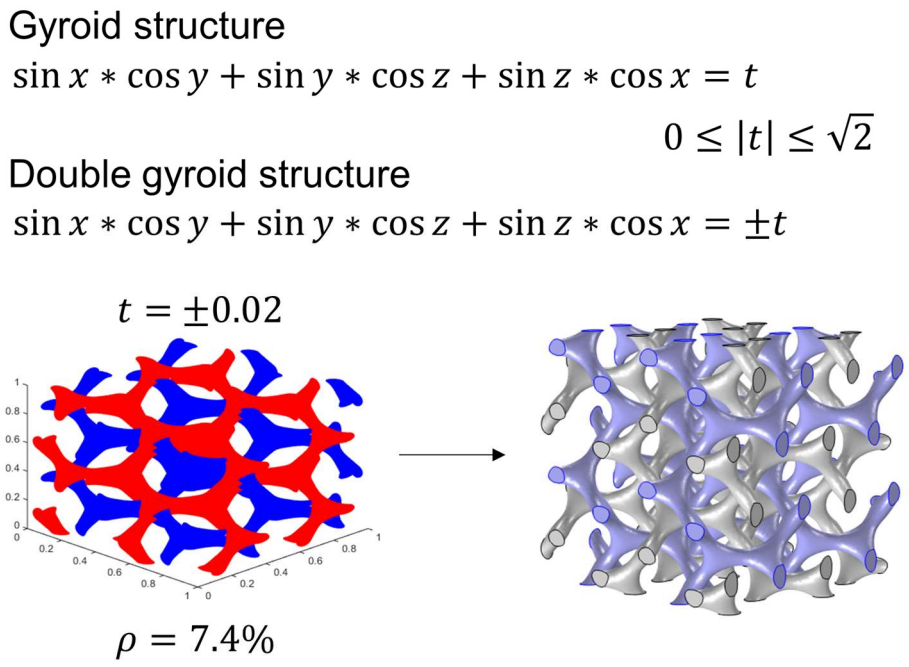

Figure 3.2. Gyroid and double-gyroid structure modeling for the continuum scale analysis.

In order to analyze the volume expansion of Si particles in the prepared 3D structure, we have compared the changes in volume expansion of the Si particle in different structures. Figure 3.3a shows the volume evolution of a free-standing Si particle up to 280 %. Figure 3.3b shows the finite element analysis results for an embedded Si particle in a SiO_2 nanowire. During full

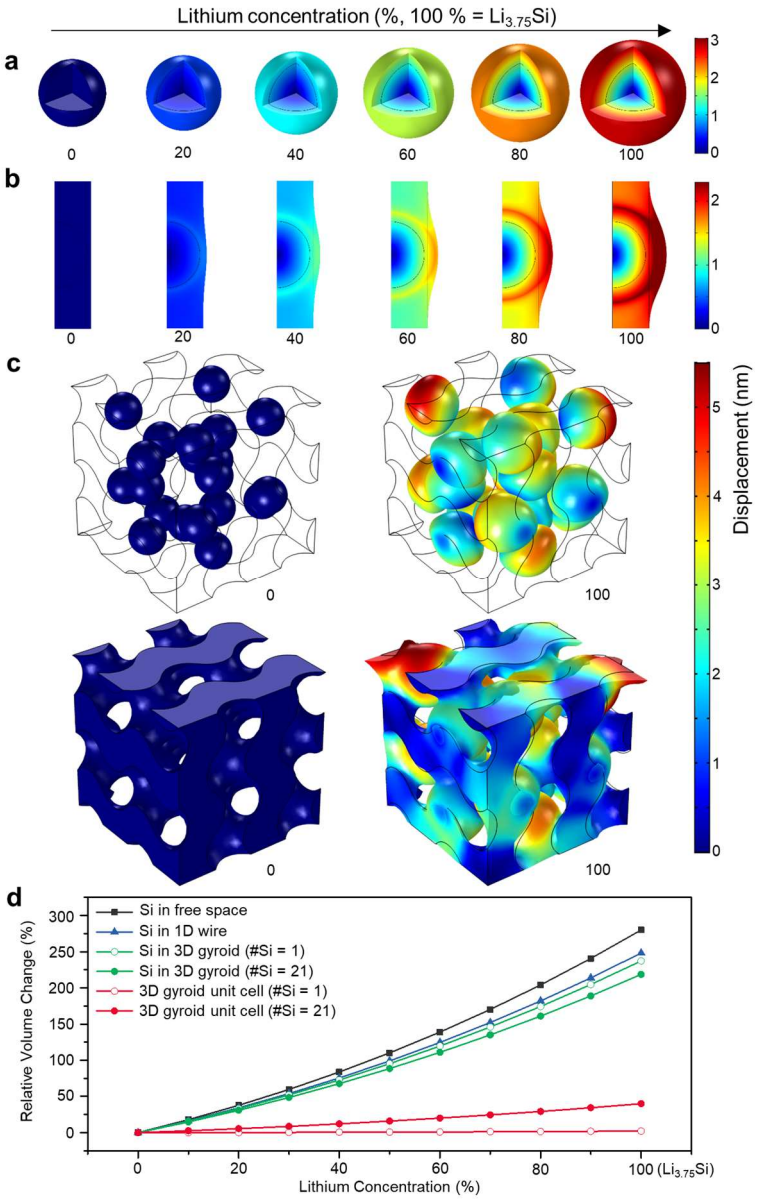

Figure 3.3. Continuum scale analysis for the simulation of particle and unit volume changes in silicon-based materials before and after full lithiation. (a) Si nanoparticle in free space. (b) Si nanoparticle embedded in 1D-SiO_2 structure. (c) Si nanoparticles embedded in a 3D network gyroid structure and the total unit of the gyroid 3D network Si@SiO_x. (d) Comparison of the relative volume changes of (a-d) during lithiation. #Si indicates the number of Si nanoparticles randomly located inside the gyroid structure from #Si = 1 to #Si = 21 (fully packed).

lithiation, the Si core experiences compressive stress because the SiO_2 matrix prevents expansion outward. Due to the rigid matrix, there was a decrease in the volume change of about 30 %. The thickness of nanowire matrix in the radial direction is thin, however, so the elastic supporting effects on Si were only applied in the direction of the height axis (z-axis). In the gyroid SiO_2 matrix, the Si particle shows lower volume expansion from 200 % to 230 % depending on the number of Si particles or the volume ratio of Si compared to the gyroid matrix, as shown in Figure 3.3c and 3.3d. The perfect gyroid lattice has cubic symmetry, and the embedded Si particle deforms under macroscopic hydrostatic pressure. Compared to the 1D nanowire, the effective suppression of lithium compositional expansion is attributed to the axisymmetric 3D network geometry. Furthermore, the unit cell of the gyroid structure provides free space to accommodate the volume changes of the embedded Si particles. The overall volume expansion ratio is greatly reduced by up to 50 %.

3.4.2. Synthesis of the 3D-Si@SiOx/C

Figure 3.4a shows a schematic illustration of the strategically designed 3D-Si@SiO_x/C synthetic process from double-gyroid KIT-6, including the polymer template. According to the results of the simulation of the volume changes, we adopted the KIT-6 that is interlaced with two gyroidal forms of silica and polymer as a precursor.[35] We expect that the KIT-6 will give a 3D network structure with appropriate contents of silicon, and it is also suitable for controlling the formation of the pores and Si materials. Moreover, the polymer template could be partly converted to carbonized form which will play a role in the enhancement of the electric conductivity and the mechanical strength of the material.[33] Owing to our series of the logical ways to seek an optimum material, the obtained material is expected to provide exceptional value in battery performance.

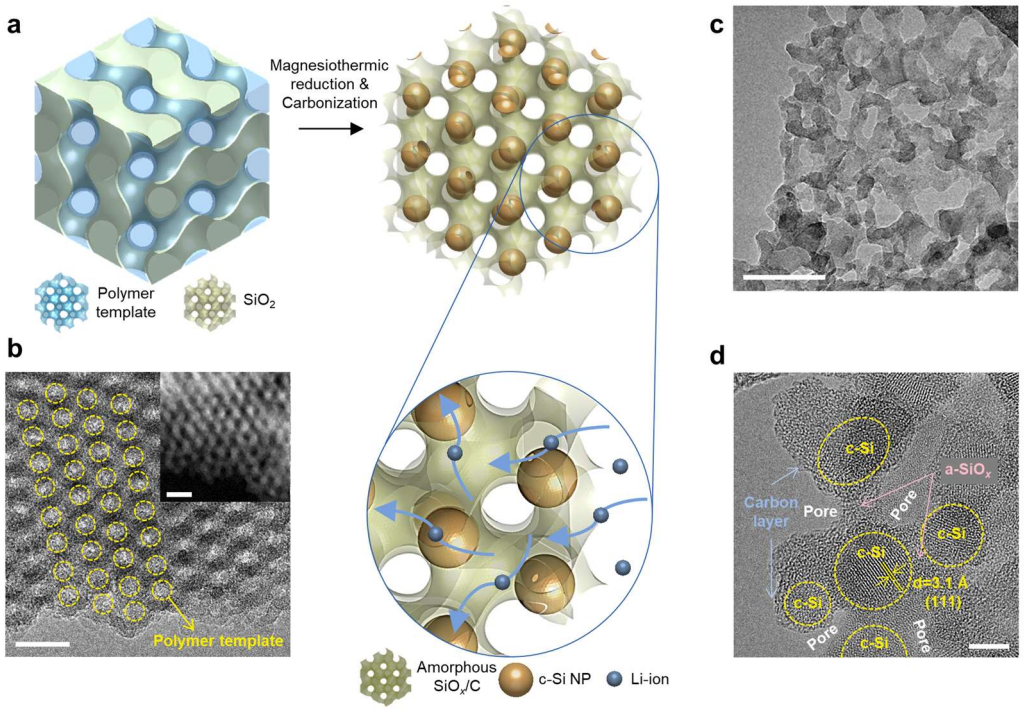

Figure 3.4. Synthesis of gyroid 3D network of Si@SiO_x/C. (a) Schematic illustration of the synthetic route for the 3D-Si@SiO_x/C via one-pot magnesiothermic reduction and carbonization of the KIT-6, including the polymer template. (b) Transmission electron microscope (TEM) image of highly ordered double-gyroid KIT-6 including polymer template with its high angle annular dark field – scanning TEM (HAADF-STEM) image in the inset. (c-d) TEM image of the 3D-Si@SiO_x/C (c) and its corresponding HRTEM image (d), showing that the c-Si particles are interconnected inside the SiO_x/C network frame. Scale bars, 20 nm for (b, including inset) and (c), 5 nm for (d).

To meet the requirements above, the KIT-6, including the polymer template mixed with magnesium (Mg) as reducing agent, is sealed in a stainless steel reactor and activated at 750 °C for 2 h in argon. Subsequently, the resulting product is washed with hydrochloric acid (HCl) to remove residual Mg compounds. Finally crystalline Si nanoparticles (c-Sis) embedded in a SiO_x/C network are obtained. That is to say, well-aligned gyroid SiO_x with carbon shell as well as embedded c-Sis cores is derived from highly ordered double-gyroid KIT-6, including the polymer template (Figure 3.4b). Although the morphology of the obtained material appeared slightly distorted compared to its precursor (Figure 3.4c), the gyroid 3D network structure was still maintained, and it also possessed mesopores where the polymer template was located.

Moreover, the polymer templates were transformed into carbon shells. The c-Si particles were interconnected inside the SiO_x/C network frame (Figure 3.4d). Detailed high resolution transmission electron microscope (HRTEM) image confirms the presence of c-Si with a lattice spacing of 0.31 nm, corresponding to the (111) planes of the face-centered cubic structure.[36,37,27]

3.4.3. Material Optimization and Characterizations of the 3D-Si@SiO_x/C

According to the predictions of the model, our desirable material should maintain its 3D network mesoporous structure with a large fraction of c-Si particles and SiO_x/C (or SiO_x) as a shell-like frame. To meet the above requirements, two kinds of synthesis were conducted. Firstly, heat-treatment temperatures were fixed at 675, 750, and 825 °C (with the samples denoted as 675, 750, and 825, respectively) for yielding an optimum ratio of c-Si particles while inducing partial reduction of silica. Secondly, calcined KIT-6 (which contains only silica) and uncalcined KIT-6 (which includes polymer template) were used as precursors (denoted as w/o and w/ polymer template, respectively) for determining the effects of the carbon which was acquired from the carbonization of the polymer template.[38] For comparative study, characterizations and electrochemical measurements of commercial Si nanopowder (denoted as Si-NP, 50 nm, Sigma Aldrich) were also conducted concurrently.

Figure 3.5a shows the X-ray diffraction (XRD) patterns of the reference Si-NP and the as-prepared six samples after HCl washing. Diffraction peaks of face-centered cubic silicon are clearly shown at 28.6, 47.6, 56.5, 69.7, and 77.0°, whereas c-Si and other magnesium compounds (MgO, Mg_2Si, and Mg_2SiO_4) co-existed in all six samples before HCl washing (Figure 3.6a).[39] The content of c-Si also increased with increasing reaction temperature. Interestingly, there was unwanted Mg_2SiO_4, which could not be removed in HCl solution in

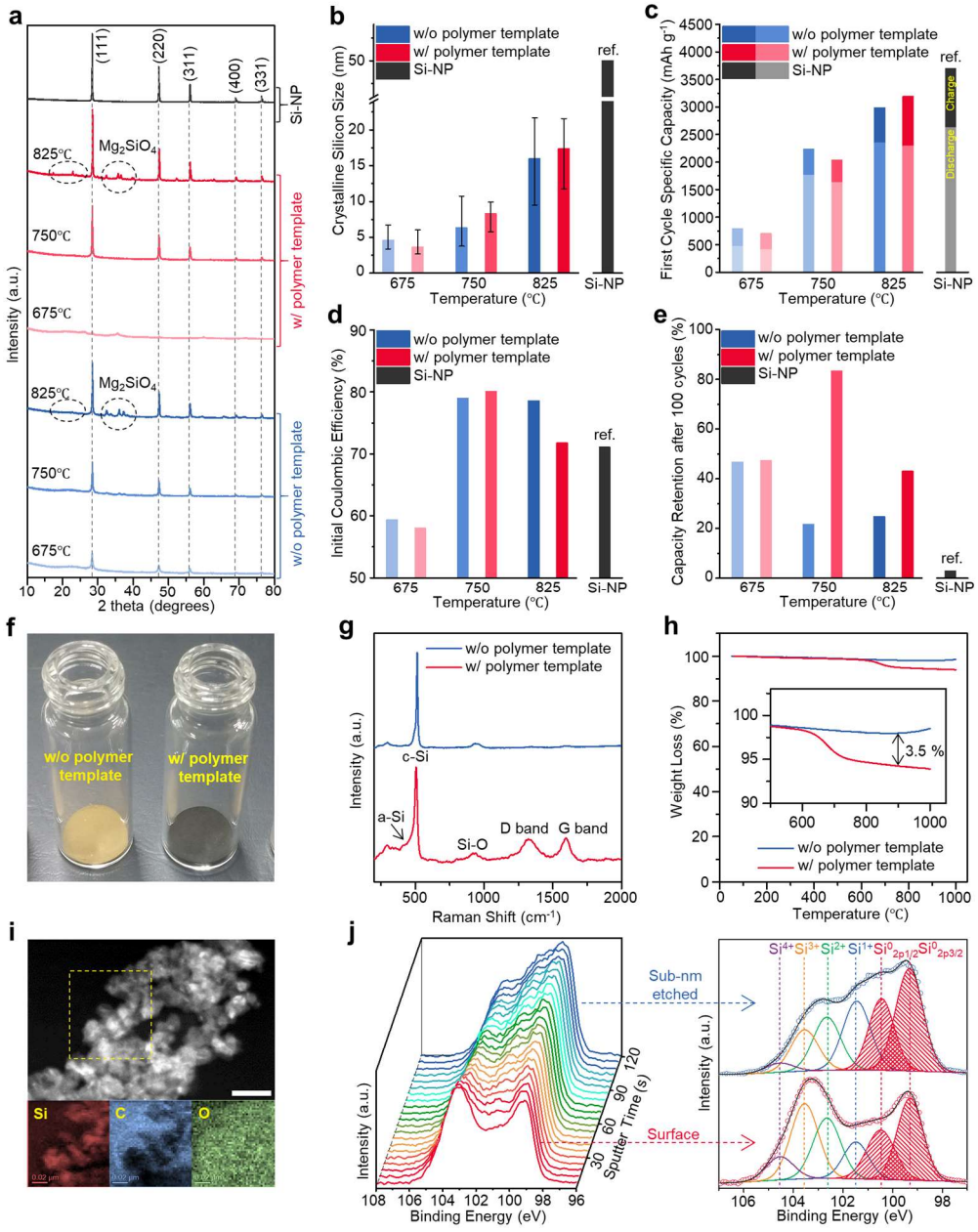

Figure 3.5. Structural and electrochemical characterizations of various types of products. (a) XRD patterns of 6 products and reference Si NP. (b-e) Physical and electrochemical properties of 6 products and reference Si NP: c-Si particle sizes (b), specific capacities (c), initial Coulombic efficiencies (d), and cyclability (e). (f-h) confirmation of the presence of carbon: powder images (f), Raman spectra (g) and thermogravimetric analysis (TGA) curves (h) of 750-w/o and w/ polymer template samples. (i) Electron energy loss spectroscopy (EELS) elemental mapping images of the 750-w/ polymer template. (j) XPS Si 2p spectra of the 750-w/ polymer template during Ar^+ sputtering for 120 seconds. Scale bar, 50 nm for (i).

the case of the 825 samples (825s).[40,41] Through detailed transmission electron microscopy (TEM) of the six products, predominant morphological differences were observed as a function

of the heat-treatment temperature. While 675s and 750s maintained their original mesoporous structures, the pores were collapsed and the particles were agglomerated to form larger lumps in the 825s (Figure 3.6b). On increasing the temperature from 675 °C to 825 °C, the average

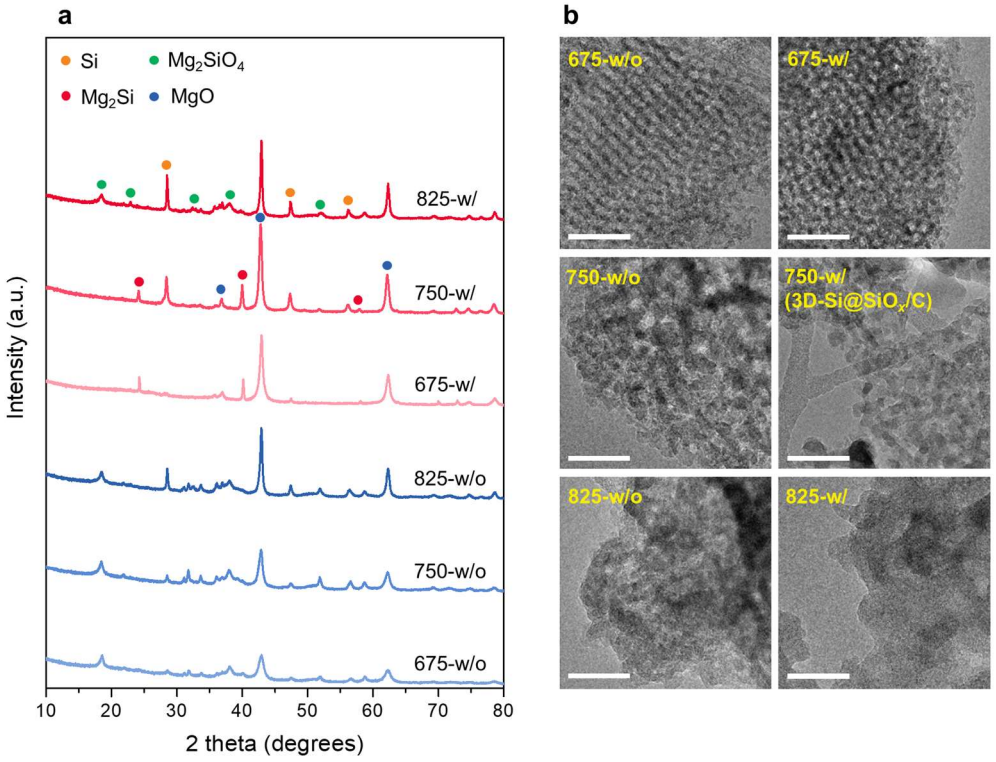

Figure 3.6. (a) XRD patterns collected before HCl washing, (b) TEM images of samples obtained under different synthesis conditions. (w/ / w/o: synthesized from calcined / uncalcined KIT-6, 675 / 750 / 825: synthesis temperatures) Scale bars, 50 nm for (b).

crystalline silicon size had a tendency to increase from ~4 nm in the 675s and ~8 nm in the 750s to ~17 nm in the 825s, respectively (Figure 3.5b). Due to these morphological differences and the content/size diversity of the c-Si particles, it could be expected that distinguishing electrochemical outputs would be shown. Figure 3.5c, 3.5d, and 3.5e show the electrochemical properties of the six products and Si-NP. The specific discharge capacities (at the first cycle) of the 825s are the highest, as expected (2294 and 2349 mAh g^{-1} for the w/o and w/ polymer template, respectively), whereas the 675s showed insignificant specific capacities due to insufficient reduction of silica. On the other hand, compared to the other products and also the

Si-NP reference, the 750s showed better initial coulombic efficiencies of up to 80.1 %. In particular, outstanding cycling performance was shown in the 750-w/ polymer template sample (over 80 % capacity retention after 100 cycles) in spite of the poor cyclability of all the other samples (under 50 %). (Detailed information, including numerical figures, is introduced in Figure 3.7)

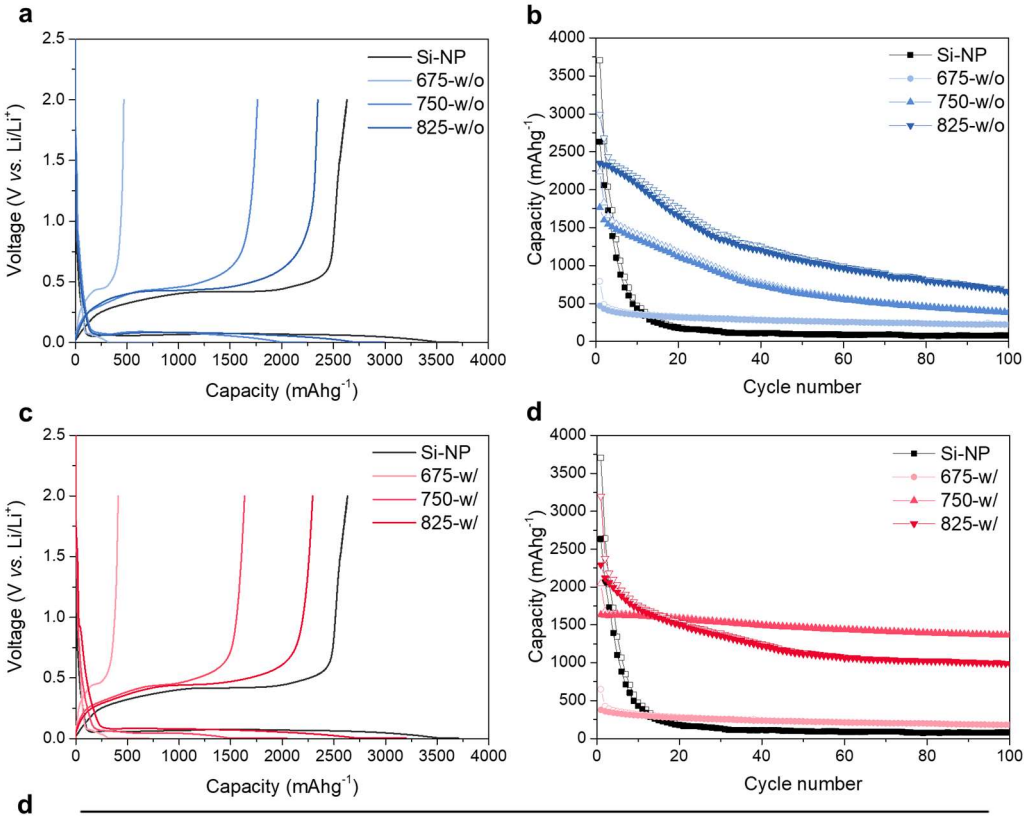

d

	Si-NP	675-w/o	750-w/o	825-w/o	675-w/	750-w/	825-w/
Charge Capacity (mAh/g)	3704	793	2235	2990	706	2043	3196
Discharge Capacity (mAh/g)	2631	471	1765	2349	410	1635	2294
ICE (%)	71.1	59.4	79.0	78.6	58.0	80.1	71.8
Capacity Retention (%)	3.0	46.8	21.7	24.8	47.3	83.3	43.1

Figure 3.7. Galvanostatic charge-discharge profiles (a, c) and cycling performances (b, d) of three w/o samples (a, b) and three w/ samples (c, d) with Si-NP anode. (e) Table of their electrochemical properties. (w/ / w/o: synthesized from calcined / uncalcined KIT-6, 675 / 750 / 825: synthesis temperatures, ICE: initial Coulombic efficiency).

In order to investigate the distinction between the w/o and w/ polymer template samples, we conducted additional analyses on 750s. At first, from the color of the samples (w/o polymer template: light brown, w/ polymer template: black, as shown in Figure 3.5f), the presence of carbon on the w/ polymer template can be detected. Figure 3.5g shows Raman spectra of samples w/o and w/ polymer templates. Each exhibited three distinct peaks at 506, 299, and 940 cm^{-1}, which indicated crystalline silicon with its long-range order.[42,43] In the w/ polymer template sample, there was a broad peak near 450 cm^{-1}, which indicated amorphous silicon containing amorphous oxides due to its SiO_x framework whereas this barely appeared on the w/o polymer template sample. In particular, 2 broad peaks at 1331 and 1595 cm^{-1} corresponded to the D band and G band of carbon.[44] By thermogravimetric analysis, the content of carbon in the w/ polymer template sample was estimated to be 3.5 wt % (Figure 3.5h). Also, it was confirmed that amorphous carbon covered all of the material, as determined from the electron energy loss spectroscopy (EELS) mapping images (Figure 3.5i). These results indicated that 3.5 wt % of amorphous carbon was derived from the polymer template, which played a significant role between the c-Si particles and the SiO_x framework, enhancing the electrochemical reversibility and cyclability.

To confirm in-depth the mechanical and chemical properties of 750-w/ polymer template (target product), further characterizations were performed by using the Brunauer-Emmett-Teller (BET) method, and XRD and X-ray photoelectron spectroscopy (XPS) measurements. The N_2 adsorption/desorption isotherm and pore size distribution results shown in Figure 3.8 indicate that 750-w/ polymer template still maintained the surface area of 161 $m^2\ g^{-1}$ and its average pore size of 8.7 nm after one-step reduction/carbonization and further HCl washing, even if the amorphous silica (KIT-6, broad peak located approximately at $2\theta = 22.5°$) underwent crystallization of silicon and partly transformed to amorphous silicon suboxides, as identified from XRD results (Figure 3.9). Moreover, we confirmed that the metallic silicon is

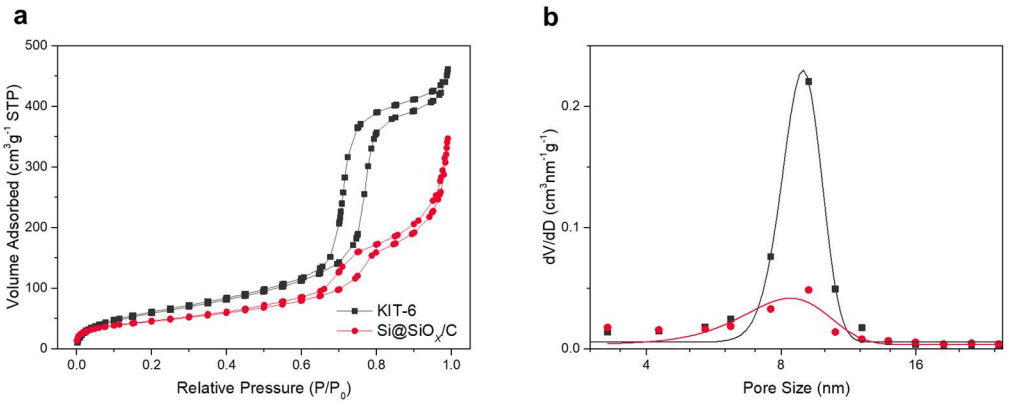

c

Samples	Surface Area (m^2/g)	Average Pore Diameter (nm)
KIT-6	225	8.9
3D-Si@SiO$_x$/C	161	8.7

Figure 2.8. N_2 adsorption/desorption isotherms and (b) pore size distributions of the KIT-6 including the polymer template and the 3D-Si@SiO$_x$/C. (c) Table of calculated surface area and average pore diameter, as determined by the Brunauer-Emmett-Teller (BET) and Barrett-Joyner-Halenda (BJH) methods, respectively.

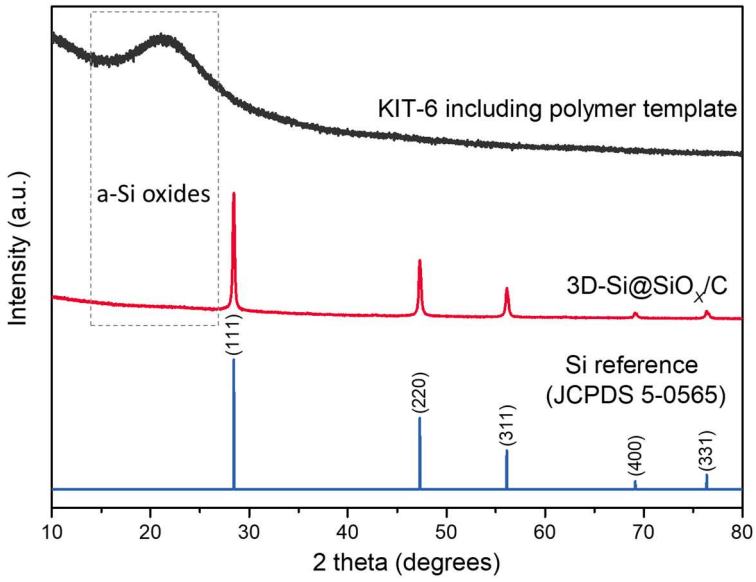

Figure 3.9. XRD patterns of the KIT-6 including the polymer template (precursor) and the 3D-Si@SiO$_x$/C (product).

embedded inside nonstoichiometric silicon oxides by changes in the XPS Si 2p signals, which were continuously measured 21 times for 120 seconds during Ar^+ sputtering (Figure 3.5j).

From the surface to a sub-nm depth of the material, metallic Si^0 peaks at about 99.2 and 100.1 eV showed a gradual increase, while other silicon oxides peaks, which can be divided into Si^{1+}, Si^{2+}, Si^{3+} and Si^{4+} ($SiO_{0.5}$, $SiO_{1.0}$, $SiO_{1.5}$, and SiO_2, respectively) in the range from 101.4 to 104.6 eV, showed an obvious decrease.[45] Also, a slight increase and decrease in the atomic concentrations of elemental Si and O, respectively, were confirmed by the calculations based on the XPS survey scans (Figure 3.10a and 3.10b). In addition, the C 1s and O 1s signals indicate that carbon exists in an independent amorphous carbon form, while the oxygen in the material is mainly from silicon oxides (Figure 3.10c and 3.10d).[46] Overall, it is demonstrated that 750-w/ polymer template has 10 nm crystalline silicon particles embedded in nonstoichiometric silicon oxides with an amorphous carbon layer forming a 3D network (Note that the name of the target product, which has been called 750-w/ polymer template so far will be changed again to 3D-Si@SiO_x/C hereafter.)

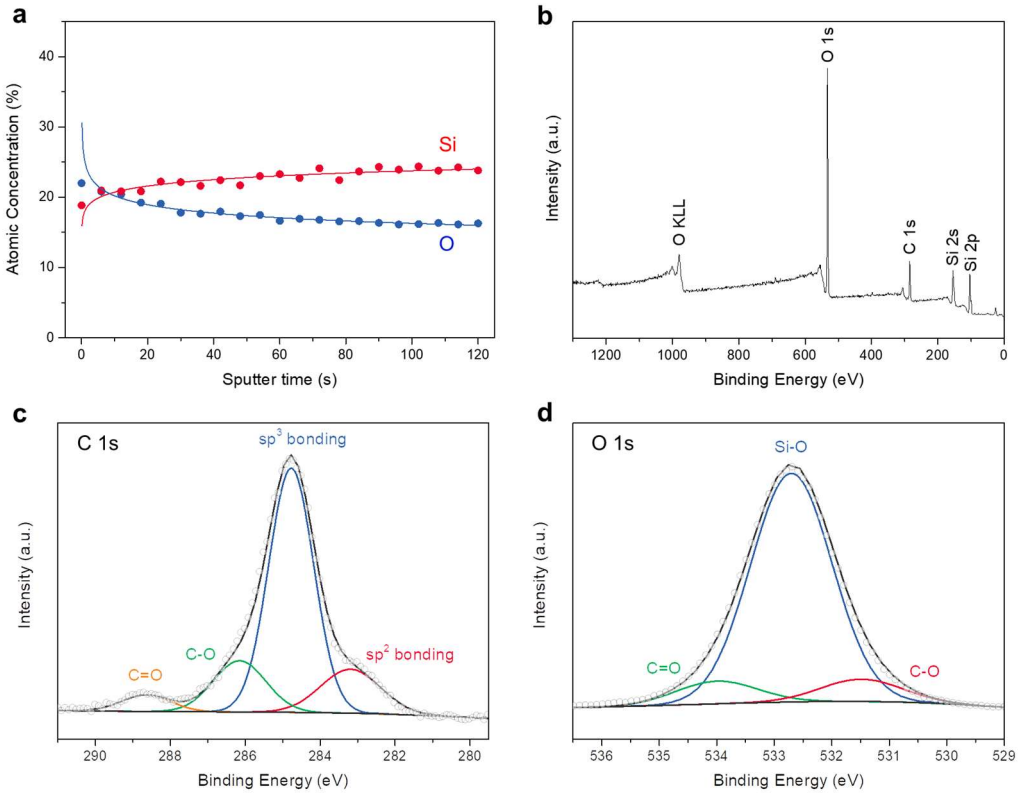

Figure 3.10. (a) XPS depth profiling, and (b) survey, (c) C 1s, and (d) O 1s spectra of the 3D-Si@SiO_x/C.

3.4.4. Effect of Defects in Silicon Nanoparticles

Meanwhile, the 3D-Si@SiO_x/C possesses abundant defects inside most of the Si nanoparticles. As shown in Figure 3.11a, defects such as twins and stacking faults, are extended from one side to the other side, passing through the bulk of Si nanoparticles. Moreover, each defect is randomly located on different positions. This might be because the 3D-Si@SiO_x/C was synthesized by the method of partial reduction of silica at relatively low temperature, which caused imperfect formation of the c-Si particles.[47] It is well known that defects in the crystal structure enhance ionic conductivity because they provides more free volume to accommodate the interstitial Li atoms than a perfect lattice.[48] In addition, according to a recent report, a defect-abundant Si anode shows better electrochemical performance in LIBs.[49] In order to investigate in depth how the defects affect the electrochemical properties of the 3D-Si@SiO_x/C anode, two different types of lithiation behavior depending on the existence of defects in the Si nanoparticles were also investigated. To obtain clear lithiated samples with no interference from a binder or a conductive agent, chemical lithiation by direct contact between the 3D-Si@SiO_x/C powder and Li-metal foil in the electrolyte for 6 hours was induced, as shown in Figure 3.11b. In the TEM observation shown in Figure 3.11c, the Si nanoparticle without defects exhibited a typical behavior in which amorphous lithium silicide (a-Li_xSi) enclosed c-Si (lattice spacing of 3.1 Å corresponding to the (111) planes) from the surface to deep inside of the bulk. On the other hand, interestingly, the Si nanoparticle which had a twin boundary formed crystalline lithium silicide (c-$Li_{15}Si_4$, lattice spacing of 6.1 Å, corresponding to the (111) planes) around the twin boundary. Morover, the c-$Li_{15}Si_4$ began to form even from inside of the bulk, not from the surface. This contrasting result clearly indicates that defects provide not only enhanced Li-ion diffusivity, which facilitates easy Li-ion transport to the bulk, but also a stable configuration in fully lithiated form without significantly affecting the mechanical strength in the case of the first cycle lithiation. Consequently, this result reflects the reason why

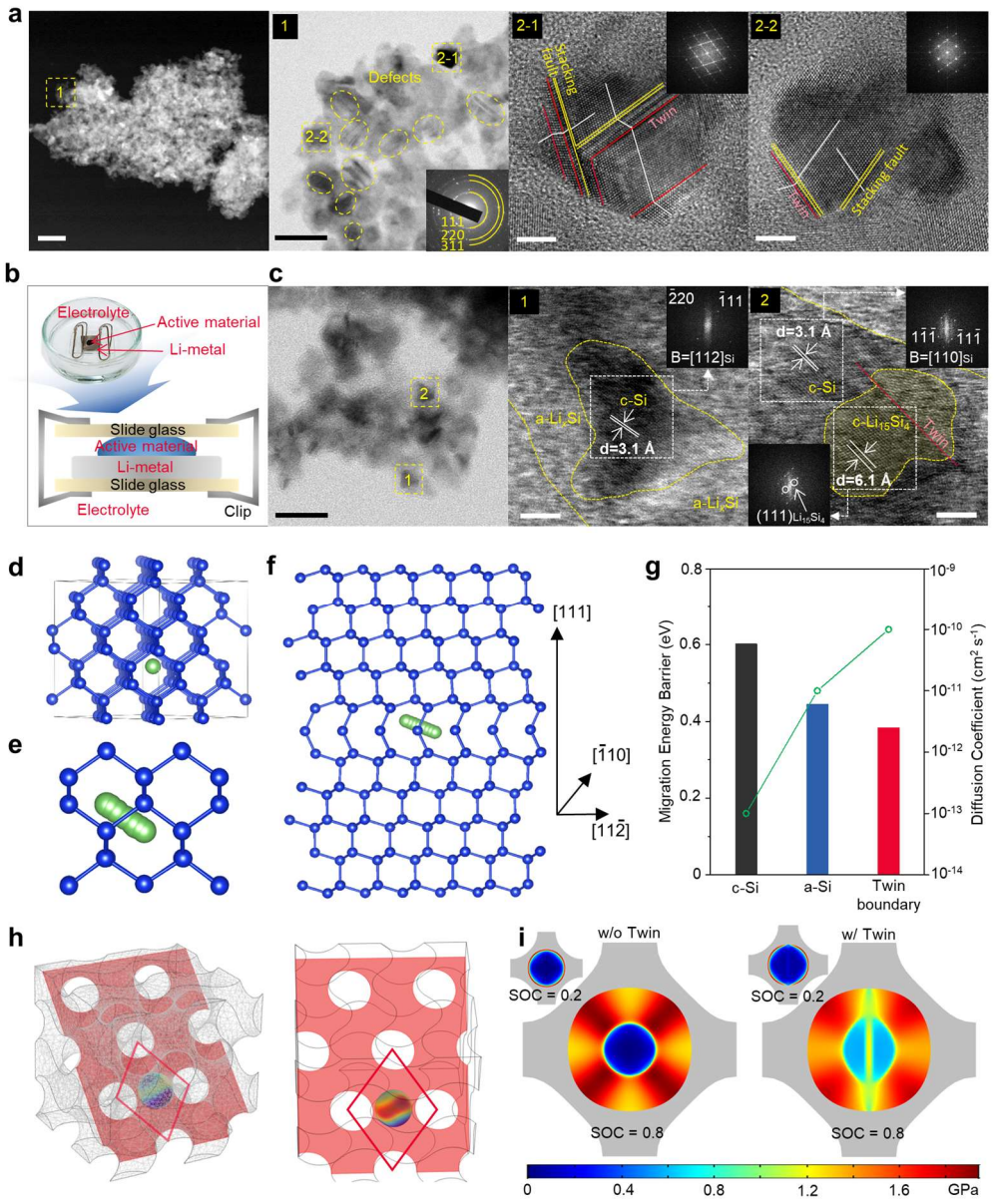

Figure 3.11. Effect of defects in Si NPs. (a) TEM observations of abundant defects in Si NPs of the 3D-Si@SiO_x/C, with SAED patterns in the insets. (b) Photograph with description of the method for inducing chemical lithiation on the 3D-Si@SiO_x/C. (c) TEM observations of different types of lithiation behavior, depending on the existence of defects in the Si NPs. Scale bars, 100 nm, 50 nm, 5 nm, 5 nm for (a), 50 nm, 5 nm, 5 nm for (b). (d) Li interstitial atom in tetrahedral pore of Si supercell. (e) Li atom transition to the neighbouring tetrahedral sites. (f) Atomistic configuration of twin boundary and representative Li migration. (g) Migration energy barriers calculated by the climbing-image nudged elastic band (NEB) method and corresponding diffusion coefficient in c-Si, amorphous (a)-Si, and through the twin boundary. (h) Geometry of 3D gyroid structure with Si nanoparticle and 2D projected representative volume element for the Si@SiO_x/C network structure. (i) Stress evolution of Si particle in SiO_x matrix during lithiation without and with a twin defect. (SOC: state of charge)

the 3D-Si@SiO_x/C exhibits outstanding initial coulombic efficiency with no drastic capacity

degradation in the first several cycles, in contrast with conventional Si-based anode.[50,27] (Detailed outcomes regarding the electrochemical performance of the 3D-Si@SiO_x/C will be discussed next.)

To demonstrate Li kinetics in defects of c-Si structure, we conducted a density functional theory (DFT) simulation of Li migration in both defect-free c-Si and a particle with a twin grain boundary. We first examined Li migration in a c-Si structure composed of 64 Si atoms (2 × 2 × 2 supercell). An interstitial Li atom was positioned at a tetrahedral (Td) site (Figure 3.11d). The diffusion pathways and activation energy barriers were carried out using the nudged elastic band (NEB) method. As shown in Figure 3.11e, the Li migration is allowed along the pathway from one Td to another Td site through a hexagonal (Hex) ring where the migration energy barrier was calculated to be 0.602 eV in the [111] direction.[51] As shown in Figure 3.11f, the twin defect was generated using a supercell oriented along the usual axis for defect modeling, $\hat{x} = [11\bar{2}], \hat{y} = [\bar{1}10], \hat{z} = [111]$. The mirror plane is normal to $\hat{y}$ and placed in the middle of the surface. To reduce effects from the periodic boundary condition, we introduced void space more than 3.7 Å in thickness into the supercell in the z-direction. The stable Li interstitial sites were determined by the Delaunay triangulation method to find the large void sites. The Li interstitial diffuses along the spacious octagon ring, where the corresponding migration barrier is 0.384 eV. The Li interstitial is easier to diffuse along the twin boundary and harder to diffuse out along the Td→Hex→Td pathway in the c-Si lattice. Furthermore, the energy barrier of Li hopping in the twin boundary is lower than that in the amorphous structures, and the diffusion coefficient is also higher (Figure 3.11g).[52] This indicates that the twin boundary provides enhanced Li-ion diffusivity. Figure 3.12 shows representative results for the Li concentration distribution in the case of Si nanoparticle with and without a twin defect. Sharp phase evolution is observed during first lithiation in c-Si.[53] The enhanced diffusivity in the twin defect changes the Li distribution for c-Si. The radial Li concentration shows that both center and surface

regions are quickly lithiated in the case with the twin defect (Figure 3.12c), while the Li barely exists in the central region of the particle without the twin defect (Figure 3.12d).

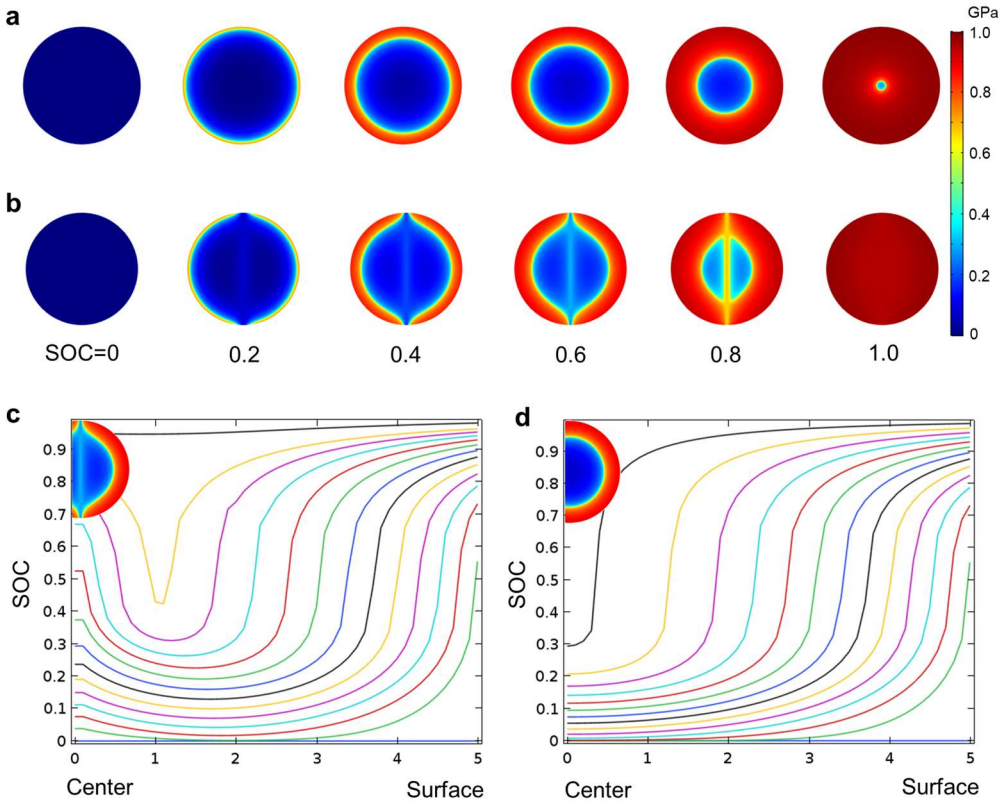

Figure 3.12. Continuum scale analysis for the lithiation evolution of a crystalline Si particle. Li contour plots during Li evolution (a) without and (b) with a twin defect. Normalized radial Li concentration distribution during lithiation (c) with and (d) without a twin defect. (SOC: state of charge)

To explain the mechanical stability in detail, we present the stress variation in a representative volume element of the 3D gyroid structure, and a 2D projected gyroid structure with a Si particle is used for reducing the computational cost (Figure 3.11h). In the initial lithiation, the newly generated Li-Si interphase expands more toward the surface direction rather than the core direction. The Si core experiences hydrostatic pressure (compressive stress) because the SiO_x matrix prevents outward expansion. Although the interconnected network frame of the SiO_x matrix well supports the Si nanoparticle, the relatively thin matrix in the void generates large von Mises stress, which results in mechanical failure. On the other hand, with the twin

defect, the enhanced diffusion of Li makes the Li concentration distribution more even. The asymmetric von Mises stress is also generated, but the magnitude of values for the von Mises stress is reduced (Figure 3.11i). We can argue that more evenly distributed lithiation ensures mechanical stability and that the defects in the Si nanoparticles of the 3D-Si@SiO_x/C significantly affect the mechanical strength at the first cycle.

3.4.5. Electrochemical Performances and ex Situ TEM and SEM Observations

The electrochemical properties of the 3D-Si@SiO_x/C and the commercially available Si-NP as a reference were estimated to validate the feasibility of the 3D-Si@SiO_x/C as an anode material. Figure 3.13a shows galvanostatic charge-discharge curves of the first cycle at a current density of 200 mA g^{-1} in the voltage window of 0.01 V to 2.00 V (*vs.* Li/Li^+). The 3D-Si@SiO_x/C anode presented the same reduction/oxidation behavior as the Si-NP anode at a typical redox potential of 0.4 V during discharge,[5] even though it was a mixed composite of c-Si, SiO_x, and C. This is because c-Si plays a major role in the specific capacity of the anode. It should be noted that the 3D-Si@SiO_x/C anode showed specific charge and discharge capacities of 2043 and 1635 mAh g^{-1}, respectively. In contrast, the Si-NP anode exhibited almost doubled specific capacities (3704 and 2631 mAh g^{-1}, respectively). Nevertheless, in terms of an anode performance, the 3D-Si@SiO_x/C anode showed not only a large enough reversible capacity of 1635 mAg g^{-1}, but also an outstanding value for the initial coulombic efficiency (80.1 %). In addition, 83.3 % discharge capacity retention was observed even after 100 cycles, maintaining over 99.8 % coulombic efficiency (Figure 3.13b and inset). Thus, it seems that the 3D-Si@SiO_x/C anode would give a high energy density even at a reasonable electrode loading mass of 3.0 mg cm^{-1}. Moreover, the rate-capability was also characterized, as shown in Figure 3.13c and 3.13d. Compared to the discharge capacity of the 3D-Si@SiO_x/C anode at the current

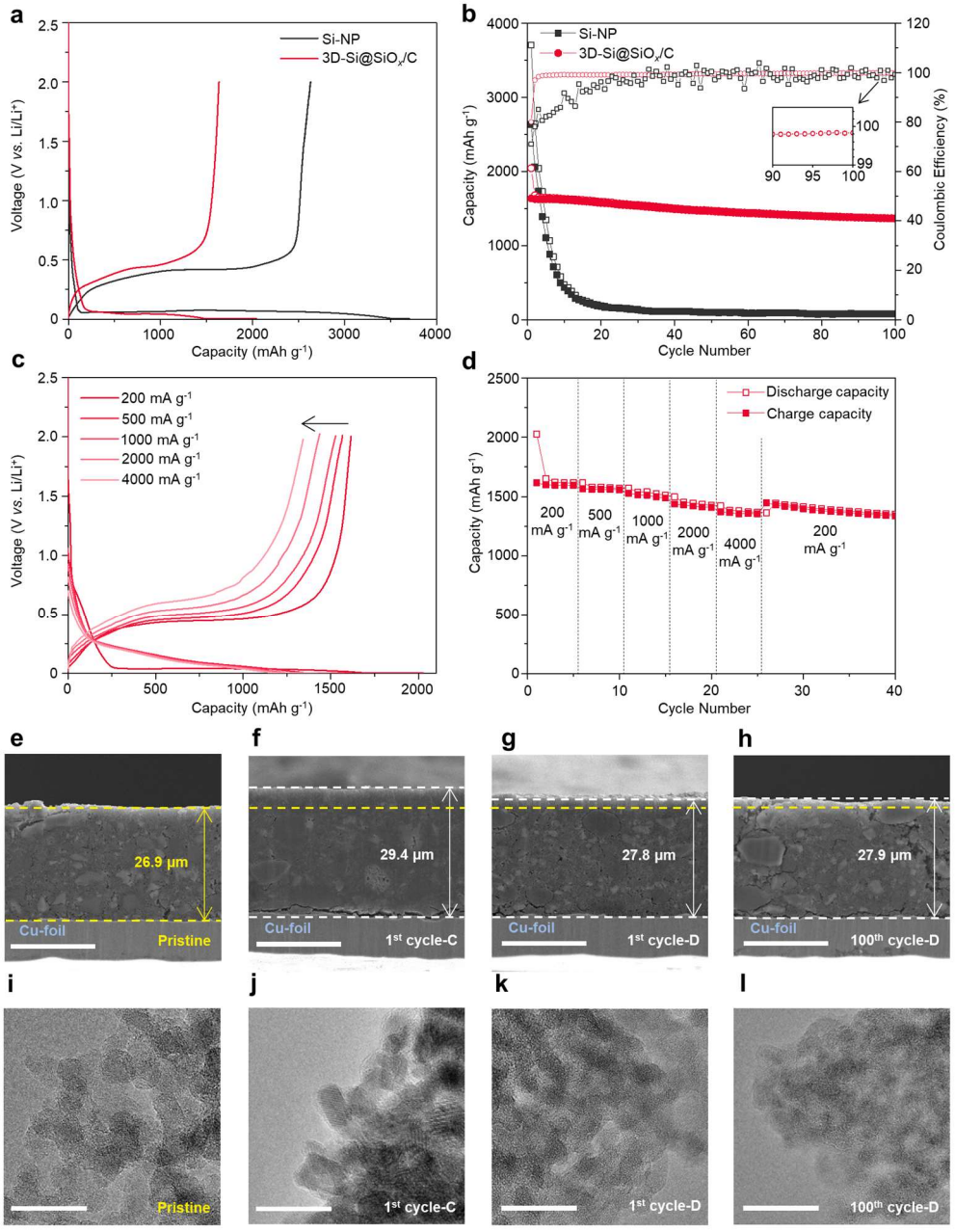

Figure 3.13. Electrochemical performances and ex situ TEM and SEM observations. (a) Galvanostatic charge-discharge profiles of the 3D-Si@SiO_x/C and Si NP anodes. (b) Cycling performances (closed symbol: discharge capacity, open symbol: charge capacity) and Coulombic efficiencies of the 3D-Si@SiO_x/C and Si NP anodes at a current density of 200 mA g^{-1}. (c-d) Galvanostatic charge-discharge profiles (c) and cycling performance (d) of the 3D-Si@SiO_x/C at different output current densities of 200, 500, 1000, 2000, and 4000 mA g^{-1} (0.12, 0.31, 0.61, 1.22, and 2.45C, respectively, 1C = 1635 mA g^{-1}). (e-h) Cross-sectional SEM images of the 3D-Si@SiO_x/C electrodes at different cycles: pristine (e), first cycle charged (1st cycle-C) (f), first cycle discharged (1st cycle-D) (g), and hundredth cycle discharged (100th cycle-D) (h). (i-l) HRTEM observations of the Si-NP particles at different reaction states; pristine (i), 1st cycle-C (j), 1st cycle-D (k), and 100th cycle-D (l). Scale bars, 20 μm for (e-h), 20 nm for (i-l).

density of 200 mA g^{-1}, 85 % of the discharge capacity (1342 mAh g^{-1}) was still retained when

a current density of 4000 mA g^{-1} was applied. Also, the capacity returned back stably to its original specific capacity at the current density of 200 mA g^{-1}, even after undergoing a high current density of 4000 mA g^{-1}.

In order to understand the structural stability of both the electrode and the particles inside of the 3D-Si@SiO_x/C anode during cycling, detailed microscopic observations were carried out by using ex situ field emission SEM (FESEM) and TEM observations. Figure 3.13e, 3.13f, 3.13g, and 3.13h show cross-sectional FESEM images of the 3D-Si@SiO_x/C electrode at different states of charge. The thickness of the pristine electrode was 26.9 μm after compression of the electrode. After full lithiation, the electrode volume expanded by only 9.3 % from its initial status. In principle, this result is well consistent with our computational simulation results on the volume expansion of the gyroid 3D network with Si@SiO_2. Moreover, the electrode still maintained its volume, even at 100 cycles, after undergoing a slight shrinkage due to the delithiation. It is expected that the stable cyclability was caused by its mechanical stability. Other *ex-situ* observations for determining the structural stability of the 3D-Si@SiO_x particles during cycling were conducted, as shown in Figures 3.13i, 3.13j, 3.13k, and 3.13l. In these TEM observations, we confirmed that the expanded Li_xSi particles occupied the spaces where the voids originally were, and the Si particles returned back to their original positions while maintaining the mesoporous structure due to the robust SiO_x/C framework. Even after 100 cycles, the structure mainly remained the same, although partially collapsed and agglomerated particles can be observed (Figure 3.14). Therefore, in sum, the 3D-Si@SiO_x/C surely has the potential for high electrochemical performance, even after long-term cycling, due to its outstanding high capacity in coordination with its structural stability.

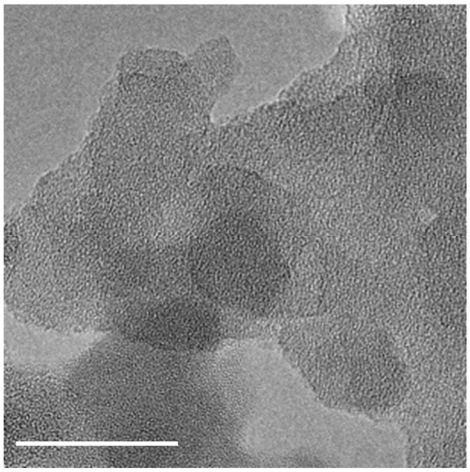

Figure 3.14. HRTEM observation of partially collapsed 3D-Si@SiO_x/C particles after 100 cycles. Scale bar, 20 nm.

3.4.6. Thermostability Properties

In order to confirm the thermal stability of the 3D-Si@SiO_x/C anode, we first examined its high-temperature cyclability, which gives a direct reflection of its thermostability characteristics. Figure 3.15a shows first cycle charge-discharge profiles at different temperatures: room temperature (23 °C, RT) and 60 °C. It is generally understood that slightly increased reversible capacity (1746 mAh g^{-1}) and relatively low over potential were shown at 60 °C compared to at RT (1635 mAh g^{-1}) due to the increase in thermodynamic activity and ionic mobility at high temperature.[54] Above all, the 3D-Si@SiO_x/C anode showed good high temperature cyclability with capacity retention of 79.4 % over 70 cycles as well as maintaining high coulombic efficiency of 99.6 % (Figure 3.15b). To investigate the thermal stability with temperature, which is closely related to the thermal reliability of full-cell configurations, DSC measurements of fully lithiated anodes were performed. Figure 3.15c shows the DSC curves of the 3D-Si@SiO_x, 3D-Si@SiO_x/C, and Si-NP electrodes in the state of full lithiation together with electrolyte inside each cells. The Si-NP electrode underwent severe exothermic reactions at the temperatures of 270 and 310 °C due to structural collapse followed by continuous

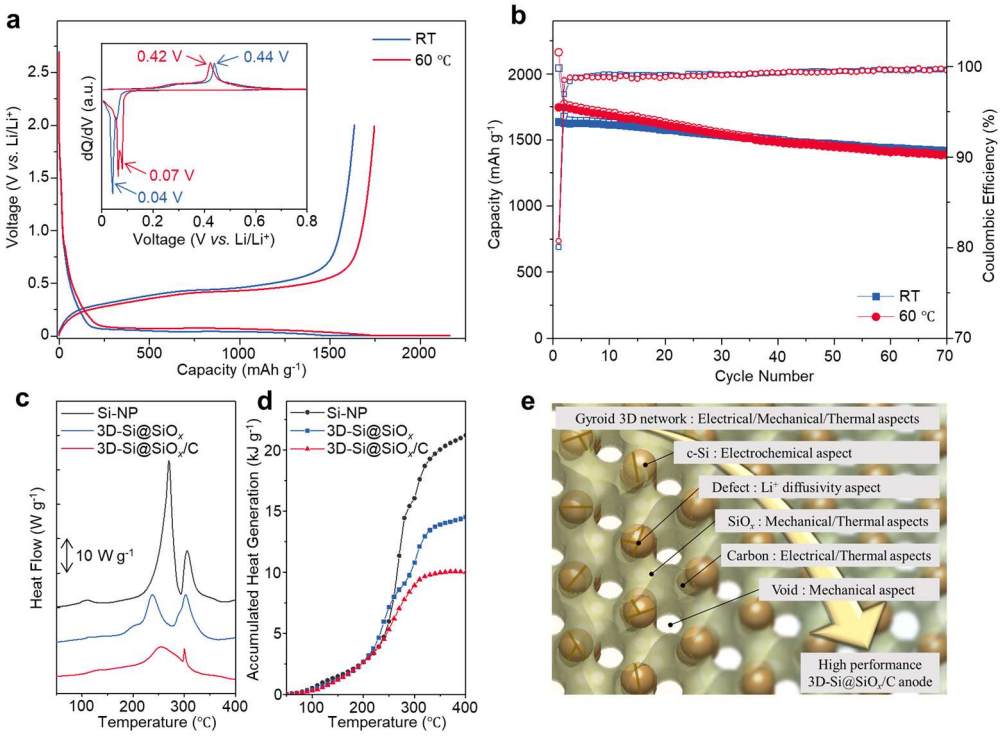

Figure 3.15. Thermostability properties. (a) First cycle charge-discharge profiles, corresponding differential capacity plots (inset).(b) Cycling performances of 3D-Si@SiO_x/C at RT and 60 °C. (c-d) DSC curves (c) and corresponding cumulative heat generation profiles (d) of the 3D-Si@SiO_x/C, Si@SiO_x, and Si NP electrodes after full lithiation. (e) Various aspects of the individual contents of the 3D-Si@SiO_x/C.

decomposition of lithium silicide phases and the electrolyte.[55] On the other hands, the 3D-Si@SiO_x/C showed gentle exothermic peaks due to its enhanced thermal stability by incorporation of carbon, while the 3D-Si@SiO_x also showed relatively sharp peaks in the temperature range from 200 °C to 350 °C. In addition, the accumulated heat generation calculated from the DSC curves was also investigated, as shown in figure 3.15d. From room temperature up to 400 °C, the exothermic enthalpy, that is to say, the overall heat generation of the 3D-Si@SiO_x/C, the 3D-Si@SiO_x, and Si-NP electrodes is 10.0, 14.5, and 21.2 kJ g^{-1}, respectively. This result indicates that the 3D-Si@SiO_x/C exhibits improved thermal stability compared to the Si-NP and even the 3D-Si@SiO_x.[56] We strongly argue that thermal reliability is a necessary condition that anode materials must satisfy and that the importance of thermal

stability cannot be emphasized enough. Consequently, our material can be effective for preventing a sudden explosion of the battery under harsh conditions such as exposure to high temperature or mechanical compression/ distortion/ stabbing of the battery.

Overall, In order to obtain a high performance Si-based material, each component in the anode material should systematically play its role in various aspects, as shown in Figure 3.15e. In detail, (I) the gyroid 3D network nanoarchitecture in electrical, mechanical, and thermal aspects, (II) the c-Si in the electrochemical aspect, (III) the defects in c-Si in the Li^+ diffusivity aspect, (IV) the SiO_x in mechanical and thermal aspects, (V) the carbon in electrical and thermal aspects, and finally (VI) the void space in the mechanical aspect; all should be combined for the final goal of the Si-anode material.

3.5. Conclusion

In this study, in order to optimize the material to obtain better electrochemical performance, both computational prediction of the structure and synthetic optimization of the products were considered. With the synergetic interaction between the two separate methods, we identified that the Si-based anode should have a robust and well-aligned 3D network structure with nanopores to prevent the volume expansion which affects electrode-level dilatation, as well as having suitable Si, SiO_x, and C contents in order to perform their own roles. Moreover, by controlling the synthetic conditions, the optimum materials could be obtained, and the computational predictions could also be proved.

From the point of view of Si-based anode materials, this 3D-Si@SiO_x/C exhibits three main features. (I) The 3D network and mesoporous structure prevents volume expansion and promotes ion/electron transport when it reacts with Li.[57,58] Consequently, it provides excellent electrochemical performance. (II) Incorporation of carbon enhances the thermal stability of the electrode, which was determined from the reduced heat flow and moderate exothermic reaction in the DSC results, and hence, the 3D-Si@SiO_x/C showed stable high temperature cyclability. (III) One-step magnesiothermic reduction and carbonization synthesis without the use of hydrofluoric acid indicates the feasibility of mass production due to its cost-effectiveness and safety. We believe that this innovative 3D-Si@SiO_x/C nanoarchitecture will lead to the development of anode materials for the next generation of LIBs.

3.6. References

[1] C.-M. Park, J.-H. Kim, H. Kim, H.-J. Sohn, *Chem. Soc. Rev.* **2010**, 39, 3115.

[2] M. Armand, J. M. Tarascon, *Nature* **2008**, 451, 652.

[3] C. K. Chan, H. Peng, G. Liu, K. McIlwrath, X. F. Zhang, R. A. Huggins, Y. Cui, *Nat. Nanotechnol.* **2007**, 3, 31.

[4] S. Chae, M. Ko, K. Kim, K. Ahn, J. Cho, *Joule* **2017**, 1, 47.

[5] X. Zuo, J. Zhu, P. Müller-Buschbaum, Y.-J. Cheng, *Nano Energy* **2017**, 31, 113.

[6] U. Kasavajjula, C. Wang, A. J. Appleby, *J. Power Sources* **2007**, 163, 1003.

[7] W.-J. Zhang, *J. Power Sources* **2011**, 196, 13.

[8] N. Liu, H. Wu, M. T. McDowell, Y. Yao, C. Wang, Y. Cui, *Nano Lett.* **2012**, 12, 3315.

[9] L. Y. Yang, H. Z. Li, J. Liu, Z. Q. Sun, S. S. Tang, M. Lei, *Sci. Rep.* **2015**, 5, 10908.

[10] G. Liang, X. Qin, J. Zou, L. Luo, Y. Wang, M. Wu, H. Zhu, G. Chen, F. Kang, B. Li, *Carbon* **2018**, 127, 424.

[11] A. M. Chockla, K. C. Klavetter, C. B. Mullins, B. A. Korgel, *Chem. Mater.* **2012**, 24, 3738.

[12] A. Gohier, B. Laïk, J.-P. Pereira-Ramos, C. S. Cojocaru, P. Tran-Van, *J. Power Sources* **2012**, 203, 135.

[13] Z. Wen, G. Lu, S. Mao, H. Kim, S. Cui, K. Yu, X. Huang, P. T. Hurley, O. Mao, J. Chen, *Electrochem. Commun.* **2013**, 29, 67.

[14] X. Wang, L. Sun, X. Hu, R. A. Susantyoko, Q. Zhang, *J. Power Sources* **2015**, 280, 393.

[15] X. Yu, F. Xue, H. Huang, C. Liu, J. Yu, Y. Sun, X. Dong, G. Cao, Y. Jung, *Nanoscale* **2014**, 6, 6860.

[16] Y. Liu, B. Chen, F. Cao, H. L. W. Chan, X. Zhao, J. Yuan, *J. Mater. Chem.* **2011**, 21, 17083.

[17] Z. Jiang, C. Li, S. Hao, K. Zhu, P. Zhang, *Electrochim. Acta* **2014**, 115, 393.

[18] Q. Xiao, M. Gu, H. Yang, B. Li, C. Zhang, Y. Liu, F. Liu, F. Dai, L. Yang, Z. Liu, X. Xiao, G. Liu, P. Zhao, S. Zhang, C. Wang, Y. Lu, M. Cai, *Nat. Commun.* **2015**, 6, 8844.

[19] J.-I. Lee, K. T. Lee, J. Cho, J. Kim, N.-S. Choi, S. Park, *Angew. Chem. Int. Ed.* **2012**, 51, 2767.

[20] Z. Xu, J. Yang, T. Zhang, Y. Nuli, J. Wang, S. -I. Hirano, *Joule* **2018**, 2, 950.

[21] S. Choi, T.-W. Kwon, A. Coskun, J. W. Choi, *Science* **2017**, 357, 279.

[22] R. Zhang, Y. Du, D. Li, D. Shen, J. Yang, Z. Guo, H. K. Liu, A. A. Elzatahry, D. Zhao, *Adv. Mater.* **2014**, 26, 6749.

[23] A. Magasinski, P. Dixon, B. Hertzberg, A. Kvit, J. Ayala, G. Yushin, *Nat. Mater.* **2010**, 9, 353.

[24] M. Ko, S. Chae, S. Jeong, P. Oh, J. Cho, *ACS Nano* **2014**, 8, 8591.

[25] J.-K. Yoo, J. Kim, Y. S. Jung, K. Kang, *Adv. Mater.* **2012**, 24, 5452.

[26] H. Wu, G. Chan, J. W. Choi, I. Ryu, Y. Yao, M. T. McDowell, S. W. Lee, A. Jackson, Y. Yang, L. Hu, Y. Cui, *Nat. Nanotechnol.* **2012**, 7, 310.

[27] E. Park, H. Yoo, J. Lee, M.-S. Park, Y.-J. Kim, H. Kim, *ACS Nano* **2015**, 9, 7690.

[28] R. Ma, Y. Liu, Y. Yang, M. Gao, H. Pan, *Appl. Phys. Lett.* **2014**, 105, 213901.

[29] H. Jung, Y.-U. Kim, M.-S. Sung, Y. Hwa, G. Jeong, G.-B. Kim, H.-J. Sohn, *J. Mater. Chem.* **2011**, 21, 11213.

[30] R. Dash, S. Pannala, *Sci. Rep.* **2016**, 6, 27449.

[31] M. Yoshio, H. Wang, K. Fukuda, T. Umeno, N. Dimov, Z. Ogumi, *J. Electrochem. Soc.* **2002**, 149, A1598.

[32] Z. Bao, M. R. Weatherspoon, S. Shian, Y. Cai, P. D. Graham, S. M. Allan, G. Ahmad, M. B. Dickerson, B. C. Church, Z. Kang, H. W. Abernathy Iii, C. J. Summers, M. Liu, K. H. Sandhage, *Nature* **2007**, 446, 172.

[33] K. P. Gierszal, T.-W. Kim, R. Ryoo, M. Jaroniec, *J. Phys. Chem. B* **2005**, 109, 23263.

[34] J. H. Moon, Y. Xu, Y. Dan, S. M. Yang, A. T. Johnson, S. Yang, *Adv. Mater.* **2007**, 19, 1510.

[35] Y. Doi, A. Takai, Y. Sakamoto, O. Terasaki, Y. Yamauchi, K. Kuroda, *Chem. Commun.* **2010**, 46, 6365.

[36] A. M. Morales, C. M. Lieber, *Science* **1998**, 279, 208.

[37] M.-S. Park, E. Park, J. Lee, G. Jeong, K. J. Kim, J. H. Kim, Y.-J. Kim, H. Kim, *ACS Appl. Mater. Interfaces* **2014**, 6, 9608.

[38] K. Ariga, A. Vinu, Y. Yamauchi, Q. Ji, J. P. Hill, *Bull. Chem. Soc. Jpn.* **2011**, 85, 1.

[39] P. Gao, H. Tang, A. Xing, Z. Bao, *Electrochim. Acta* **2017**, 228, 545.

[40] J. Entwistle, A. Rennie, S. Patwardhan, *J. Mater. Chem. A* **2018**, DOI: 10.1039/C8TA06370B.

[41] W. Chen, Z. Fan, A. Dhanabalan, C. Chen, C. Wang, *J. Electrochem. Soc.* **2011**, 158, A1055.

[42] E. Park, M.-S. Park, J. Lee, K. J. Kim, G. Jeong, J. H. Kim, Y.-J. Kim, H. Kim, *ChemSusChem* **2015**, 8, 688.

[43] A. Janotta, Y. Dikce, M. Schmidt, C. Eisele, M. Stutzmann, M. Luysberg, L. Houben, *J. Appl. Phys.* **2004**, 95, 4060.

[44] A. C. Ferrari, *Solid State Commun.* **2007**, 143, 47.

[45] C. Cao, I. I. Abate, E. Sivonxay, B. Shyam, C. Jia, B. Moritz, T. P. Devereaux, K. A. Persson, H.-G. Steinrück, M. F. Toney, *Joule* **2019**, 3, 762.

[46] S. T. Jackson, R. G. Nuzzo, *Appl. Surf. Sci.* **1995**, 90, 195.

[47] R. C. Newman, *Rep. Prog. Phys.* **1982**, 45, 1163.

[48] C.-Y. Wang, L-J. Yang, W. Zhao, Q.-Y. Meng, G.-X. Wu, B.-L. Wang, C.-L. Li, *J. Appl. Phys.* **2014**, 116, 213504.

[49] J. Wang, X. Meng, X. Fan, W. Zhang, H. Zhang, C. Wang, *ACS Nano* **2015**, 9, 6576.

[50] N. Liu, Z. Lu, J. Zhao, M. T. McDowell, H.-W. Lee, W. Zhao, Y. Cui, *Nat. Nanotechnol.* **2014**, 9, 187.

[51] H. Kim, K. E. Kweon, C.-Y. Chou, J. G. Ekerdt, G. S. Hwang, *J. Phys. Chem. C* **2010**, 114, 17942.

[52] J. Moon, B. Lee, M. Cho, K. Cho, *J. Power Sources* **2014**, 272, 1010.

[53] J. W. Wang, Y. He, F. Fan, X. H. Liu, S. Xia, Y. Liu, C. T. Harris, H. Li, J. Y. Huang, S. X. Mao, T. Zhu, *Nano Lett.* **2013**, 13, 709.

[54] M. Winter, R. J. Brodd, *Chem. Rev.* **2004**, 104, 4245.

[55] I. A. Profatilova, C. Stock, A. Schmitz, S. Passerini, M. Winter, *J. Power Sources* **2013**, 222, 140.

[56] G. Jeong, J.-G. Kim, M.-S. Park, M. Seo, S. M. Hwang, Y.-U. Kim, Y.-J. Kim, J. H. Kim, S. X. Dou, *ACS Nano* **2014**, 8, 2977.

[57] J. Cho, *J. Mater. Chem.* **2010**, 20, 4009.

[58] Y. Shi, J. Zhang, L. Pan, Y. Shi, G. Yu, *Nano Today* **2016**, 11, 738.

[59] V. B. Shenoy, P. Johari, Y. Qi, *J. Power Sources* **2010**, 195, 6825.

[60] H. Yang, F. Fan, W. Liang, X. Guo, T. Zhu, S. Zhang, *J. Mech. Phys. Solids* **2014**, 70, 349.

[61] P. E. Blöchl, *Phys. Rev. B* **1994**, 50, 17953.

[62] G. Kresse, J. Hafner, *Phys. Rev. B* **1993**, 48, 13115.

Chapter 4. Electrochemical Properties of Nonstoichiometric Silicon Suboxide Anode Materials with Controlled Oxygen Concentration

4.1. Abstract

Among the silicon (Si)-based anode materials, Si/SiO_x is likely to be the best candidate for maintaining structural stability while taking advantage of the high capacity of Si as well as the compatible functionality between Si and SiO_x. The oxygen content of SiO_x is an especially significant factor for obtaining better performance, because it directly affects electrochemical properties such as reversible capacity, structural stability, and electrical conductivity. Herein, we have synthesized SiO_x materials with different oxygen contents *via* magnesiothermic reduction of silica. The theoretical capacities of a series of Si/SiO_x samples were estimated by using X-ray photoelectron spectroscopy, and then those results were compared with empirical results. This work paves the way to predicting the electrochemical performances of lithium-ion battery anodes based on oxygen content in the nonstoichiometric Si/SiO_x structure.

4.2. Introduction

With increasing global demand for the development of environmentally friendly and renewable energy sources, lithium-ion batteries (LIBs) have emerged as one of the most promising energy storage applications[1-4]. The conventional graphite system is insufficient, however, for satisfying rapidly changing industrial needs due to its intrinsically low theoretical capacity (372 mA h g^{-1})[5]. Thus, newly developed anode materials have become a prerequisite for advances in the next generation of LIBs.

Over the past decade, silicon (Si) has been developed as an alternative anode material owing to its attractive high capacity (3580 mA h g^{-1}) and relatively low reaction potential (0.4 V vs. Li/Li^+), and thus, mainstream research has been focused on how to overcome the intrinsic drawbacks of Si such as its low structural stability and low conductivity while taking advantage of the high capacity of Si[6-8]. Among them, Si/SiO_x anodes represent one of the strongest candidates, because SiO_x acts as not only an active material itself that can increase the specific capacity, but also as a buffer for reducing mechanical stress from the volume expansion of Si[9-11]. Moreover, Si/SiO_x shows good synthetic compatibility because it can be synthesized from single silica precursors by the method of oxygen reductio[12,13]. Nevertheless, Si/SiO_x still has issues that need to be resolved before it can be utilized as a high performance anode material. Firstly, its specific capacity and initial coulombic efficiency should be maximized by determining the optimum Si content. Secondly, its structural stability and electrical conductivity should be guaranteed by adjusting the SiO_x content. Consequently, it is highly important to find the optimum ratio between Si and SiO_x that can coexist with a mechanically stable architecture[14].

Herein, we demonstrate Si/SiO_x anode materials with different oxygen contents, which were synthesized *via* magnesiothermic reduction of highly ordered mesoporous silica precursor with

a double-gyroid structure. With three kinds of Si/SiO_x material, as well as commercial Si nanopowder (Si-NP) as a reference, the electrochemical properties of each anode were measured by testing in half-cells. In addition, the theoretical capacities were calculated, based on X-ray photoelectron spectroscopy. Through comparative studies between the calculations of theoretical capacities and the empirical measurements, additional significant factors which could not be verified from the calculations were traced. Also, we propose the optimum oxygen content for Si/SiO_x to enable its further development to approach suitability for high-performance LIBs.

4.3. Experimental

4.3.1. Materials Synthesis

Highly ordered mesoporous silica (SiO_2) with double-gyroid structure (KIT-6) was used as precursor. The KIT-6 can be synthesized by the method of Doi et al.[15]. For the purpose of obtaining different oxygen contents in the Si/SiO_x, KIT-6 (0.5 g) and magnesium powder (Mg, 0.5 g, Sigma Aldrich) were put inside an argon-filled and sealed stainless steel reactor, and then heated in a tube furnace at different temperatures of 675, 750, and 825 °C for 2 h. The obtained powders were first immersed in hydrochloric acid solution (HCl, 1 M, 100 ml) for 24 h, then washed with ethanol and distilled water in order to remove Mg compounds (with the samples hereafter denoted as Si/SiO_x-1, Si/SiO_x-2, and Si/SiO_x-3, respectively).

4.3.2. Materials Characterization

Morphological observations and structural investigations of the prepared samples were conducted using a transmission electron microscope (TEM, JEOL ARM-200F) equipped with energy-dispersive X-ray spectroscopy (EDS). The X-ray diffraction patterns were collected using an X-ray diffractometer (Empyrean-XRD, PANalytical) with Cu Kα radiation (λ = 1.54056 Å). To determine the surface and in-depth chemistry of the Si/SiO_x samples, X-ray photoelectron spectroscopy (XPS) measurements were performed using a surface analysis instrument (Sigma probe, Thermo Scientific) equipped with an argon ion beam sputtering system.

4.3.3. Electrochemical Measurements

The working electrodes were prepared by coating a slurry containing 80 wt% active materials, 10 wt% polyacrylic acid (PAA) binder, and 10 wt% Super-P carbon conductor onto Cu-foil 10 μm in thickness. In the CR2032 coin-type cells, lithium metal foil and a polyethylene membrane were used as counter electrode and separator, respectively. 1 M $LiPF_6$ dissolved in mixed ethylene carbonate (EC) and ethyl methyl carbonate (EMC) with a volume ratio of 1:2, including 2 wt % fluoroethylene carbonate (FEC) additive, was used as the electrolyte. The cells were galvanostatically charged/discharged at a current density of 200 mAg^{-1} in the voltage range of 0.01 V to 2.0 V *vs.* Li/Li^+ for 100 cycles (WBSC3000, WonATech).

4.4. Results and Discussion

Figure 4.1 shows a schematic illustration of the synthetic route for nonstoichiometric Si/SiO_x materials. After magnesiothermic reduction at different temperatures (675, 750, and 825 °C)

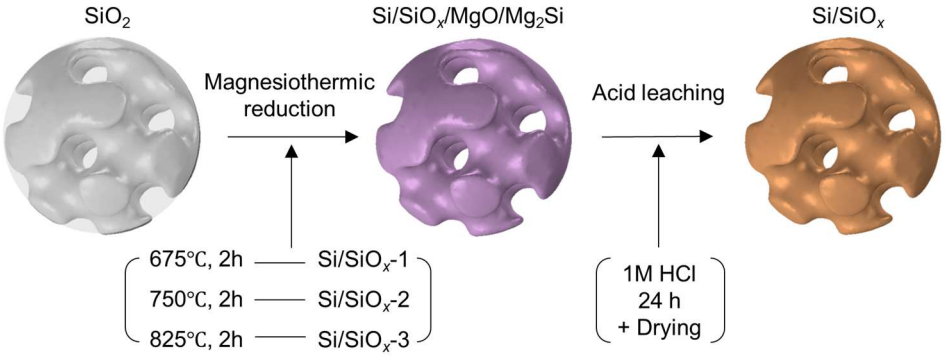

Figure 4.1. Schematic illustration of the synthesis of nonstoichiometric Si/SiO_x anode materials via magnesiothermic reduction at various heat-treatment temperatures.

and subsequent acid leaching, various oxygen contents of Si/SiO_x were obtained. Figure 4.2 shows a high-angle annular dark-field –scanning transmission electron microscopy (HAADF-STEM) image and its corresponding bright field STEM (BF-STEM) image of KIT-6 precursor. The right inset shows the corresponding x-ray diffraction (XRD) pattern. It is confirmed that the amorphous SiO_2 structure contains highly ordered mesopores around 10 nm in diameter

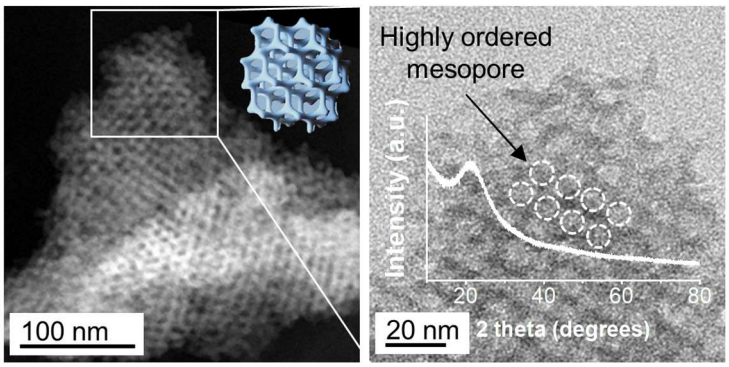

Figure 4.2. HAADF-STEM image and its corresponding BF-STEM image of the KIT-6. The left inset shows the structure of KIT-6, and the right inset the corresponding XRD pattern.

that can enhance the mechanical stability, when the active material undergo volume expansion/contraction during the electrochemical lithiation/delithiation.

Figure 4.3a, b, and c shows high-resolution TEM (HRTEM) images of Si/SiO$_x$-1, Si/SiO$_x$-2, and Si/SiO$_x$-3. While Si/SiO$_x$-1 and Si/SiO$_x$-2 maintained their original mesoporous structures after oxygen reduction, the pores were collapsed, and the particles were agglomerated together to form larger lumps in Si/SiO$_x$-3. In addition, the detailed HRTEM images confirm the presence of crystalline Si (c-Si) with a lattice spacing of 3.1 Å, corresponding to the (111) planes of the face-centered cubic (*fcc*) structure[16]. It should be noted that each sample showed different fractions and sizes of c-Si. Consequently, Si/SiO$_x$-3 was expected to show relatively

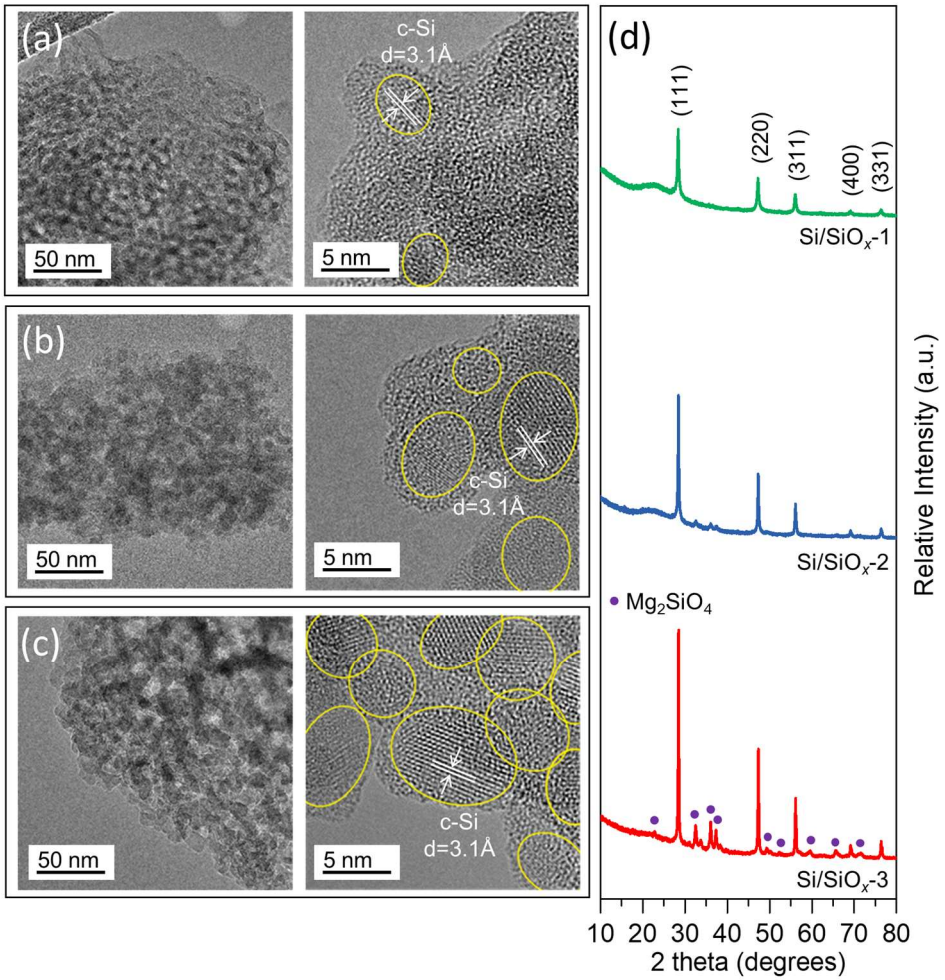

Figure 4.3. HRTEM images of (a) Si/SiO$_x$-1, (b) Si/SiO$_x$-2, and (c) Si/SiO$_x$-3. (d) XRD patterns of this series of Si/SiO$_x$ samples.

poor cycling performance due to its collapsed structure[14]. XRD patterns of each product were further collected, as shown in Figure 4.3d. In all the series of Si/SiO_x products, diffraction peaks of *fcc* Si are clearly shown at 28.6, 47.6, 56.5, 69.7, and 77.0˚with different relative intensities, indicating that the fraction of c-Si is proportional to the reaction temperature[17]. It should be noted that unwanted Mg_2SiO_4 impurity could not be removed, even after acid leaching (HCl treatment), in the case of the Si/SiO_x-3[12,18]. This impurity would bring loss of specific capacity due to consequent loss of active material as much as the amount that the impurity occupied in anode electrode.

To investigate the surface chemistry in detail, X-ray photoelectron spectroscopy (XPS) measurements were conducted. As a reference, commercial silicon nanopowder (Si-NP, Sigma Aldrich, 50 nm) were also included, as shown in Figure 4.4. Figure 4.5a shows the Si 2p XPS spectra of Si/SiO_x-1, Si/SiO_x-2, Si/SiO_x-3, and Si-NP, which were deconvoluted to each oxidation state of Si, as shown by the fitted curves. Before fitting, all the spectra were calibrated by shifting the C 1s peaks to 248.6 eV. In the Si-NP spectrum, there are mainly two distinct, symmetric peaks at 99.3 and 100.1 eV, which indicate metallic Si $2p_{3/2}$ and Si $2p_{1/2}$ orbitals, together with relatively much lower intensity peaks indicating various states of oxides[19]. On the other hands, the XPS spectra of a series of Si/SiO_x samples show every available oxide

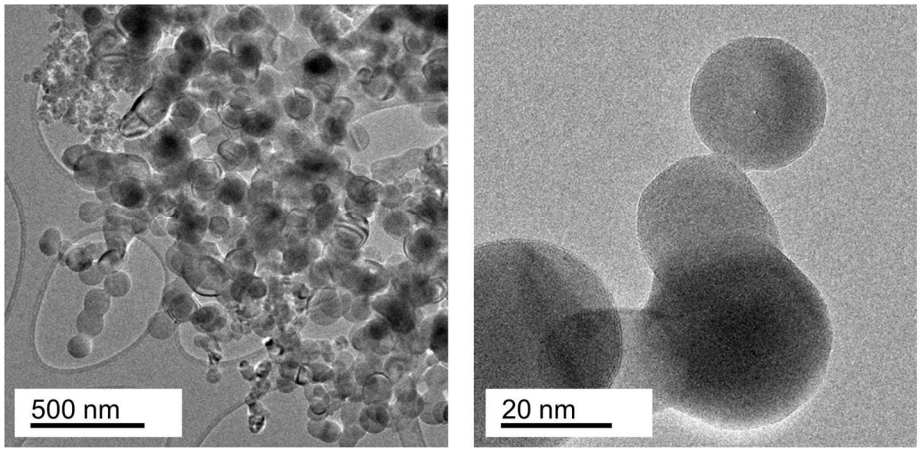

Figure 4.4. Low- and high-resolution transmission electron microscope (TEM) images of the Si-NP as a reference.

peak along with metallic Si peaks as well. For all of them, the centers of the oxide peaks, which can be assigned to the oxidation states of Si^{4+}, Si^{3+}, Si^{2+}, and Si^{1+} are located at 104.5, 103.5, 102.5, and 101.4 eV, respectively. The corresponding values can be attributed to $SiO_{2.0}$, $SiO_{1.5}$, $SiO_{1.0}$, and $SiO_{0.5}$, respectively[20]. We argue that Si/SiO_x-1 consists of mainly $SiO_{1.5}$ and $SiO_{2.0}$ phases with a small fraction of lower oxidized forms. Interestingly, all kinds of chemical states, including metallic Si, exist, and in particular, the Si^0 state of Si/SiO_x-3 is dominant over the others. Through these clear spectra and well deconvoluted curves, as well as the baselines, the areal ratio of each curve can be calculated accurately. Figure 4.5b shows the areal ratio of each material according to all the oxidation states from metallic Si to SiO_2, calculated from the areal ratios of the deconvoluted curves. In order from Si/SiO_x-1, Si/SiO_x-2, and Si/SiO_x-3 to Si-NP, the areal ratio of Si^0 is estimated to be 6.82, 35.55, 41.06, and 89.54 %, respectively. In contrast,

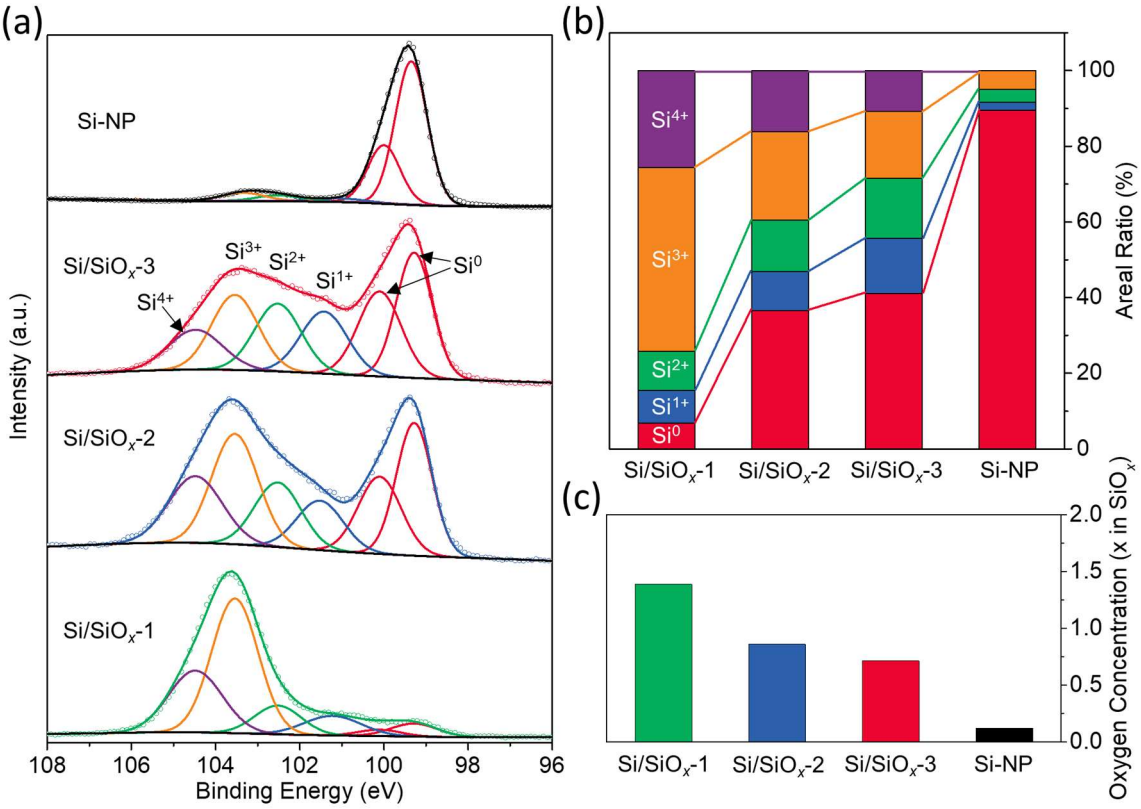

Figure 4.5. (a) Si 2p X-ray Photoelectron spectroscopy (XPS) spectra of the Si/SiO_x-1, Si/SiO_x-2, and Si/SiO_x-3 samples with Si-NP, de-convoluted to the individual silicon oxidation states. (b) Their areal ratios, and (c) their estimated oxygen concentrations (stoichiometric ratio of oxygen divided by total silicon, including metallic silicon).

the areal ratios of Si^{3+} and Si^{4+} decreased drastically (Table 4.1 for the detailed numerical results). Moreover, in order to determine the stoichiometry between Si and oxygen, the total oxygen concentration was estimated from the areal ratio of each material, as shown in Figure 4.5c and Table 4.1b[21]. By estimating the oxygen content divided by the total Si content, without

(a)

Oxidation state	Areal ratio (%)			
	Si/SiO_x-1	Si/SiO_x-2	Si/SiO_x-3	Si-NP
Si^0	6.82	35.55	41.06	89.54
Si^{1+}	8.66	10.42	14.58	2.10
Si^{2+}	10.37	13.60	15.91	3.42
Si^{3+}	48.49	23.24	17.66	4.88
Si^{4+}	25.66	16.19	10.79	0.06

(b)

Oxygen Concentration	Si/SiO_x-1	Si/SiO_x-2	Si/SiO_x-3	Si-NP
x in SiO_x	1.39	0.86	0.71	0.12

Table 4.1. Numerical results corresponding to (a) Figure 4.5b and (b) Figure 4.5c.

distinction between metallic Si or Si oxides, the stochiometries of the series of Si/SiO_x samples and Si-NP can be specified as $SiO_{1.39}$, $SiO_{0.86}$, $SiO_{0.71}$, and $SiO_{0.12}$, repectively. These specific oxygen concentrations for each Si oxide will help to further inform estimations of electrochemical properties such as the reversible capacity and irreversible capacity, considering the electrochemical reactions between $Si/SiO/SiO_2$ and lithium[22].

In order to investigate the electrochemical properties of each material and to validate its feasibility as an anode material, electrochemical tests were carried out. Figure 4.6 shows the galvanostatic charge-discharge curves and the corresponding differential capacity plots for the

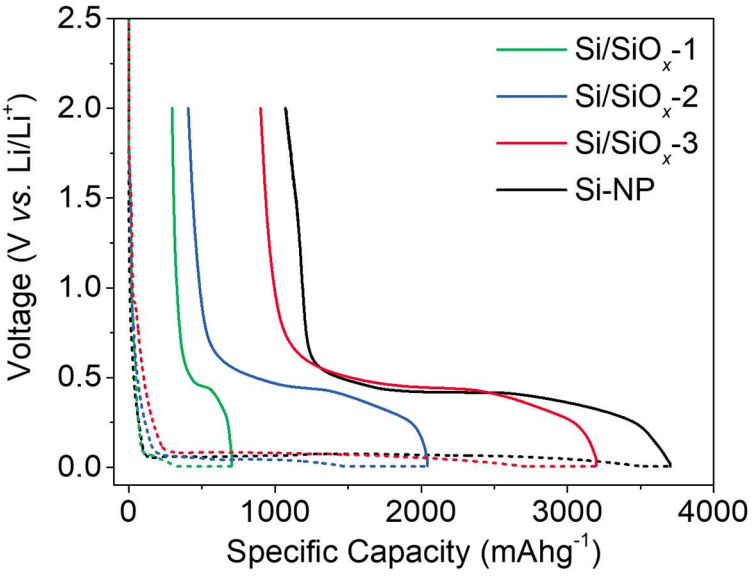

Figure 4.6. First cycle charge/discharge profiles of the Si/SiO_x-1, Si/SiO_x-2, and Si/SiO_x-3 anodes, together with the Si-NP anode.

first cycle. Except for Si-NP, the first-cycle specific discharge capacity of Si/SiO_x-3 was the highest (2294 mA h g^{-1}), as expected, whereas Si/SiO_x-1 showed an insignificant specific discharge capacity (410 mA h g^{-1}) due to insufficient reduction of silica (a small fraction of Si). Interestingly, the Si/SiO_x-2 anode showed not only satisfactory reversible capacity of 1635 mAh g^{-1}, but also an outstanding value for its initial Coulombic efficiency (ICE, 80.1 %). Moreover, even after 100 cycles, discharge capacity retention of 83.3 % was observed, and

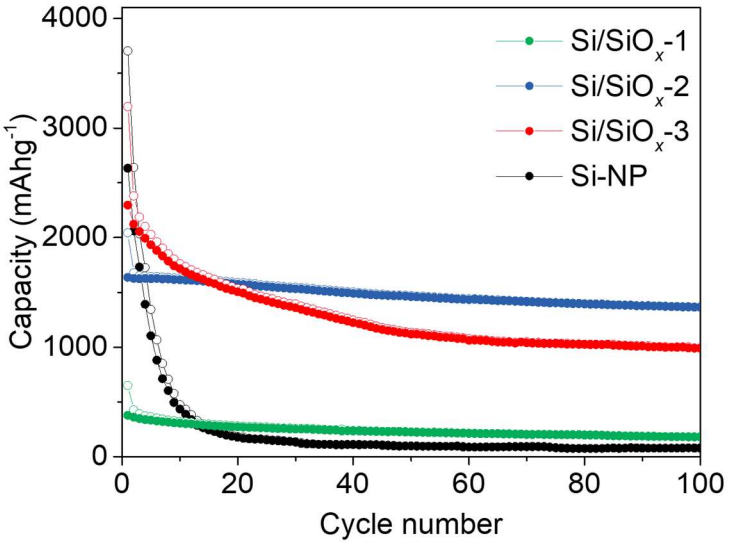

Figure 4.7. Cycling performances of the Si/SiO_x-1, Si/SiO_x-2, and Si/SiO_x-3 anodes, together with the Si-NP anode.

Coulombic efficiency of 99.8 % was maintained in case of the Si/SiO_x-2, although other higher Si content samples (Si/SiO_x-3 and Si-NP) showed drastic capacity degradations even at hundredth cycle (43.1 % and 3.0 %, respectively), (Figure 4.7). This result reflects stcuctural stability with the support of SiO_x buffer should be considered to assure long term cyclability[11]. In addition, further electrochemical studies were conducted in order to estimate the lithiation/delithiation mechanisms of the respective materials. In Figure 4.8a, the Si-NP anode showed typical lithiation behaviour at a potential of 0.05 V, indicating the formation of lithium silicide ($Li_{15}Si_4$, if full lithiation) from most of the c-Si in Si-NP (region L[I], indicated in Fig 5b)[23]. Si/SiO_x-1 anode as shown in Figure 4.8d, however, reacted mainly below 0.05 V, including a constant voltage of 0.01 V (L[II]), which indicates complex electrochemical behaviour, involving mixed reactions of SiO_x to form silicides (Li_xSi) and silicates (Li_xSiO_y), as well as relatively high overpotential due to its intrinsic low electrical conductivity[24]. This feature gradually stands out in the order of Si-NP, Si/SiO_x-3, Si/SiO_x-2, and Si/SiO_x-1 with increasing oxygen content. In the delithiation process, however, every anode showed the same electrochemical behaviour, which can be represented by two stepwise reversible delithiation mechanisms from $Li_{15}Si_4$: i) c-$Li_{15}Si_4$ to Li_xSi at 0.2 to 0.4 V (D[I]) and ii) Li_xSi to amorphous Si at 0.4 V (D[II])[23,25].

To compare the electrochemical properties of the individual anodes, the corresponding results are shown in Figure 4.9a. In these results, it is clearly shown that Si/SiO_x-2 is the anode with the highest energy density when considering overall electrochemical properties. In particular, a large fraction of Si samples (i.e., Si/SiO_x-3 and Si-NP) showed insufficient ICE of approximately 70 %, while the ICE of the Si/SiO_x-2 reached the highest value of 80.1 %. This might be because of the interaction between the intrinsic electrochemical reversibility (lower at higher oxygen content) and the structural stability (poorer at higher Si content) of the Si/SiO_x materials.

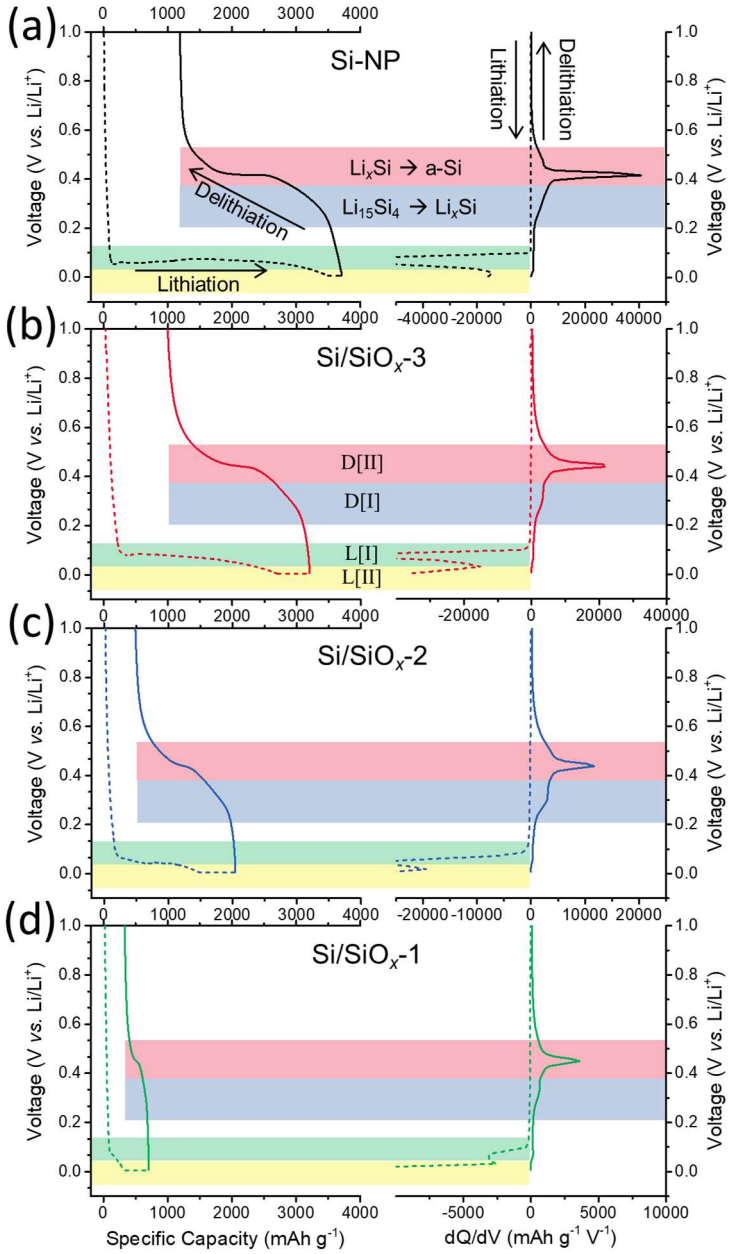

Figure 4.8. Galvanostatic charge-discharge profiles and the corresponding differential capacity plots of (a) Si-NP, (b) Si/SiO$_x$-3, (c) Si/SiO$_x$-2, and (d) Si/SiO$_x$-1.

In the meanwhile, reversible and irrevesible capacities can be calculated theoretically, given quantitative information on the chemical states of Si/SiO$_x$[26]. While metallic Si undergoes a completely reversible reaction to form lithium silicide ($Li_{15}Si_4$), the Si oxides produce irreversible phases such as Li_2O and Li_4SiO_4. SiO_2 in particular consumes more than half of the lithium to form an irreversible phase, which is directly reflected by its decreased ICE in the

lithium-ion cell[8]. Consequently, the reaction mechanisms of individual SiO_x samples ($0 \leq x \leq 2$) can be summarized in chemical equations as follows[27]:

$$Si + 3.75Li \rightarrow Li_{3.75}Si \quad (1)$$

$$SiO + 5.75Li \rightarrow Li_{3.75}Si + Li_2O \quad (2)$$

$$SiO_2 + 3.88Li \rightarrow 0.5Li_{3.75}Si + 0.5Li_4SiO_4 \quad (3)$$

On consideration of the above equations, it is assumed that interstitial oxidised forms such as, $SiO_{0.5}$ and $SiO_{1.5}$ can be represented in chemical equations as follows:

$$SiO_{0.5} + 4.75Li \rightarrow Li_{3.75}Si + 0.5Li_2O \quad (4)$$

$$SiO_{1.5} + 4.81Li \rightarrow 0.75Li_{3.75}Si + 0.5Li_2O + 0.25Li_4SiO_4 \quad (5)$$

From the previous XPS results regarding the atomic ratios of the individual oxidation states of Si, we determined their theoretical specific capacities according to the corresponding chemical equations, which indicate both chemical reversibility and irreversibility in the reactions between various Si oxides and lithium[22]. Figure 4.9b shows the theoretical capacities of all four types of samples, which match the same oxidation states of the as-prepared materials (see Table

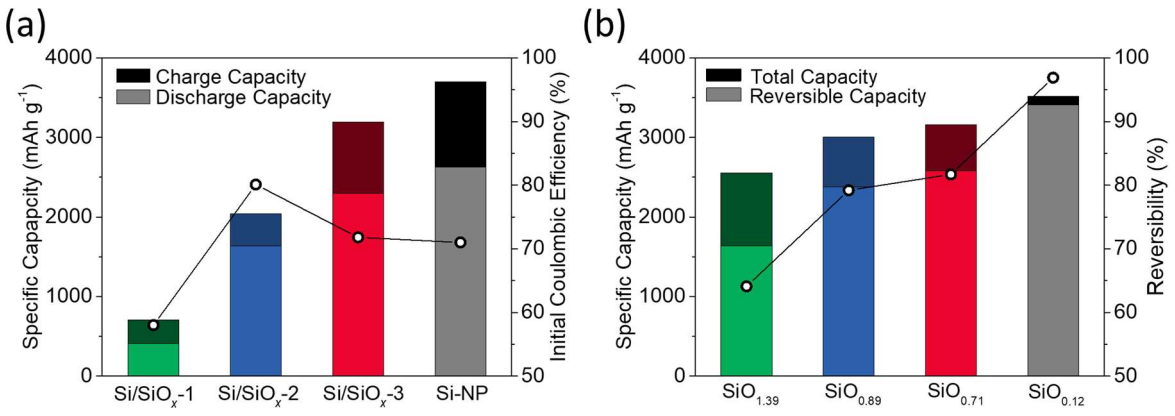

Figure 4.9. (a) Experimental results on the charge and discharge capacities of the samples (corresponding to the results in Figure 4.8). (b) Calculated total and reversible capacities for different stoichiometries of SiO_x from the XPS results.

4.2 for detailed numerical results corresponding to Figure 4.9). From comparison of the empirical results with the theoretical calculations, meaningful parallels and differences in electrochemical properties can be determined. As the *x* value of SiO_x (in the total silicon content) decreases, the capacity tends to increase in both sets of results. There is a big gap in the capacities, however, especially in the highly oxidized samples (Si/SiO_x-1 *vs.* $SiO_{1.39}$). This is

(a)

	Si/SiO_x-1	Si/SiO_x-2	Si/SiO_x-3	Si-NP
Charge capacity (mAh/g)	706	2043	3196	3704
Discharge capacity (mAh/g)	410	1635	2294	2631
Initial Coulombic efficiency (%)	58.0	80.1	71.8	71.0
Capacity retention (%)	92.0	83.3	43.1	3.0

(b)

	$SiO_{1.39}$	$SiO_{0.86}$	$SiO_{0.71}$	$SiO_{0.12}$
Total capacity (mAh/g)	2556	3006	3164	3520
Reversible capacity (mAh/g)	1638	2380	2584	3412
Reversibility (%)	64.1	79.2	81.7	96.9

table 4.2. Numerical results corresponding to (a) Figure 4.9a and (b) Figure 4.9b.

probably because their relatively low conductivity results in insufficient activation of materials that are closer to SiO_2[28]. When the sample composition is close to metallic Si, the initial Coulombic efficiency is only around 70 %, although the theoretical reversibility is increased up to 100 % (Si-NP *vs.* $SiO_{0.12}$). From this circumstance, it is clearly revealed that pure Si cannot guarantee structural stability without the support of SiO_x as a buffer phase, and

eventually, poor cyclability is unavoidable[11]. As a result, it is the Si/SiO_x-2 anode that can offer both sufficiently high content of Si and sufficient structural stability with the assistance of SiO_x buffer including mesopores, as shown in Figure 4.10 and Figure 4.3b. Moreover, in N_2 adsorption/desorption isotherm results as shown in Figure 4.11, KIT-6 precursor showed the surface area of 225 m^2 g^{-1} and the total pore volume of 0.71 cm^3 g^{-1}. Interestingly, the Si/SiO_x-2 still maintained mesoporous structure with the surface area of 161 m^2 g^{-1} and the total pore volume of 0.53 cm^3 g^{-1} in spite of harsh chemical changes during reduction and etching process. Thus, it can provide high specific capacity and better cycling performance simultaneously.

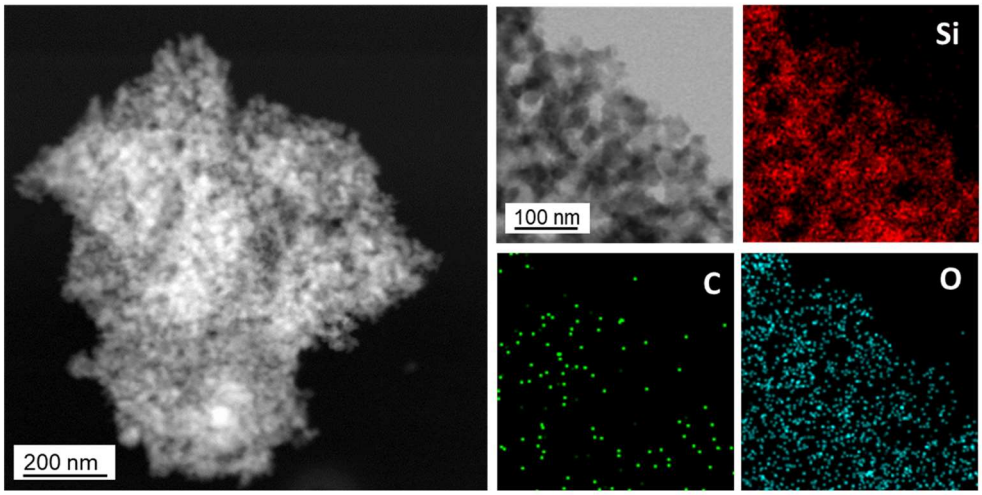

Figure 4.10. HAADF-STEM image and EDS elemental mapping images of the Si/SiO_x-2.

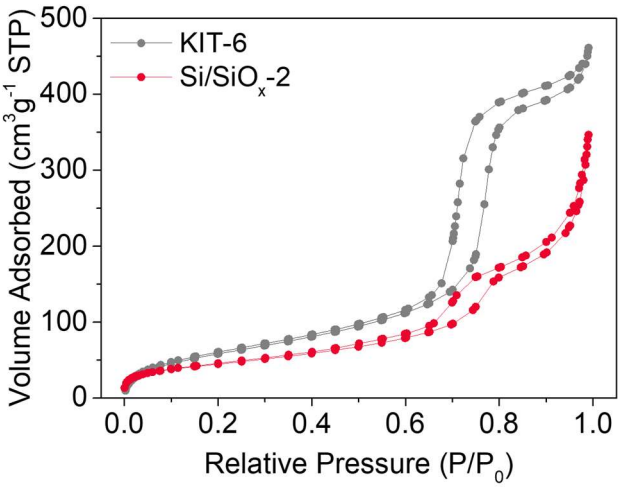

Figure 4.11. N_2 adsorption/desorption isotherms of the KIT-6 and Si/SiO_x-2.

Meanwhile, Si/SiO_x anode should be theoretically at least above $SiO_{0.9}$ to show acceptable reversibility (over 80 %) and moderate cyclability.

4.5. Conclusion

We synthesized nonstoichiometric Si/SiO_x with different oxygen contents *via* magnesiothermic reduction of silica. The optimum Si/SiO_x anode shows not only high specific capacity with acceptable initial Coulombic effiency, but also excellent cycling performance. Furthermore, through the confirmation of parallels and differences between calculations of the theoretical capacity of each material and experimental measurements, we propose the optimum oxygen content of Si/SiO_x that shows the comprehensively best performance in consideration of all electrochemical properties. We desire to contribute to the development of Si/SiO_x to approach suitability for next-generation LIBs.

4.6. References

[1] M. Armand, J.M. Tarascon, *Nature*, **2008**, 451, 652.

[2] S. Wu, Y. Han, K. Wen, Z. Wei, D. Chen, W. Lv, T. Lei, J. Xiong, M. Gu, W. He, *Compos. B. Eng.* **2019**, 106, 369.

[3] K. Mishra, X.-C. Liu, F.-S. Ke, X.-D. Zhou, *Compos. B. Eng.* **2019**, 163, 158.

[4] J.H. Um, J. Lim, K. Hengge, C. Scheu, W.-S. Yoon, J.-K. Lee, Y.-E. Sung, *Compos. B. Eng.* **2019**, 166, 613.

[5] W. Kohs, H.J. Santner, F. Hofer, H. Schröttner, J. Doninger, I. Barsukov, H. Buqa, J.H. Albering, K.C. Möller, J.O. Besenhard, M. Winter *J. Power Sources* **2003**, 119-121, 528.

[6] C.-M. Park, J.-H. Kim, H. Kim, H.-J. Sohn *Chem. Soc. Rev.* **2010**, 39, 3115.

[7] C.K. Chan, H. Peng, G. Liu, K. McIlwrath, X.F. Zhang, R.A. Huggins, Y. Cui, *Nat. Nanotechnol.* **2007**, 3, 31.

[8] G. Jeong, J.-G. Kim, M.-S. Park, M. Seo, S.M. Hwang, Y.-U. Kim, Y.-J. Kim, J.H. Kim, S.X. Dou, *ACS Nano* **2014**, 8, 2977.

[9] J. Yang, Y. Takeda, N. Imanishi, C. Capiglia, J.Y. Xie, O. Yamamoto, *Solid State Ion.* **2002** 152-153, 125.

[10] E. Park, H. Yoo, J. Lee, M.-S. Park, Y.-J. Kim, H. Kim, *ACS Nano*, **2015**, 9, 7690.

[11] M.-S. Park, E. Park, J. Lee, G. Jeong, K.J. Kim, J.H. Kim, Y.-J. Kim, H. Kim, *ACS Appl. Mater. Interfaces* **2014**, 6, 9608.

[12] J. Entwistle, A. Rennie, S. Patwardhan, *J. Mater. Chem. A* **2018**, 6, 18344.

[13] W.-S. Chang, C.-M. Park, J.-H. Kim, Y.-U. Kim, G. Jeong, H.-J. Sohn, *Energy Environ. Sci.* **2012**, 5, 6895.

[14] E. Park, M.-S. Park, J. Lee, K.J. Kim, G. Jeong, J.H. Kim, Y.-J. Kim, H. Kim, *ChemSusChem* **2015**, 8, 688.

[15] Y. Doi, A. Takai, Y. Sakamoto, O. Terasaki, Y. Yamauchi, K. Kuroda, *Chem. Commun.*, **2010**, 46, 6365.

[16] .M. Morales, C.M. Lieber, *Science* **1998**, 279, 208.

[17] H. Yoo, E. Park, J. Bae, J. Lee, D.J. Chung, Y.N. Jo, M.-S. Park, J.H. Kim, S.X. Dou, Y.-J. Kim, H. Kim, *Sci. Rep.* **2018**, 8, 6904.

[18] S.H. Tamin, S.B.R.S. Adnan, M.H. Jaafar, N.S. Mohamed, *Ionics* **2018**, 24, 2665.

[19] E.G. Barbagiovanni, L.V. Goncharova, P.J. Simpson, *Phys. Rev. B*, **2011**, 83, 035112.

[20] M. Miyachi, H. Yamamoto, H. Kawai, T. Ohta, M. Shirakata, *J. Electrochem. Soc.* **2005**, 152, A2089.

[21] J.W. He, X. Xu, J.S. Corneille, D.W. Goodman, *Surf. Sci.* **1992**, 279, 119.

[22] T. Chen, J. Wu, Q. Zhang, X. Su, *J. Power Sources* **2017**, 363, 126.

[23] M.N. Obrovac, L.J. Krause, *J. Electrochem. Soc.* **2007**, 154, A103.

[24] M.A. Al-Maghrabi, J. Suzuki, R.J. Sanderson, V.L. Chevrier, R.A. Dunlap, J.R. Dahn, *J. Electrochem. Soc.* **2013**, 160, A1587.

[25] C. Huang, A. Kim, D.J. Chung, E. Park, N.P. Young, K. Jurkschat, H. Kim, P.S. Grant, *ACS Appl. Mater. Interfaces* **2018**, 10, 15624.

[26] S.C. Jung, H.-J. Kim, J.-H. Kim, Y.-K. Han, *J. Phys. Chem. C* **2016**, 120, 886.

[27] J.-H. Kim, C.-M. Park, H. Kim, Y.-J. Kim, H.-J. Sohn, *J. Electroanal. Chem.* **2011**, 661, 245.

[28] H.P. Zhou, D.Y. Wei, S. Xu, S.Q. Xiao, L.X. Xu, S.Y. Huang, Y.N. Guo, S. Khan, M. Xu, *J. Phys. D Appl. Phys.* **2012**, 45, 395401

Chapter 5. Strategically Designed Zeolitic Imidazolate Frameworks for Controlling the Degree of Graphitization and Carbonization Temperature

5.1. Abstract

The zeolitic imidazolate frameworks (ZIFs) ZIF-8 and ZIF-67 are well-known as belonging to the series of metal-organic frameworks. Using different types of metal ions in them, such as Zn^{2+} and Co^{2+} simultaneously, brings both advantages and disadvantages with respect to the carbonization process. For tailoring their properties, we suggest that the best approach involves control of the bimetallic ZIF-derived carbon nanoarchitecture, which is hybridized through the synergistic effects of each metal ion. In this study, the bimetallic ZIFs were designed by controlling the molar ratio of zinc (Zn^{2+}) and cobalt (Co^{2+}) ions, and the carbon nanoarchitecture was subsequently formed by a facile heat treatment and acid leaching. We demonstrate this approach to achieve tailored ZIF derived carbon nanoarchitectures with different pore sizes, surface areas, and degree of graphitization. In addition, the physical/structural properties of carbon nanoarchitecture derived from ZIF-8 composed of Zinc ions (Zn^{2+}) and 2-methylimidazole are greatly affected by the process temperature during carbonization. The temperature caused differences such as elemental ratio, pore volume, powder density, and electrical conductivity. We can get the porous carbon framework suitable for each application by simply controlling the carbonization temperature. Overall, these pave the way to finding the optimal carbon nanoarchitecture for specific applications such as Li-metal batteries

.

5.2. Introduction

Metal-organic frameworks (MOFs) (or porous coordination polymers (PCPs)) are well known to consist of metal ions and organic molecule (called the 'linker') to build a permanent porous structure with different functionalities.[1-11] Without any soft or hard template, the MOFs possess a unique feature, forming pore structures or certain voids because the repeated organic linker and secondary building blocks act as the template.[12,13] Two important ways to tune MOF-derived nanoarchitectures are by the linker geometries and selection of metal ions.[14] Importantly, the MOFs can easily be converted to various metal oxides or new carbonaceous materials through different calcination temperatures /atmospheres and chemical treatment. Thus, these structures are highly attractive for a variety of industrial applications, such as energy storage/harvesting devices, sensors, H_2/CO_2 capture, drug delivery, and catalysts.[15-26]

The synthesis of the MOFs was originally developed based on zeolite chemistry. Kitagawa[27] and Yaghi[28,29] strategically designed and developed various inorganic-organic structures. Since then, approximately 20,000 MOFs have been reported.[30] In particular, MOF-5[31] and HKUST-1[32] are representative of the first step for various applications. Zeolitic imidazolate frameworks (ZIFs) are one subclass in the MOF family.[33,34] The thermal, chemical, and mechanical satability of the MOFs still needs to be further enhanced to reach commercial quality. However, ZIFs follow the crystalline structure of natural zeolite, which is suitable for thermal stability in a wide temperature range, thus thermal expansion and chemical stability are much higher than for other MOFs. To overcome these drawbacks, ZIFs or covalent organic frameworks (COFs) are highly expected to open up many possibilities. Representative ZIF-8 and ZIF-67 MOFs, which composed of metal ions of Zn^{2+} and Co^{2+}, respectively, strongly coordinated by 2-methylimidazole (2-MIM) organic linkers, are formed as rhombic dodecahedra with a large cavity (11.6 Å).[35,36] The interior cavities directly introduce robust pores, but form different

features through the calcination process. More significantly, Yamauchi[37] and Park[38] suggested a straightforward way to make hierarchically porous carbons without a secondary carbon precursor. These have gained great attention because they allow a direct carbonaceous approach with the ZIF series.

In this study, combining the different metal ions Zn^{2+} and Co^{2+} is expected to yield different properties, such as high surface area, a good degree of graphitization, electrical conductivity, high nitrogen content, and chemical stability. For various applications, we have carefully evaluated our ZIF derived carbons with different molar ratios of Zn^{2+} and Co^{2+}, and then systematically compared them with directly carbonized ZIF-8 and ZIF-67 structures.

5.3. Experimental

5.3.1. Preparation of ZIF-8 Crystals

Zinc nitrate hexahydrate ($Zn(NO_3)_2 \cdot 6H_2O$, 891 mg, 3 mmol) was dissolved in methanol (CH_3OH, 30 mL). 2-methylimidazole ($CH_3C_3H_2N_2H$, 984 mg, 12 mmol) was separately dissolved in methanol (10 mL). Subsequently, the metal precursor solution was poured into the solution in which 2-methylimidazole was dissolved and stirred. The resulting solution was kept at 100 °C for 12 hours. The product was filtered, thoroughly washed with methanol, and then dried at 80 °C. The ZIF-8 powder was further activated at 120 °C under vacuum for 24 hours.

5.3.2. Preparation of ZIF-67 Crystals

Cobalt nitrate hexahydrate ($Co(NO_3)_2 \cdot 6H_2O$, 873 mg, 3 mmol) was dissolved in methanol (CH_3OH, 30 mL). 2-methylimidazole ($CH_3C_3H_2N_2H$, 984 mg, 12 mmol) was separately dissolved in methanol (CH_3OH, 10 mL). Subsequently, the metal precursor solution was poured into the solution in which 2-methylimidazole was dissolved and stirred. The resulting solution was kept at 100 °C for 12 hours. The product was filtered, thoroughly washed with methanol and then dried at 80 °C. The ZIF-67 powder was further activated at 120 °C under vacuum for 24 hours.

5.3.3. Preparation of Co/Zn ZIF Crystals

The synthesis procedure for the Zn/Co ZIF crystals is similar to the synthesis procedure for other members of the ZIF series. The desired molar ratio of zinc to cobalt ions (Zn^{2+}/ Co^{2+}) was dissolved in methanol (30 ml) using zinc nitrate hexahydrate and cobalt nitrate hexahydrate, and stirred for 1 hour. 2-methylimidazole was dissolved in methanol (10 ml), and the two metal

precursor solutions were poured into the as-prepared imidazole solution and stirred until the mixture was homogeneous. The resulting solution was kept at 100 °C for 12 hours. The product was filtered, thoroughly washed with methanol and then dried at 80 °C. The bimetallic Zn/Co ZIF powder was further activated at 120 °C under vacuum for 24 hours.

5.3.4. Preparation of Nanoporous Carbon Materials from Bimetallic ZIFs

To obtain the nanoporous ZIF derived carbon material, the activated hybrid ZIF powder was sintered at a heating rate of 2-5 °C·min^{-1} and carbonized at 900 °C for 2 hours under Ar atmosphere, before being cooled down to room temperature. The resulting bimetallic ZIF derived carbon was washed with hydrogen fluoride solution (HF(aq)) and a large amount of water and methanol to remove any remaining metal ions. The product was finally dried at 120 °C for 12 hours.

5.3.5. Characterizations

The morphologies and particle sizes of the ZIF-8, ZIF-67, and bimetallic ZIF derived carbon nanoarchitectures were confirmed using field emission scanning electron microscopy (FESEM, JEOL JSM-7000F). The crystalline structure were investigated using an X-ray diffraction (XRD, Malvern Panalytical, Empyrean) with Cu-Kα radiation (λ = 1.54056 Å). The crystallinity and microstructure were obtained using high resolution transmission electron microscopy (HRTEM, JEOL ARM-200F) with a Cs corrector (CEOS GmbH). The specific surface area and pore volume were characterized by the Brunauer-Emmett-Teller (BET) and Barrett-Joyner-Halenda (BJH) methods using a surface area and porosimetry analyzer (Micromeritics, Tristar II 3020).

5.4. Results and Discussion

The strategic design of the synthesis for various ZIF derived carbons is simply summarized in Figure 5.1. In order to obtain the bare ZIF-8, ZIF-67, and bimetallic ZIF, different metal precursors and 2-methylimidazole were used along with methanol in an aqueous solution. In addition, the bimetallic ZIFs were obtained by controlling the molar ratio of zinc to cobalt ions ($Zn2^{+}/Co2^{+}$). Herein, the molar ratios of zinc to cobalt ions were 199:1, 19:1, 9:1, 2:1, 1:2, and 1:4, and denoted as $Zn_{0.995}{\cdot}Co_{0.005}$, $Zn_{0.95}{\cdot}Co_{0.05}$, $Zn_{0.9}{\cdot}Co_{0.1}$, $Zn_{0.67}{\cdot}Co_{0.33}$, $Zn_{0.33}{\cdot}Co_{0.67}$, and $Zn0.2{\cdot}Co_{0.8}$, respectively.

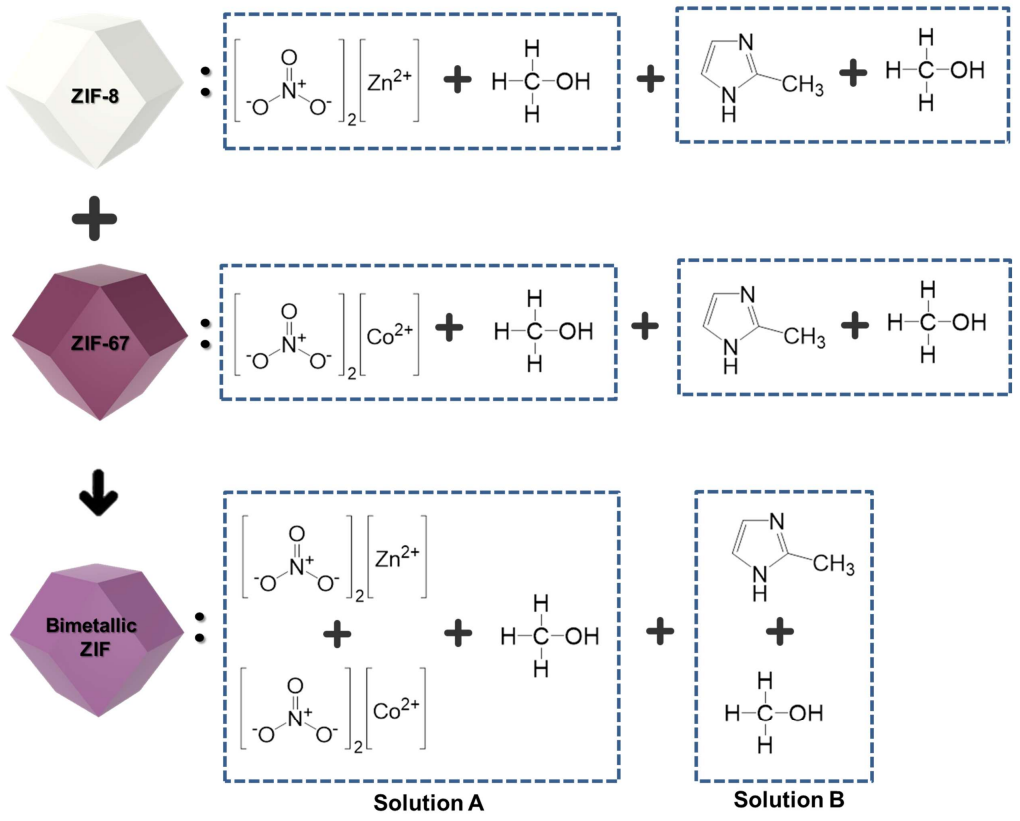

Figure 5.1. Schematic illustration of the concept of this paper, the synthesis of bimetallic ZIFs by hybridization of ZIF-8 and ZIF-67. Zinc nitrate hexahydrate and cobalt nitrate hexahydrate sources (Solution A) were used as the metal precursor and 2-methylimidazole (Solution B) was used as the organic linker.

Figure 5.2 shows FESEM images and their size distribution results for ZIF-8 and ZIF-67 derived carbons as reference, and various bimetallic ZIF derived carbons with different molar ratios of zinc to cobalt ions. From our observations, the morphology of bimetallic ZIFs derived carbons is the same as for the parent structures of bare ZIF-8 and ZIF-67, having a rhombic dodecahedral particle shape. Interestingly, the shape shows some swelling with increasing relative molar ratios of zinc to cobalt ions. This indicates that one role of the zinc ions is to maintain the polyhedral structure in the bimetallic ZIFs derived carbon. It should be noted that the ZIF derived carbon with excess cobalt ions ($Zn_{0.33}$·$Co_{0.67}$) clearly generates rich graphitic structure on the surface, as can be seen in Figure 5.2f. This can be attributed to its superior electrical conductivity. We also found that the particle size for all carbons is distributed in the range of 200 nm to 1000 nm, with each carbon having a different average diameter. For

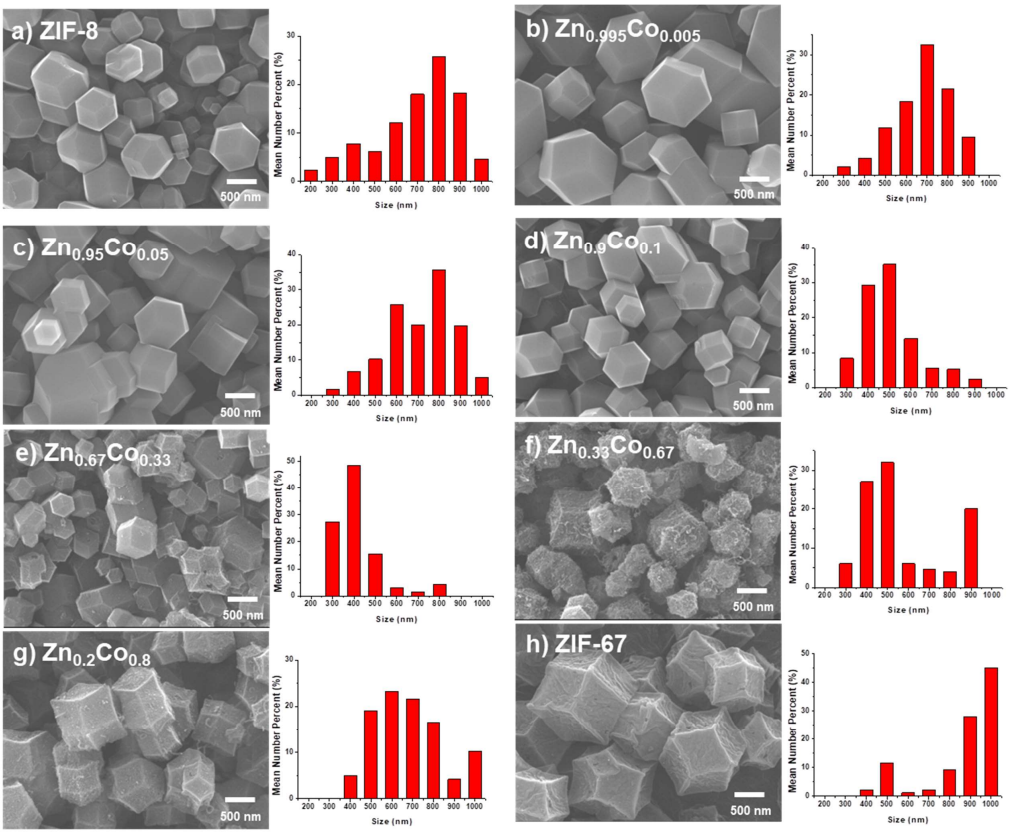

Figure 5.2. FESEM images and size distribution graphs of ZIF derived carbons: (a) ZIF-8 derived carbon; bimetallic ZIF derived carbons with different molar ratios of zinc to cobalt ions: (b) $Zn_{0.995}$·$Co_{0.009}$, (c) $Zn_{0.95}$·$Co_{0.05}$, (d) $Zn_{0.9}$·$Co_{0.1}$, (e) $Zn_{0.67}$·$Co_{0.33}$, (f) $Zn_{0.33}$·$Co_{0.67}$, and (g) $Zn_{0.2}$·$Co_{0.8}$: and (h) ZIF-67 derived carbon.

example, the average particle size of ZIF-8 or ZIF-67 derived carbon is estimated to be 500 nm and 1000 nm, respectively. In particular, the ZIF-67 derived carbon has a relatively large particle size compared to other ZIF series carbons. This is due to the different kinetic reactions of cobalt and zinc ions in 2-methylimidazole. Even in this work, however, there is no particular tendency in the size distribution according to the molar ratio of zinc to cobalt ions. Only a trend in surface roughness is clearly visible in our results.

XRD analysis was performed to confirm the degree of graphitization for various bimetallic ZIF derived carbons, as can be seen in Figure 5.3. In the case of ZIF-8 derived carbon with only zinc ions, the broad diffraction peaks at 24° and 44° represent the (002) and (101) planes of typical amorphous carbon. It should be noted that the full-width at half maximum of the C (002) peak at about 24° becomes narrow due to the molar ratio of the cobalt ions of 0.33. This

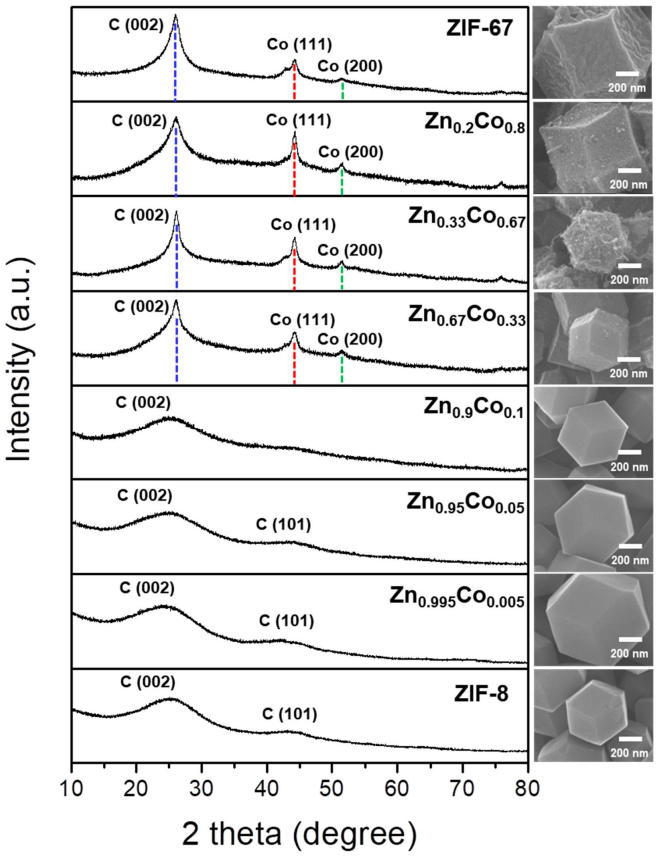

Figure 5.3. XRD patterns of ZIF-8, ZIF-67 and various bimetallic ZIFs derived carbons with different molar ratios of zinc to cobalt ions. Right column shows representative FESEM images.

indicates that the amorphous carbon gradually becomes graphitic, and its crystallinity also improves. These results indicate that cobalt metal ions can be related to the degree of graphitization. Moreover, as the molar ratio of cobalt to zinc ions increases, Co (111) and (200) peaks clearly appear, which are not seen from ZIF-8 to $Zn_{0.9}{\cdot}Co_{0.1}$. That is to say, trapped cobalt particles are hard to remove by carbonization and the acid leaching process. Zinc ones have relatively low melting and boiling temperatures, however, at around 419 °C and 907 °C, respectively. During the carbonization at 900 °C in this study, most zinc particles can be easily removed.

The crystallinity of as-prepared carbons can also be confirmed from the HRTEM images shown in Figure 5.4. The insets show the corresponding low-magnification images of various ZIF derived carbons with different molar ratios of zinc to cobalt ions. From cobalt-ion-free ZIF-8 to $Zn_{0.9}{\cdot}Co_{0.1}$ derived carbon, where the cobalt ions content is less than the zinc one, amorphous carbon is obviously formed, as shown in Figure 5.4a–5.4d. It can be seen that the crystallinity of the thus-formed ZIF derived carbons is improved as the molar ratio of cobalt ions increases, as shown in Figure 5.4e–5.4h. These results clearly argued that the bimetallic ZIFs are effectively graphitized in the existence of certain cobalt amount, which indicate the shrinkage of facets and distorted polyhedral structure. Especially in the case of $Zn_{0.33}{\cdot}Co_{0.67}$ derived carbon, it can be confirmed that carbon nanotubes (CNTs) are formed on the surface with very well aligned carbon structure. Very interestingly, the $Zn_{0.67}{\cdot}Co_{0.33}$, $Zn_{0.2}{\cdot}Co_{0.8}$, and ZIF-67 derived carbons also had particles with graphite carbon shells (see Figure 5.3), but no CNTs were observed. This suggests that there is an optimum molar ratio of zinc to cobalt ions in bimetallic ZIFs to promote the growth of CNTs on the surface. This will be discussed in more detail in Figure 5.5. All HRTEM observations show once again the importance of the cobalt content in the formation of bimetallic ZIF derived carbon, as discussed in connection with the XRD results (Figure 5.3).

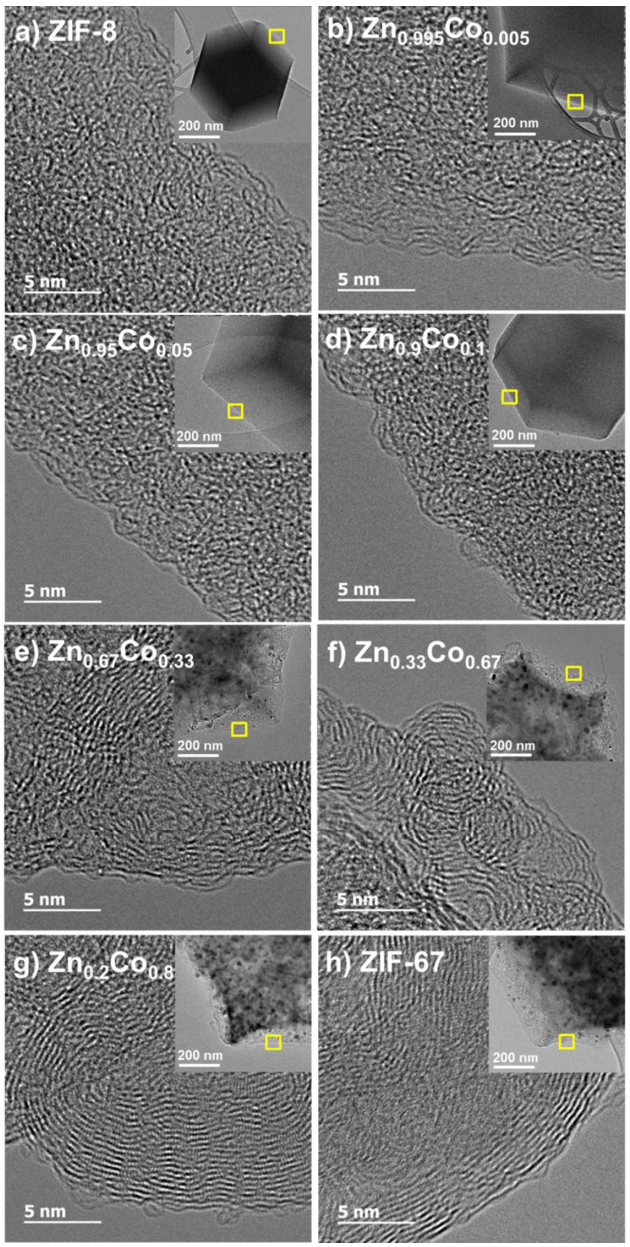

Figure 5.4. HRTEM images of (a) ZIF-8 derived carbon; (b) bimetallic ZIF derived carbons with different molar ratios of zinc to cobalt ions with (b) $Zn_{0.995}$·$Co_{0.009}$, (c) $Zn_{0.95}$·$Co_{0.05}$, (d) $Zn_{0.9}$·$Co_{0.1}$, (e) $Zn_{0.67}$·$Co_{0.33}$, (f) $Zn_{0.33}$·$Co_{0.67}$, and (g) $Zn_{0.2}$·$Co_{0.8}$: and (h) ZIF-67 derived carbon.

The CNT structure that appears in the $Zn_{0.33}$·$Co_{0.67}$ derived carbon is shown in Figure 5.5 and should be discussed in more detail. Figure 5.5a is a schematic illustration of the CNT structure formed on the $Zn_{0.33}$·$Co_{0.67}$ derived hierarchical carbon structure. This can be further confirmed by HRTEM images (Figure 5.5b and 5.5c). From the images, the formation of CNTs basically improves the electrical conductivity and might provide some voids/space between

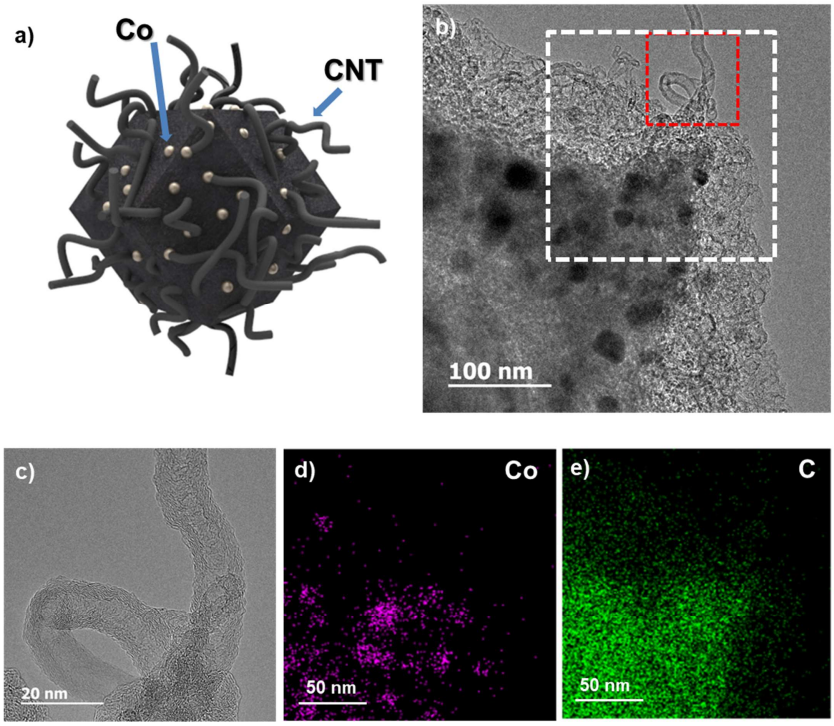

Figure 5.5. (a) Schematic illustration of bimetallic ZIF derived carbon with zinc to cobalt molar ratio of $Zn_{0.33}$·$Co_{0.67}$. (b) TEM image of $Zn_{0.33}$·$Co_{0.67}$ bimetallic ZIF derived carbon. (c) High resolution TEM image of CNT structure in the area enclosed by the red dashed line in (b). Element mapping images of (d) cobalt and (e) carbon in the area enclosed by the white dashed line in (b).

$Zn_{0.33}$·$Co_{0.67}$-derived carbons. It has been reported that CNTs are formed due to the cobalt nanoparticles acting as a catalyst on the surface.[16] The energy dispersive X-ray spectroscopy (EDX) of the white square in Figure 5.5b shows that most of the $Zn_{0.33}$·$Co_{0.67}$ derived carbon is well carbonized, but a small fraction of cobalt particles still exist. In contrast, zinc nanoparticles (not shown here) have almost disappeared due to their low vaporization temperature. This confirms that cobalt element plays a key role in the existing of CNTs.

The porosity of bimetallic ZIF derived carbons with different molar ratios of zinc to cobalt ions was investigated using nitrogen adsorption - desorption isotherms. In Figure 5.6a, sharp nitrogen uptake at $P/P_0 < 0.1$ can be related to the strong nitrogen adsorption in micropores. We clearly observed that the ZIF-8, $Zn_{0.995}$·$Co_{0.005}$, $Zn_{0.95}$·$Co_{0.05}$, and $Zn_{0.9}$·$Co_{0.1}$ derived carbon samples show much sharper nitrogen uptake compared to the $Zn_{0.67}$·$Co_{0.33}$, $Zn_{0.33}$·$Co_{0.67}$,

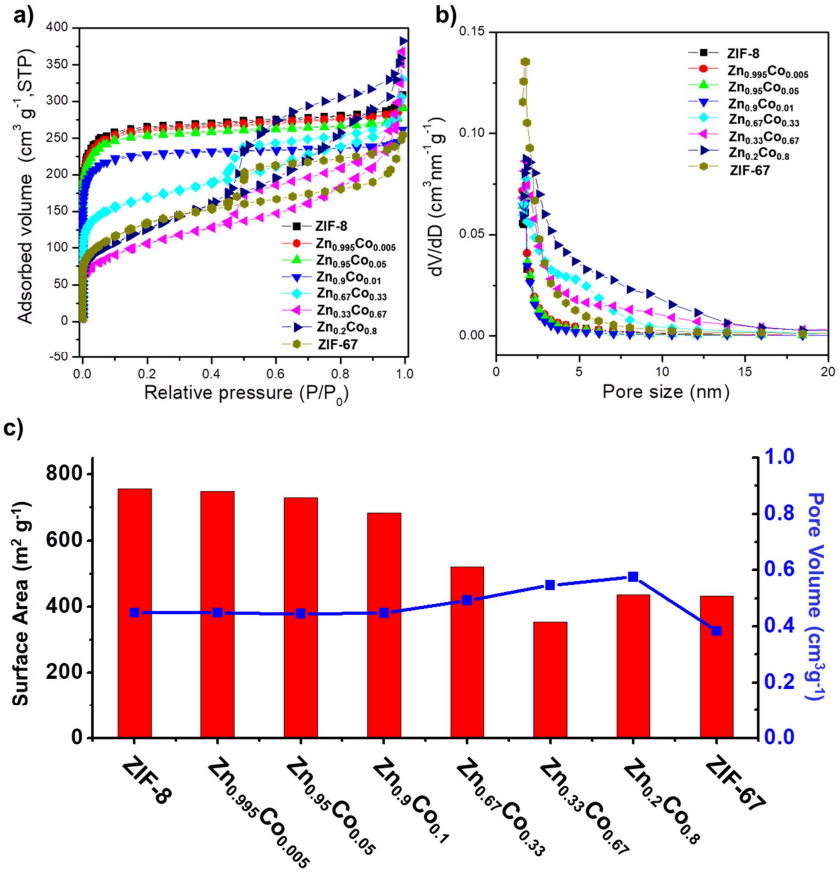

Figure 5.6. (a) N2 adsorption-desorption isotherms results, (b) pore size distribution results, and (c) surface area and pore volume graph of ZIF-8, bimetallic ZIF derived carbons, which have zinc to cobalt molar ratios of $Zn_{0.995}$·$Co_{0.009}$, $Zn_{0.95}$·$Co_{0.05}$, $Zn_{0.9}$·$Co_{0.1}$, $Zn_{0.67}$·$Co_{0.33}$, $Zn_{0.33}$·$Co_{0.67}$, $Zn_{0.2}$·$Co_{0.8}$, and ZIF-67 derived carbon.

$Zn_{0.2}$·$Co_{0.8}$, and ZIF-67 derived carbon samples. As a result, zinc ions as an additive can generate a majority population of micropores, rather than mesopores. All samples show gradual nitrogen uptake in the intermediate relative pressure region between 0.3 and 0.9, indicating the presence of mesopores with a broad size distribution. Most interestingly, the $Zn_{0.67}$·$Co_{0.33}$, $Zn_{0.33}$·$Co_{0.67}$, $Zn_{0.2}$·$Co_{0.8}$, and ZIF-67 derived samples show obvious hysteresis loops. This is mainly due to the increase in widespread mesopores.

The pore size distributions show that the majority population of micropores gradually changes to mesopores with increasing cobalt ions in the bimetallic ZIF derived carbon, as shown in Figure 5.6b. From ZIF-8 derived carbon to the bimetallic ZIF one derived from $Zn_{0.9}$·$Co_{0.1}$,

most pores are less than 2 nm in size. We argue that the surface area of each sample is strongly related to the molar ratio of cobalt to zinc in bimetallic ZIFs. Figure 5.6c also shows the pore volume and specific surface area of ZIF-8, ZIF-67, and bimetallic ZIF derived carbons with various molar ratio of zinc to cobalt ions. The specific surface areas decrease from ZIF-8 (756 $m^2 \cdot g^{-1}$), to $Zn_{0.995} \cdot Co_{0.005}$ (748 $m^2 \cdot g^{-1}$), $Zn_{0.95} \cdot Co_{0.05}$ (729 $m^2 \cdot g^{-1}$), $Zn_{0.9} \cdot Co_{0.1}$ (683 $m^2 \cdot g^{-1}$), $Zn_{0.67} \cdot Co_{0.33}$ (520 $m^2 \cdot g^{-1}$), and $Zn_{0.33} \cdot Co_{0.67}$ (354 $m^2 \cdot g^{-1}$). It then slightly increases in $Zn_{0.2} \cdot Co_{0.8}$ (436 $m^2 \cdot g^{-1}$) and ZIF-67 (432 $m^2 \cdot g^{-1}$). In contrast, pore volume tends to decrease as the molar ratio of zinc ions increases. In other words, on decreasing the molar ratio of zinc ions to cobalt ions, the pore size of the thus-formed carbon structure increases, thereby reducing the surface area and increasing the pore volume. This suggests that carbon structures with the desired characteristics such as optimized surface area and pore size can be formed by adjusting the molar ratio of zinc to cobalt ions in the synthesis of Zn/Co bimetallic ZIFs

Strategically designed bimetallic ZIF derived carbons with different molar ratios of cobalt to zinc ions were synthesized to clearly understand their material properties for various applications. In this system, the role of zinc ions is to create micropores and maintain a rhombic dodecahedral particle shape without any morphological damage. The role of cobalt ions is to form cobalt nanoparticles, which act as catalytic sites to activate CNTs growth in the carbon. This can improve the electrical conductivity and the amount of space between ZIF derived carbons. By controlling other factors for bimetallic ZIFs, we expect that this type of functional carbon will be highly attractive for Li-metal anode materials

.

5.5. Additional Study: The Effect of Carbonization Temperature on Zeolitic Imidazolate Framework Derived Carbon Nanoarchitecture

Porous carbon nanoarchitectures have attracted significant attention as promising candidates for an application such as energy storage and harvesting[39-41]. Especially, MOFs, consist of metal ions and organic linkers, are very attractive due to their diversity. The properties of MOFs such as pore size, surface area, and stability are easily controlled by adjusting the kinds of metal ions or organic linkers for the purpose[1,42,43]. Zeolitic imidazolate frameworks (ZIFs) as a kind of MOFs, consist of imidazole as organic linkers, show the outstanding structural and chemical stability due to its zeolitic structure. Especially, porous carbon nanoarchitecture derived from ZIF-8, made with Zinc ions (Zn^{2+}) and 2-methylimidazole (2-MIM), have received considerable attention due to its easy-synthesis, large pore volume, and high surface area[12].

ZIF-8 can be directly carbonized into nanoporous carbon architecture without secondary carbon sources. The carbonization conditions greatly affect the properties of carbon nanoarchitecture, such as elemental porosity, crystallinity, and electrical conductivity[44,45]. In this work, we controlled the carbonization temperatures (800 ºC and 1000 ºC) of ZIF-8 and expected the dramatic differences in carbon architecture. Higher carbonization temperature induced the decrease of Zn content due to the boiling point of Zn (907 ºC), but it dramatically increased pore volume and electrical conductivity. We can adjust the properties of ZIFs-derived carbon nanoarchitecture for the purpose by controlling the carbonization temperature. For example, as our previous research, large pore volume and good electrical conductivity are the essential prerequisites as the host materials of Li-metal storage[46-48]. Therefore, we can expect that carbon nanoarchitecture under higher carbonization temperature will be suitable for stable host materials.

A schematic illustration of the synthetic process for ZIF-8 and ZIF-8-derived carbon nanoarchitecture is shown in Figure 5.7. Typically, ZIF-8 has a thermodynamically stable rhombic dodecahedral shape with exposed twelve {110} facets[49].

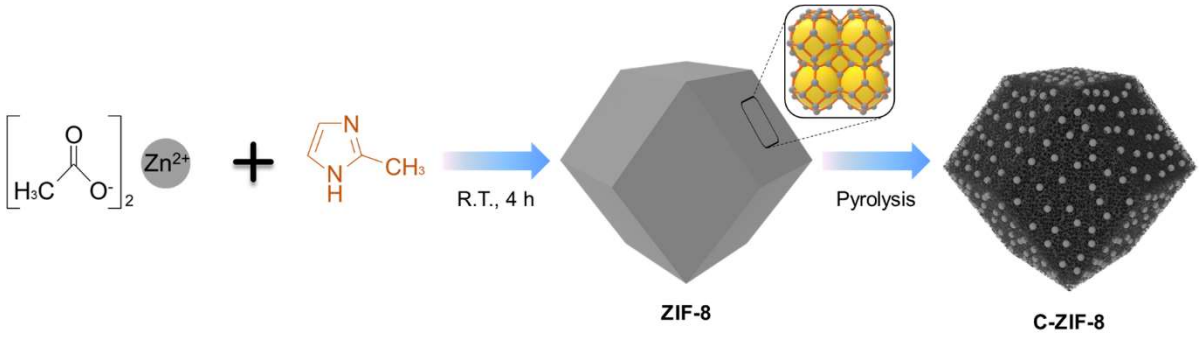

Figure 5.7. Schematic diagram representing the synthetic process.

As-prepared ZIF-8 shows the excellent uniformity with about 600 nm in size (Figure 5.8a). The carbonization process is conducted at 800 ºC (800C-ZIF-8) and 1000 ºC (1000C-ZIF-8) under Ar atmosphere to compare the effect of carbonization temperature on the properties of ZIF-derived carbon nanoarchitecture. Even after the carbonization process, both 800C-ZIF-8 and 1000C-ZIF-8 retain its polyhedral shape with slight size reduction compared to original ZIF-8 crystal (Figure 5.8b-5.8e). Besides, according to Raman spectra, both ZIF-8-derived nanoarchitectures are made with amorphous carbon structures (Figure 5.9)[50]. Elemental contents, however, showed remarkable differences depending on the carbonization temperature (Figure 5.8f-5.8h). In the case of 800C-ZIF-8, there is much nitrogen (N), oxygen (O), and Zn. On the other hand, 1000C-ZIF-8 almost consists of C with a little amount of N, O, and Zn. Especially, Zn rarely exists in the 1000C-ZIF-8 because Zn is evaporated during the carbonization process due to its low boiling point (907 ºC).

Given the elemental contents of 800C-ZIF-8 and 1000C-ZIF-8, we can expect that the size of 1000C-ZIF-8 is smaller than 800C-ZIF-8. We can also infer that 1000C-ZIF-8 is lighter than

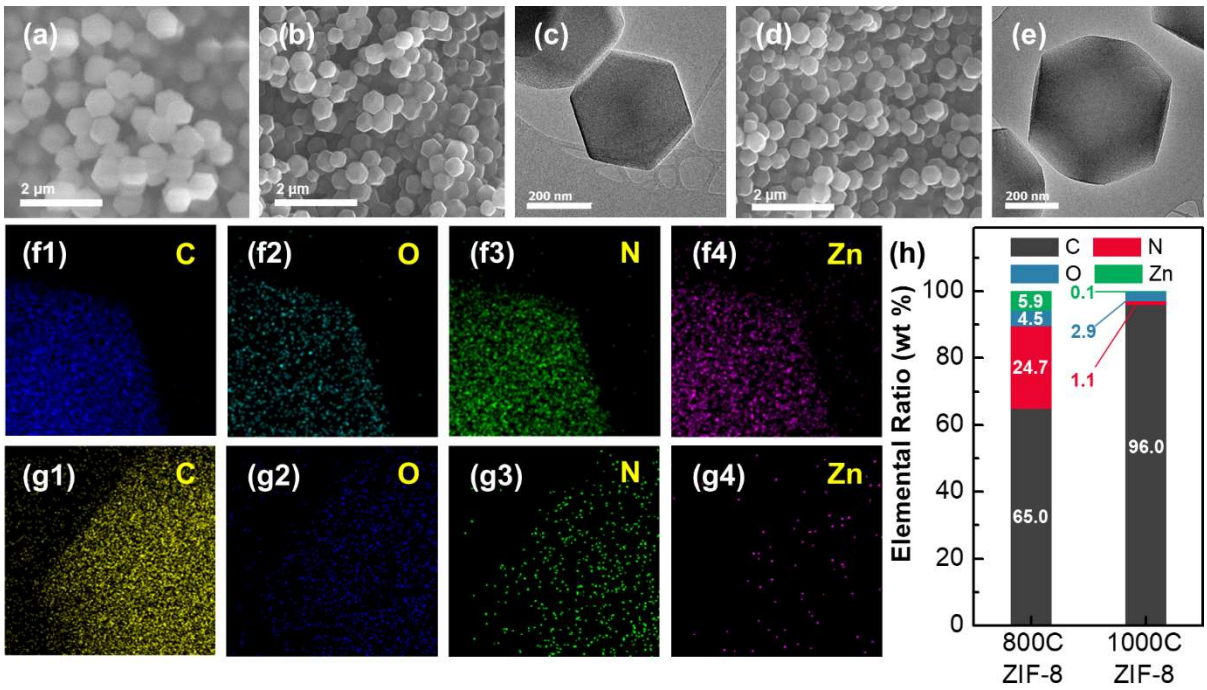

Figure 5.8. Low magnification SEM images of (a) ZIF-8, (b) 800C-ZIF-8, and (d) 1000C-ZIF-8. Bright field TEM (BF-TEM) images of (c) 800C-ZIF-8 and (e) 1000C-ZIF-8. High-angle annular dark field-scanning TEM (HAADF-STEM) elemental mapping images of (f) 800C-ZIF-8 and (g) 1000C-ZIF-8. (h) The elemental ratio of ZIF-8 derived carbon structures at 800 ºC and 1000 ºC of temperature.

800C-ZIF-8 because there is no heavy element such as Zn. As shown in Figure 5.10a and 5.10b, our expectations are well fit with real experimental results. As estimated from SEM (Figure 5.8b and 5.8d), the average size of each ZIF-8-derived carbon nanoarchitecture is estimated to

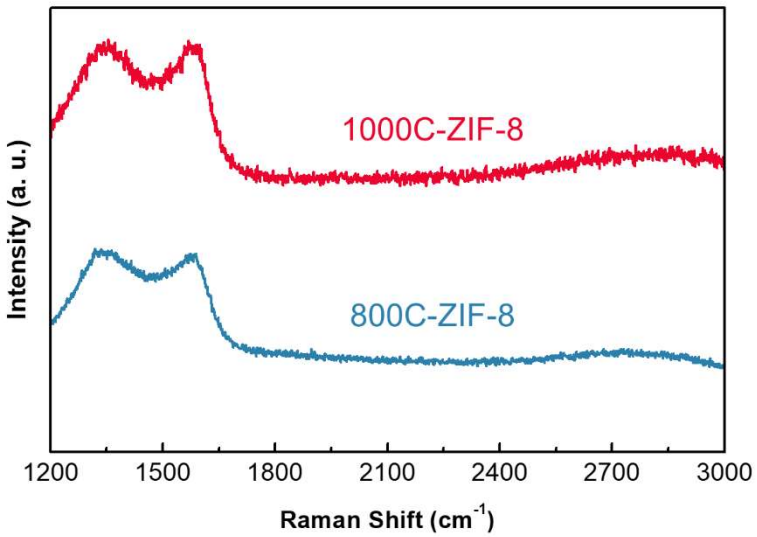

Figure 5.9. Raman spectra of 800C-ZIF-8 and 1000C-ZIF-8.

be 510 nm and 460 nm, which shows the size difference of about 10 % . The electrical conductivity and density of as-prepared powder-type samples were confirmed under 64 MP of pressure. The difference in density is about 25 %, which is resulted from the difference between elemental contents. The electrical property is dramatically improved via carbonization under higher temperature even with less Zn metal. The electrical conductivity of 1000C-ZIF-8 is more than two orders higher than that of 800C-ZIF-8.

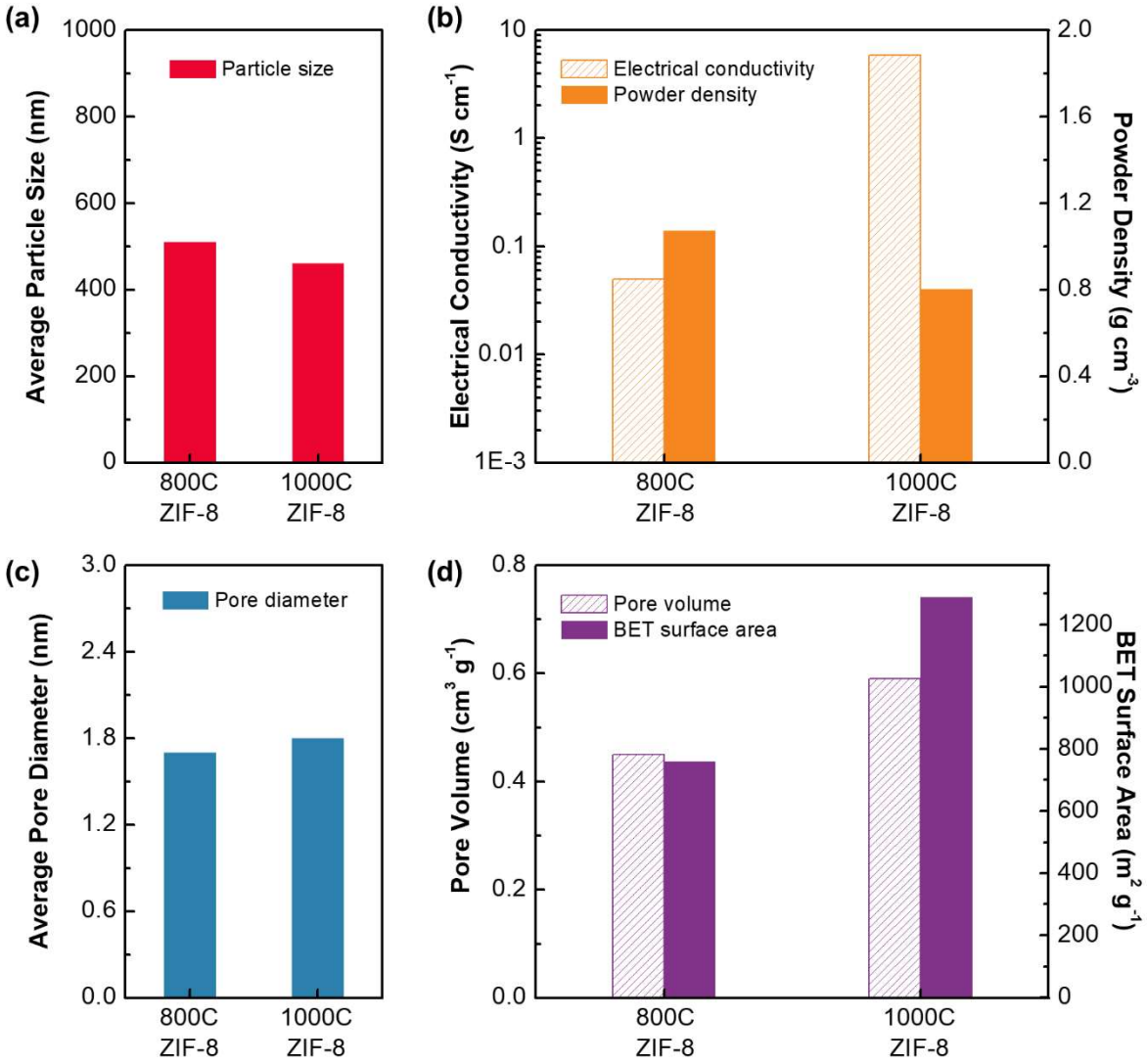

Figure 5.10. (a) Average particle size of 800C-ZIF-8 and 1000C-ZIF-8. (b) Electrical conductivity and powder density at 64 MP. (c) The average pore diameter and (d) pore volume and BET surface area of each porous carbon nanoarchitecture.

The pore-related structural information is obtained from BET and BJH methods. Two ZIF-8-derived carbon nanoarchitectures have a similar average pore diameter regardless of carbonization temperature. The average pore diameters are estimated to be 1.7 nm and 1.8 nm, respectively, and both ZIF-8-derived carbon nanoarchitectures are microporous structure (Type I according to the IUPAC classification) estimated from N_2 adsorption/desorption isotherms (Figure 5.11)[50]. There are, however, a dramatic increase of pore volume and surface area under higher carbonization temperature. The pore volume and BET surface area of 800C-ZIF-8 are 0.45 cm^3 g^{-1} and 760 m^2 g^{-1}. On the other hand, the pore volume and BET surface area of 1000C-ZIF-8 are 0.59 cm^3 g^{-1} and 1288 m^2 g^{-1}, which increased by about 30 % and 70 % compared to 800C-ZIF-8, respectively. These differences can be attributed to the evaporation of Zn-related species during a higher carbonization process. The area where Zn existed in the ZIF-8 crystal produces additional micropores and induces a higher surface area and a larger pore volume. In summary, the carbonization process of ZIF-8 at 1000 ºC shows a high electrical conductivity, pore volume, and surface area compared to carbonization at 800 ºC. Thus, the higher temperature process would be more suitable for some applications where electrical conductivity is essential such as electrical/electrochemical fields. For example, as previous our

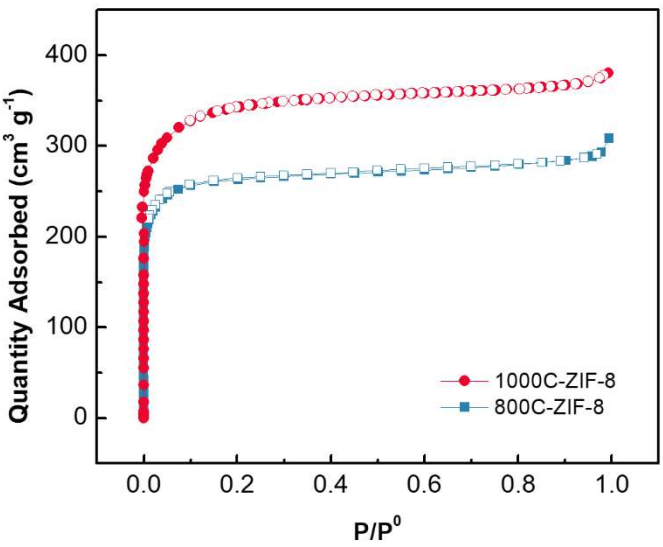

Figure 5.11. N2 adsorption/desorption isotherms of 800C-ZIF-8 and 1000C-ZIF-8.

research about host materials of Li-metal storage, the pore volume, surface area, and electrical conductivity are essential requirements for host materials to store Li-metal stably. In terms of these requirements, a higher temperature carbonization process is suitable for satisfying the basic conditions.

We prepared two kinds of ZIF-8-derived porous carbon nanoarchitectures under different carbonization temperatures. Higher temperature carbonization induced more reduction of polyhedral size and powder density. However, the higher temperature ZIF-8-derived carbon nanoarchitecture showed significantly increased electrical conductivity, pore volume, and surface area compared to the lower temperature sample. Since the carbonization temperature can control physical/electrical properties of carbon nanoarchitecture, we can choose the suitable carbon materials for each application via selecting the process temperature.

5.6. Perspective: Zeolitic Imidazolate Framework (ZIF)-derived Nanoarchitectures for Lithium Metal Storage Medium

Figure 5.12 is an illustration of various ZIF-derived carbons, which were originally derived from different kinds of ZIF crystals, single ZIFs (Zn, Co), bimetallic ZIFs (Zn/Co hybrid), and hollow ZIFs (tannic acid etching). For practical energy storage applications, it is necessary to control their surface area/pore volume, particle size/shape, monodispersity, and element doping.

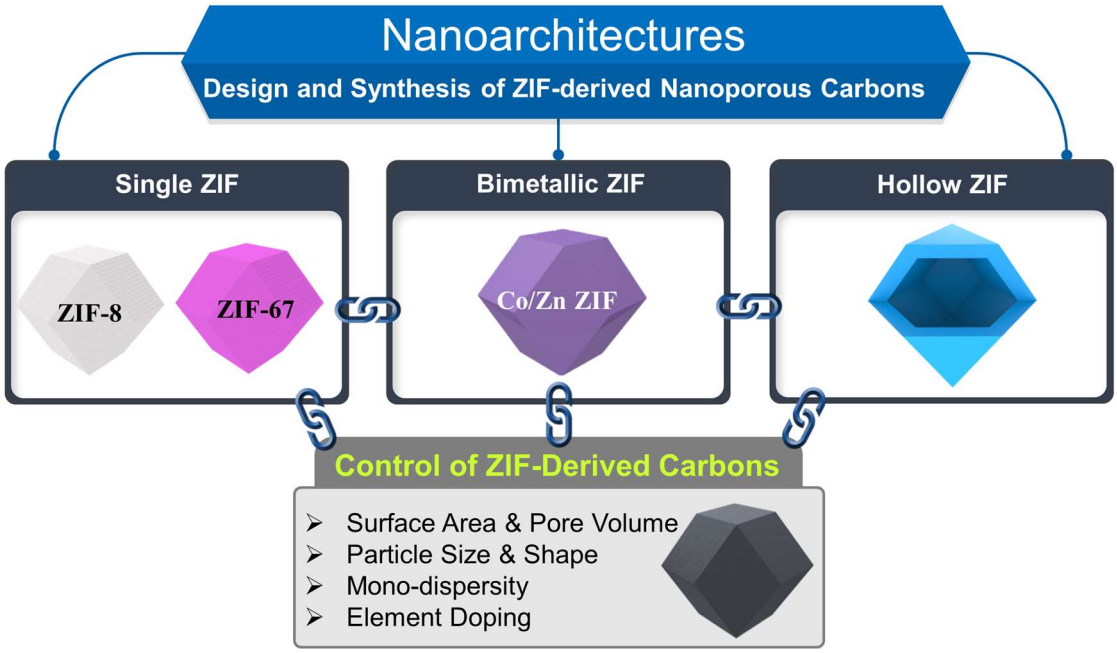

Figure 5.12. Illustration of various types of ZIF crystals with their carbonized forms.

Based on our results regarding the carbons derived from ZIF-8, ZIF-67, and bimetallic ZIF,[41,52] each of these properties can be comfirmed and compared, as shown in Table 5.1.

Recently, the development of Li-metal storage anodes is under the spotlight among Li-ion battery researchers because it provides much higher energy density compared to the conventional graphite-based anode system.[53] The prevention of Li dendritic growth, however, as well as a facile synthesis for reducing production costs, should be considered when exploring

Properties	ZIF-8-C	ZIF-67-C	Bimetallic ZIF-C
Surface area (m^2/g)	765	354	432
Pore volume (cm^3/g)	0.45	0.38	0.55
Pore size	micropores	mesopores	micropores /mesopores
Particle size[a] (nm)	500	1200	500
Electrical Conductivity (S/cm)	< 0.1	~ 10	> 10

[a] controllable by simple change of synthetic conditions

Table 5.1. Illustration Intrinsic properties of each type of ZIF-derived carbon.

an appropriate Li-metal storage medium. In this respect, ZIF-derived carbons could pave the way towards the practical application of Li-metal anodes, due to their large pore volume and easy adjustable properties.[54]

Meanwhile, the theoretical volumetric capacity of Li-metal is 2062 mAh cm^{-3} (3861 mAh g^{-1} × 0.534 g cm^{-3})[55] Based on this, the theoretical gravimetric capacity of a ZIF-derived carbon when it reaches full capacity for storing Li-metal in its pores, including Li-ion intercalation into carbon, can be calculated by the simple equation below:

$$\text{Gravimetric capacity of a ZIF-derived carbon (mAh g}^{-1}) =$$

$$[2062\ (\text{mAh cm}^{-3}) \times \text{pore volume (cm}^3\ \text{g}^{-1})] + 372\ (\text{mAh g}^{-1}) \quad (1)$$

As shown in Figure 5.13, the calculated theoretical capacities of ZIF-67-C, ZIF-8-C, and bimetallic ZIF-C are 1156, 1300, and 1506 mAh g^{-1}, respectively. In addition, the theoretical gravimetric capacity of hollow ZIF-carbon can be estimated by finding the macroporous hollow volume and dividing it by the total volume of the material. In previous studies, hollow ZIF-carbons contained approximately 20 to 50 % hollow macropore volume.[56,57] Thus, they

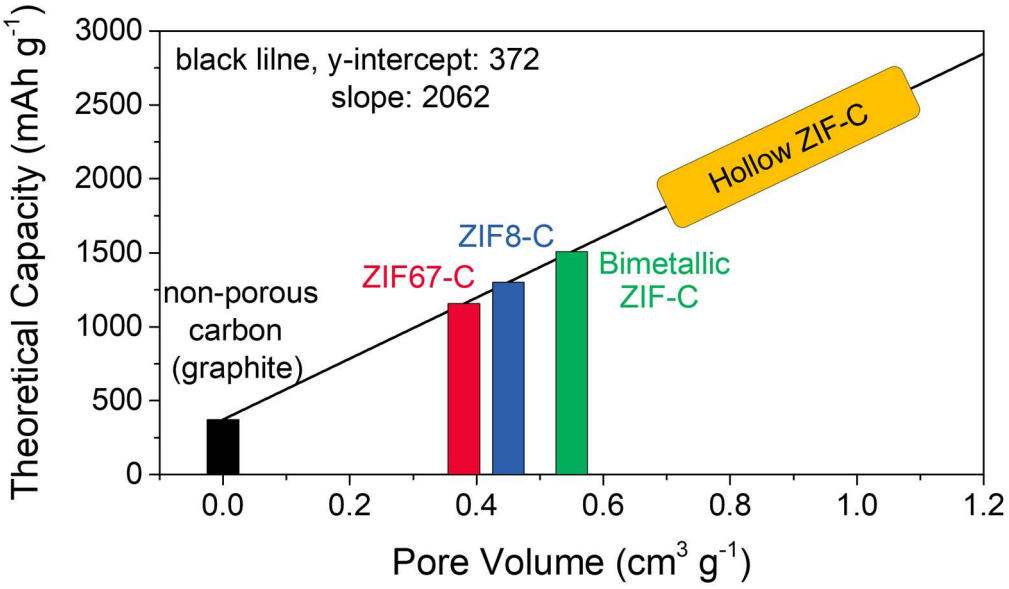

Figure 5.13. Theoretical capacities of each type of ZIF-derived carbon.

had 0.7 to 1.1 cm^3 g^{-1} of total pore volume, including micro-, meso-, and even macropore volume, and consequently, the hollow ZIF-carbon showed higher capacity than the other types of ZIF-derived carbons.

Nevertheless, the adequacy of its electrical conductivity for inducing a smooth electrochemical reaction is not guaranteed, and its etching process with consequent low production yield will decrease the production efficiency. On the other hands, bimetallic ZIF-carbon shows high electrical conductivity with reasonable pore volume, as well as having a relatively facile synthetic process. For this reason, it is necessary to consider every relevant factor comprehensively, when exploring the optimum ZIF-carbon Li-metal storage medium.

5.7. Conclusion

To sum up, in order to discover ZIF-derived carbons that are suitable Li-metal storage media, i) large pore volume, ii) suitable pore size, iii) acceptable electrical conductivity, iv) cost effectiveness, and v) particle size and surface area that are fit for purpose should be considered concurrently. From this aspect, we are optimistic about the development of an advanced Li-metal storage medium through devoting research efforts to studying the ZIF-derived carbons in the future. Moreover, with the exceptionally easily adjustable properties of ZIFs, it is also expected that the role of ZIF-derived carbons will be increased with the development of Li-metal anode batteries.

5.8. References

[1] K. S. Park, Z. Ni, A. P. Côté, J. Y. Choi, R. Huang, F. J. Uribe-Romo, H. K. Chae, M. O'Keeffe, O. M. Yaghi, *Proc. Natl. Acad. Sci. USA* **2006**, 103, 10186.

[2] R. R. Salunkhe, J. Tang, N. Kobayashi, J. Kim, Y. Ide, S. Tominaka, J. H. Kim, Y. Yamauchi, *Chem. Sci*. **2016**, 7, 5704.

[3] W. Chaikittisilp, M. Hu, H. Wang, H. S. Huang, T. Fujita,K. C. Wu, L. C. Chen, Y. Yamauchi, K. Ariga, *Chem. Commun*. **2012**, 48, 7259.

[4] H. Wang, Q.-L. Zhu, R. Zou, Q. Xu, Chem 2017, 2, 52.

[5] V. Malgras, Q. Ji, Y. Kamachi, T. Mori, F. –K. Shieh, K. C. –W. Wu, K. Ariga, Y. Yamauchi, *Bull. Chem. Soc. Jpn.* **2015**, 88, 1171.

[6] T. Yamada, M. Sadakiyo, A. Shigematsu, H. Kitagawa, *Bull. Chem. Soc. Jpn.* **2016**, 89, 1.

[7] Y. Guo, J. Tang, R. R. Salunkhe, Z. A. Alothman, Md. S. A. Hossain, V. Malgras, Y. Yamauchi, *Bull. Chem. Soc. Jpn.* **2017**, 90, 939.

[8] M. Ishidoshiro, H. Imoto, K. Naka, *Bull. Chem. Soc. Jpn.* **2016**, 89, 1057.

[9] F. –K. Shieh, S. –C. Wang, C. –I. Yen, C. –C. Wu, S. Dutta, L. –Y. Chou, J. V. Morabito, P. Hu, M. –H. Hsu, K. C. –W. Wu, C. –K. Tsung, *J. Am. Chem. Soc*. **2015**, 137, 4276.

[10] F. –S. Liao, W. –S. Lo, Y. –S. Hsu, C. –C. Wu, S. –C. Wang, F. –K. Shieh, J. V. Morabito, L. –Y. Chou, K. C. –W. Wu, C. –K. Tsung, *J. Am. Chem. Soc*. **2017**, 139, 6530.

[11] Y. V. Kaneti, J. Tang, R. R. Salunkhe, X. Jiang, A. Yu, K. C. –W. Wu, Y. Yamauchi, *Adv. Mater.* **2017**, 29, 1604898.

[12] R. R. Salunkhe, Y. V. Kaneti, J. Kim, J. H. Kim, Y. Yamauchi, *Acc. Chem. Res*. **2016**, 49, 2796.

[13] S. Dang, Q.–L. Zhu, Q. Xu, *Nature Reviews Materials* **2017**, 3, 17075.

[14] W. Lu, Z. Wei, Z. –Y. Gu, T. –F. Liu, J. Park, J. Park, J. Tian, M. Zhang, Q. Zhang, T. Gentle III, M. Bosch, H. –C. Zhou, *Chem. Soc. Rev.*, **2014**, 43, 5561.

[15] A. V. Vinogradov, H. Z. Hertling, E. H. Hawkins, A. V. Agafonov, G. A. Seisenbaeva, V. G. Kessler, V. V. Vinogradov, *Chem. Commun*. **2014**, 50, 10210

[16] S. Goswami, L. Ma, A. B. F. Martinson, M. R. Wasielewski, O. K. Farha, J. T. Hupp, *ACS Appl. Mater. Interfaces* **2016**, 8, 30863

[17] Y.-J. Li, J.-M. Fan, M.-S. Zheng, Q.-F. Dong, *Energy Environ. Sci*. **2016**, 9, 1998

[18] B. Yang, H. Liu, R. Lv, H. Li, X. Fu, J. Su, X. Liu, W. Gu, *Bull. Chem. Soc. Jpn.*, **2018**, 91, 548.

[19] J. Kim, C. Young, J. Lee, M.-S. Park, M. Shahabuddin, Y. Yamauchi, J. H. Kim, *Chem. Commun*. **2016**, 52, 13016.

[20] M. Ding, W. Shi, L. Guo, Z. Y. Leong, A. Baji, H. Y. Yang, *J. Mater. Chem. A* **2017**, 5, 6113

[21] Y. Wu, Z. Zhang, S. Bandow, K. Awaga, *Bull. Chem. Soc. Jpn.* **2017**, 90, 1382.

[22] K. Inoue, *Bull. Chem. Soc. Jpn.* **2016**, 89, 1416.

[23] K. C. –W. Wu, Y. Yamauchi, *J. Mater. Chem.* **2012**, 22, 1251.

[24] H. Kataoka, T. Nakanishi, S. Omagari, Y. Takabatake, Y. Kitagawa, Y. Hasegawa, *Bull. Chem. Soc. Jpn.* **2016**, 89, 103.

[25] Y. Tobe, K. Tahara, S. D. Feyter, *Bull. Chem. Soc. Jpn.* **2016**, 89, 1277.

[26] T. Wang, Z. Kou, S. Mu, J. Liu, D. He, I. S. Amiinu, W. Meng, K. Zhou, Z. Luo, S. Chaemchuen, F. Verpoort, *Adv. Funct. Mater.* **2018**, 28, 1705048.

[27] S. Kitagawa, M. Munakata, T. Tanimura, *Inorg. Chem.*,**1992**, 31, 1714.

[28] O. M. Yaghi, G. Li, H. Li, *Nature*, **1995**, 378, 703.

[29] O. M. Yaghi, H. Li, *J. Am. Chem. Soc*, **1995**, 117, 10401.

[30] H. Furukawa, K. E. Cordova, M. O'Keffe, O. M. Yaghi, *Science*, **2013**, 341, 1230444.

[31] N. L. Rosi, J. Eckert, M. Eddaoudi, D. T. Vodak, J. Kim, M. O'Keffe, O. M. Yaghi, *Science*, **2003**, 300, 1127.

[32] K. –S, Lin, A. K. Adhikari, C. –N. Ku, C. –L. Chiang, H. Kuo, *Int J Hydrogen Energy*, **2012**, 37, 13865.

[33] N. –L. Liu, S. Dutta, R. R. Salunkhe, T. Ahamad, S. M. Alshehri, Y. Yamauchi, C. –H. Hou, K. C. –W. Wu, *Sci. Rep.* **2016**, 6, 28847.

[34] F. –K. Shieh, S. –C. Wang, S. –Y. Leo, K. C. –W. Wu, *Chem. Eur. J*. **2013**, 19, 11139.

[35] S. Gadipelli, T. Zhao, S. A. Shevlin, Z. Guo, *Energy Environ. Sci*., **2016**, 9, 1661.

[36] J. Tang, R. R. Salunkhe, H. Zhang, V. Malgras, T. Ahamad, S. M. Alshehri, N. Lobayashi, S. Tominaka, Y. Ide, J. H. Kim, Y. Yamauchi, *Sci. Rep*. **2016**, 6, 30295.

[37] M. Hu, J. Reboul, S. Furukawa, N. L. Torad, Q. Ji, P. Srinivasu, K. Ariga, S. Kitagawa, Y. Yamauchi, *J. Am. Chem. Soc*. **2012**, 134, 2864.

[38] S. J. Yang, T. Kim, J. H. Im, Y. S. Kim, K. Lee, H. Jung, C. R. Park, *Chem. Mater*. **2012**, 24, 464.

[39] J. Kim, J. H. Kim, K. Ariga, *Joule* **2017**, 1, 739.

[40] J. Kim, C. Young, J. Lee, Y.-U. Heo, M.-S. Park, M. S. A. Hossain, Y. Yamauchi, J. H. Kim, *J. Mater. Chem. A* **2017**, 5, 15065.

[41] S. A Han, J. Lee, K. Shim, J. Lin, M. Shahabuddin, J.-W. Lee, S.-W. Kim, M.-S. Park, J. H. Kim, *Bull. Chem. Soc. Jpn.* **2018**, 91, 1474.

[42] A. Phan, C. J. Doonan, F. J. Uribe-Romo, C. B. Knobler, M. O'Keeffe, O. M. Yaghi, *Acc. Chem. Res.* **2010**, 43, 58.

[43] R. Banerjee, A. Phan, B. Wang, C. Knobler, H. Furukawa, M. O'Keeffe, O. M. Yaghi, *Science* **2008**, 319, 939.

[44] R. R. Salunkhe, J. Tang, Y. Kamachi, T. Nakato, J. H. Kim, Y. Yamauchi, *ACS Nano* **2015**, 9, 6288.

[45] Y. Hyeon, S.-H. Jung, W. Jang, M. Kim, B.-S. Kim, J.-H. Lee, K. R. Nandanapalli, N. Jung, D. Whang, *ACS Appl. Mater. Interfaces* **2019**, 11, 5037.

[46] Y. Hyeon, J. Lee, H. Qutaish, S. A Han, S. H. Choi, S. W. Moon, M.-S. Park, D. Whang, J. H. Kim, *Energy Storage Mater.* **2020**, in press.

[47] J. Kim, J. Lee, J. Yun, S. H. Choi, S. A Han, J. Moon, J. H. Kim, J.-W. Lee, M.-S. Park, *Adv. Funct. Mater.* **2020**, 30, 1910538.

[48] L. Wang, X. Zhu, Y. Guan, J. Zhang, F. Ai, W. Zhang, Y. Xiang, S. Vijayan, G. Li, Y. Huang, G. Cao, Y. Yang, H. Zhang, *Energy Storage Mater.* **2018**, 11, 191.

[49] C. Avci, J. Arinez-Soriano, A. Carne-Sanchez, V. Guillerm, C. Carbonell, I. Imaz, D. Maspoch, *Angew. Chem., Int. Ed.* **2015**, 127, 14625.

[50] A. C. Ferrari, J. Robertson, *Phys. Rev. B* 61 **2000**, 61, 14095.

[51] J. McEwen, J.-D. Hayman, A. O. Yazaydin, *Chem. Phys.* **2013**, 412, 72.

[52] Kim, J.; Young, C.; Lee, J.; Park, M. -S.; Shahabuddin, M.; Yamauchi, Y.; Kim, J. H. *Chem. Commun.* **2016**, 52, 13016.

[53] Lin, D.; Liu, Y.; Cui, Y. *Nat. Nanotech.* **2017**, 12, 194.

[54] Furukawa, H.; Cordova, K. E.; O'keeffe, M.; Yaghi, O. M. *Science* **2013**, 341, 1230444.

[55] Li, S.; Jiang, M.; Xie, Y.; Xu, H.; Jia, J.; Li, J. *Adv. Mater.* **2018**, 30, 1706375.

[56] Zhang, W.; Jiang, X.; Zhao, Y.; Carné-Sánchez, A.; Malgras, V.; Kim, J.; Kim, J. H.; Wang.

[57] Yang, D. -H.; Zhou, H. -Y; Liu, H.; Han, B. -H. *iScience* **2019**, 13, 243.

Chapter 6. Structurally Stabilized Lithium-Metal Anode via Surface Chemistry Engineering

6.1. Abstract

Dendrite-free lithium (Li) has been the primary issue for the practical application of metallic Li anode. Repeated Li plating/stripping is known to inevitably lead to severe volume changes and gradual Li dendrite growth, eventually resulting in irreversible Li (called dead-Li) as an unexpected feature. In order to avoid the dead-Li, a lithiophilic surface is highly desirable and a nanoarchitectured host for metallic Li is also required. Herein, cobalt-embedded, mesoporous, nitrogen-doped graphite (N-doped graphite) is strategically proposed as new innovative Li-metal storage host. After tuning the surface chemistry, the material shows high Li ion affinity as well as a highly lithiophilic surface, which is attributed to the low formation energy of N-doped graphite, strongly supported by density functional theory calculations. As a result, the desirable anode shows excellent electrochemical performance with high Li-metal reversible capacity and even stable long-term cyclability with no dead-Li formation. Our findings pave the way to optimize the Li-metal host up to the limit of the theoretical capacity.

6.2. Introduction

Metallic lithium (Li-metal), the Holy Grail of lithium battery anodes, has been regarded as the most attractive anode material among battery researchers[1-3]. The reason is because it has the highest theoretical gravimetric and volumetric capacities (3860 mA h g^{-1} and 2061 mA h cm^{-3}) as well as the lowest redox potential (-3.04 V vs. the standard hydrogen electrode) among all other anode materials[4]. Moreover, the development of stable Li-metal anode is an essential precondition for the so-called next-generation Li batteries, such as Li-sulfur and Li-air batteries, which can offer advanced energy densities compared to the conventional Li-ion battery system[5].

Unfortunately, as of now, there are still technical difficulties for putting Li-metal into practical usage for Li battery anode due to its perplexing problems that remain to be solved. First, because only Li-metal itself plays the role of an active material, severe volume changes occur in the case of the hostless anode when Li-metal undergoes repeated plating and stripping. This reduces the mechanical strength of the electrode as well as leading to the continuous formation of new solid elelctrolyte interphase (SEI)[6]. Second, during plating, Li naturally forms needle-like structures known as whiskers (or dendrites), and they grow unceasingly during cycling. The growth of dendritic Li gives rise to electrical short-circuits and finally causes safety problems such as fires and explosions[7]. To overcome these difficulties, nowadays, various kinds of approaches have been explored, but all directed towards achieving an identical goal, namely, to make Li-metal stable by following three representative solutions: i) Adopting solid-state electolytes[8-12]; ii) Constructing artificial SEI layers[13-17]; and iii) Guided Li-metal growth in host frameworks[18-22].

Meanwhile, metal-organic frameworks (MOFs) have received great attention as attractive porous materials due to their high surface area, controllable pore size/volume, and facile synthesis[23,24]. The MOFs simply consist of metal ions and organic molecules, stitched together

through strong interactions. The important ways to modify their intrinsic properties are based on varying their metal precursors and linker geometries. Most of the transition metals in the periodic table can be used as candidates[25]. Representative examples are zeolitic imidazolate frameworks-8 and -67 (ZIF-8 and ZIF-67), which are composed of Zinc (Zn) and Cobalt (Co) metal ions, respectively, which are strongly coordinated by 2-methylimidazole (2-MIM) as the organic linker. These ZIFs are formed in rhombic dodecahedral shapes with a large cavity (11.6 Å)[26]. From these two types of ZIFs, typical nanoporous carbon can be obtained through calcination and chemical etching.

Based on our work on the MOFs, we have reported that the porous carbon host material derived from ZIF-8 can be a promising Li-metal storage candidate due to its large pore volume and sufficient high electrical conductivity[27]. Its Zn atoms play an effective role in increasing lithiophilicity and promoting stable Li-metal formation in the host. Moreover, dual-phase lithiation and metallization can be realized in a single anode electrode and, in consequence, this anode enables a large amount of Li storage. It is still necessary to strengthen its weak points, however, such as a less stable surface chemistry that causes unwanted dead-Li production.

Herein, as a further improved work, we propose highly stable cobalt nanoparticles embedded in nanoporous nitrogen doped graphite (Co@N-graphite), which is derived from a bimetallic ZIF (Zn/Co). This material shows high Li affinity as well as highly lithiophilic surface chemistry, which is attributable to the low formation energy of N-doped graphite. As a result, the anode shows excellent elelctrochemical performance with high Li-metal reversible capacity and even stable long-term cyclability with no dead-Li formation.

6.3. Experimental

6.3.1. DFT Calculations

All atomic simulations were performed in the density functional theory (DFT) calculation framework. Projector-augmented wave (PAW) pseudopotentials were used, as implemented in the Vienna *ab initio* simulation package (VASP)[48,49]. For the exchange-correlation functional, the Perdew-Burke-Ernzerhof (PBE) generalized gradient approximation (GGA) was employed[50]. To build amorphous carbon structures, we randomly sampled a distribution of 64 carbon atoms placed in a P1 cell with a size of $10 \times 6 \times 9$ Å^3, with periodic boundary conditions. The *ab-initio* molecular dynamics simulation was performed at 5000 K to randomize the initial crystalline configurations with gamma point sampling. A time step of 1.0 fs and 10000 overall simulation steps were used. For the standard computational parameters, the Brillouin zone sampling was set at $5 \times 5 \times 5$ for the graphite layer structure and $3 \times 3 \times 3$ for the amorphous carbon structure in the Monkhorst-Pack scheme. The atomic positions and cells were fully relaxed until each atomic force was less than 0.01 eV Å^{-1}. An energy cut-off of 500 eV was set for the plane wave basis points. To consider van der Waals interaction in the graphite layer, the DFT-D2 method were chosen in our DFT simulation. To model bilayer graphite, the layered structures were stacked in the form of AB stacking.

6.3.2. Materials Preparations

To synthesize the ZC and BZC series, specified atomic ratios of zinc acetate dihydrate (Merck)/cobalt acetate tetrahydrate (Merck) were dissolved in deionized water and then put into 2-methylimidazole (Merck) solution with stirring for 10 minutes. Each well mixed solution was kept at room temperature for 24 hours. Then the precipitates were filtered and collected after drying at 80 ℃ for 24 hours in a convection oven. The obtained powder was heated in a

tube furnace at 1000 ℃ for 6 hours in argon gas with a rampling rate of 5 ℃ min^{-1}. After that, the carbonized powder was washed twice in 1 M HCl solution and then washed several times in a large amount of deionized water. Then, the ZC and BZC series were finally obtained after drying at 80 ℃ for 24 hours in a convection oven.

6.3.3. Structural Characterizations

Microscopic obsevations were conducted by using a field emission scanning electron microscope (FESEM, JEOL, JSM-700F) and a transmission electron microscope (TEM, JEOL, JEM-2100F) equipped with energy dispersive X-ray spectroscopy (EDX). X-ray powder diffraction (XRD) patterns were collected by using an X-ray diffractometer (MMA, GBC Scientific). Surface areas, pore volumes, and average pore widths were measured by using a porosity analyzer (Tristar II 3020, Micrometrics). Electrical conductivities were measured by using a powder resistivity measuring system (MCP-PD51, NITTOSEIKO ANALYTECH). X-ray photoelectron spectroscopy (XPS) measurements were performed by using a surface analysis system equipped with an ion-beam sputter system (Sigma Probe, Thermo Fisher Scientific).

6.3.4. Electrochemical Measurements

The ZC and BZC series host electrodes were prepared by casting a slurry consisting of 80 % host material, 10 % Super-P carbon conductor and 10 % polyvinylidene fluoride (PVDF) in N-methyl-2-pyrrolidone (NMP) solution. (In the case of the Super-P electrode, 90 % Super-P and 10 % PVDF were mixed.) The loading level of every electrode was fixed at 2.0 mg cm^{-2}. CR2032 coin-type cells were assembled with Li-metal foil as counter electrode, polyethylene

(PE) membrane as separator, and 1 M lithium bis(trifluoromethanesulfonyl) imide (LiTFSI) dissolved in mixed 1,3-dioxolane (DOL) and dimethyl ether (DME) in a volume ratio of 1:1 including 1 wt% $LiNO_3$ additive, as electrolyte. The electrochemical tests were performed using a multichannel battery cycler (WBCS300, WonATech). Each fresh cell was first charged galvanostatically to 2 mAh cm^{-2} at a current density of 0.2 mA cm^{-2}. Then, galvanostatic discharge and charge process were repeated to different areal capacities of 0.2, 0.4, and 0.6 mAh cm^{-2} at 0.2 mA cm^{-2} with voltage cut-offs of -0.1 V (when charging) and 0.1 V (when discharging). Every interval between charging and discharging was set for 10 minutes as a rest time.

6.4. Results and Discussion

6.4.1. Effect of Hetero-Atom Doping for Chemically Enhancing Surface Lithiophilicity

Figure 6.1a and 6.1b illustrate two distinctive types of Li-metal growth behaviour on surfaces of ZIF-derived carbon with different metal-ion sources. As reported[27], by simple carbonization of ZIF-8 as the only Zn-ion precursor, Zn-N-amorphous carbon is known to be obtained, which showed exceptional Li-metal storage performance due to its highly porous and highly conductive physical properties, as enhanced by Zn and N. As shown in transmission electron microscope (TEM) observations of the anode particle after 2 mAh cm^{-2} charging (Figure 6.1a), however, we confirmed that there were a large number of Li-metal whiskers on its surface when 1 M $LiPF_6$ in ethylene carbonate/dimethyl carbonate (EC/DMC, 50:50 in vol%) was used as the carbonate electrolyte (see Figure 6.2 for detailed TEM observations). This whisker-growth behaviour (resulting in irreversible Li or dead-Li) on the anode electrode would have a negative effect on the long-term cycling performance and consequently on safety issues[28]. On the other hand, Co-N-graphitic carbon derived from a bimetallic Zn/Co-ZIF, as shown in Figure 6.1b, exhibits, interestingly, stable axial-type Li-metal growth on its surface in identical electrolyte as for the Zn-N-amorphous carbon (Figure 6.3). As of now, carbonate-based electrolytes are known for too severe conditions to apply to Li-metal anode because these types of electrolytes are easily forming the whisker or wire-like Li-metal during Li plating/stripping[29]. Nevertheless, the reason we used carbonate-based electrolytes was to clearly show the difference of materials properties themselves. Due to these contrasting properties, such as plenty of nitrogen dopants in graphite defects due to the catalytic effect of cobalt-ions in the case of the Co-N-graphitic carbon[30], it will provide, undoubtedly, great Li-metal anode performances, including even long-term cycling stability for any type of electrolytes.

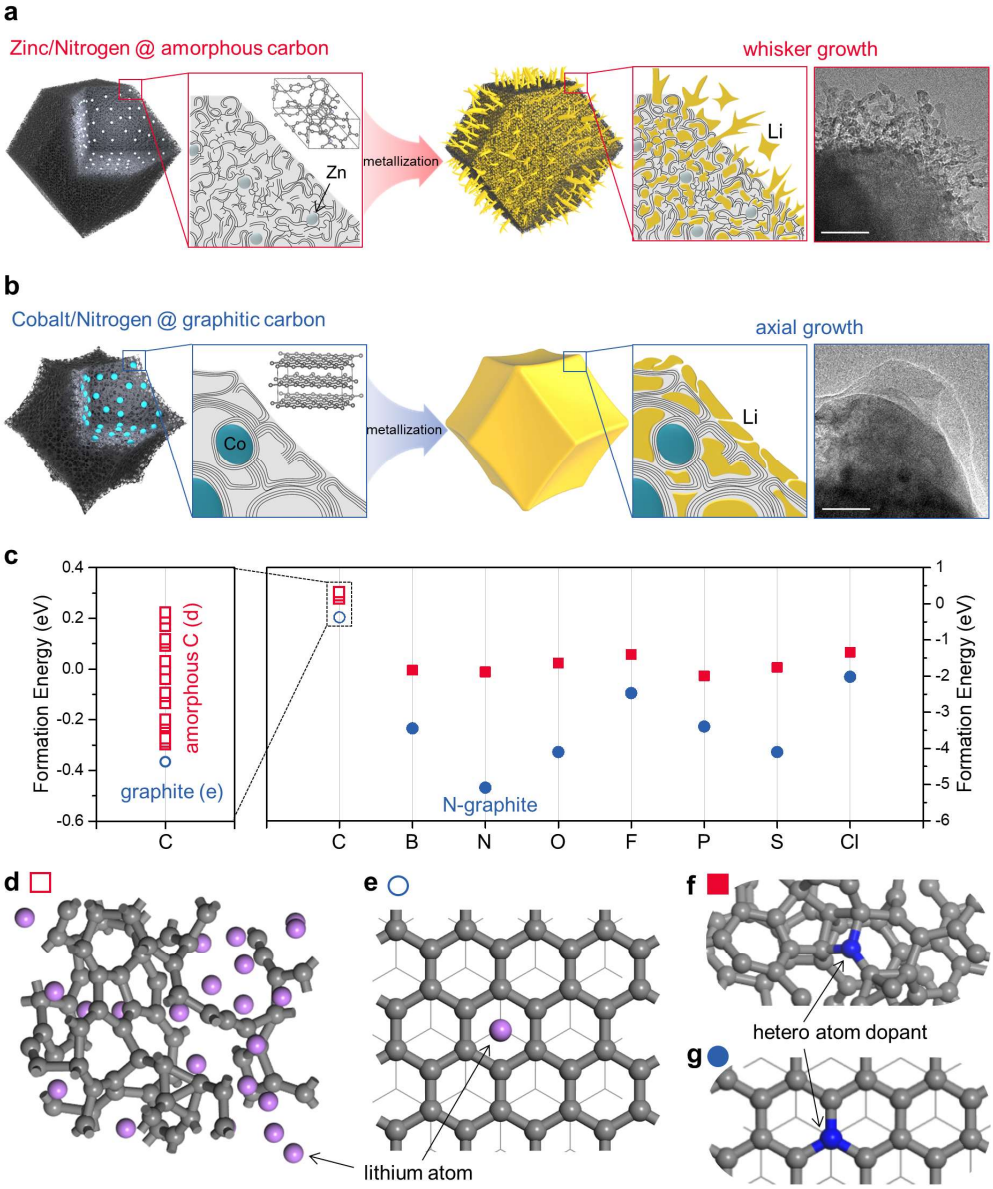

Figure 6.1. Li-metal growth behaviour and effects of hetero-atom doping for chemically enhancing surface lithiophilicity. a, b, Illustrations and representative TEM images explaining two types of distinctive Li-growth behaviour of porous carbon composites: zinc/nitrogen@amorphous carbon (a) and cobalt/nitrogen@graphitic carbon (b). c, Density functional theory (DFT) calculations of the Li formation energies on two different carbon structures with possible hetero-atom dopants. d, e, Atomic modelling of Li interstitial formation energy in amorphous carbon (d) and graphite (e). f, g, Atomic models of hetero-atoms doped in amorphous carbon (f) and graphite (g). Scale bars, 50 nm for a, 50 nm for b.

To investigate the causes of the different types of Li-metal growth behaviour, as discussed above, as well as exploring the best candidate carbon structures from the aspect of lithiophilicity surface chemistry, first of all, we conducted density functional theory (DFT)

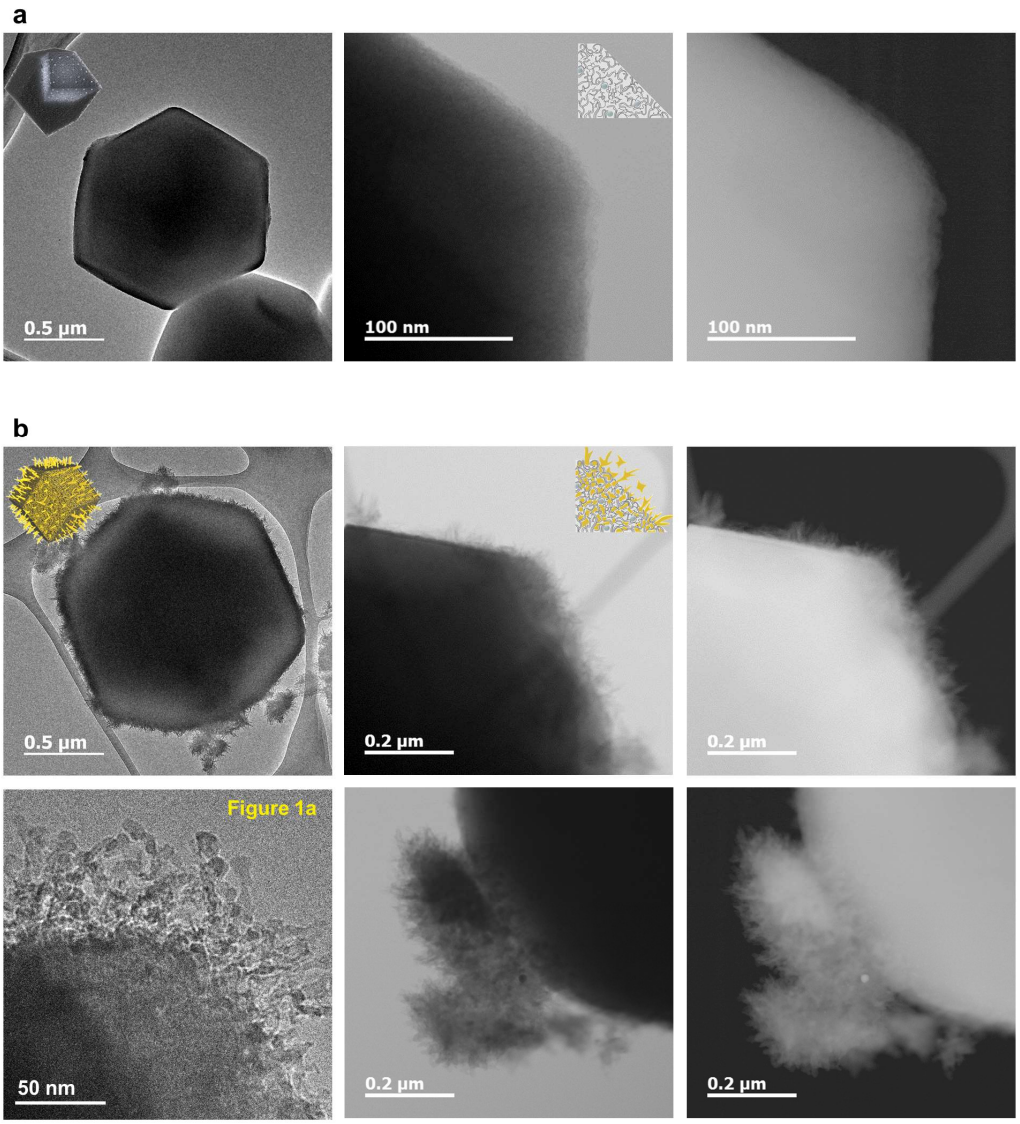

Figure 6.2. a, TEM image of the pristine Zn-N-amorphous carbon. b, TEM images of the Li-plated Zn-N-amorphous carbon (2 mAh cm^{-2}) in 1 M $LiPF_6$ in EC/DMC (50 : 50 in vol %) electrolyte.

calculations of the Li interstitial formation energy for two different types of carbons (amorphous or graphite) and possible hetero-atom dopants, as shown in Figure 6.1c. Based on the atomic model, the Li interstitial formation energies were computed for amorphous carbon and the graphite structure with various dopants by DFT calculations[32]. The Li interstitial formation energy in amorphous carbon depends on the local geometrical configuration, so we used the Delaunay triangular method to identify 20 potential insertion sites in the structure[31] (Figure 6.1d). The calculated energies for Li insertion vary from -0.31 to 0.25 eV, and the

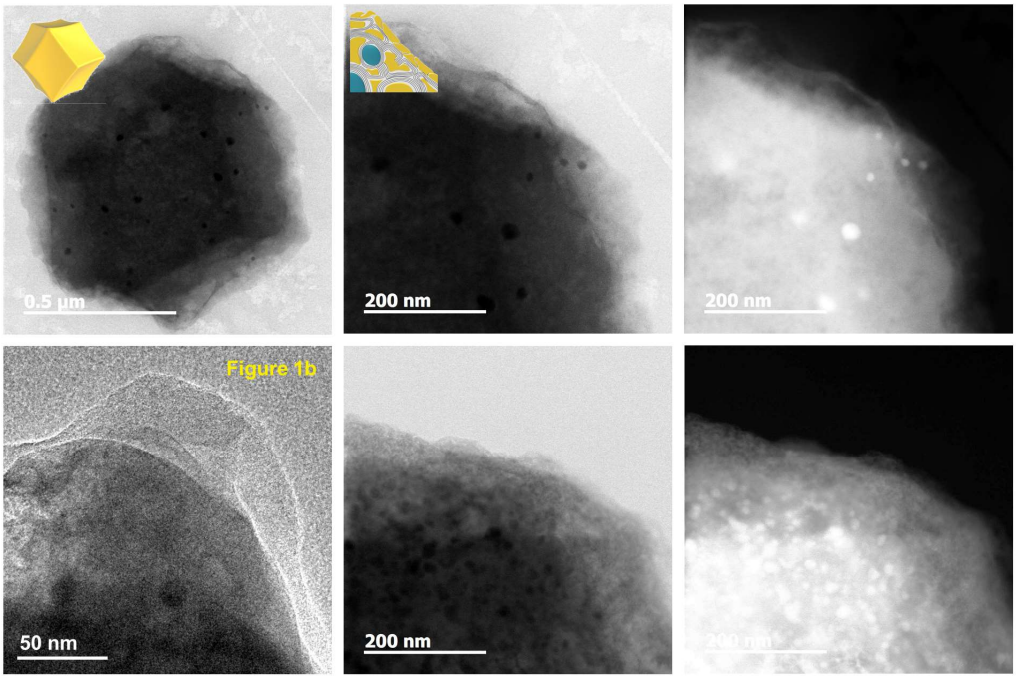

Figure 6.3. TEM images of the Li-plated Co-N-graphitic carbon (2 mAh cm-2) in 1 M LiPF6 in EC/DMC (50 : 50 in vol %) electrolyte.

lowest energy sites in graphite (Figure 6.1e) were also calculated for comparison, as shown in Figure 6.1c.

From the comparison in Figure 6.1c, the Li interstitial formation energy can be effectively lowered by elemental doping into graphite and amorphous carbon. Among the various single dopants, N dopant has the lowest Li interstitial formation energy in the graphite structure. Even if lowering the Li interstitial formation energy in the amorphous structure is observed, the large fraction of sp^3 character, which was determined to have a coordination number of ~ 3.5, is not affected by doping in terms of lowering the formation energy[33]. We can expect N dopant in the case of graphitic sp^2 bonding character to enhance the nucleation and adsorption rate in our bimetallic MOF structure.

6.4.2. Characterizations and Optimization of ZIF-Carbon Series

Based on these findings from our observations of Li-metal growth and the following formation energy calculations with different carbon structures and hetero-atom dopants, we

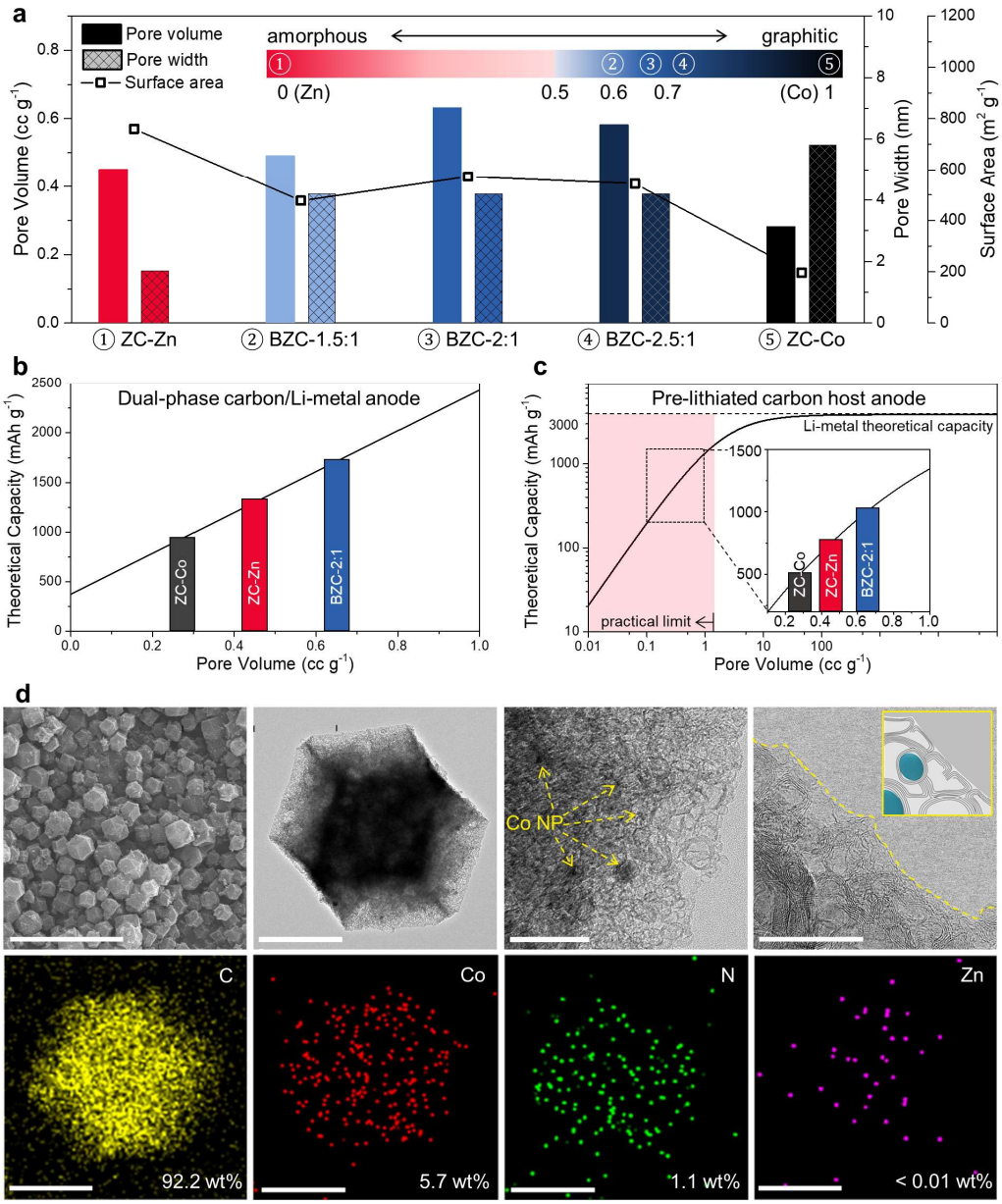

Figure 6.4. Characterizations and optimization of ZIF-carbon series. a, Comparison of the physical properties of pore volume, average pore diameter, and surface area on a series of five ZIF-carbons. b, c, Theoretical gravimetric capacity calculations, dependent on the pore volume for each host material, including dual-phase carbon/Li-metal anode (b) and pre-lithiated carbon host anode (c). d, scanning electron microscope (SEM) and TEM images with corresponding energy dispersive X-ray spectroscopy (EDX) elemental mapping images of BZC-2:1. Scale bars, 5 µm, 500 nm, 50 nm, 20 nm, 500 nm, 500 nm, 500 nm and 500 nm for d.

concluded that the best candidate as a Li-metal host should be a plenty of N doped graphitic carbon, having, of course, a high pore volume and acceptable electrical conductivity. In this respect, various kinds of bimetallic ZIF-carbons with different atomic ratios, Co^{2+}:Zn^{2+} = 1.5:1, 2:1, and 2.5:1 (denoted as BZC-1.5:1, BZC-2:1, and BZC-2.5:1, respectively), as well as Co^{+} only ZIF-carbon (denoted as ZC-Co, i.e., ZIF-67 derived carbon), were investigated, and their physical properties were compared. As shown in the chart on Figure 6.4a, bimetallic ZIF-

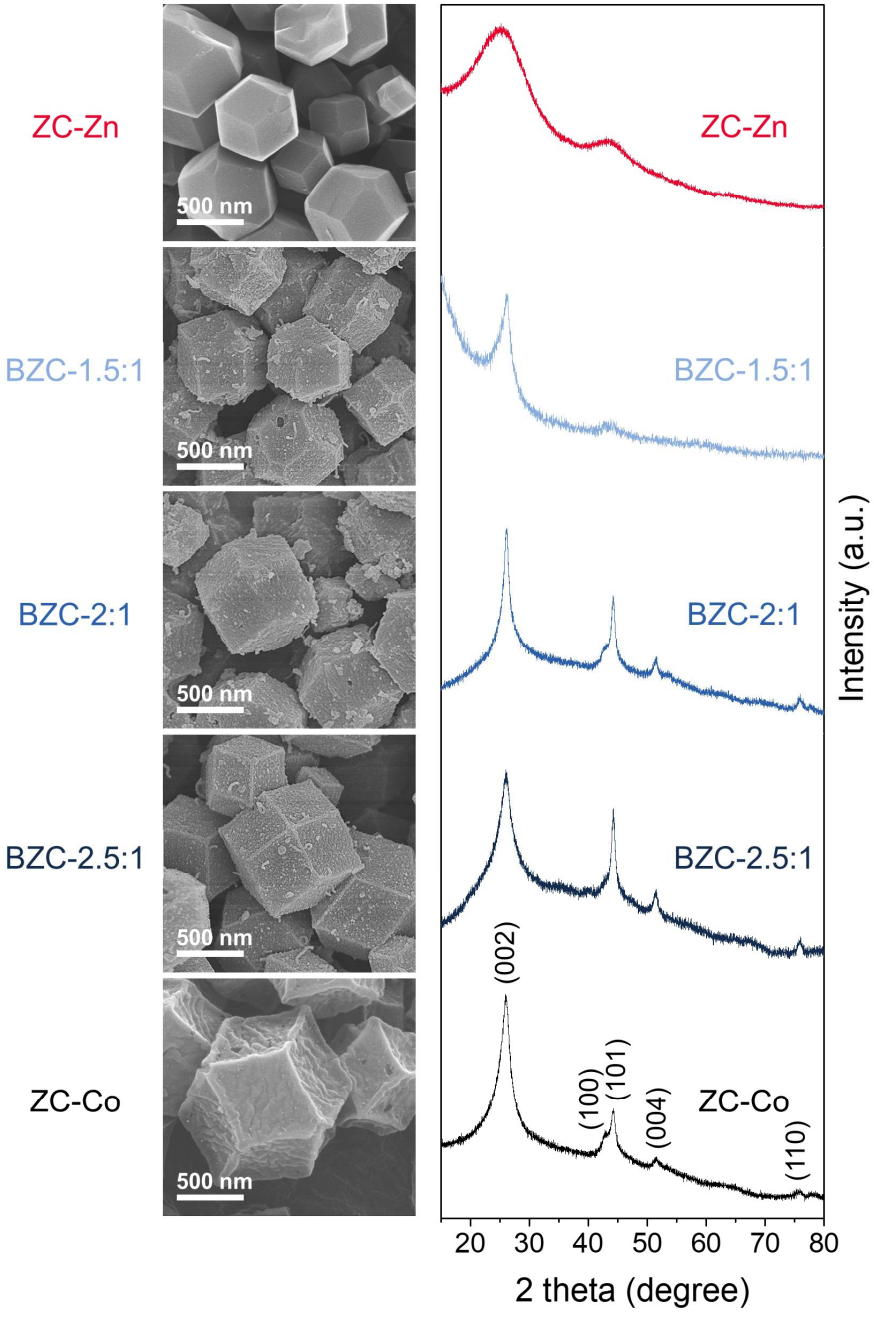

Figure 6.5. SEM observations and XRD patterns of ZIF-carbon series.

carbons with higher content of Co^{2+} (than Zn^{2+}, blue color region) were mainly chosen in order to satisfy the conditions for the formation of graphitic carbon[34]. As a result, the three as-synthesized BZC series, including ZC-Co, show graphitic crystalline peaks on their X-ray diffraction (XRD) patterns, while the ZC-Zn (i.e. ZIF-8 derived carbon) shows broad peaks indicating a typical amorphous carbon structure (Figure 6.5). Moreover, the three bimetallic

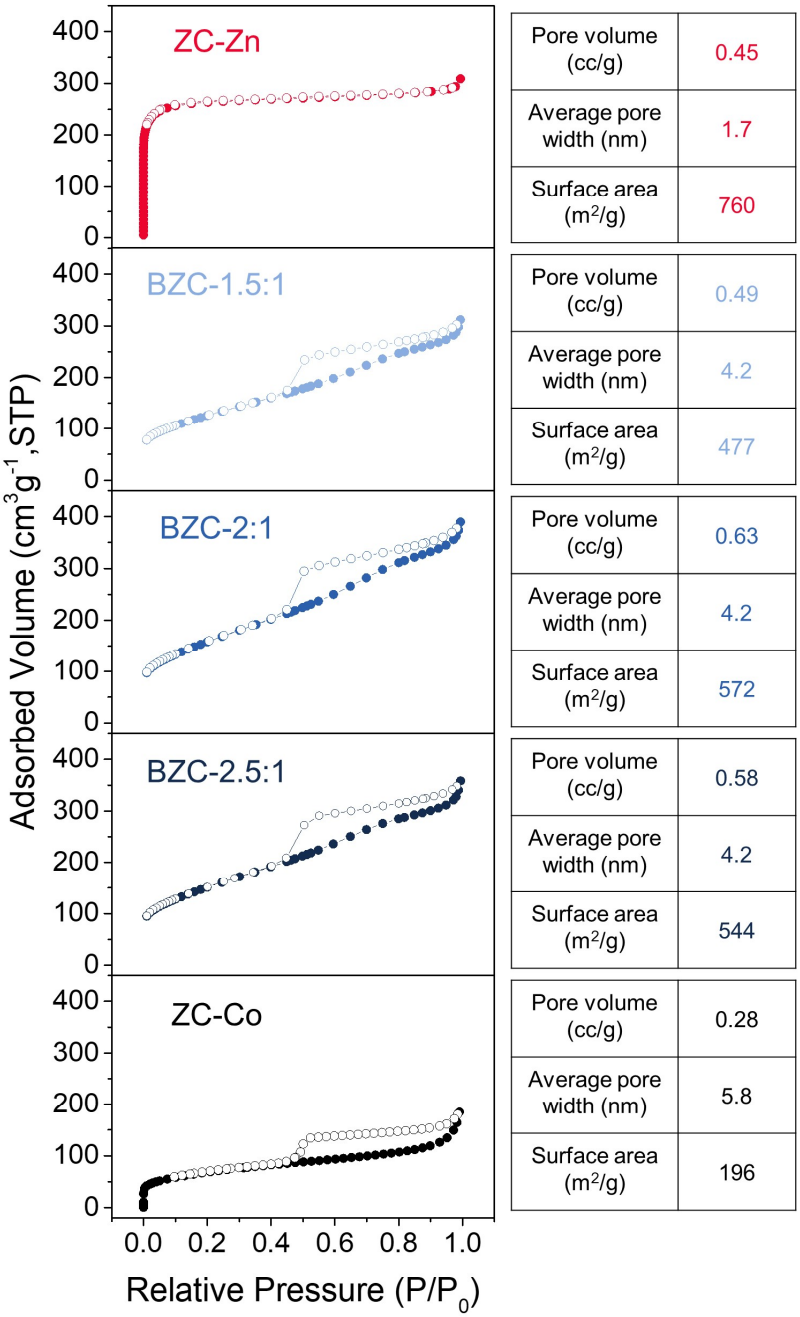

Figure 6.6. N_2 adsorption/desorption isotherms and calculated physical properties of samples in the ZIF-carbon series.

samples show mixed micro/meso-porous properties (average pore width, ~ 4 nm), whereas the ZC-Zn and ZC-Co possess mainly micropores and mesopores, respectively (which correspond to diameters of 1.7 nm and 5.8 nm, respectively, in Figure 6.6). Interestingly, BZC-2:1 shows the highest pore volume (0.63 cc g^{-1}) among all the other ZIF carbons. This might be because the introduction of the two different Zn and Co ions would cause separate shrinkage deformations under pyrolysis for carbonization, which would consequently result in the formation of a larger number of pores than for the single metal ZIF carbons[34,35]. Moreover, the BZC-2:1 shows high electrical conductivity, which is sufficient for its usage as a Li-metal host anode (16.7 S cm^{-1}, Figure 6.7).

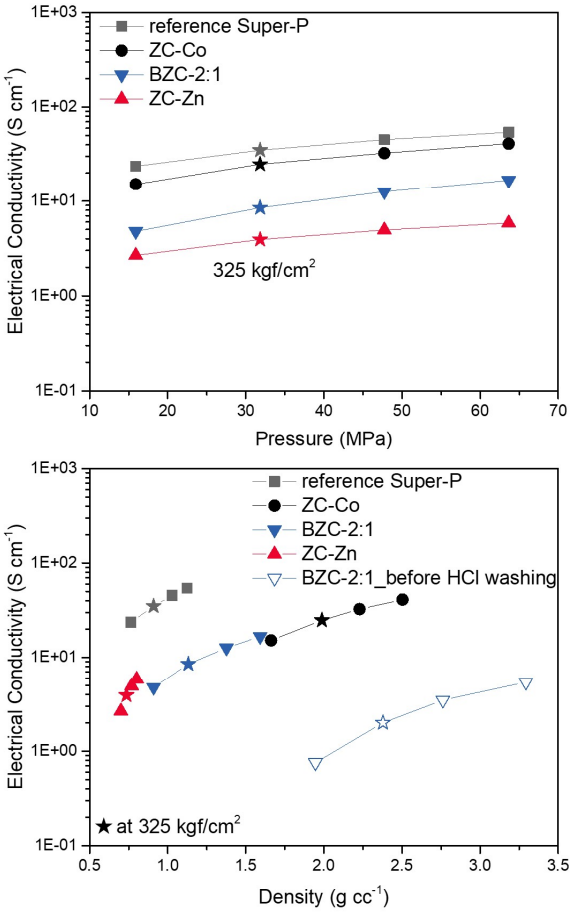

Figure 6.7. Electrical conductivity measurements of the ZIF-carbon series when compressed under different pressures. Pressure-conductivity plots (top) and density-conductivity plots (bottom).

Meanwhile, as dual-phase carbon/Li-metal anodes, the theoretical gravimetric capacities of the ZIF carbons could be calculated on the basis of their pore volume characteristics (Figure 6.4b). When Li-ions are intercalated into the carbons and the Li-metal is completely stored in their pores, BZC-2:1 shows 1712 mAh g^{-1} of theoretical capacity, which is four times higher than the capacity of conventional graphite anode[36,37]. In consideration of the pre-lithiated carbon host anodes, as shown in Figure 6.4c, the BZC-2:1 also shows 991 mAh g^{-1} of theoretical capacity, which is a suitable electrochemical property when it is coupled with sulfur (S) cathode for Li-S battery application, even though it is less than the actual theoretical capacity of the Li-metal itself (3861 mAh g^{-1}). Details, including the equations regarding Figure 6.4b and 6.4c, are introduced in Note 6.1 below.

1. Dual phase carbon/Li-metal anode (Figure 6.4b)

Theoretical volumetric capacity of Li-metal: 2062 mAh cm^{-3}

Density of Li-metal: 0.534 g cm^{-3}

Theoretical gravimetric capacity of carbon: 372 mAh g^{-1} (graphite)

Based on these values, the theoretical gravimetric capacity of a dual phase carbon/Li-metal anode when it completely stores Li-metal in its pores. as well as when Li-ions are fully intercalated into carbon, can be calculated in the following Supplementary equation (1):

Gravimetric capacity of a dual phase carbon/Li-metal anode (mAh g^{-1})

$$= [2062\ (\text{mAh cm}^{-3}) \times \text{pore volume}\ (\text{cm}^3\ \text{g}^{-1})] + 372\ (\text{mAh g}^{-1}) \quad (1)$$

2. Pre-lithiated carbon host anode (Figure 6.4c)

In this case, the mass of Li-metal itself which is already lithiated in the carbon host framework is considered together with the mass of the carbon host, and the intercalation capacity of carbon is not considered for adopting versatile applications of Li-metal anodes.

Gravimetric capacity of a pre-lithiated carbon host anode (mAh g^{-1})

$$= [2062\ (\text{mAh cm}^{-3}) \times \text{pore volume}\ (\text{cm}^3\ \text{g}^{-1})] / [1 + [\text{pore volume}\ (\text{cm}^3\ \text{g}^{-1}) \times 0.534\ (\text{g cm}^{-3})]] \quad (2)$$

Note 6.1. Theoretical Capacity Calculations

Figure 6.4d shows images of the morphology of BZC-2:1. During the HCl washing, large-size Co metal particles more than 100 nm in diameter were removed, and extra pores were

formed where the Co particles originally were (Figure 6.8). Finally, uniform polyhedral particles 1 μm in size were synthesized. By TEM analysis, it was confirmed that a small amount of nanosized Co particles, which might be trapped inside the graphite layers, still remained. In addition, 3 to 10 layers of graphite were irregularly formed with a number of 2 to 10 nm voids, while Co, N, and a negligible amount of Zn were spread uniformly in the major carbon structure.

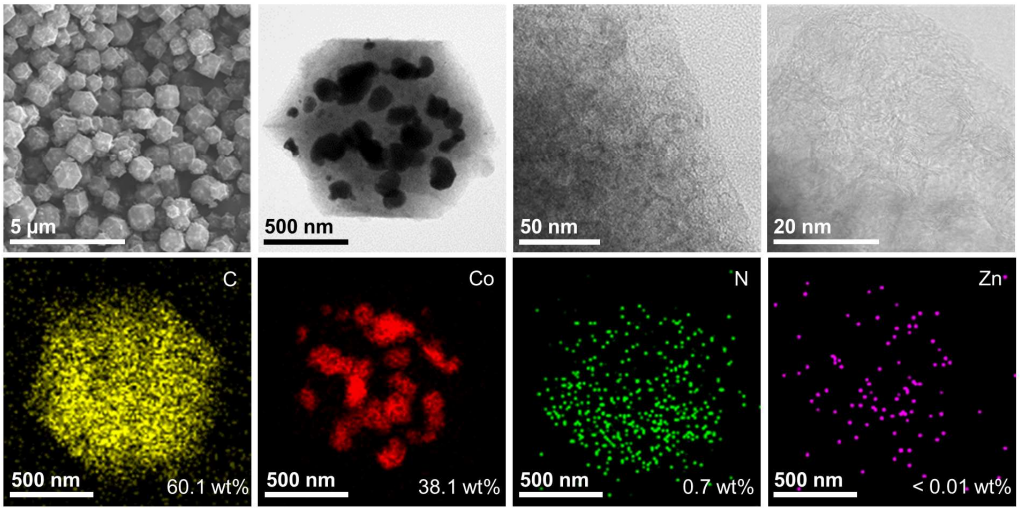

Figure 6.8. SEM and TEM images with EDX elemental mapping images of the BZC-2:1 before HCl washing.

6.4.3. Effects of Nitrogen Doping in BZC-2:1

To find the chemical states of the elements composing BZC-2:1, X-ray photoelectron spectroscopy (XPS) analysis was then conducted. Figure 6.9a, 6.9b, and 6.9c show the XPS Co 2p, C 1s, and N 1s spectra after 600 seconds of Ar-ion sputtering, respectively. Metallic Co peaks at 778.9 eV and 793.9 eV, indicating embedded Co nanoparticles (Co NPs), mainly stand out in the spectra, while Co^{2+} and Co^{3+} peaks indicating oxidised chemical formation on the surfaces of Co NPs show low intensities[39]. According to the C 1s spectrum, we confirmed C-N bonding from the peak at 285.5 eV. which indicates that there is N dopings in defects in the graphite structure. To be clear, the N 1s spectrum was also investigated and it showed 3

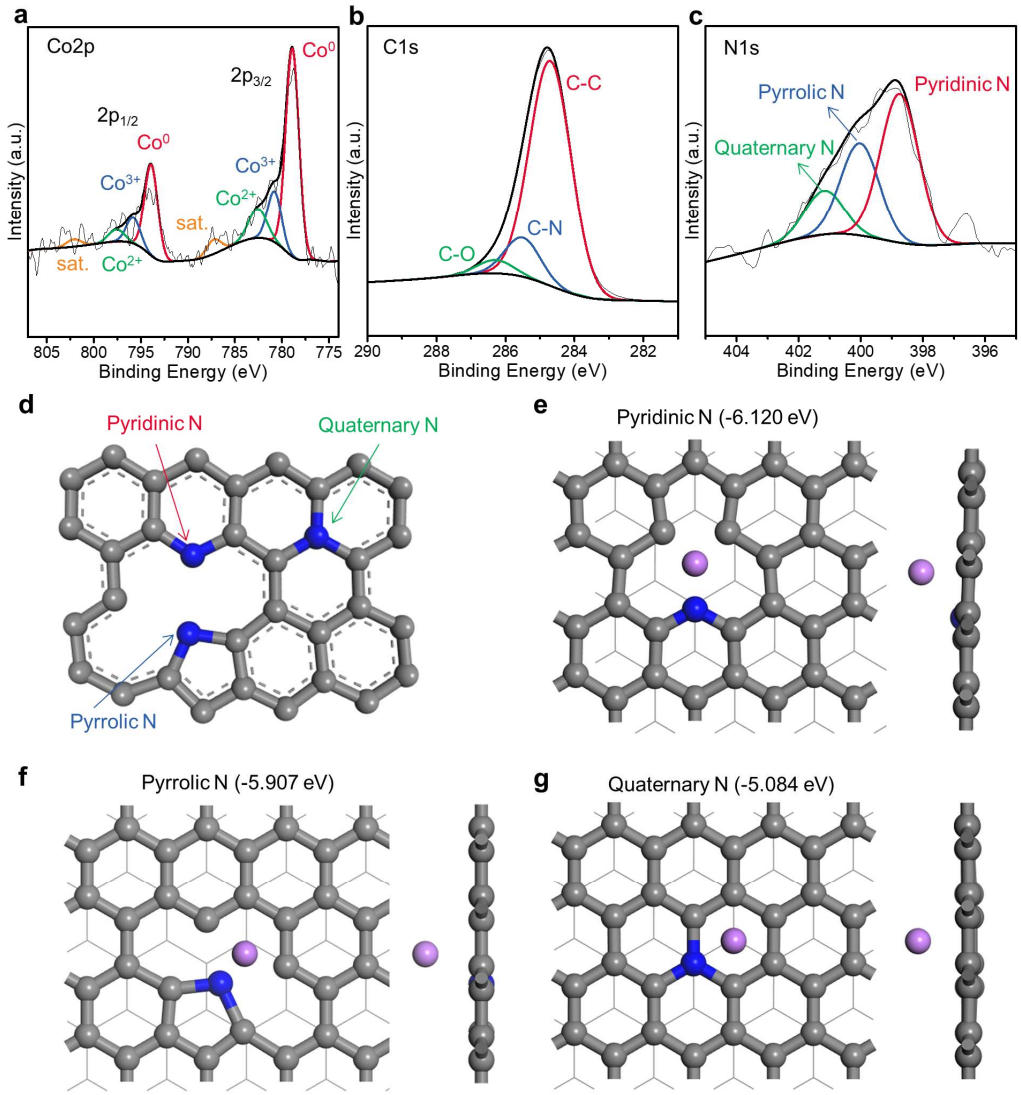

Figure 6.9. SEM and Effects of nitrogen doping in the BZC-2:1. a, b, c, XPS spectra of the BZC-2:1 measured after 120 seconds of Ar ion beam sputtering: Co 2p (a), C 1s (b), and N 1s (c). d, illustration of three types of nitrogen doping in graphite defects. e, f, g, Atomic modelings of Li interstitial formation energy in three types of nitrogens doped into the graphite structure: pyridinic N (e), pyrrolic N (f), and quaternary N (g).

distinctive peaks indicating pyridinic N (398.8 eV), pyrrolic N (400.0 eV), and quaternary N (401.2 eV), respectively. As mentioned, these N dopants play an effective role in stable Li-metal formation in the BZC-2:1 (see Figure 6.10 for more analyses regarding XPS)[39].

To gain more insight into Li adsorption in the N doped graphitic structure, mainly three bonding configurations were modelled within graphite: i) pyridinic N, ii) pyrrolic N, and iii) quaternary N. Previous investigations have shown that the pyridinic N bonding in N dopant

graphitic structure is stable when mono-vacancy is present, and pyrrolic N energetically prefers a di-vacancy defect[40]. The pyrrolic N was obtained by removing a pair of C atoms to create a di-vacancy defect and adding one N atom to form five membered heterocyclic compound. The most favourable Li adsorption site was determined by considering three possible adsorption sites, i.e. on the centre of the hexagon ring, on the top of C or N atom, and on the bridge site above the midpoint of C-C or C-N bond. A more negative value of Li interstitial formation energy refers to stronger interaction between N dopant graphitic structure and Li atoms. DFT calculations were carried out to find most stable configurations of Li interstitial atom in various N dopant graphitic for each structure, and the calculated values of Li interstitial formation energy are shown in Figure 6.9d-g. Pyridinic N exhibits significantly higher adsorption energy of -6.120 eV towards Li than pyrrolic N and quaternary N, with -5.907 and -5.084 eV, respectively. In all the structures, Li maintains stability at the centre of the defect, as the surface

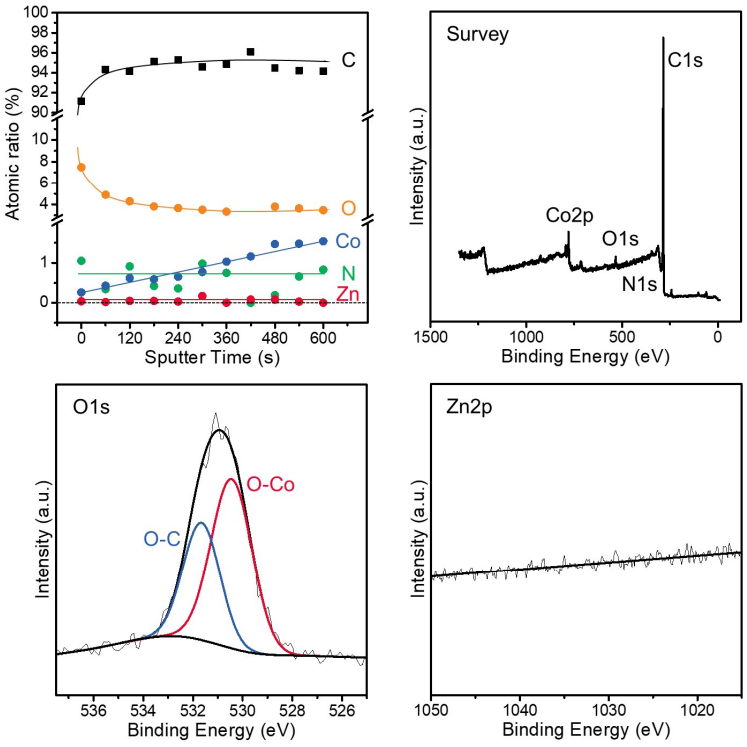

Figure 6.10. XPS spectra and depth profiles of the BZC-2:1.

dangling bonds generated by the formation of vacancies have induced strong attraction for Li[33,41].

6.4.4. Electrochemical Measurements for Li-Metal Anode Performance

In order to maximize cell performance, 1 M LiTFSI in DOM/DME (50:50 in vol%) with $LiNO_3$ was used for evaluating Li-metal anode performance because ether-based electrolytes can make Li-metal anode more prolonged[29,42]. Especially, since $LiNO_3$ as additive helps to improve the surface chemistry of Li-metal anode, this type of electrolyte can elucidate a realistic possibility of Li-metal anode as well as the stability of materials (see Figure 6.11 for Li-growth behaviour observations of BZC-2:1 in ether-based electrolyte)[43]. Electrochemical measurements were performed in the cases of BZC-2:1 (Co-N-graphite) electrode, Super-P (non-porous carbon) electrode, and ZC-Zn (Zn-N-amorphous carbon) electrode as references. In the first cycle charging with the areal capacity of 2 mAh cm^{-2}, as shown in Figure 6.12a, the BZC-2:1 showed much flatter potential and lower overpotential than the other electrodes at 0.2 mA cm^{-2}. This lower voltage hysteresis indicates that our BZC-2:1 had better Li-metal affinity, due to, as mentioned, the higher pore volume and lower Li formation energy (N-graphite) of the BZC-2:1[44]. Figure 6.12b shows voltage profiles of the three different electrodes under the

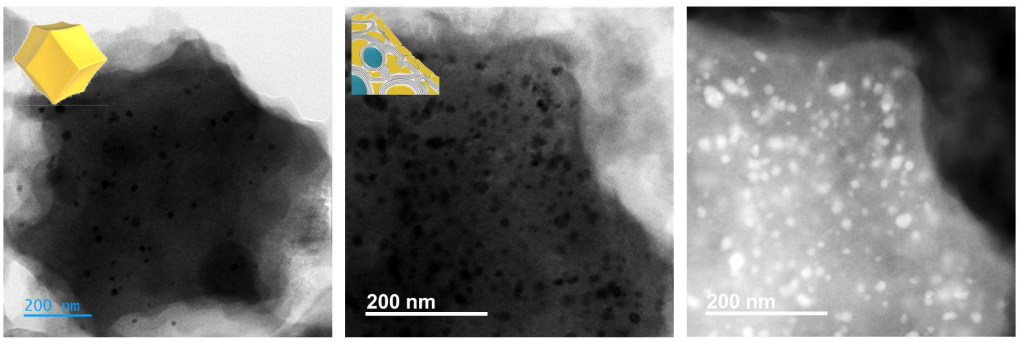

Figure 6.11. TEM images of the Li-plated BZC-2:1 (2 mAh cm^{-2}) in 1 M LiTFSi in DOL/DME (50 : 50 in vol %) + 1 wt % $LiNO_3$ electrolyte.

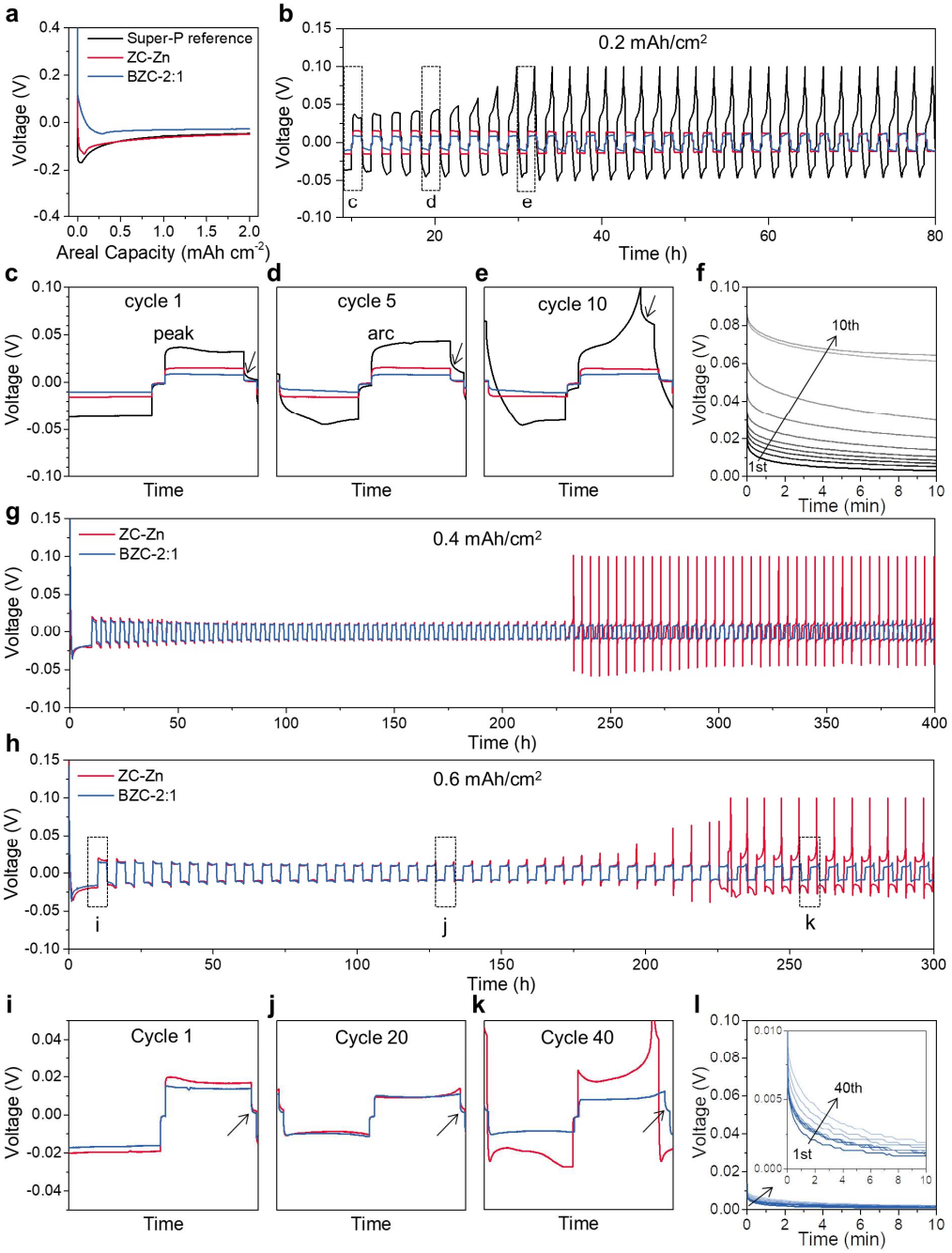

Figure 6.12. Electrochemical measurements on Super-P, ZC-Zn, and BZC-2:1 electrodes for Li-metal anode performances. a, voltage hysteresis observations in the first cycle charging with the areal capacity of 2 mAh cm^{-2}; b, voltage profiles of the three electrodes with areal capacity 0.2 mAh cm^{-2} at 0.2 mA cm^{-2}. c, d, e, Voltage behaviour of each cycle on test b; cycle 1 (c), cycle 5 (d), and cycle 10 (e). f, Concentration relaxation behaviour of the Super-P electrode during ten minutes of rest time. g, h, voltage profiles of the ZC-Zn and BZC-2:1 electrodes at 0.2 mA cm^{-2} with different charge/discharge capacities of 0.4 mAh cm^{-2} (g) and 0.6 mAh cm^{-2} (h). i, j, k, voltage behaviour of each cycle on test h: cycle 1 (i), cycle 20 (j), and cycle 40 (k). l, Concentration relaxation behaviour of the BZC-2:1 electrode during ten minutes of rest time.

condition that all the charge/discharge capacities were limited to 0.2 mAh cm^{-2} at 0.2 mA cm^{-}

^{2}, and the loop repeated until any of the electrodes showed failure. For 80 hours of measurement time (around 30 cycles), the ZC-Zn and the BZC-2:1 electrodes showed stable performances with different overpotentials because of their large pore volumes in which Li-metal could be stored. Non-porous Super-P electrode showed a typical failure mechanism even even after a few cycles, as can be found in the case of electrodes with dead-Li growth. In detail, the voltage profiles in the early cycles of the Super-P electrode showed a broad peak directly after the discharging current was applied (Figure 6.12c). This peak indicates that direct pathways still exist for ions to move through the electrode/electrolyte interphase, even though a minor amount of dead-Li interferes with ion transport. In the mid-term cycles, however, as shown in Figure 6.12d, arc-type behaviour can be observed on the Super-P electrode which is attributed to interference with convoluted Li-ion pathways by a complete covering of dead-Li on the interphase between the electrode and the electrolyte[45]. Then, this arc becomes larger and larger in accordance with the gradual growth of dead-Li. Eventually, the Super-P electrode losses its reversible Li source (Figure 6.12e). In consequence, the tails indicating the relaxation needed to reach equilibrium concentration during ten minutes of rest time became larger, up to 70 mV in 10 cycles (Figure 6.12f)[46].

To determine the reversibility at higher charge/discharge capacities, cycling tests of the ZC-Zn and the BZC-2:1 were performed under the conditions of constant capacity of 0.4 mAh cm^{-2} at 0.2 mA cm^{-2} (Figure 6.12g). In these results, the BZC-2:1 still showed stable performance while maintaining 100 % of Coulombic efficiency, even over 100 cycles, while the ZC-Zn experienced discharge capacity degradation from 50 cycles (Figure 6.13). Besides, it was also confirmed that the BZC-2:1 electrode is clearly capable of more stable cycling performance under the conditions of constant capacity of 0.6 mAh cm^{-2} at 0.2 mA cm^{-2}, as shown in Figure 6.12h. These two electrodes showed stable voltage profiles without any arc behaviour caused by the accumulation of Li-dendrites, even after 20 cycles (Figure 6.12i and 6.12j). In the 40th

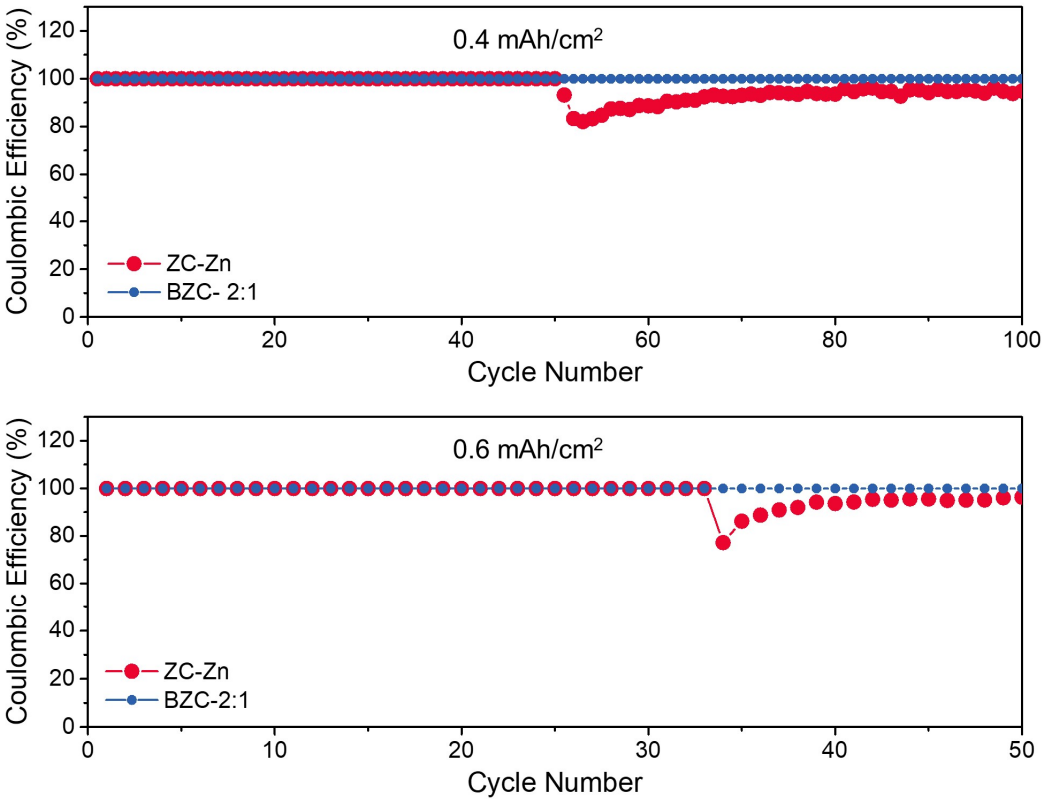

Figure 6.13. Coulombic efficiencies on each cycle of the ZC-Zn and the BZC-2:1 electrodes from the tests shown in Figure 6.11c and 6.11d, respectively.

cycle of the ZC-Zn electrode, however, high overpotential with distinctive peak behaviour, but without arc behaviour is observed, as shown in Figure 6.12k. This failure phenomenon might have occurred because the ZC-Zn electrode does not form bulky Li-dendrites on the electrode surface but gradually forms an SEI along with gradual growth of Li whiskers due to its relatively less lithiophilic surface chemistry. Moreover, this gradual growth would cause unwanted electrolyte consumption as well as an increase in the internal resistance[47]. Then, it consumes its reversible Li source by converting it to irreversible Li phase and it increases, consequently, overpotential during repeated plating/stripping. On the other hand, the BZC-2:1 shows no significant voltage change during repeated cycling under these conditions. In consequence, the relaxation tails of the BZC-2:1 electrode are still maintained below 2 mV, even after 40 cycles (Figure 6.12l).

6.4.5. Microscopic Observations of Li-Metal Plated BZC-2:1

To understand the Li plating behaviour on our BZC-2:1 electrode, microscopic observations of the BZC-2:1 electrode together with a reference non-porous carbon (Super-P) elelctrode were performed after charging to 2 mAh cm^{-1} at a current density of 0.2 mA cm^{-2}. Figure 6.14a and 6.13b shows scanning electron microscope (SEM) images, both top view and cross-sectional view, for the Super-P and the BZC-2:1 electrodes, respectively. As shown in Figure 6.14a, light-colored Li-metal covered the surface of the Super-P electrode (inset, left), and its original form was also collapsed due to the disorderly Li-metal plating inside the electrode (right). On the other hand, there is no visible Li-metal growth on the BZC-2:1 electrode surface, and polyhedral ZIF carbon particles are still clearly visible on every spot, as for the pristine electrode in spite of the 2 mAh cm^{-1} charging. That is to say, 2 mAh cm^{-1} indicates the amount of Li-metal that was stably stored into the pores of the BZC-2:1 (Figure 6.14b).

To confirm in-depth the Li-metal plating behaviour both on the surface and in the host framework of the BZC-2:1, further TEM observations were performed under the condition that the TEM specimen was intentionally exposed to the electron beam (EB) for thirty minutes in order to induce the decomposition of the plated Li-metal[44]. As a result, as illustrated in Figure 6.14c, it can be observed that full covering of Li-metal on the surface as well as interior Li-metal is gradually removed over time by continuous EB exposure with the beam current of 13 μm at 200 keV. In addition, around 100 nm thickness of axial type residue for Li-metal was stably formed on the surface of the BZC-2:1 particle with no confirmation of Li-metal whiskers (time, t =0, Figure 6.14d). As shown in the insets in Figure 6.14d (with yellow arrows), the Co NPs that were positioned deeper inside the particle and were invisible without EB exposure, can be clearly detected after EB exposure. As well, they show different brightness in the center of the particle, indicating the removal of Li-metal by EB exposure (Figure 6.14e). In

consequence, these results demonstrate that Li-metal is fully and stably settled in, both on the surface and inside the host framework of the BZC-2:1.

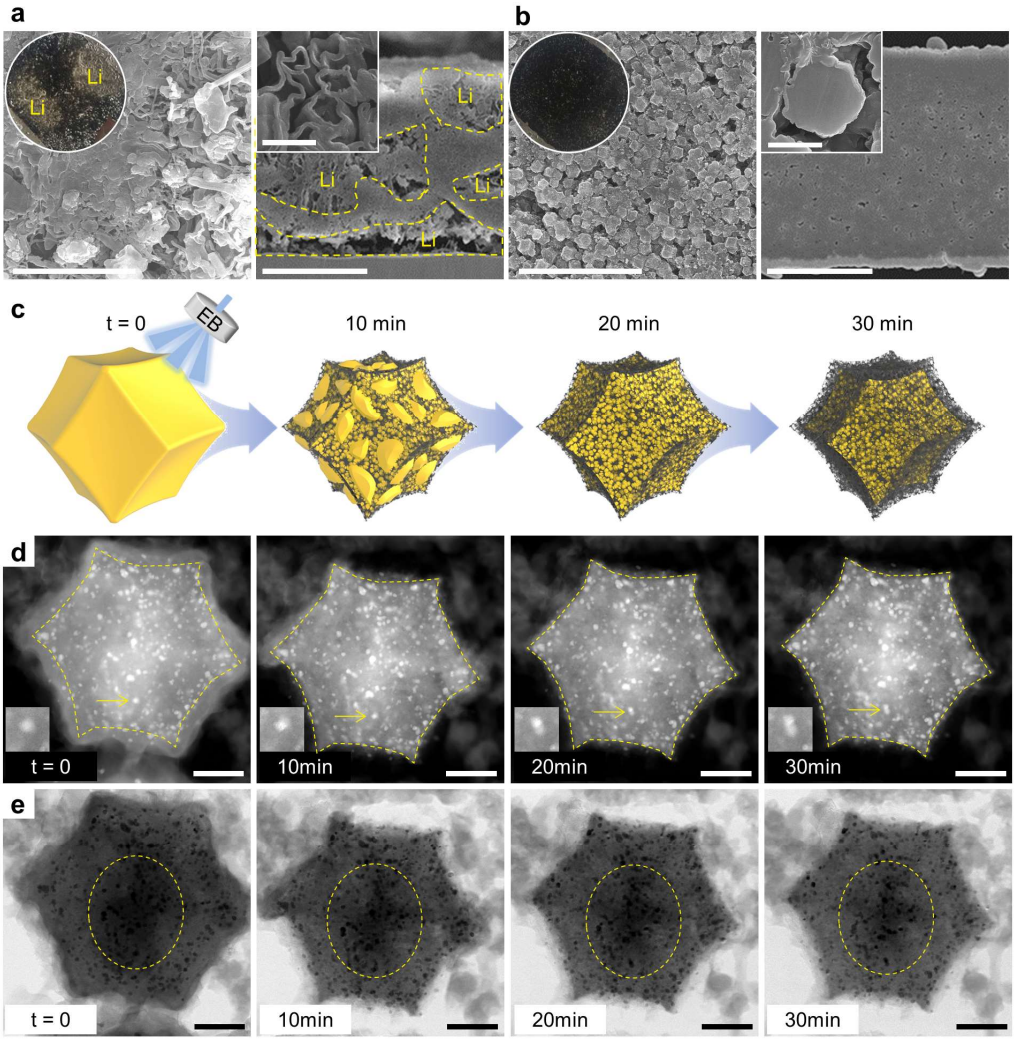

Figure 6.14. Microscopic observations of Li-metal plated BZC-2:1. a, b, Top view (left, photograph in inset) and cross-sectional view (right) SEM images of the super-P electrode (a) and the BZC-2:1 electrode (b). c, Schematic illustration of Li-metal decomposition behaviour in a TEM specimen with electron beam exposure. d, e, TEM images of the Li-metal plated BZC-2:1 particle after different times under electron beam exposure; high angle annular dark field – scanning TEM (HAADF-STEM) images (d), bright field (BF)-STEM images (e). Scale bars, 10 µm and 20 µm (1 µm, inset) for a, 10 µm and 20 µm (1 µm, inset) for b, 200 nm for d and e.

6.4.6. Critical Role of Co. Charge Density Difference Calculations of Li Adsorption on N Doped Graphite and on Co-N Doped Graphite.

To investigate the critical role of Co, we analized the charge density difference (ρ_{diff}) of Li adsorption on Co-N doped graphite and N doped graphite (Figure 6.15a and 6.15b). The charge transfer (yellow part of isosurface) from the Li insertion is occurred in Li-C and Li-N, which indicates a positive charge, as calculated by Equation (1)

$$\rho_{\text{diff}} = \rho_{Li-Gra\ or\ Co} - (\rho_{Gra\ or\ Co-Gra} + \rho_{Li}) \quad (1)$$

The charge depletion represented by the cyan region can be a driving force for local charge separation during polarization. On doping with Co, the charge depletion is observed near the Co atom and the donated charge participate a generation of chemical bonding to Li. The Co-N doped graphite also causes delocalized electrons to be accumulated on graphite from the large number of electrons around the graphite. Thus, the interaction between Li and Co-N doped

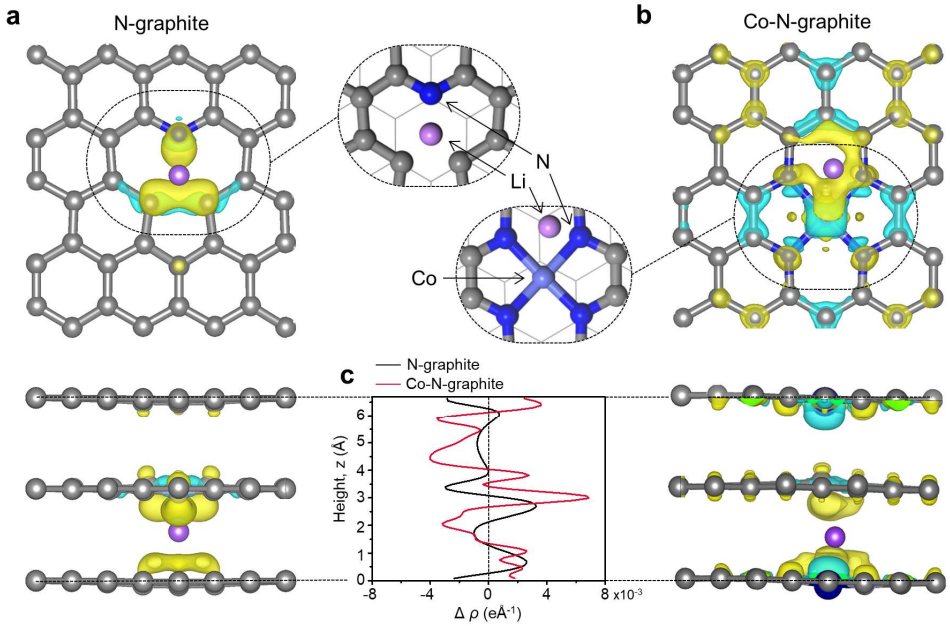

Figure 6.15. Critical role of Co. Charge density difference calculations of Li adsorption on N doped graphite and on Co-N doped graphite. a, b, transferred charge behaviours on N-graphite (a) and Co-N-graphite (b). c, Their charge deficiency in relation to the z-axis hexagonal structure of graphite.

graphite is enhanced by Co doping. Planar Li plating is also expected because the influence of Co-N extends to the second nearest neighbours of C atoms, whereas N appears to only affect the nearest neighbour C atoms. Using charge analysis, we found that a Li atom donates a charge of 0.8*e* to Co-N doped graphite, almost completely ionizing the Li atom. The saturation of the electron-deficient Co-N bond results in a strong chemical bond between graphite and the Li ion.

6.5. Conclusion

In summary, by a simple synthetic method highly mesoporous N-graphite embedded with Co NPs can be obtained. The BZC-2:1 sample showed high Li ion affinity as well as highly lithiophilic surface chemistry, attributable to the low formation energy of N-doped graphite. As a result, the BZC-2:1 shows excellent electrochemical performance with high Li-metal reversible capacity and even stable long-term cyclability with no dead-Li formation. We believe that BZC-2:1 could lead to the development of Li-metal anode material for next-generation Li battery applications (Figure 6.16).

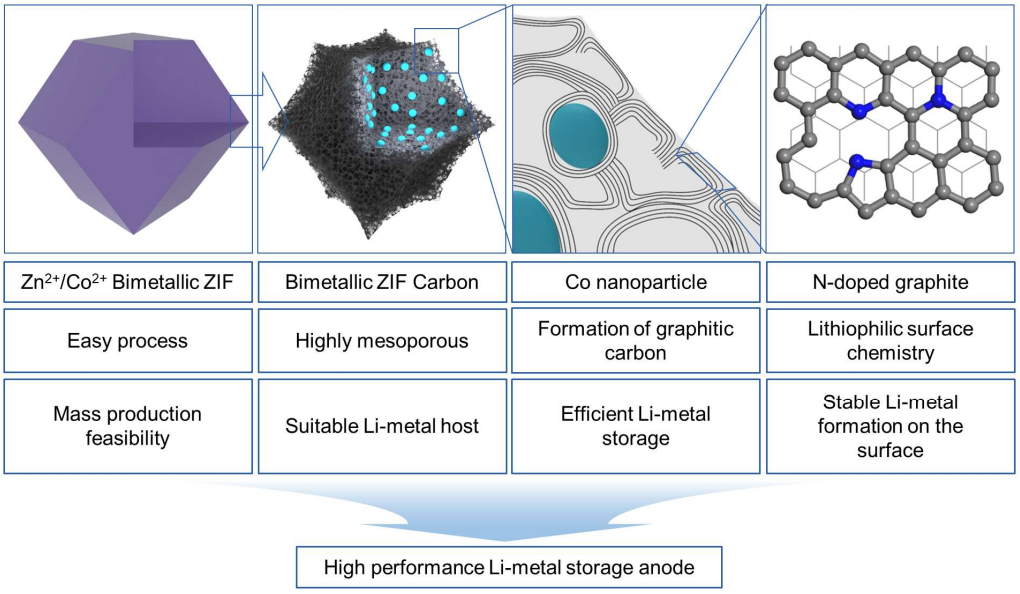

Figure 6.16. Summary of main results, containing schematic illustrations for understanding BZC-2:1.

6.6. References

[1] M. Armand, J.-M. Tarascon, *Nature* **2008**, 451, 652.

[2] Y. Sun, N. Liu, Y. Cui, *Nat. Energy* **2016**, 1, 16071.

[3] D. Lin, Y. Liu, Y. Cui, *Nat. Nanotechnol.* **2017**, 12, 194.

[4] J. Lee, J. Moon, S. A Han, J. Kim, V. Malgras, Y. -U. Heo, H. Kim, S. -M. Lee, H. K. Liu, S. X. Dou, Y. Yamauchi, M. -S. Park, J. H. Kim, *ACS Nano* **2019**, 13, 9607.

[5] C. Brissot, M. Rosso, J. -N. Chazalviel, S. Lascaud, *J. Power Sources* **1999**, 81-82, 925.

[6] Y. S. Cohen, Y. Cohen, D. Aurbach, *J. Phys. Chem. B* **2000**, 104, 12282.

[7] D. Lu, Y. Shao, T. Lozano, W. D. Bennett, G. L. Graff, B. Polzin, J. Zhang, M. H. Engelhard, N. T. Saenz, W. A. Henderson, P. Bhattacharya, J. Liu, J. Xiao, *Adv. Energy Mater.* **2015**, 5, 1400993.

[8] A. Manthiram, X. Yu, S. Wang. *Nat. Rev. Mater.* **2017**, 2, 16103.

[9] Y. Chen, Z. Wang, X. Li, X. Yao, C. Wang, Y. Li, W. Xue, D. Yu, S. Y. Kim, F. Yang, A. Kushima, G. Zhang, H. Huang, N. Wu, Y.-W. Mai, J. B. Goodenough, J. Li, *Nature* **2020**, 578, 251.

[10] S. Randau, D. A. Weber, O. Kötz, R. Koerver, P. Braun, A. Weber, E. Ivers-Tiffée, T. Adermann, J. Kulisch, W. G. Zeier, F. H. Richter, J. Janek, *Nature Energy* **2020**, 5, 259.

[11] K. Fu, Y. Gong, B. Liu, Y. Zhu, S. Xu, Y. Yao, W. Luo, C. Wang, S. D. Lacey, J. Dai, Y. Chen, Y. Mo, E. Wachsman, L. Hu, *Sci. Adv* **2017**, 3, e1601659.

[12] X.-B. Cheng, C.-Z. Zhao, Y.-X. Yao, H. Liu, Q. Zhang, *Chem* **2019**, 5, 74.

[13] N.-W. Li, Y.-X. Yin, C.-P. Yang, Y.-G. Guo, *Adv. Mater.* **2016**, 28, 1853.

[14] H.-K. Kang, S.-G. Woo, J.-H. Kim, S.-R. Lee, D.-G. Lee, J.-S. Yu, *J. Power Sources* **2019**, 413, 467.

[15] L. Wang, Q. Wang, W. Jia, S. Chen, P. Gao, J. Li, *J. Power Sources* **2017**, 342, 175.

[16] R. Pathak, K. Chen, A. Gurung, K. M. Reza, B. Bahrami, J. Pokharel, A. Baniya, W. He, F. Wu, Y. Zhou, K. Xu, Q. Qiao, *Nat. Commun.* **2020**, 11, 93.

[17] G. Li, Y. Gao, X. He, Q. Huang, S. Chen, S. H. Kim, D. Wang, *Nat. Commun.* **2017**, 8, 850.

[18] C. Niu, H. Pan, W. Xu, J. Xiao, J.-G. Zhang, L. Luo, C. Wang, D. Mei, J. Meng, X. Wang, Z. Liu, L. Mai, J. Liu, *Nat. Nanotechnol.* **2019**, 14, 594.

[19] D. Lin, Y. Liu, Z. Liang, H.-W. Lee, J. Sun, H. Wang, K. Yan, J. Xie, Y. Cui, *Nat. Nanotechnol.* **2016**, 11, 626.

[20] T. Wang, R. Villegas Salvatierra, A. S. Jalilov, J. Tian, J. M. Tour, *ACS Nano* **2017**, 11, 10761.

[21] L. Liu, Y.-X. Yin, J.-Y. Li, S.-H. Wang, Y.-G. Guo, L.-J. Wan, *Adv. Mater.* **2018**, 30, 1706216.

[22] Z. Liang, D. Lin, J. Zhao, Z. Lu, Y. Liu, C. Liu, Y. Lu, H. Wang, K. Yan, X. Tao, Y. Cui, *Proc. Natl. Acad. Sci. U.S.A.* **2016**, 113, 2862.

[23] H. Furukawa, K. E. Cordova, M. O'Keeffe, O. M. Yaghi, *Science* **2013**, 341, 1230444.

[24] H. Li, M. Eddaoudi, M. O'Keeffe, O. M. Yaghi, *Nature* **1999**, 402, 276.

[25] S. Abednatanzi, P. Gohari Derakhshandeh, H. Depauw, F.-X. Coudert, H. Vrielinck, P. Van Der Voort, K. Leus, *Chem. Soc. Rev.* **2019**, 48, 2535.

[26] J. Tang, R. R. Salunkhe, H. Zhang, V. Malgras, T. Ahamad, S. M. Alshehri, N. Kobayashi, S. Tominaka, Y. Ide, J. H. Kim, Y. Yamauchi, *Sci. Rep.* **2016**, 6, 30295.

[27] J. Kim, J. Lee, J. Yun, S. H. Choi, S. A. Han, J. Moon, J. H. Kim, J.-W. Lee, M.-S. Park, *Adv. Funct. Mater.* **2020**, 30, 1910538.

[28] D. Wang, W. Zhang, W. Zheng, X. Cui, T. Rojo, Q. Zhang, *Adv. Sci.* **2017**, 4, 1600168.

[29] A. Pei, G. Zheng, F. Shi, Y. Li, Y. Cui, *Nano Lett.* **2017**, 17, 1132.

[30] J. Kim, C. Young, J. Lee, M.-S. Park, M. Shahabuddin, Y. Yamauchi, J. H. Kim, *Chem. Commun.* **2016**, 52, 13016.

[31] J. P. Perdew, K. Burke, M. Ernzerhof, *Phys. Rev. Lett.* **1996**, 77, 3865.

[32] J. Moon, B. Lee, M. Cho, K. Cho, *J. Power Sources* **2014**, 272, 1010.

[33] X. Chen, X.-R. Chen, T.-Z. Hou, B.-Q. Li, X.-B. Cheng, R. Zhang, Q. Zhang, *Science Advances* **2019**, 5, eaau7728.

[34] S. A. Han, J. Lee, K. Shim, J. Lin, M. Shahabuddin, J.-W. Lee, S.-W. Kim, M.-S. Park, J. H. Kim, *Bull. Chem. Soc. Jpn.* **2018**, 91, 1474.

[35] J. Hwang, A. Ejsmont, R. Freund, J. Goscianska, B. V. K. J. Schmidt, S. Wuttke, *Chem. Soc. Rev.* **2020**, 49, 3348.

[36] J. Lee, S. A Han, H, Qutaish, L. K. Shrestha, K. Ariga, J. H. Kim, *General Chemistry* **2020**, 6, 190011.

[37] Y. Sun, G. Zheng, Zhi W. Seh, N. Liu, S. Wang, J. Sun, Hye R. Lee, Y. Cui, *Chem* **2016**, 1, 287.

[38] J. Zhao, M. Konh, A. Teplyakov, *Appl. Surf. Sci.* **2018**, 455, 438.

[39] J. Kim, C. Young, J. Lee, Y.-U. Heo, M.-S. Park, M. S. A. Hossain, Y. Yamauchi, J. H. Kim, *J. Mater. Chem. A* **2017**, 5, 15065.

[40] Y. Fujimoto, S. Saito, *Phys. Rev. B* **2011**, 84, 245446.

[41] Y.-X. Yu, *Phys. Chem. Chem. Phys.***2013**, 15, 16819.

[42] G. Bieker, M. Winter, P. Bieker, *Phys. Chem. Chem. Phys.* **2015**, 17, 8670.

[43] S. S. Zhang, *Electrochim. Acta* **2012**, 70, 344.

[44] K. Yan, Z. Lu, H.-W. Lee, F. Xiong, P.-C. Hsu, Y. Li, J. Zhao, S. Chu, Y. Cui, *Nat. Energy* **2016**, 1, 16010.

[45] K. N. Wood, E. Kazyak, A. F. Chadwick, K.-H. Chen, J.-G. Zhang, K. Thornton, N. P. Dasgupta, *ACS Cent. Sci.* **2016**, 2, 790.

[46] K.-H. Chen, K. N. Wood, E. Kazyak, W. S. LePage, A. L. Davis, A. J. Sanchez, N. P. Dasgupta, *J. Mater. Chem. A* **2017**, 5, 11671.

[47] D. Lu, Y. Shao, T. Lozano, W. D. Bennett, G. L. Graff, B. Polzin, J. Zhang, M. H. Engelhard, N. T. Saenz, W. A. Henderson, P. Bhattacharya, J. Liu, J. Xiao, *Adv. Energy Mater.* **2015**, 5, 1400993.

[48] P. E. Blöchl, *Phys. Rev. B* **1994**, 50, 17953.

[49] G. Kresse, J. Hafner, *Phys. Rev. B* **1993**, 48, 13115.

[50] J. P. Perdew, K. Burke, M. Ernzerhof, *Phys. Rev. Lett.* **1996**, 77, 3865.

Chapter 7. Thesis Conclusion & Future Prospects

7.1. Thesis Conclusion

As the title of this thesis suggests it, this doctoral work aims to develop advanced anode materials, that fulfill high energy and highly stable properties applying in lithium battery applications. From the perspective of "beyond graphite", both Si and Li-metal are all obviously attractive materials to replace conventional graphite system. However, these two disparate researches, in fact, could not combine into one research subject, because the challenge and the solution of each for realization are considerably different. Nonetheless, the processes from initialization to completion of each work follow clearly same steps because all the works in this thesis mainly focus on "how to design materials using nanostructural engineering".

In this regard, this doctoral work can be summarized as below five aspects:

i) Recent researches and the challenges that each Si and Li-metal anode is facing, were firstly studied.

Most of the existing research on Si-based anodes has focused mainly on resolving the mechanical issue regarding the considerable volume expansion (~300%), which is indeed the main prerequisite to practical application. Moreover, the Si-based anode materials should have high reversible capacity with an acceptable coulombic efficiency in order to surpass the energy density of the conventional graphite system. On the other hand, Li-metal faces unavoidable technical issues such as uncontrollable dendritic growth of Li and severe volume changes during Li plating-stripping. Recently, the utilization of three-dimensional (3D) frameworks as a host for Li-metal storage has aroused great interest as an effective strategy that can address the technical issues of Li metal.

ii) Strategical material design by "nanostructural engineering" for the development of each Si and Li-metal anode was proposed.

Based on the challenges, we found Si anode material should have, firstly, high Si content for higher energy density, robust structure with a combination of stable components such as carbon and compatible SiO_x, and high conductivity and thermal properties with facile synthesis. Secondly, we also found Li-metal anode material (as host framework) should have high pore volume for more Li-metal storage, high electrical conductivity and high Li affinity for ease of Li diffusion, and highly lithiophilic surface chemistry for the prevention of dendritic growth.

iii) Computational predictions and calculations for material design were conducted.

By computational predictions and calculations, firstly in the Si anode research, we concluded double-gyroid highly ordered mesoporous silica is one of the best Si sources to relieve volume expansion and maintain mechanical strength through the comparative analysis among different nanostructures such as 0D and 1D Si-based materials. Secondly in the Li-metal anode research, it can be found that cobalt embedded, mesoporous, nitrogen-doped graphite show high Li affinity and highly lithiophilic surface chemistry which is attributable to the low formation energy of N-doped graphite. Consequently, bimetallic Zn/Co ZIF-derived carbon was introduced due to its physical/chemical properties that satisfy every condition from the caculation.

iv) Material synthesis of each Si and Li-metal anode based on the design was performed and its outstanding electrochemical performance was confirmed.

As synthesized gyroid 3D network Si embedded in SiO_x/C as Si-anode (3D-Si@SiO_x/C) and cobalt embedded, mesoporous, nitrogen-doped graphite (Co@N-graphite) as Li-metal anode showed outstanding electrochemical performances compared to those of previous researches in terms of cyclability, Coulombic efficiency and stability at high current density. In addition,

each of material can be synthesized in facile and cost-effective ways that might be available in mass production.

v) Additional state-of-art analysis techniques were proposed.

one of our findings is that the Li-ion diffusivity is promoted along the twin boundaries in defect-abundant Si nanocrystals. The enhanced diffusivity in the defects homogeneously changes the Li-ion distribution for crystalline silicon, paving the way to reversible enhancement of Li-ion migration. Moreover, the redistribution of Li-ions relieves the concentration of stress in crystalline Si, resulting in acceptable performance in the first cycle, as is reflected by coulombic efficiency. In addition, TEM observation technique of Li-metal is proposed. In fact, microscopic observation of Li-metal is challenging because Li-metal easily transforms in air and easily decomposes in electron beam environment. By careful sampling and controlled electron beam exposure, it can be detected minute changes in Li-metal plated porous carbon frame finally.

Finally, this thesis suggests that applicability and useful information can be derived for developing Si and Li-metal anodes with high energy density. This is also believed to be of broad and significant interest to the community of researchers in the fields of nanomaterials science and computation theory related to energy storage and conversion.

7.2. Recommendations for Further Work

In order to let the development of Li-metal anode enter commercialization stage, there are still practical hurdles left. A practical cell coupled with ZIF-derived carbon host containing Li-metal and high-capacity cathode should show an energy level of at least 300 Wh kg^{-1}, which exceeds those of graphite and silicon-based anodes[1-3], like Figure 7.1a. Many previous studies have conducted electrochemical testing in coin cells to understand the basic electrochemical behavior. although there are remarkable differences between coin cells and practical cells. For instance, coin cells are tested under mild conditions, such as with a thin cathode and flooded electrolyte (Figure 7.1c), and coin cells (mAh) are much smaller than practical cells (Ah), even at cell-level capacity[1,2]. On the other hand, practical cells are cycled with thick cathode materials and lean electrolyte, as shown in Figure 7.1d. In the case of practical pouch cells, the capacity ratio of the negative electrode to the positive electrode (N/P ratio or cell balance) is strictly limited to below 2, and the ratio of electrolyte mass to cathode capacity (E/C ratio) is kept below 3.0 g Ah^{-1} [4]. This testing conditions dramatically shorten the cycle life of Li-metal battery. The coin cell type, however, is operated in much higher N/P ratio and E/C ratio conditions compared to those of the pouch cell, as shown in Figure 7.1e, which are far from practical operation conditions. It implies that the extremely stable anode materials are needed in practical cell.

Figure 7.1b shows the weight percentages of the components of the Li-metal battery pouch cell satisfying these restricted conditions, and it shows that the cathode is responsible for most of the weight, while the weight of the anode occupies only 5.5 %. This implies that the loss of gravimetric capacity due to the weight of host materials may be a disadvantage in the coin cell, but the effects of host weight are not significant in the practical cell. That is, harsh testing conditions are actually more dominant in the practical pouch cell. In this regard, because the

anode material, working in conjunction with rationally designed host materials, will effectively control huge volume expansion and Li dendritic growth during harsh cell operations, it would be suitable to withstand such harsh testing conditions. Furthermore, it is expected that an energy storage device could be obtained with stable high energy densities over 300 Wh kg^{-1} if fully pre-lithiated host materials with theoretical capacity over 1500 mAh g^{-1} could be applied by coupling with a high capacity cathode.

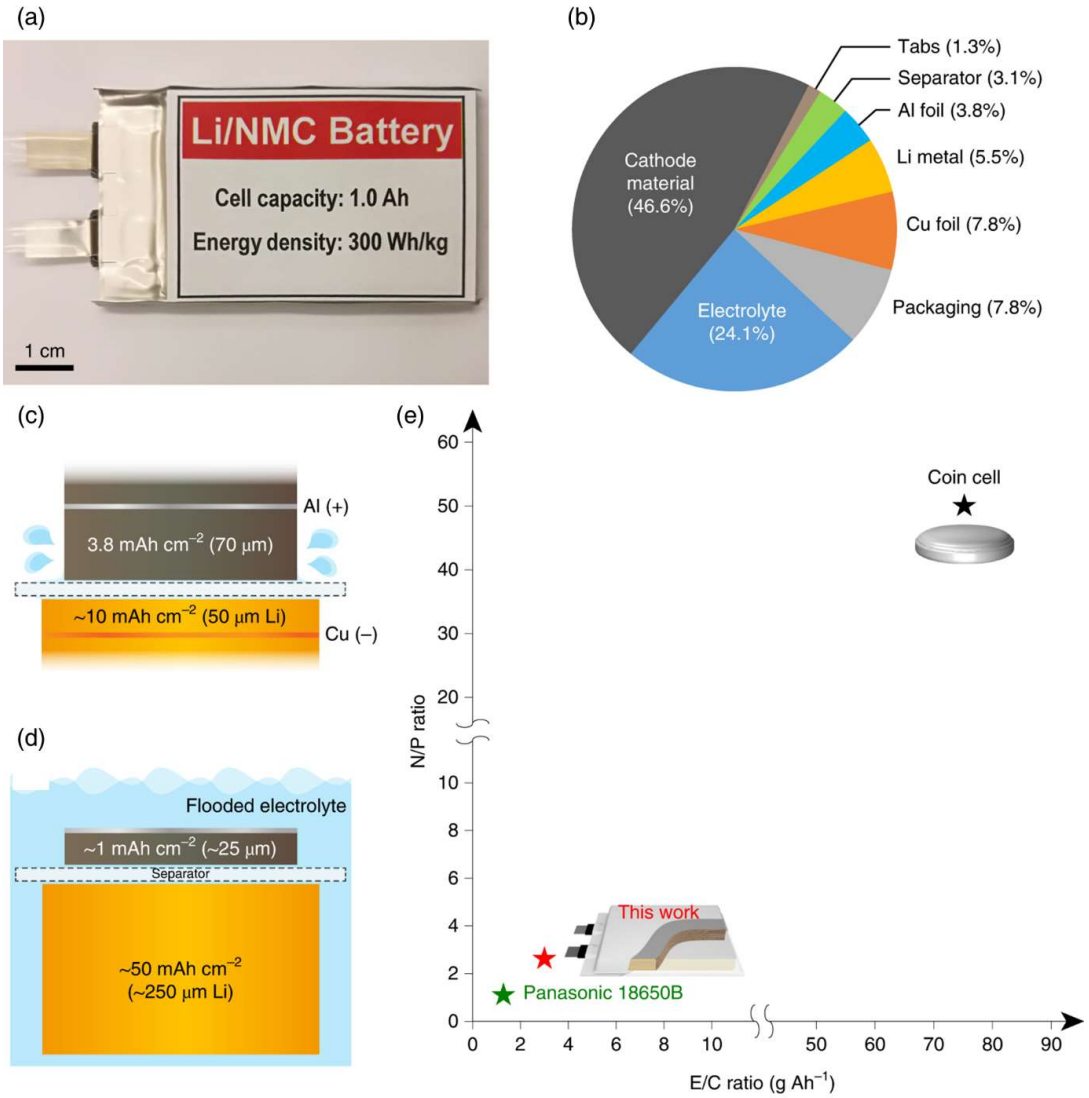

Figure 7.1. (a) Digital photograph of an Li-metal pouch cell containing Li-metal anode coupled with NMC 622 cathode. (b) A pie chart showing the weight percentages of all the components in the pouch cell. A schematic diagram of (c) one repeating unit in the pouch cell with an N/P ratio of 2.6 and an E/C ratio of 3.0 g Ah^{-1}, and (d) a typical coin cell configuration with an N/P ratio of 50 and an E/C ratio of 75 g Ah^{-1}. (e) A comparative plot for the N/P and E/C ratios[1].

In this regard, Li-metal host material should exhibit much more stable and higher specific capacity performaces than, as tested with coin-type cell configuration in previous reports. For example, to reach 1500 mAh g^{-1}, pore volume of porous carbon ought to exceed at least 1.2 cm^3g^{-1} (in the condition that fully dense Li-metal is fully packed in pores in host frame.). That is, however, tough or even infeasible value to satisfy only in micro/mesoporous carbon itself.

In this respect, as recommended future works based on this thesis work experiences, it is suggested that macropore supported (e.g. hollow sphere, hierarchical structure or mesh/foam), high conductive hosts (e.g. carbon or metals), with high Li-metal affinity (e.g. incorporation of N, Co, Ag or Si), by applying dual-phase lithiation/metallization (e.g. with carbon or silicon), be considered on the development of Li-metal host anodes.

7.3. References

[1] C. Niu, H. Lee, S. Chen, Q. Li, J. Du, W. Xu, J.-G. Zhang, M. S. Whittingham, J. Xiao, J. Liu, *Nat. Energy* **2019**, 4, 551.

[2] S. Chen, C. Niu, H. Lee, Q. Li, L. Yu, W. Xu, J-G. Zhang, E. J. Dufek, M. S. Whittingham, S. Meng, J. Xiao, J. Liu, *Joule* **2019**, 3, 1094.

[3] J. Liu, Z. Bao, Y. Cui, E. J. Dufek, J. B. Goodenough, P. Khalifah, Q. Li, B. Y. Liaw, P. Liu, A. Manthiram, Y. S. Meng, V. R. Subramanian, M. F. Toney, V. V. Viswanathan, M. S. Whittingham, J. Xiao, W. Xu, J. Yang, X.-Q. Yang, J.-G. Zhang, *Nat. Energy* **2019**, 4, 180.

[4] C. Niu, H. Pan, W. Xu, J. Xiao, J.-G. Zhang, L. Luo, C. Wang, D. Mei, J. Meng, X. Wang, Z. Liu, L. Mai, J. Liu, *Nat. Nanotechnol.* **2019**, 14, 594.

Appendix A: List of Abbreviations & Symbols

Abbreviations

0D	zero-dimensional
1D	one-dimensional
2D	two-dimensional
2-MIM	2-methylimidazolate
3D	three-dimensional
3-DOM	three-dimensional-ordered macro-microporous
BET	Brunauer-Emmett-Teller
BF-STEM	bright field scanning TEM
BJH	Barrett-Joyner-Halenda
BZC	bimetallic ZIF-carbon
c-$Li_{15}Si_4$	crystalline lithium silicide
CNT	carbon nanotube
COF	covalent organic framework
c-Si	crystalline Si
CVD	chemical vapor deposition
DEC	diethyl carbonate
DFT	Density Functional Theory
DMC	dimethyl carbonate
DME	dimethyl ether
DOL	1,3-dioxolane
DSC	differential scanning calorimetry
EC	ethylene carbonate

EDS, EDX	energy-dispersive X-ray spectroscopy
EELS	electron energy loss spectroscopy
EV	electric vehicle
fcc	face-centered cubic
FEC	fluoroethylene carbonate
FESEM	field emission scanning electron microscopy
GGA-PBE	generalized gradient approximation developed by Perdew, Burke and Ernzerhof
HAADF-STEM	high angle annular dark field scanning TEM
h-BN	hexagonal boron nitride
Hex	hexagonal
ICE	initial Coulombic efficiency
IT	information technology
KIT-6	double-gyroid highly ordered mesoporous silica
LIB	lithium-ion battery
LiTFSI	lithium bis(trifluoromethanesulfonyl) imide
LMO	lithium manganese oxide
MOF	metal-organic framework
NCA	nickel cobalt aluminum oxide
NEB	nudged elastic band
NMC	lithium nickel manganese cobalt oxide
PAA	polyacrylic acid
PAW	projector augmented wave
PCF	porous carbon framework

PCP	porous coordination polymer
PI	polyimide
PMF	poly melamine formaldehyde
PS	polystyrene
rGO	reduced graphene oxide
RT	room temperature
SBA-15	Santa Barbara Amorphous-15
SEI	solid electrolyte interphase
Si-NP	Si nanopowder
SOD	sodalite
Td	tetrahedral
TEM	transmission electron microscope
TGA	Thermogravimetric analysis
VASP	Vienna *Ab-initio* Simulation Package
vs.	versus
XPS	X-ray photoelectron spectroscopy
XRD	X-ray diffraction
ZC	ZIF-carbon
ZIF	zeolitic imidazolate framework

Symbols

ΔG^{*}_{het}	energy barrier for heterogeneous nucleation
S	shape factor
ΔG^{*}_{hom}	energy barrier for homogeneous nucleation
$d\varepsilon^{e}_{ij}$	elastic strain
E	Young's modulus
v	Poisson's ratio
σ_{kk}	diagonal components of stress
δ_{ij}	Kronecker delta
$\dot{\lambda}$	scalar coefficient
Ω	partial molar volume
c	normalized Li concentration
D	Li diffusivity
D_0	chemical diffusion coefficient
α	constant to determine the thickness of phase boundary
ρ_{diff}	charge density difference

Appendix B: List of Figures, Tables & Notes

schematic illustration at (e) earlier cycles and (f) later cycles. The scanning electron microscopy (SEM) images in (e) and (f) show the anode appearance after Li plating[40].

Figure 2.9. Schematic diagrams of Li-metal research strategies through an artificial SEI.

Figure 2.10. Schematic diagrams of Li-metal research strategies through an interfacial layer.

Figure 2.11. Schematic diagrams of Li-metal research strategies through a 3D structured electrode.

Figure 2.12. Schematic diagrams of Li-metal research strategies through a stable host for Li storage[68].

Table 2.1. Representative host materials for Li-metal storage and the electrochemical performance of each material.

Figure 2.13. (a) Requirements for suitable host material to store Li-metal and (b) schematic diagram showing the Li-metal stored in lithiopilic pore of suitable host material.

Figure 2.14. Illustrations of typical zeolitic imidazolate frameworks (ZIFs)[86].

Figure 2.15. The synthesis and carbonization processes for (a) ZIF-8, (b) ZIF-67, and (c) a bimetallic ZIF.

Figure 2.16. (a, c, e) Schematic illustrations showing representative host materials for Li-metal storage based on ZIF-derived carbon. (a) ZnO/carbon framework[77], (c) cMOFs[78], and (e) PCF[79]. (b, d, f) Electrochemical characterization corresponding to each host material.

Figure 2.17. Schematic illustrations showing further strategies to improve the pore structure of ZIF-derived carbon and the corresponding transmission electron microscope (TEM) images. (a) KOH activation[99], (b) hollow carbon activated by tannic acid etching[103], and (c) ordered macro-microporous structure via polystyrene (PS) templating[107].

Figure 3.1. Graphical abstract.

Figure 3.2. Gyroid and double-gyroid structure modeling for the continuum scale analysis.

Figure 3.3. Continuum scale analysis for the simulation of particle and unit volume changes in silicon-based materials before and after full lithiation. (a) Si nanoparticle in free space. (b) Si nanoparticle embedded in 1D-SiO_2 structure. (c) Si nanoparticles embedded in a 3D network gyroid structure and the total unit of the gyroid 3D network Si@SiO_x. (d) Comparison of the relative volume changes of (a-d) during lithiation. #Si indicates the number of Si nanoparticles randomly located inside the gyroid structure from #Si = 1 to #Si = 21 (fully packed).

Figure 3.4. Synthesis of gyroid 3D network of Si@SiO_x/C. (a) Schematic illustration of the synthetic route for the 3D-Si@SiO_x/C via one-pot magnesiothermic reduction and carbonization of the KIT-6, including the polymer template. (b) Transmission electron microscope (TEM) image of highly ordered double-gyroid KIT-6 including polymer template with its high angle annular dark field – scanning TEM (HAADF-STEM) image in the inset. (c-d) TEM image of the 3D-Si@SiO_x/C (c) and its corresponding HRTEM image (d), showing that the c-Si particles are interconnected inside the SiO_x/C network frame. Scale bars, 20 nm for (b, including inset) and (c), 5 nm for (d).

Figure 3.5. Structural and electrochemical characterizations of various types of products. (a) XRD patterns of 6 products and reference Si NP. (b-e) Physical and electrochemical properties of 6 products and reference Si NP: c-Si particle sizes (b), specific capacities (c), initial Coulombic efficiencies (d), and cyclability (e). (f-h) confirmation of the presence of carbon: powder images (f), Raman spectra (g) and thermogravimetric analysis (TGA) curves (h) of 750-w/o and w/ polymer template samples. (i) Electron energy loss spectroscopy (EELS)

elemental mapping images of the 750-w/ polymer template. (j) XPS Si 2p spectra of the 750-w/ polymer template during Ar^+ sputtering for 120 seconds. Scale bar, 50 nm for (i).

Figure 3.6. (a) XRD patterns collected before HCl washing, (b) TEM images of samples obtained under different synthesis conditions. (w/ / w/o: synthesized from calcined / uncalcined KIT-6, 675 / 750 / 825: synthesis temperatures) Scale bars, 50 nm for (b).

Figure 3.7. Galvanostatic charge-discharge profiles (a, c) and cycling performances (b, d) of three w/o samples (a, b) and three w/ samples (c, d) with Si-NP anode. (e) Table of their electrochemical properties. (w/ / w/o: synthesized from calcined / uncalcined KIT-6, 675 / 750 / 825: synthesis temperatures, ICE: initial Coulombic efficiency).

Figure 3.8. N_2 adsorption/desorption isotherms and (b) pore size distributions of the KIT-6 including the polymer template and the 3D-Si@SiO_x/C. (c) Table of calculated surface area and average pore diameter, as determined by the Brunauer-Emmett-Teller (BET) and Barrett-Joyner-Halenda (BJH) methods, respectively.

Figure 3.9. XRD patterns of the KIT-6 including the polymer template (precursor) and the 3D-Si@SiO_x/C (product).

Figure 3.10. (a) XPS depth profiling, and (b) survey, (c) C 1s, and (d) O 1s spectra of the 3D-Si@SiO_x/C.

Figure 3.11. Effect of defects in Si NPs. (a) TEM observations of abundant defects in Si NPs of the 3D-Si@SiO_x/C, with SAED patterns in the insets. (b) Photograph with description of the method for inducing chemical lithiation on the 3D-Si@SiO_x/C. (c) TEM observations of different types of lithiation behavior, depending on the existence of defects in the Si NPs. Scale bars, 100 nm, 50 nm, 5 nm, 5 nm for (a), 50 nm, 5 nm, 5 nm for (b). (d) Li interstitial atom in tetrahedral pore of Si supercell. (e) Li atom transition to the neighbouring tetrahedral sites. (f)

Atomistic configuration of twin boundary and representative Li migration. (g) Migration energy barriers calculated by the climbing-image nudged elastic band (NEB) method and corresponding diffusion coefficient in c-Si, amorphous (a)-Si, and through the twin boundary. (h) Geometry of 3D gyroid structure with Si nanoparticle and 2D projected representative volume element for the Si@SiO_x/C network structure. (i) Stress evolution of Si particle in SiO_x matrix during lithiation without and with a twin defect. (SOC: state of charge)

Figure 3.12. Continuum scale analysis for the lithiation evolution of a crystalline Si particle. Li contour plots during Li evolution (a) without and (b) with a twin defect. Normalized radial Li concentration distribution during lithiation (c) with and (d) without a twin defect. (SOC: state of charge)

Figure 3.13. Electrochemical performances and ex situ TEM and SEM observations. (a) Galvanostatic charge-discharge profiles of the 3D-Si@SiO_x/C and Si NP anodes. (b) Cycling performances (closed symbol: discharge capacity, open symbol: charge capacity) and Coulombic efficiencies of the 3D-Si@SiO_x/C and Si NP anodes at a current density of 200 mA g^{-1}. (c-d) Galvanostatic charge-discharge profiles (c) and cycling performance (d) of the 3D-Si@SiO_x/C at different output current densities of 200, 500, 1000, 2000, and 4000 mA g^{-1} (0.12, 0.31, 0.61, 1.22, and 2.45C, respectively, 1C = 1635 mA g^{-1}). (e-h) Cross-sectional SEM images of the 3D-Si@SiO_x/C electrodes at different cycles: pristine (e), first cycle charged (1^{st} cycle-C) (f), first cycle discharged (1^{st} cycle-D) (g), and hundredth cycle discharged (100^{th} cycle-D) (h). (i-l) HRTEM observations of the Si-NP particles at different reaction states; pristine (i), 1^{st} cycle-C (j), 1^{st} cycle-D (k), and 100^{th} cycle-D (l). Scale bars, 20 μm for (e-h), 20 nm for (i-l).

Figure 3.14. HRTEM observation of partially collapsed 3D-Si@SiO_x/C particles after 100 cycles. Scale bar, 20 nm.

Figure 3.15. Thermostability properties. (a) First cycle charge-discharge profiles, corresponding differential capacity plots (inset).(b) Cycling performances of 3D-Si@SiO_x/C at RT and 60 °C. (c-d) DSC curves (c) and corresponding cumulative heat generation profiles (d) of the 3D-Si@SiO_x/C, Si@SiO_x, and Si NP electrodes after full lithiation. (e) Various aspects of the individual contents of the 3D-Si@SiO_x/C.

Figure 4.1. Schematic illustration of the synthesis of nonstoichiometric Si/SiO_x anode materials via magnesiothermic reduction at various heat-treatment temperatures.

Figure 4.2. HAADF-STEM image and its corresponding BF-STEM image of the KIT-6. The left inset shows the structure of KIT-6, and the right inset the corresponding XRD pattern.

Figure 4.3. HRTEM images of (a) Si/SiO_x-1, (b) Si/SiO_x-2, and (c) Si/SiO_x-3. (d) XRD patterns of this series of Si/SiO_x samples.

Figure 4.4. Low- and high-resolution transmission electron microscope (TEM) images of the Si-NP as a reference.

Figure 4.5. (a) Si 2p X-ray Photoelectron spectroscopy (XPS) spectra of the Si/SiO_x-1, Si/SiO_x-2, and Si/SiO_x-3 samples with Si-NP, de-convoluted to the individual silicon oxidation states. (b) Their areal ratios, and (c) their estimated oxygen concentrations (stoichiometric ratio of oxygen divided by total silicon, including metallic silicon).

Table 4.1. Numerical results corresponding to (a) Figure 4.5b and (b) Figure 4.5c.

Figure 4.6. First cycle charge/discharge profiles of the Si/SiO_x-1, Si/SiO_x-2, and Si/SiO_x-3 anodes, together with the Si-NP anode.

Figure 4.7. Cycling performances of the Si/SiO_x-1, Si/SiO_x-2, and Si/SiO_x-3 anodes, together with the Si-NP anode.

Figure 4.8. Galvanostatic charge-discharge profiles and the corresponding differential capacity plots of (a) Si-NP, (b) Si/SiO_x-3, (c) Si/SiO_x-2, and (d) Si/SiO_x-1.

Figure 4.9. (a) Experimental results on the charge and discharge capacities of the samples (corresponding to the results in Figure 4.8). (b) Calculated total and reversible capacities for different stoichiometries of SiO_x from the XPS results.

Table 4.2. Numerical results corresponding to (a) Figure 4.9a and (b) Figure 4.9b.

Figure 4.10. HAADF-STEM image and EDS elemental mapping images of the Si/SiO_x-2.

Figure 4.11. N_2 adsorption/desorption isotherms of the KIT-6 and Si/SiO_x-2.

Figure 5.1. Schematic illustration of the concept of this paper, the synthesis of bimetallic ZIFs by hybridization of ZIF-8 and ZIF-67. Zinc nitrate hexahydrate and cobalt nitrate hexahydrate sources (Solution A) were used as the metal precursor and 2-methylimidazole (Solution B) was used as the organic linker.

Figure 5.2. FESEM images and size distribution graphs of ZIF derived carbons: (a) ZIF-8 derived carbon; bimetallic ZIF derived carbons with different molar ratios of zinc to cobalt ions: (b) $Zn_{0.995}{\cdot}Co_{0.009}$, (c) $Zn_{0.95}{\cdot}Co_{0.05}$, (d) $Zn_{0.9}{\cdot}Co_{0.1}$, (e) $Zn_{0.67}{\cdot}Co_{0.33}$, (f) $Zn_{0.33}{\cdot}Co_{0.67}$, and (g) $Zn_{0.2}{\cdot}Co_{0.8}$: and (h) ZIF-67 derived carbon.

Figure 5.3. XRD patterns of ZIF-8, ZIF-67 and various bimetallic ZIFs derived carbons with different molar ratios of zinc to cobalt ions. Right column shows representative FESEM images.

Figure 5.4. HRTEM images of (a) ZIF-8 derived carbon; (b) bimetallic ZIF derived carbons with different molar ratios of zinc to cobalt ions with (b) $Zn_{0.995}{\cdot}Co_{0.009}$, (c) $Zn_{0.95}{\cdot}Co_{0.05}$, (d) $Zn_{0.9}{\cdot}Co_{0.1}$, (e) $Zn_{0.67}{\cdot}Co_{0.33}$, (f) $Zn_{0.33}{\cdot}Co_{0.67}$, and (g) $Zn_{0.2}{\cdot}Co_{0.8}$: and (h) ZIF-67 derived carbon.

Figure 5.5. (a) Schematic illustration of bimetallic ZIF derived carbon with zinc to cobalt molar ratio of $Zn_{0.33}{\cdot}Co_{0.67}$. (b) TEM image of $Zn_{0.33}{\cdot}Co_{0.67}$ bimetallic ZIF derived carbon. (c) High resolution TEM image of CNT structure in the area enclosed by the red dashed line in (b). Element mapping images of (d) cobalt and (e) carbon in the area enclosed by the white dashed line in (b).

Figure 5.6. (a) N2 adsorption-desorption isotherms results, (b) pore size distribution results, and (c) surface area and pore volume graph of ZIF-8, bimetallic ZIF derived carbons, which have zinc to cobalt molar ratios of $Zn_{0.995}{\cdot}Co_{0.009}$, $Zn_{0.95}{\cdot}Co_{0.05}$, $Zn_{0.9}{\cdot}Co_{0.1}$, $Zn_{0.67}{\cdot}Co_{0.33}$, $Zn_{0.33}{\cdot}Co_{0.67}$, $Zn_{0.2}{\cdot}Co_{0.8}$, and ZIF-67 derived carbon.

Figure 5.7. Schematic diagram representing the synthetic process.

Figure 5.8. Low magnification SEM images of (a) ZIF-8, (b) 800C-ZIF-8, and (d) 1000C-ZIF-8. Bright field TEM (BF-TEM) images of (c) 800C-ZIF-8 and (e) 1000C-ZIF-8. High-angle annular dark field-scanning TEM (HAADF-STEM) elemental mapping images of (f) 800C-ZIF-8 and (g) 1000C-ZIF-8. (h) The elemental ratio of ZIF-8 derived carbon structures at 800 ºC and 1000 ºC of temperature.

Figure 5.9. Raman spectra of 800C-ZIF-8 and 1000C-ZIF-8.

Figure 5.10. (a) Average particle size of 800C-ZIF-8 and 1000C-ZIF-8. (b) Electrical conductivity and powder density at 64 MP. (c) The average pore diameter and (d) pore volume and BET surface area of each porous carbon nanoarchitecture.

Figure 5.11. N_2 adsorption/desorption isotherms of 800C-ZIF-8 and 1000C-ZIF-8.

Figure 5.12. Illustration of various types of ZIF crystals with their carbonized forms.

Table 5.1. Illustration Intrinsic properties of each type of ZIF-derived carbon.

Figure 5.13. Theoretical capacities of each type of ZIF-derived carbon.

Figure 6.1. Li-metal growth behaviour and effects of hetero-atom doping for chemically enhancing surface lithiophilicity. a, b, Illustrations and representative TEM images explaining two types of distinctive Li-growth behaviour of porous carbon composites: zinc/nitrogen@amorphous carbon (a) and cobalt/nitrogen@graphitic carbon (b). c, Density functional theory (DFT) calculations of the Li formation energies on two different carbon structures with possible hetero-atom dopants. d, e, Atomic modelling of Li interstitial formation energy in amorphous carbon (d) and graphite (e). f, g, Atomic models of hetero-atoms doped in amorphous carbon (f) and graphite (g). Scale bars, 50 nm for a, 50 nm for b.

Figure 6.2. a, TEM image of the pristine Zn-N-amorphous carbon. b, TEM images of the Li-plated Zn-N-amorphous carbon (2 mAh cm^{-2}) in 1 M $LiPF_6$ in EC/DMC (50 : 50 in vol %) electrolyte.

Figure 6.3. TEM images of the Li-plated Co-N-graphitic carbon (2 mAh cm-2) in 1 M LiPF6 in EC/DMC (50 : 50 in vol %) electrolyte.

Figure 6.4. Characterizations and optimization of ZIF-carbon series. a, Comparison of the physical properties of pore volume, average pore diameter, and surface area on a series of five ZIF-carbons. b, c, Theoretical gravimetric capacity calculations, dependent on the pore volume for each host material, including dual-phase carbon/Li-metal anode (b) and pre-lithiated carbon host anode (c). d, scanning electron microscope (SEM) and TEM images with corresponding

energy dispersive X-ray spectroscopy (EDX) elemental mapping images of BZC-2:1. Scale bars, 5 μm, 500 nm, 50 nm, 20 nm, 500 nm, 500 nm, 500 nm and 500 nm for d.

Figure 6.5. SEM observations and XRD patterns of ZIF-carbon series.

Figure 6.6. N_2 adsorption/desorption isotherms and calculated physical properties of samples in the ZIF-carbon series.

Figure 6.7. Electrical conductivity measurements of the ZIF-carbon series when compressed under different pressures. Pressure-conductivity plots (top) and density-conductivity plots (bottom).

Note 6.1. Theoretical Capacity Calculations

Figure 6.8. SEM and TEM images with EDX elemental mapping images of the BZC-2:1 before HCl washing.

Figure 6.9. SEM and Effects of nitrogen doping in the BZC-2:1. a, b, c, XPS spectra of the BZC-2:1 measured after 120 seconds of Ar ion beam sputtering: Co 2p (a), C 1s (b), and N 1s (c). d, illustration of three types of nitrogen doping in graphite defects. e, f, g, Atomic modelings of Li interstitial formation energy in three types of nitrogens doped into the graphite structure: pyridinic N (e), pyrrolic N (f), and quaternary N (g).

Figure 6.10. XPS spectra and depth profiles of the BZC-2:1.

Figure 6.11. TEM images of the Li-plated BZC-2:1 (2 mAh cm^{-2}) in 1 M LiTFSi in DOL/DME (50 : 50 in vol %) + 1 wt % $LiNO_3$ electrolyte.

Figure 6.12. Electrochemical measurements on Super-P, ZC-Zn, and BZC-2:1 electrodes for Li-metal anode performances. a, voltage hysteresis observations in the first cycle charging with the areal capacity of 2 mAh cm^{-2}; b, voltage profiles of the three electrodes with areal capacity

0.2 mAh cm^{-2} at 0.2 mA cm^{-2}. c, d, e, Voltage behaviour of each cycle on test b; cycle 1 (c), cycle 5 (d), and cycle 10 (e). f, Concentration relaxation behaviour of the Super-P electrode during ten minutes of rest time. g, h, voltage profiles of the ZC-Zn and BZC-2:1 electrodes at 0.2 mA cm^{-2} with different charge/discharge capacities of 0.4 mAh cm^{-2} (g) and 0.6 mAh cm^{-2} (h). i, j, k, voltage behaviour of each cycle on test h: cycle 1 (i), cycle 20 (j), and cycle 40 (k). l, Concentration relaxation behaviour of the BZC-2:1 electrode during ten minutes of rest time.

Figure 6.13. Coulombic efficiencies on each cycle of the ZC-Zn and the BZC-2:1 electrodes from the tests shown in Figure 6.11c and 6.11d, respectively.

Figure 6.14. Microscopic observations of Li-metal plated BZC-2:1. a, b, Top view (left, photograph in inset) and cross-sectional view (right) SEM images of the super-P electrode (a) and the BZC-2:1 electrode (b). c, Schematic illustration of Li-metal decomposition behaviour in a TEM specimen with electron beam exposure. d, e, TEM images of the Li-metal plated BZC-2:1 particle after different times under electron beam exposure; high angle annular dark field – scanning TEM (HAADF-STEM) images (d), bright field (BF)-STEM images (e). Scale bars, 10 μm and 20 μm (1 μm, inset) for a, 10 μm and 20 μm (1 μm, inset) for b, 200 nm for d and e.

Figure 6.15. Critical role of Co. Charge density difference calculations of Li adsorption on N doped graphite and on Co-N doped graphite. a, b, transferred charge behaviours on N-graphite (a) and Co-N-graphite (b). c, Their charge deficiency in relation to the z-axis hexagonal structure of graphite.

Figure 6.16. Summary of main results, containing schematic illustrations for understanding BZC-2:1.

Figure 7.1. (a) Digital photograph of an Li-metal pouch cell containing Li-metal anode coupled with NMC 622 cathode. (b) A pie chart showing the weight percentages of all the components in the pouch cell. A schematic diagram of (c) one repeating unit in the pouch cell with an N/P ratio of 2.6 and an E/C ratio of 3.0 g Ah^{-1}, and (d) a typical coin cell configuration with an N/P ratio of 50 and an E/C ratio of 75 g Ah^{-1}. (e) A comparative plot for the N/P and E/C ratios[1].

Appendix C: List of Publications & Awards

Publications

1. **Jaewoo Lee**, Seung Hyun Choi, Hamzeh Qutaish, Yuhwan Hyeon, Sang A Han, Yoon-Uk Heo, Dongmok Whang, Jong-Won Lee, Janghyuk Moon, Min-Sik Park, Jung Ho Kim "*Structurally Stabilized Lithium-Metal Anode via Surface Chemistry Engineering*" Submitted to **Energy Storage Materials** in October 2020.

2. **Jaewoo Lee**, Sang A Han, Hamzeh Qutaish, Hien Thi Thu Pham, Min-Sik Park, Jung Ho Kim "*The effect of carbonization temperature on zeolitic imidazolate framework derived carbon nanoarchitecture*" Submitted to **Materials Today Communications** in August 2020 (under review).

3. Yuhwan Hyeon, **Jaewoo Lee**, Hamzeh Qutaish, Sang A Han, Seung Hyun Choi, Sung Won Moon, Min-Sik Park, Dongmok Whang, Jung Ho Kim "*Lithium metal storage in metal-organic framework derived nanoarchitectures*" **Energy Storage Materials** 33 (2020) 95-107.

4. Junyoung Kim, **Jaewoo Lee**, Jonghyeok Yun, Seung Hyun Choi, Sang A Han, Janghyuk Moon, Jung Ho Kim, Jong-Won Lee, Min-Sik Park "*Functionality of Dual-Phase Lithium Storage in a Porous Carbon Host for Lithium-Metal Anode*" **Advanced Functional Materials** 30 (2020) 1910538

5. Sang A Han, Ju-Hyuck Lee, Wanchul Seung, **Jaewoo Lee**, Sang-Woo Kim, Jung Ho Kim "*Patchable and Implantable 2D Nanogenerator*" **Small** (2019) 1903519

6. **Jaewoo Lee**, Janghyuk Moon, Sang A Han, Junyoung Kim, Victor Malgras, Yoon-Uk Heo, Hansu Kim, Sang-Min Lee, Hua Kun Liu, Shi Xue Dou, Yusuke Yamauchi, Min-Sik Park, Jung Ho Kim "*Everlasting living and breathing gyroid 3D network in Si@ SiOx/C nanoarchitecture for lithium ion battery*" **ACS Nano** 13 (2019) 9607-9619

7. **Jaewoo Lee**, Sang A Han, Sang-Min Lee, Min-Sik Park, Jung Ho Kim "*Electrochemical properties of nonstoichiometric silicon suboxide anode materials with controlled oxygen concentration*" **Composites Part B: Engineering** 171 (2019) 107024

8. **Jaewoo Lee**, Sang A Han, Hamzeh Qutaish, Lok Kumar Shrestha, Katsuhiko Ariga, Jung Ho Kim "*Zeolitic Imidazolate Framework-Derived Nanoarchitectures for Lithium Metal Storage Medium*" **General Chemistry**" (2019) doi: 10.21127/yaoyigc20190011

9. Sang A Han, **Jaewoo Lee**, Jianjian Lin, Sang-Woo Kim, Jung Ho Kim "*Piezo/triboelectric nanogenerators based on 2-dimensional layered structure materials*" **Nano Energy** 57 (2019) 680-691

10. Sang A Han, **Jaewoo Lee**, Kyubin Shim, Jianjian Lin, Mohammed Shahabuddin, Jong-Won Lee, Sang-Woo Kim, Min-Sik Park, Jung Ho Kim "*Strategically designed zeolitic imidazolate frameworks for controlling the degree of graphitization*" **Bulletin of the Chemical Society of Japan** 91 (2018) 1474-1480

11. Peng Mei, **Jaewoo Lee**, Malay Pramanik, Abdulmohsen Alshehri, Jeonghun Kim, Joel Henzie, Jung Ho Kim, Yusuke Yamauchi "*Mesoporous manganese phosphonate nanorods as a prospective anode for lithium-ion batteries*" **ACS applied materials & interfaces** 10 (2018) 19739-19745

12. Hyundong Yoo, Eunjun Park, Juhye Bae, **Jaewoo Lee**, Dong Jae Chung, Yong Nam Jo, Min-Sik Park, Jung Ho Kim, Shi Xue Dou, Young-Jun Kim, Hansu Kim "*Si Nanocrystal-Embedded SiO x nanofoils: Two-Dimensional Nanotechnology-Enabled High Performance Li Storage Materials*" **Scientific reports** 8 (2018) 1-9

13. Jeonghun Kim, Ju-Hyuck Lee, **Jaewoo Lee**, Yusuke Yamauchi, Chang Ho Choi, Jung Ho Kim "*Research Update: Hybrid energy devices combining nanogenerators and energy storage systems for self-charging capability*" **Apl Materials** 5 (2017) 073804

14. Peng Mei, Malay Pramanik, **Jaewoo Lee**, Yusuke Ide, Zeid Abdullah Alothman, Jung Ho Kim, Yusuke Yamauchi "*Highly Ordered Mesostructured Vanadium Phosphonate toward Electrode Materials for Lithium-Ion Batteries*" **Chemistry–A European Journal** 23 (2017) 4344-4352

15. Jeonghun Kim, Christine Young, **Jaewoo Lee**, Yoon-Uk Heo, Min-Sik Park, Md Shahriar A Hossain, Yusuke Yamauchi, Jung Ho Kim "*Nanoarchitecture of MOF-derived nanoporous functional composites for hybrid supercapacitors*" **Journal of Materials Chemistry A** 5 (2017) 15065-15072

16. Peng Mei, Malay Pramanik, **Jaewoo Lee**, Toshiaki Takei, Yusuke Ide, Md Shahriar A Hossain, Jung Ho Kim, Yusuke Yamauchi "*Facile synthesis of nanoporous Li 1+ x V 1− x O 2@ C composites as promising anode materials for lithium-ion batteries*" **Physical Chemistry Chemical Physics** 19 (2017) 9156-9163

17. Malay Pramanik, **Jaewoo Lee**, Satoshi Tominaka, Yusuke Ide, Jung Ho Kim, Yusuke Yamauchi "*Unique nanocrystalline frameworks in mesoporous tin phosphate prepared through a hydrofluoric acid assisted chemical reaction*" **Journal of Materials Chemistry A** 4 (2016) 18091-18099

18. Jeonghun Kim, **Jaewoo Lee**, Jungmok You, Min-Sik Park, Md Shahriar Al Hossain, Yusuke Yamauchi, Jung Ho Kim "*Conductive polymers for next-generation energy storage systems: recent progress and new functions*" **Materials Horizons** 3 (2016) 517-535

Awards

1. **Matching Scholarship** (2016-2019) & **Faculty Scholarship** (2019-2020), Institute for Superconducting & Electronic Materials, Australian Institute of Innovative Materials, University of Wollongong, Australia.

2. **International Postgraduate Tuition Award** (2016-2020), Institute for Superconducting & Electronic Materials, Australian Institute of Innovative Materials, University of Wollongong, Australia.

3. **Poster Award**, 2019 International Conference on Nanospace Materials, 1-4 October 2019, The University of Queensland, St Lucia Campus, Australia.